GRAPHENE AND MoS_2 BASED NANO FUNCTIONAL MATERIALS FOR ELECTROCHEMICAL SENSING/STORAGE APPLICATIONS

A Thesis submitted
in partial fulfillment for the Degree of

Doctor of Philosophy

by

ASWATHI R.

Department of Chemistry

INDIAN INSTITUTE OF SPACE SCIENCE AND TECHNOLOGY
THIRUVANANTHAPURAM

April, 2019

CERTIFICATE

This is to certify that the thesis entitled **Graphene and MoS_2 Based Nano Functional Materials for Electrochemical Sensing/Storage Applications** submitted by **Aswathi R** to the Indian Institute of Space Science and Technology, Thiruvananthapuram, in partial fulfillment of the degree of **Doctor of Philosophy** is a *bonafide* record of research work carried out by her under my supervision. The contents of this thesis, in full or in parts, have not been submitted to any other Institution or University for the award of any degree or diploma.

Dr. K.Y. Sandhya
Supervisor
Department of Chemistry
IIST

Thiruvananthapuram – 695547
April, 2019

Counter signature of HOD with seal

DECLARATION

I declare that this thesis entitled **Graphene and MoS_2 Based Nano Functional Materials for Electrochemical Sensing/Storage Applications** submitted in partial fulfillment of the degree of **Doctor of Philosophy** is a record of original work carried out by me under the supervision of Dr. K.Y. Sandhya and has not formed the basis for the award of any other degree or diploma, in this or any other Institution or University. In keeping with the ethical practice in reporting scientific information, due acknowledgements have been made wherever the findings of others have been cited.

Aswathi R
SC13D003

Thiruvananthapuram – 695547
April, 2019

ACKNOWLEDGEMENTS

This thesis has been the consummation of the past five years of my doctoral research work in the Department of Chemistry, IIST. At this moment when I look back, it feels extremely rewarding and fascinating to write this thesis as it has been a journey well mixed with passion, excitement, setbacks, emotions, patience and joy, along with new/unexpected experiences and exciting achievements. Hereby, I wish to express my sincere appreciation to many people who have helped and supported me in one way or the other, intellectually and emotionally throughout this amazing expedition.

I am fully indebted and grateful to the person who made me acquiring the biggest educational achievement in my life, my research supervisor, my mentor, Dr. K.Y. Sandhya. She has opened me the door of fine fortune of working in a field of significant impact, devotedly and patiently, and thereby enriched me with a great sense of satisfaction and happiness to get hold of the knowledge and power of critical reasoning via these years of my research endeavor. Her intelligent ideas, thought provoking discussions, healthy criticisms, comprehensive understanding, scientific discernments, eternal enthusiasm, trust and patience in students and imperishable hard work, inspired and influenced me to establish the overall direction of my research, to move forward with investigations in depth, and to grow as an independent researcher and a noble individual at the end of this ride. She has been there always with her priceless support and care during my peaks and valleys regardless of whether the matter is related to research or personal life. It is difficult to describe my heartfelt gratitude for her invaluable guidance, patience and encouragement, which lead me to the successful completion of this thesis. Thank you very much Ma'am.

I thank Dr. K.S. Dasgupta, Former Director, IIST and Dr. V.K. Dhadhwal, Director IIST for providing me opportunity to accomplish my research work in the excellent ambience of IIST with the fine facilities provided. It is my profound privilege to express my extreme sense of gratefulness to Prof. Kuruvilla Joseph, Former HOD of Chemistry, and Dean Student activities, for his care and

support, who have generously spent his busy time to offer me valuable comments towards improving my working environment. I express my sincere gratitude to Prof. Nirmala Rachael James, HOD Chemistry, for her kind patience and readiness to hear all our problems in lab, finding solutions for the same and providing a healthy working atmosphere. I am immensely obliged to my doctoral committee members, Dr. S. Sampath, Dr. G. Ranga Rao, Dr. R.S. Rajeev, Dr. V. Seena and Dr. K. Prabhakaran for their constructive criticism and valuable suggestions at various phases of this research program and for lending me their expertise and intuition to investigate my scientific and technical problems. I render my sincere thanks to all the faculty members of Department of Chemistry for their boundless support during these years.

I owe my special and genuine thanks to my senior group member Dr. Mohamed Mukthar Ali, not only for his prompt support and encouragement, but for his kind care and brotherly affection which made me feel comfortable in the lab, especially during my initial months with the research when it was really hard to cope with the alien environment. His vigor and hunger to perform in adverse situation has inspired me a lot to thrive for excellence. I am very much thankful to all the staff members of Chemistry Department, specially Mr. Sreekumaran Nair, Mr. Loveson Albert, Mr. K. G. Dileepkumar, Mrs. Jayasree L, Mrs. Bindu, Mrs. Jayasree R, Mrs. Remya and Mrs. Rahna who have helped me in many ways for the healthy completion of my research works.

I am extremely thankful to Dr. S.A. Ilangovan, Mrs. S. Sujatha and Mr. V.R. Prabhu, Scientists, VSSC, Thiruvananthapuram for helping and extending their facility for battery analysis, STIC-CUSAT for providing SEM and TEM analysis, Department of Aerospace, IIST for Raman measurements, Kerala University, Thiruvananthapuram for SEM analysis, PSG College of Engineering, Coimbatore and NIIST, Thiruvananthapuram for TEM and SEM and AIMS Cochin for XPS analyses.

I sincerely admire the unfading help of all the senior research fellows of our Department, Dr. Raneesh Konnola, Dr. Rakesh R, Dr. Manjunatha Ganiga, Dr. Narasimman Rajaram, Dr. Sujith Vijayan, Dr. Roymon Joseph, Dr. Sarah Titus, Dr. Jalaja K, Dr. Sarika P.R, Dr. Kavitha M.K, Dr. Lavanya J and Dr.

Remyamol T for extending their unstinted support during the course of this study. Special thanks to my friend Dr. Sreejith M, for the timely motivation, fruitful discussions, healthy arguments and whole hearted support throughout these years. At this stage of my life, I gratefully acknowledge all my teachers who have taught me since my childhood, their blessings made me what I am.

My time at IIST was made memorable and enjoyable in large part due to the love and support of my friends and fellow researchers those became a part of my life. I take this opportunity to express my appreciation from the core of my heart to all my friends particularly Arya, Saisree, Meegle, Devi, Veena, Reshmi, Neema, Haritha, Rahul, Jayalekshmi, Praveen, Yogesh, Shiju, Randeep, Dheeraj, Sanu, Varsha, Ann and Sreekala who have granted me greatly contented, stimulating and fun filled surroundings.

Completing this venture would have been all the more difficult devoid of the lasting support and companionship of my dear friend Reshma, who has been there in all my ups and downs, went through my hard times together, cheered me on, helped me endure the frequent frustrations and celebrated each accomplishment with me. I really feel obliged to her.

Nobody has been more important to me in the pursuit of this endeavor, than the members of my family; my mother, father and brother, whose prayers and encouragement were what sustained me this far. They are the ultimate pillars of my strength and the prime source of support in my life. It was their love that raised me up again when I got weary. I owe everything to them. I also thank for the heart-warming kindness, care and patience from my mother-in law, father-in-law and sister-in-law for all of the sacrifices that they have made on my behalf during this long ride. And most of all, special thanks to my husband for his care, encouragement, faithful support and patience all through the different stages of this research work. Finally, I thank God Almighty for all his blessings, to have bestowed upon me ample strength, knowledge, good health, courage, inspiration, ability and opportunity to undertake this research study and to persevere and complete it satisfactorily.

Aswathi R

ABSTRACT

Electrochemistry, the chapter of chemistry that deals with the relations between electrical and chemical phenomena, has an ever increasing impact in everybody's daily life. Out of the myriad applications of electrochemistry, considerable attention has been devoted to the fields of electrochemical (EC) sensing and energy storage in recent decades. The emergence of nanotechnology as an indispensable tool for great advancement in science and technology has generated great capability of controlling materials at the nanometer scale and has enabled exciting opportunities to design materials with desirable electronic, ionic, photonic, and mechanical properties. This development has also contributed to develop and fabricate new structures and devices for EC sensing and energy storage applications in the recent years. In this scenario, this thesis work aims to address the challenges in the fields of EC sensing and storage by the rational design of nanofunctional materials, using 2D materials such as graphene (Gr) and Molybdenum disulphide (MoS_2).

The on-site monitoring of various analyte species in the diversity of fields by EC sensor requires considerable improvements in sensitivity, selectivity, and accuracy along with its inherently fast, accurate, compact, portable and cost-effective properties. Herein, we are trying to meet the aforementioned needs by developing various nanofunctional materials based on Gr and MoS_2. The various steps involved in the study are: the preparation of different types of Gr and MoS_2 based materials, their characterization, development of modified electrodes using the prepared materials, study of their EC sensing properties and finally examining the reasons/mechanisms behind the effective sensing behaviors.

A gold nanoparticle functionalized Gr (Au-Gr) is synthesized using a green synthetic strategy which exhibits excellent non-enzymatic sensing properties towards the detection of biomolecules glucose and ascorbic acid (AA). The limit of detection (LOD) values obtained were as low as 10 and 40 nM respectively for glucose and AA. The principal reason behind the remarkable electrocatalytic behavior is assigned to the synergistic effect of better conductivity properties of the atomically thin Gr sheets due to the cyclodextrin (CD) molecules and the catalytic properties of Au NPs (This work was published in *RSC Advances, 2015*). Mechanical pulverization of graphite for an optimized duration leads to highly solvent dispersible and high surface area Gr nanosheets called pulverized graphite (pGr) which displays highly sensitive and selective EC sensing towards dopamine (DA) with nanomolar detection capability and enables the simultaneous sensing of DA, AA and uric acid (UA). The sensor was found to be effective for real blood sample analysis also. The mechanism of sensing is explained on the basis of the unique aromatic basal plane structure of pGr with fewer oxidation sites and the edges rich with functional groups and/or defects (This work was published in *Sensors and Actuators, 2018*).

Further, this thesis tries to scrutinize the use of MoS_2/Gr based nanofunctional materials as EC sensing platforms for the effective environmental monitoring also. A solvent exfoliated MoS_2 prepared by a simple ultrasonication procedure has been subjugated for the parts per quadrillion (ppq) levels EC detection of mercury (II) ions (Hg^{2+}) exploiting the affinity of S^{2-} towards Hg^{2+}. The sensor assures its excellence towards Hg^{2+}detection in real sea water and tap water samples as well. Further it was found that the spontaneous redox reactions resulting from the affinity between the S^{2-} groups of MoS_2 and Hg^{2+} play the dominant role in achieving the unusual EC sensing realization (This work was published in *Journal of Materials Chemistry A, 2018*). A novel and simple hydrothermal method was utilized to prepare Nitrogen-doped graphene quantum dots (N-GQD) from polyaniline (PANI) and its EC sensing behavior was examined by taking nitrocompounds as analytes. The N-GQD exhibits ultra trace detection (0.2 ppb) of 2, 4, 6- trinitrophenol (TNP) and provides effective differentiation of various nitroaromatics. The unparalleled EC behavior of N-GQD is allocated to the richly N-doped aromatic structure of the N-GQD resulting from PANI, which can possibly promote closer molecular interactions with nitroaromatic compounds along with the enhanced conductivity and improved electron transfer ability owing to the *insitu* N-doping (This work was published in *ACS Sustainable Chemistry and Engineering, 2019*).

The final part of this thesis tries to explore the energy storage possibilities of Gr based nanofunctional composites contributing ideas to improve the capacity and cycle life of Si based anode materials in lithium ion batteries (LIBs). A novel and simple core-shell strategy for the preparation of a Si-Gr based composite, named as Si-nanographene oxide (Si-nGO) as an anode in LIB, results in an incomparable stability and remarkable storage capacity. The exceptional EC properties of the Si-nGO anode are attributed to the core-shell structure which limits the volume expansion of the Si NPs in all the directions, minimizing its volume expansion and the improved flexibility & conductivity offered by the thin nGO sheet matrix (This work was published in *Chemistry Select, 2018*).

In conclusion, this thesis presents an understanding of, how the logical designing of nanofunctional materials can meet the needs and conquer the challenges in the EC sensing of various analytes and the energy storage in LIBs.

TABLE OF CONTENTS

LIST OF FIGURES

LIST OF TABLES

ABBREVIATIONS

% RSD	Relative standard deviations
µA	microampere
°C	Degree Celsius
µF	microfarad
µL	microliter
µM	micromolar
2D	Two-dimensional
AA	Ascorbic acid
Ach	Acetyl choline
AFM	Atomic force microscopy
Ag^+	Silver ion
APS	Ammonium peroxydisulfate
AuNPs	Gold nanoparticles
BET	Brunauer-Emmett-Teller
CD	Beta cyclodextrin
CE	Counter electrode
CV	Cyclic voltammetry
DA	Dopamine
DMF	N,N dimethyl formamide
DMSO	Dimethyl sulphoxide
DNP	2,4-dinitrophenol

DNT	2,4 dinitrotoluene
DPV	Differential pulse voltammetry
EC	Electrochemical
EC-DEC	Ethylene carbonate-Diethylene carbonate
EC-DMC	Ethylene carbonate Dimethyl carbonate
EIS	Electrochemical impedance spectroscopy
eV	electron volt
FESEM	Field emission scanning electron microscope
FTIR	Fourier transform Infra-red
GC	Glassy carbon
GCE	Glassy carbon electrode
GO	Graphite oxide/ Graphene oxide
GQD	Graphene quantum dots
Gr	Graphene
H	Hydrogen
Hg^{2+}	Mercury (II)
HOMO	Highest occupied molecular orbital
HRTEM	High resolution transmission electron microscopy
IPA	Isopropanol
LDR	Linear dynamic range
LIBs	Lithium ion batteries
LOD	Limit of detection/Detection limit
LSV	Linear-sweep voltammetry

LUMO	Lowest unoccupied molecular orbital
M	Molar
mAh g^{-1}	milliampere hour per gram
mg	milligram
min	minutes
ml	milliliter
mm	millimeter
mM	millimolar
mV	millivolt
nM	nanomolar
nm	nanometer
NMP	N-methyl pyrrolidone
NP	2-nitrophenol
NPs	Nanoparticles
NPV	Normal pulse voltammetry
PANI	Polyaniline
Pb^{2+}	Lead (II)
PBS	Phosphate buffer solution
PL	Photoluminescence
ppb	parts per billion
ppm	parts per million
ppq	parts per quadrillion
ppt	parts per trillion
Pt	Platinum

PVDF	Polyvinylidene fluoride
RE	Reference electrode
rGO	Reduced graphene oxide
RT	Room temperature
S/N	Signal-to-noise
SA	Surface area
SAED	Selected area electron diffraction
SEI	Solid electrolyte interphase
SEM	Scanning electron microscope
Si NPs	Silicon nanoparticles
SPR	Surface plasmon resonance
STM	Scanning tunnelling microscope
SWV	Square wave voltammetry
TGA	Thermogravimetric analysis
THF	Tetrahydrofuran
TMDs	Transition-metal dichalcogenides
TNP	2,4,6-trinitrophenol
UA	Uric acid
UV	Ultra-violet
WE	Working electrode
XPS	X-ray photoelectron spectroscopy
XRD	X-ray diffraction
ZP	Zeta potential

NOTATIONS

C_{ox}	Concentration of the oxidized species
C_{red}	Concentration of the reduced species.
E	Potential
E^o	Standard potential of the redox couple
E_p	Peak potential
E_{pa}	Anodic peak potentials
E_{pc}	Cathodic peak potential
F	Faraday's constant;
i	Current
I_p	Peak current
i_{pa}	Anodic peak current
i_{pc}	Cathodic peak current
k_s	Heterogeneous electron transfer rate constant
n	Number of electrons transferred
R	Universal gas constant
RS	Solution resistance
T	Temperature (K)
t	Time
υ	Scan rate
α	Charge transfer coefficient
ΔE_p	Peak potential separation

NOMENCLATURE

Ag/AgCl	Silver/Silver chloride
$AgNO_3$	Silver nitrate
$CdCl_2$	Cadmium chloride
$Co(NO_3)_2$	Cobalt(II) nitrate
$CuSO_4$	Copper(II) sulfate
$FeCl_2$	Ferrous chloride
$FeCl_3$	Ferric chloride
H_2O_2	Hydrogen peroxide
H_2SO_4	Sulphuric acid
$HAuCl_4$	Hydrogen tetrachloroaurate (III)
HCl	Hydrochloric acid
Hg/Hg_2Cl_2	Mercury/Mercuric chloride
Hg_2Cl_2	Mercury(II) chloride
HNO_3	Nitric acid
$K_2Cr_2O_7$	Potassium dichromate
$KMnO_4$	Potassium permanganate
$LiCoO_2$	Lithium cobalt oxide
$LiPF_6$	Lithium hexafluorophosphate
MoO_3	Molybdenum oxide
MoS_2	Molybdenum disulphide
NaOH	Sodium hydroxide

$NiSO_4$	Nickel(II) sulfate
$PbNO_3$	Lead(II) nitrate
S	Sulfur
Si	Silicon
$SnCl_2$	Stannous chloride
$SnCl_4$	Stannic chloride
$Zn(NO_3)_2$	Zinc nitrate
-COOH	Carboxylic acid group
-OH	Hydroxyl group
-C=O	Carbonyl group
$-NO_2$	Nitro group
$-NH_2$	Amino group
-C-O-C	Ether group

CHAPTER 1

INTRODUCTION

This chapter comprises of the basics and fundamentals of electrochemistry, electrochemical (EC) sensors, various EC methods such as voltammetric, amperometric, potentiometric etc. and electrode processes. It provides a state-of-the-art literature survey on graphene (Gr) and molybdenum disulphide (MoS_2) based materials in EC sensing and a brief knowledge on the EC properties of Gr and MoS_2. Further this chapter explores the basics and challenges of EC energy storage, particularly silicon (Si) based anodes in lithium ion batteries (LIBs), and a brief literature survey on the strategies adopted to improve the battery performance of Si anodes in LIBs, and the role of Gr for the same. Finally, the chapter briefs about the motivation of our research work, research problem, objectives and the expected outcomes of the proposed work. In addition, the outline of the thesis and a brief introduction of each chapter are provided at the end of the chapter.

1.1. Electrochemistry: A Historical Overview

Electrochemistry, in simple terms, can be defined as the study of the utilization of chemical reactions to produce electric power or, alternatively, the use of electricity to effect chemical processes or systems (Kaifer & Gómez-Kaifer, 1999; J. Wang, 1994). Hence, electrochemistry can be described as the interplay between electricity and chemistry; the measurements of electric quantities, such as current, potential, and charge, and their relationship to chemical parameters and in turn to chemical reactions. The chemical reactions involving the transfer of electrons to and from a molecule or ion are often referred to as redox (reduction/oxidation) reactions. The use of electrical measurements for analytical purposes has found a vast range of applications, including

environmental monitoring, industrial quality control, pharmacy, medicinal chemistry and biomedical analysis (J. Wang, 1994). As we know, the functions of electrochemistry are better known in the electroanalytical techniques as well as in EC energy storage and conversion devices, where a number of EC reactions or processes are involved. The first known EC device was built around 2000 years ago and was composed of electrodes of iron and copper suspended within a natural electrolyte (likely fruit juice) (Patey, 2009).

The first systematic investigation of electrochemistry was conducted by Alessandro Volta (1745-1827) who investigated the electrochemistry of zinc and copper discs stacked together within brine, otherwise known as a "voltaic pile". This was one of the most important inventions in electrochemistry and is the first modern EC energy storage device to be used. One of the first EC sensing methods was developed in the early 1900s that measured pH utilizing a glass electrode, by Arnold Beckman (1936) and later was commercialized. This was followed by the development of the first EC sensor in 1956 for oxygen detection by Leland Clark and with the first glucose oxidase enzyme electrode in 1962. The glucose electrode was the first EC biosensor developed and was a real breakthrough in the field of medical sciences. The first commercial glucose meters were available by the 1970s and have become the gold standard of the biosensor field.

1.2. Electrochemical Sensing

A sensor can be defined as a device that provides continuous information about its environment. It is a device which measures a physical quantity and converts it into a signal which can be read by an observer or an instrument. Sensors can be broadly classified into physical and chemical sensors. Physical sensors are those which are sensitive to physical responses such as temperature, pressure, force, magnetic field etc. and do not have a chemical interface (Sindhu & Girish Kumar, 2011). On the other hand, chemical sensors rely on chemical reactions which give rise to their action. Ideally, a chemical sensor is a device which provides a certain type of response directly related to the quantity of a

specific species through a chemical reaction which leads to its qualitative and quantitative determination. A useful definition of a chemical sensor is that a device that transforms a chemical information (composition, presence of a particular element or ion, concentration, chemical activity etc.) into an analytically useful signal. All chemical sensors consist of two parts, a chemically selective layer (where the selective chemistry takes place), which isolates the response of the analyte from its immediate environment and a transducer, which transforms the response into a detectable signal using modern instrumentation. Depending on the transducer type, Chemical sensors can be categorized into EC, optical, mass or thermal sensors and are designed to detect and respond to an analyte in the gaseous, liquid or solid state (Stradiotto et al., 2003).

EC sensors represent the most rapidly growing class of chemical sensors in which an electrode is used as the transduction element. Compared to the optical, mass and thermal sensors, EC sensors are attractive because of their remarkable sensitivity, experimental and instrumentation simplicity, portability and low cost (Stradiotto et al., 2003). They encompass a leading position among the presently available sensors that have reached the commercial stage and which have found a vast range of important applications in the fields of clinical, industrial, environmental and agricultural analyses. Next generation of sensors will require considerable improvements in sensitivity, selectivity, and accuracy to meet the future needs in diverse fields (Faridbod et al., 2011). Currently most of the diagnostic assays are based on optical measurements. However, complicated readout instrumentation, long duration for sample preparation/pre-processing and the need for the labelling, make optical methods expensive, time-consuming and non-portable. In contrast, EC methods rely on much simpler instrumentation that ensures lower cost and power consumption.

Therefore, the key advantages of EC sensing methods can be summarized as,

- Experimental simplicity and low power consumption
- Portability
- Fast analysis
- Cost effectiveness
- Lower detection limits
- Good selectivity and reproducibility
- In addition, EC methods are ideally suitable for implementation of label-free detection approaches, which give a number of advantages for the biomedical assays, such as elimination of the need for modification of the molecule of interest which might otherwise lead to a change in the bioactivity, it provides the avoidance of the influence of the label on the binding properties, possibility of real-time monitoring of binding interactions, etc.

The schematic showing the working principle and operation of an EC sensor is given in Figure 1.1.

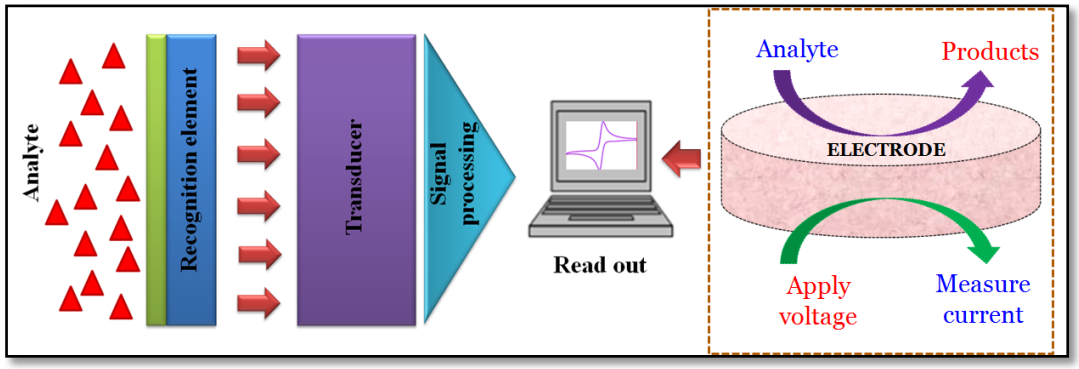

Figure 1.1. Schematic representation of an EC sensor, it's working principle and operation.

1.2.1. Types of electrochemical sensors

There are three main types of EC sensors:

a) Potentiometric,
b) Voltammetric/Amperometric and

c) Conductometric

In general, potentiometric methods are based on measuring the potential of an EC cell at minimal current flow, where the measuring set up contain two electrodes, an indicator electrode (measuring electrode) and a reference electrode, which when placed in a solution together, produce a certain potential (Sindhu & Girish Kumar, 2011). Potentiometric sensors are those in which a local equilibrium is established at the sensor interface, where either the electrode or membrane potential is measured, and information about the composition/concentration of the sample(s) in the solution is obtained from the potential difference between the two electrodes (Stradiotto et al., 2003).

Voltammetric sensors exploit the use of a potential which is varied in a systematic manner to cause the oxidation or reduction of an electroactive species; the resultant current, which is proportional to the concentration of the electroactive species is measured. Amperometric sensor is a special case of voltammetric sensor in which the current is measured at a fixed operating potential. The recording of current as a function of time, known by the name chronoamperometry can give important and useful information. On the other hand, conductometric sensors are involved with the measurement of conductivity at a series of frequencies (Stradiotto et al., 2003). Here in our work, we have majorly utilized voltammetric method for sensing purpose and the general advantages of which are described in the coming section.

1.2.2. Voltammetric sensors

As discussed in the previous section, voltammetric sensors are those in which the information about an analyte is obtained by measuring the current response as a function of the applied potential. To be more precise, all the voltammetric techniques involve the application of a potential (E) to an electrode in a varying manner from one preset value to another and then the resulting current (i) flowing through the EC cell is recorded and is monitored over a period

of time (t). Thus, all the voltammetric techniques can be described as function of E, i, and t. If this potential (or range) is conveniently chosen, it will force the electroactive species at the electrode surface to undergo either oxidation or reduction electrochemically and in turn results in a current response proportional to the concentration, based on the conditions. The analytical advantages of the various voltammetric techniques include excellent sensitivity with a very large useful linear concentration range for both inorganic and organic species (10^{-12} to 10^{-1} M), a large number of useful solvents and electrolytes, a wide range of temperatures, rapid analysis times (seconds), simultaneous determination of several analytes, the ability to determine kinetic and mechanistic parameters, a well developed theory and thus the ability to reasonably estimate the values of unknown parameters, and the ease with which different potential waveforms can be generated and small currents measured (Kounaves, 1997). The general uses of voltammetric techniques are,

- Quantitative determination of organic and inorganic compounds in aqueous and nonaqueous solutions
- Fundamental studies of oxidation and reduction processes in various media
- Determination of adsorption processes on surfaces
- Determination of electron transfer and reaction mechanisms
- Measurement of kinetic rates and constants
- Determination of thermodynamic properties of solvated species, etc.

The basic instrumentation of a voltammetric sensor comprises of a controlled-potential equipment called the potentiostat and an EC cell which requires at least two electrodes immersed in a suitable electrolyte. The working electrode (WE), which makes contact with the analyte, must apply the desired potential in a controlled way and facilitate the transfer of charge to and from the analyte resulting from the oxidation and reduction processes, and a second electrode which acts as the other half of the cell must have a known potential with which to gauge the potential of the WE, furthermore it must balance the charge added or removed by the working electrode. However, it is extremely difficult for

an electrode to maintain a constant potential while passing current to counter redox events at the working electrode. Therefore, a better arrangement involves the use of a three-electrode system, where the roles of supplying electrons and providing a reference potential are divided between two separate electrodes, referred to as the counter electrode (CE) and the reference electrode (RE) respectively, because it is necessary in order to avoid the passage of current through the RE, which otherwise would alter its potential via changes in the activities of various electroactive species. So, a typical EC cell (Figure 1.2) consists of the analyte sample dissolved in a solvent, an ionic electrolyte, and the three electrodes: the RE, WE, and the CE (also called the secondary or auxiliary electrode). While the WE is the electrode at which the reaction of interest occurs, the RE (e.g.; Ag/AgCl, Hg/Hg_2Cl_2) provides a stable potential with respect to (wrt) the WE. An inert conducting material (e.g.; platinum (Pt), graphite) is usually used as the CE/auxiliary electrode. The applied potential is measured against the RE, while the CE closes the electrical circuit for the current to flow. The experiments are performed by a potentiostat that effectively controls the voltage between the RE and WE, while measuring the current through the CE (the WE is connected to the ground). A supporting electrolyte is required in the controlled-potential experiments to eliminate electromigration effects, decrease the resistance of the solution and maintain the ionic strength constant (Stradiotto et al., 2003).

- **Working electrode (WE)**

The WE is the one on which the reaction of interest is occurring and often can be of inert metals such as gold, silver or Pt; carbon materials such as glassy carbon (GC), pyrolytic carbon or carbon paste; or mercury drop and film electrodes. The most widely used WE substrate is the GC because of its cited advantages such as, (i) low cost (ii) easy pre-treatment by polishing with metallographic paper (iii) larger overpotential for production of hydrogen and dissolved oxygen and (iv) increased reversibility for several redox couples and reactions that involve subsequent proton transfer. Glassy carbon is an electrically

conductive and gas impermeable material, highly resistant to chemical attack and is obtainable in pure state (Sindhu & Girish Kumar, 2011).

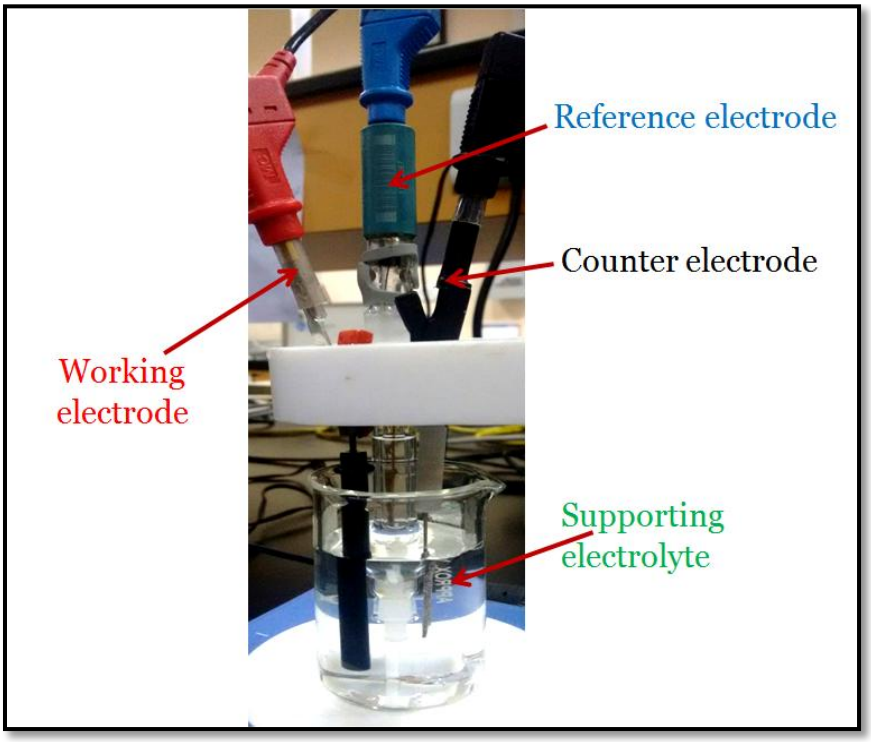

Figure 1.2. The basic instrumental set up of a voltammetric experiment: The three electrode system

- **Reference electrode (RE)**

A RE is the one with a fixed electrode potential which should not be varied with the external potential applied in the WE and must be insensitive to the composition of the analyte solution. The commonly used REs are, Silver-silver chloride electrode, Calomel electrode etc.

- **Counter electrode (CE)**

The role of the CE is to supply the current required by the WE, without limiting the measured response of the cell. In voltammetric sensors, the current flows between the WE and the CE. The key condition for an electrode to act as a

CE is that it should not dissolve in the medium of the EC cell and the reaction product at the CE should not react at the WE. It should have a large area compared to that of the WE to ensure that the area of the electrode does not control the limiting current. Most often the CE consists of a thin Pt wire or thin foil, although Au or graphite can be used.

- **Supporting electrolyte**

The supporting electrolyte is an inert soluble ionic salt added to the solvent; generally in 10-fold or 100- fold excess over the concentration of the species being studied. Inert in the sense, the ability to avoid oxidation or reduction at the indicating or RE during the course of the EC measurements. The main function of the supporting electrolyte is that it carries most of the ionic current of the cell since its concentration is much larger than that of the other species in solution. Thus it serves to complete the circuit of the EC cell and keep the cell resistance to a low value (Laina & Girish Kumar, 2013).

1.2.3. Electrode processes

Faradaic and non-Faradaic currents: Two types of processes occur at electrodes: One type involves a direct transfer of electrons via an oxidation reaction at one electrode and a reduction reaction at the other. Since such reactions are governed by Faraday's law (i.e., the amount of chemical reaction caused by the flow of current is proportional to the amount of electricity passed), they are called *faradaic processes.* Electrodes at which faradaic processes occur are sometimes called the *charge transfer electrodes.* For a thermodynamically controlled reversible process the applied potential (E) of the electrode is given by the well known Nernst equation, Eq. (1.1),

$$E = E^0 + \frac{2.303\ RT}{nF} \log \frac{C_{ox}}{C_{red}} \qquad (1.1)$$

Where E^o is the standard potential of the redox couple; R - universal gas constant; T - temperature (K); n - number of electrons transferred; F - Faraday's constant, which represents the amount of electric charge carried by one mole of electrons, i.e., Avogadro's number x charge of an electron; C_{ox} is the concentration of the oxidized species; C_{red} is the concentration of the reduced species.

Under certain conditions, a range of voltages may be applied to a cell that does not produce faradaic processes at one or both of the electrodes. Faradaic processes may be prevented either because electrons do not have sufficient energy to pass over the potential energy barrier at the electrode-solution interface (thermodynamic reasons) or because the electron-transfer reaction is not fast enough on the time scale of the experiment (kinetic reasons). However, the processes such as adsorption and desorption can occur, and the structure of the electrode-solution interface can change with changing potential or solution composition. These processes are called *nonfaradaic processes*. Under these circumstances, conduction of continuous alternating currents can still take place. With such currents, reversal of the charge relationship occurs with each half-cycle as first negative and then positive ions are attracted alternately to the electrode surface. Electrical energy from the external voltage source is consumed and converted to heat by friction associated with the motion of ions. In other terms, when the voltage changes, the ions in the double layer have to rearrange and adjust to the new potential, and this rearrangement requires energy. Thus, each electrode surface behaves as a plate of a capacitor, whose capacitance is large (several hundred to several thousand microfarads per square centimeter). The capacitive current increases with frequency and with electrode area; by controlling these variables, it is possible to adjust conditions so that essentially all of the alternating current in a cell is carried across the electrode interface by this nonfaradaic process. The basic difference between a faradaic and a nonfaradaic current can be further understood by imagining an electron travelling down the external circuit to an electrode surface. When the electron reaches the solution interface, it can either remain at the electrode surface and increase the charge on the double layer, which constitutes a nonfaradaic current; or can leave the

electrode surface and transfer to a species in the solution, thus becoming a part of the faradaic current (Skoog et al., 1998).

Therefore, the nonfaradaic current is a result of those processes that do not involve the transfer of electrons across the electrode–solution interface and they stem from the electrical capacitance present at the interface, which can be calculated using the equation, Eq. (1.2),

$$C = \frac{q}{E} \qquad (1.2)$$

Where q and E represent the charge and the potential, respectively.

Although the charge does not cross the interface, external currents can flow (at least transiently) when the potential, electrode area, or solution composition changes. Both faradaic and nonfaradaic processes occur when electrode reactions take place. Although the faradaic processes are usually of primary interest in the investigation of an electrode reaction (except in the studies of the nature of the electrode-solution interface itself), the effects of the nonfaradaic processes must be taken into account while using EC data to obtain information about the charge transfer and the associated reactions (A.J. Bard & Faulkner, 2000).

The current in a voltammetric experiment is a measure of the rate of the electrode process. When an electrode is placed in an electrolyte solution, different processes may occur (See Figure 1.3). The steps involved in an electrode reaction are;

1. Mass transfer of the species between the bulk solution and the electrode surface.
2. Heterogeneous electron transfer at the electrode/solution interface.
3. Chemical reactions, either preceding or following the electron transfer.

4. Surface reactions such as adsorption, desorption and electrodeposition–dissolution (A.J. Bard & Faulkner, 2000).

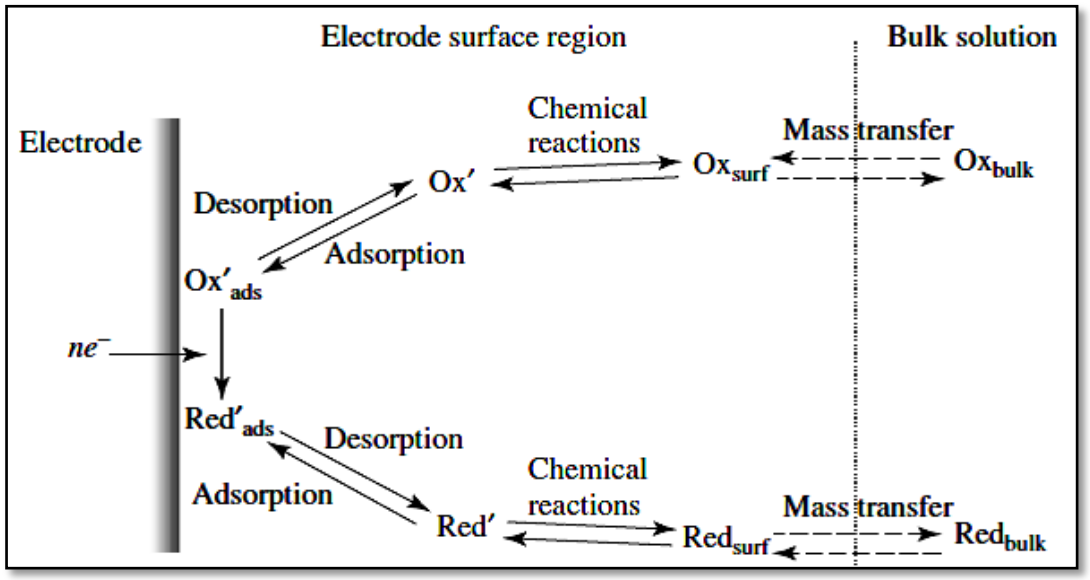

Figure 1.3. Typical steps involved in an electrode reaction (A.J. Bard & Faulkner, 2000).

The rate of mass transfer of the detecting species in the reaction onto the electrode surface and the kinetics of the faradaic/charge transfer reaction at the electrode surface determines the current-potential characteristics. This mass transfer can occur through any of the following processes,

a) Diffusion: Transport of a species under a chemical potential difference or concentration gradient.
b) Migration: Transport of ions due to the electrostatic attraction between the oppositely charged electrode and ions.
c) Convection: Transport due to natural or forced mechanical motion of the solution such as stirring.

The electrode reaction kinetics and the mass transfer processes contribute to the rate of the faradaic process in an EC cell. This provides the basis for the operation of the voltammetric sensor (Laina & Girish Kumar, 2013).

1.2.4. Different voltammetric techniques

This section discusses some of the more common forms of voltammetric techniques currently in use for a variety of analytical purposes. The uniqueness of each technique rests on the subtle differences in the manner and the timing in which the potential is applied and the current is measured (Kounaves, 1997).

1.2.4.1. Linear-Sweep Voltammetry (LSV)

LSV is the simplest among the voltammetric techniques in which the potential of the WE is altered linearly with time. LSV measures the current at the WE while the potential between the working and a RE is linearly swept in time. i.e It involves an increase in the imposed potential linearly at a constant scanning rate from an initial potential to a defined upper potential limit. A measure of the current signal is denoted by a peak or trough that is formed at the potential where the species begins to be oxidized or reduced (Pillay, 2009).

1.2.4.2. Cyclic Voltammetry (CV)

CV has become an important and most extensively used electroanalytical technique in many areas of chemistry. It is rarely used for quantitative determinations, but it is widely used for the study of redox processes, to provide information on the reversibility and kinetics of the reactions, for understanding reaction intermediates, and for obtaining the stability of the reaction products. The CV is based on varying the applied potential at a WE in both the forward and backward/reverse directions while monitoring the current. i.e. The potential of WE is scanned linearly from an initial potential to a final potential and then back to the initial potential. The potential at which the peak current occurs is known as the peak potential (Ep). The important parameters in a cyclic voltammogram are the cathodic and the anodic peak potentials (E_{pc}, E_{pa}) and peak currents (i_{pc}, i_{pa}), respectively. The magnitude of the Faradaic current (i_{pc} or i_{pa}) gives an indication of the rate at which the electrons are being transferred between the redox species

and the electrode. The cyclic voltammetric processes could be reversible, quasireversible and irreversible. If the electron transfer process is fast compared with the other processes (such as diffusion), the reaction is said to be electrochemically reversible, where the electroactive oxidised (or reduced) species in the forward scan is in equilibrium with the electroactive reduced (oxidised) species in the reverse scan and the peak separation is given by Eq. (1.3),

$$\Delta E_p = E_{pa} - E_{pc} = {}^{2.303\ RT}/_{nF} = {}^{0.0592}/_{n}\ V \qquad (1.3)$$

ΔE_p should be independent of the scan rate (υ) but in practice, ΔE_p increases slightly with increasing υ, and this is due to the solution resistance (RS) between the reference and working electrodes. Theoretically, the potential difference between the oxidation and reduction peaks is 59 mV (eqn 3) for one-electron reversible redox reactions. However, in practice, this value is difficult to attain and sometimes found in the 60-100 mV range, because of cell resistance (Pillay, 2009). Thus, for a reversible redox reaction at 25 °C with "*n*" electrons, ΔE_p should be 0.0592/*n* V or about 60 mV for a one-electron reaction.

The formal reduction potential (E_0) for a reversible couple is given by Eq. (1.4),

$$E_0 = {}^{(E_{pc} + E_{pa})}/_{2} \qquad (1.4)$$

For a reversible reaction, the concentration is related to the peak current by the Randles–Sevcik expression (at 25 °C), Eq. (1.5):

$$i_p = (2.686 \times 10^5) n^{3/2}\ A\ D^{1/2}\ C\ \upsilon^{1/2} \qquad (1.5)$$

Where i_p is the peak current in Amps, A is the electrode area (in cm^2), D is the diffusion coefficient ($cm^2\ s^{-1}$), C is the concentration in mol cm^{-3}, and υ is the scan rate in Vs^{-1} (Kounaves, 1997). A linear plot of i_p vs. $\upsilon^{1/2}$ indicates that the currents are controlled by planar diffusion to the electrode surface (***diffusion***

controlled process) and if there is a linear relationship between i_p and υ, that corresponds to an ***adsorption controlled process.***

For an irreversible process, only forward oxidation (reduction) peak is observed but at times, a weak reverse reduction (oxidation) peak as a result of slow electron exchange or slow chemical reactions at the electrode surface (Pillay, 2009) is possible. Irreversibility due to a slow electron transfer rate results in $\Delta E_p > 0.0592/n$ V, greater than, say, 70 mV for a one-electron reaction.

Quasi-reversible processes are those in which, unlike the reversible process where the current is purely mass transport controlled, the current is controlled by a mixture of mass transport and charge transfer kinetics. The process occurs when the relative rate of electron transfer with respect to that of the mass transport is insufficient to maintain the Nernst equilibrium at the electrode surface. For a quasi-reversible process, ip increases with $\upsilon^{1/2}$ but not in a linear relationship and $\Delta E_p > 0.059/n$ (Pillay, 2009) (Figure 1.4 B).

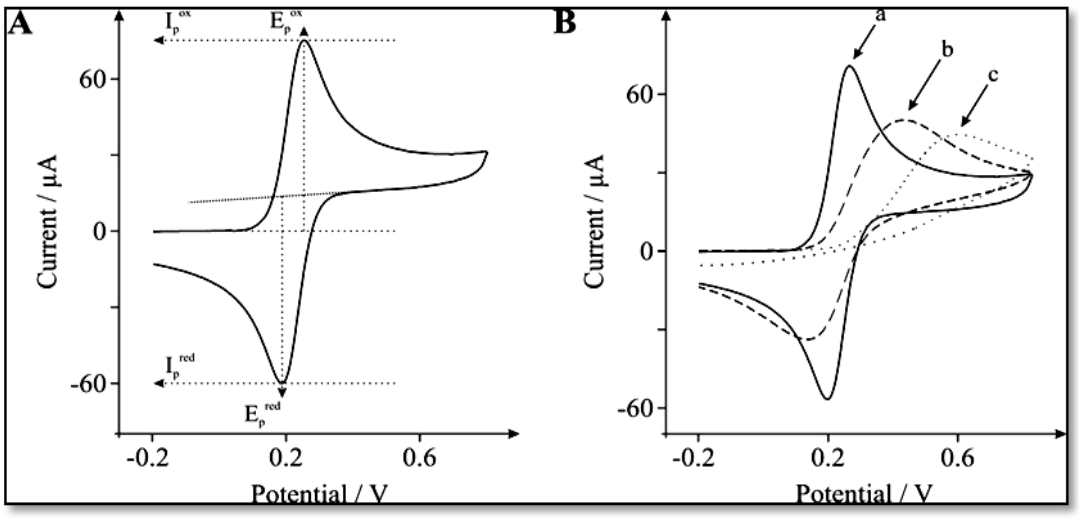

Figure 1.4. (A): Typical cyclic voltammogram depicting the peak position E_P and peak height I_P. (B): Cyclic voltammograms for (a) reversible, (b) quasi-reversible and (c) irreversible electron transfer (Brownson, 2013).

1.2.4.3. Pulse methods

Pulse voltammetric techniques introduced by Barker and Jenkin, were aimed at increasing the sensitivity or lowering the detection limits/limit of detection (LOD), and increasing the speed of voltammetric measurements. The key advantage of these techniques is that they permit convenient measurements even up to nanomolar concentration levels and because of this greatly improved performance, modern pulse techniques have largely replaced classical EC techniques to an extent. The idea behind all pulse-voltammetric methods is to measure the current at a time when the difference between the desired faradaic curve and the interfering charging current is large, the latter being on the lower side. The difference in the rate of the decay of the charging and the faradaic currents follows a potential step (or "pulse", typically 50 mV). A sequence of such potential steps, each with duration of about 50 milliseconds, is applied on to the WE. After the potential is stepped, the charging current, one of the major contributors of non-faradaic current, decays exponentially, whereas the faradaic current (for a diffusion-controlled current) decays as a function of $1/(\text{time})^{1/2}$; that is, the rate of decay of the charging current is considerably faster than the decay of the faradaic current (Aoki et al., 1980). Charging currents result in high background noise in voltammetric analyses. This ultimately compromises signal-to-noise ratios and thus limits the detection at low analyte concentrations. To be more precise, the greater sensitivity of pulse techniques can be attributed to two factors. The first is an enhancement of the faradaic current, and the second is a decrease in the non faradaic charging current. To account for the enhancement, let us consider the events that must occur in the surface layer around an electrode as the potential is suddenly increased by 50 mV. If an electroactive species is present in this layer, there will be a surge of current that lowers the reactant concentration to that demanded by the new potential. As the equilibrium concentration for that potential is approached, however, the current decays to a level just sufficient to counteract diffusion; that is, to the diffusion-controlled current. In classical voltammetry, the initial surge of current is not observed because the time scale of the measurement is long relative to the lifetime of the momentary current. On the

other hand, in pulse voltammetry, the current measurement is made before the surge has completely decayed. Thus, the current measured contains both a diffusion-controlled component and a component that has to do with reducing the surface layer to the concentration demanded by the Nernst expression; the total current is typically several times larger than the diffusion current. Note that, under hydrodynamic conditions, the solution becomes homogeneous with respect to the analyte by the time the next pulse sequence occurs. Thus, at any given applied voltage, an identical current surge accompanies each voltage pulse. When the potential pulse is first applied to the electrode, a surge in the nonfaradaic current also occurs as the charge increases. This current, however, decays exponentially with time and approaches zero with time. Thus, by measuring currents at this time only, the nonfaradaic residual current is greatly reduced, and the signal-to-noise ratio is larger. Enhanced sensitivity results (Skoog et al., 1998). Therefore, in pulse techniques, in order to maximize the signal-to-noise (S/N) ratio, linear time–potential scans have been supplemented by more complex waveforms where time and potential are manipulated to maximize the ratio of faradaic to nonfaradaic current. As discussed, this is typically done by sampling the current at a specific time interval where the faradaic response is large and the nonfaradaic charging current is small (Cazes, 2004). The discrimination against the charging current (nonfaradaic current) that is inherent in these techniques leads to lower LODs (when compared to linear sweep techniques), which makes these techniques suitable for quantitative analysis.

A number of different pulse techniques have been tried over the years, which differ in their potential pulse wave forms, the number of sampling points, and whether a solid electrode (voltammetry) or a mercury drop electrode (polarography) is used. Waveforms are simply the variation in potential with time. The simplest waveform is a linear scan (voltage ramp) where potential is scanned linearly with time [Figure. 1.5(a)]. The waveform used for CV is simply a linear scan that is scanned forward, switched, and then scanned backward [Figure. 1.5(b)]. The CV waveform may be repeated over many cycles. Pulsed waveforms are more complex and can be divided primarily into normal pulse voltammetry

(NPV), differential pulse voltammetry (DPV), and square wave voltammetry (SWV).

i. Normal Pulse Voltammetry (NPV)

NPV [Figure. 1.5(c)] consists of a series of pulses of increasing amplitude, with the potential returning to the initial value after each pulse. The current is measured at some sampling interval (S) near the end of each pulse maximum. The Faradaic response is maximized by the potential pulse (when compared with the linear scans) and a significant amount of charging current is avoided in the measurement since the current is sampled near the end of the pulse (Cazes, 2004).

ii. Differential Pulse Voltammetry (DPV)

DPV [Figure. 1.5(d)] differs from NPV, that it uses a waveform that consists of small pulses (of constant amplitude) superimposed on a staircase wave form. Like NPV, the faradaic response is maximized and charging current is minimized by sampling the current (S_2) near the end of each pulse maximum. Again, this is very advantageous over the linear-scan techniques since signal-to-noise is maximized. DPV differs from NPV in that the current is sampled at a second interval (S_1). By subtracting S_1 from S_2, a voltammogram is obtained that is a measure of the change in current with potential. This will appear very different from the shape of the NPV voltammogram. If the NPV voltammogram gives a classical, sigmoidal response (i vs. E) for the oxidation or reduction of the analyte, the equivalent response using DPV will be the derivative of the NPV response (Δi vs. E) and will result in a peak instead of a wave. This can be attributed to the fact that Δi becomes small and approaches zero as the limiting current is approached. This differential output allows the observation of individual peak maxima that differ by as little as 50 mV. In comparison, NPV (as well as classical techniques) requires approximately 200 mV between the waves to resolve them (Cazes, 2004).

iii. Square Wave Voltammetry (SWV)

SWV is similar to DPV in that current is sampled at two different times in the waveform and results in a differential output (Δi vs. E). The SWV waveform [Figure. 1.5(e)] is essentially the combination of a square wave (bold, solid line) of period τ with a staircase voltage function (dotted lines), of period τ. The "forward" current is measured at t_1 just before the "down" pulse is applied. The "reverse" current is measured at t_2. The net current is defined as the current measured at t_1 minus the current measured at t_2, or $\Delta i = i_1 - i_2$. The SWV waveform is advantageous in such a way that the detrimental effects of charging current are reduced, allowing very fast potential scans. The charging current developed on the forward scan (from the "up" pulse) is essentially subtracted out when the reverse scan (the "down" pulse) is applied. Because of the rapid analysis time, repetitive scanning can be used with SWV to increase signal-to-noise by signal-averaging. The true advantage of SWV is therefore, the speed of analysis together with excellent sensitivity and the rejection of background currents (Cazes, 2004).

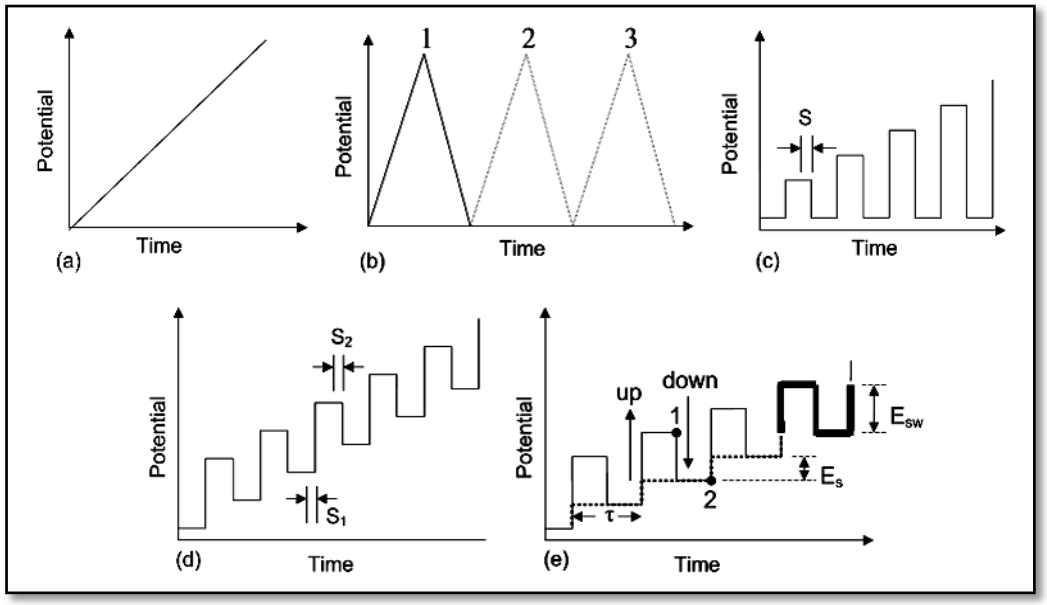

Figure 1.5. The pictorial representation of the different types of waveforms of the different voltammetric techniques; (a) LSV (b) CV (c) NPV (d) DPV and (e) SWV (Cazes, 2004).

1.2.5. Surface modification of electrodes

In recent times, electrochemists have become interested in purposely modifying electrodes by adsorbing, coating, or attaching specific molecules to the surface. A surface modified electrode is the one in which, if a specific material is attached to the electrode, then that material imparts on the electrode some chemical, EC or desirable properties which are not available at the unmodified electrode. Most frequently the layer or coating on the electrode surface is electroactive, i.e., it can exchange electrons with the underlying substrate material and be oxidized or reduced. This deliberate and controlled modification of the electrode surface can produce electrodes with new and interesting properties that may form the basis of new applications of electrochemistry and novel devices (Allen J Bard, 1983). A primary interest has been in the area of electrocatalysis. Another application is in the production of electrochromic devices that change colour on oxidation and reduction. Finally, the most important analytical use of the electrodes is as analytical sensors selectively for particular species or functional groups (Sindhu & Girish Kumar, 2011). One of the most important properties of the modified electrodes is their ability to catalyze the oxidation or reduction of solute species at comparatively lower voltages, which otherwise exhibits higher voltages or does not give a response at the unmodified surfaces. Thus they play an important role in reducing the high overvoltage required for the voltammetric determination of such analytes. Surface modification changes the surface layers of the electrode itself or creates a layer with some form of chemical as well as physical selectivity. Modified electrodes can be prepared by several different techniques which include,

- ***Chemical modification****:* The electrode surface is activated by certain chemical reactions, for example, with silane, which is then used to react with another chemical species that becomes immobilized on the surface.
- ***Adsorption****:* Some species find the surface of the electrode much more hospitable than the hulk solution and so attach spontaneously to the surface. For example, organic species such as those containing double bonds, are often

hydrophobic and strongly adsorb from aqueous solutions on carbon or Pt surfaces (Allen J Bard, 1983).

The adsorption methods involve, ***i) Drop-dry Coating/ Drop-dry casting*** *(or solvent evaporation)*, where a few drops of the polymer, modifier or catalyst solution/dispersion are dropped onto the electrode surface and left to stand for the solvent to dry out. ***ii) Dip-dry Coating****,* where the electrode is immersed in a solution/dispersion of the polymer, modifier or catalyst for a period sufficient for spontaneous film formation to occur by adsorption. The electrode is then removed from the solution and the solvent is removed by drying. ***iii) Spin-Coating*** *(or spin-casting),*which involves evaporating a drop of polymer, modifier or catalyst solution/dispersion from an electrode surface by using centrifugal force at high-speed rotations (Pillay, 2009).

- ***Electroadsorption and electrodeposition***: If adsorption is carried out under the influence of an applied potential then thicker modifier layers usually result, but there is a probably of a greater guarantee of uniformity. Electro polymerisation of monomers is possible; such procedures are used for the formation of conducting polymers.
- ***Plasma:*** The electrode surface is cleaned by plasma leaving the surface with dangling bonds which are highly active and thus promotes the adsorption of species, such as amines or ethenes or similar (Laina & Girish Kumar, 2013).

1.3. Materials of Interest: Functional Nanomaterials

Material science has always played a vital role in the evolution of technology and provisions for humans (Aized et al., 2017) and the emergence of the field of nanoscience has made huge changes in the materials applications. The science and technology of nanoscience materials, devices, and their applications in functionally classified materials, molecular electronics, sensors, actuators, nanocomputers, and molecular machines outline the world of nanotechnology (Pérez López, 2009). Nanomaterials or matrices, with dimensions (grain size, layer thickness or shapes) below 100 nm display unique physical and chemical

features that lead to new properties that are generally not available in the bulk. One of the most intuitive effects arises from the change in the surface area to volume ratio. When the size of the structure is decreased, the surface area to the volume ratio increases considerably and the surface phenomena predominate over the chemistry and physics of the bulk. Therefore, the decrease in the size of the transducer in a sensor to nanaosize can lead to new phenomena, and new sensor devices are being built taking advantage of these factors (Ambrosi, 2007). The sensitivity of the bio/chemical sensors greatly depends on the characteristics of the transducer (shape, type of the material, size, etc.). As the high surface-to-volume ratio of the transducing element can increase the efficiency of the signal transfer, nanomaterials are ideal candidates to be used as components of transducers. Another major advantage of using nanostructures in sensing is that the amount of receptors immobilized on the detector surface can be as low as a single molecule. As a result, the amount of analyte required to generate a measurable signal could be just a few providing for very low LODs (Kurkina, 2012). Therefore, in brief, the advantages of using nanomaterials in sensing include the following: nanomaterials can produce a synergic effect among catalytic activity, conductivity and biocompatibility to accelerate the signal transduction; lower LODs, analysis of samples with lower amount/volume, cost reductions, direct detection and simpler assays (Ambrosi, 2007).

The real progress in nanotechnology has been commenced since the discovery of atomically precise carbon nanomaterials and layered nanomaterials, huge activity has been generated in most areas of science due to their exceptionally unique electrical, thermal, catalytic, optical and mechanical properties. These properties made them ideal for many applications in multifunctional fields. Particularly, Gr, the thinnest known and the strongest ever measured material in the universe has emerged as a rapidly rising star in the field of material science. Likewise MoS_2, a graphite analogue is popular and has attracted the attention of the research community due to its intriguing electrical and optical properties in nanoscale. Here, we wish to detail the exciting area of

electrochemistry of Gr and MoS_2 and the many advantages that they bring forth for the development of EC sensors.

1.3.1. Graphene (Gr)

Gr, the most popular and the widely discussed carbon nanomaterial, is basically a single-atom thick, two-dimensional (2D) sheet of sp^2 bonded carbon atoms arranged in a honeycombed network with six-membered rings (Figure 1.6). As the fundamental 2D carbon structure, Gr can be conceptually viewed as an indefinitely extended, 2D aromatic macromolecule, and can be considered as the basic building block for carbon materials of all other dimensions including the wrapped 0D buckyballs (fullerenes), the rolled 1D nanotubes and the stacked 3D graphite (D. Chen et al., 2010). Though the mention of Gr has been done before (Shenderova et al., 2002), the experimental discovery of Gr happened in 2004 by Geim and coworkers. They peeled graphite to form single-layer sheets for the first time by means of mechanical exfoliation, which resulted in Gr which being the thinnest, most flexible and the strongest material known, exhibits unique and astonishing (theoretical) properties such as, 97.7 % optical transparency, high electron mobility (200,000 $cm^2 V^{-1} s^{-1}$), excellent thermal conductivity (5000 $Wm^{-1} K^{-1}$), high specific surface area (2630 $m^2 g^{-1}$) , remarkable breaking strength (42 N m^{-1}), elastic modulus (0.25 TPa) etc. (Brownson, 2013). These understandings led to an explosion of interest in the study of Gr opening up a new research area in materials science and condensed-matter physics, aiming for wide-ranging and diversified technological applications (D. Chen et al., 2010).

Recently Gr has captured the imagination of scientists and is now a hugely active area of research in a surfeit of fields, none more so than in the field of electrochemistry which has reported many benefits in the areas of sensing to energy storage and conversion. When reviewing the essential characteristics required for EC applications, Gr's 'theoretical advantage' becomes apparent. One of the essential characteristics of an electrode material is its surface area (SA), which is important in applications such as energy storage, biocatalytic devices and

sensors. Gr with a theoretical SA of 2630 m^2 g^{-1} is therefore well suited as an electrode material. Of further significance for EC applications is the electrical conductivity of Gr, which has been calculated to be *ca*. 64 mS cm^{-1} and has been shown to remain stable over a vast range of temperatures. Ultra high electron mobility has been achieved in Gr, with mobilities in excess of 200,000 cm^2 V^{-1} s^{-1} reported at room temperature (RT) (Brownson, 2013).

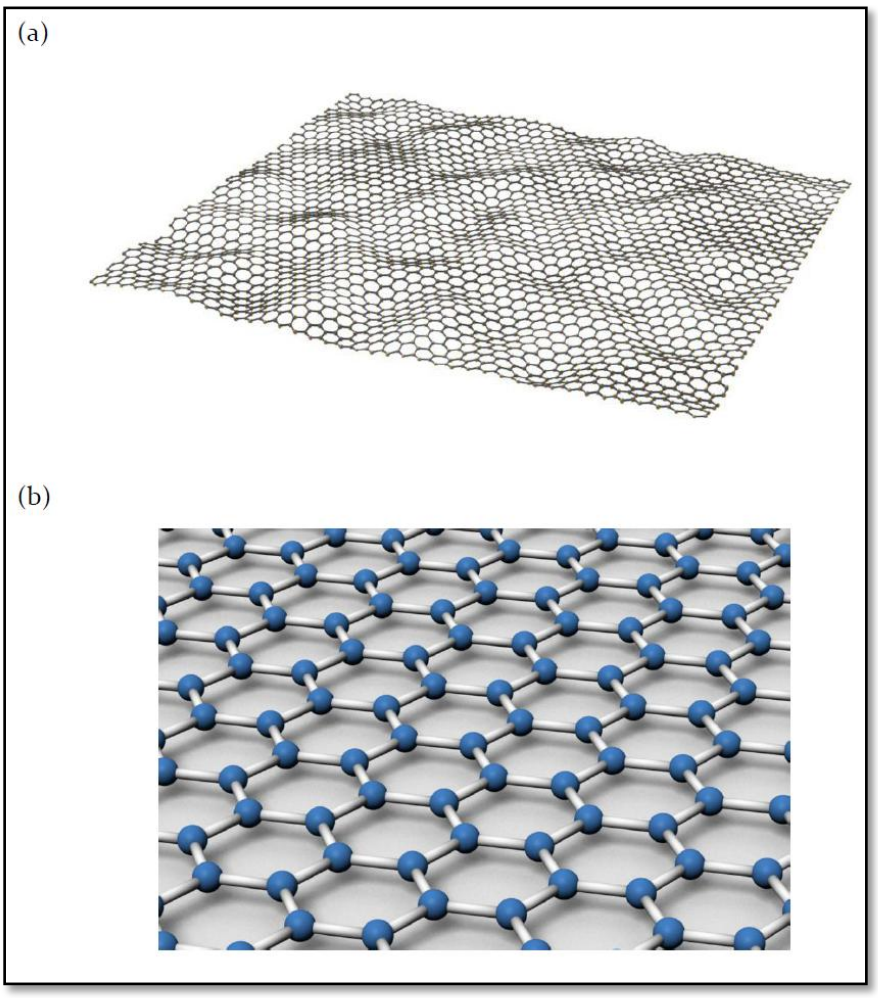

Figure 1.6. Schematic representation of graphene highlighting (a) a single Gr sheet and (b) its basic sp^2 hybridised structure (Garry, 2013).

Moreover, in addition to the above discussed properties, there are certain properties of Gr which particularly favour the EC sensing applications which include,

- large potential window,
- low charge-transfer resistance,
- excellent electrochemical activity,
- fast electron transfer rate,
- good biocompatibility, and
- relatively inert electrochemistry.

The aforementioned extraordinary physical and EC properties of Gr enhance its EC sensing application. For example, the large SA and superior electrical conductance of Gr assure it as an efficient substrate for EC sensing of analyte molecules, leading to the high sensitivity and better signal-to-noise ratio for Gr-based EC sensors. In addition, the fast electron transfer between Gr and analyte molecules promotes direct rather than mediated EC reaction (Wu et al., 2013).

1.3.2. Molybdenum disulphide (MoS_2)

In recent times, there has been a dramatic growth in the research on 2D transition-metal dichalcogenides (TMDs), of which MoS_2 has occupied a unique place. MoS_2 is constructed of S-Mo-S layers that consist of an atomic plane of molybdenum (Mo) sandwiched between two atomic planes of S, and the S-Mo-S layers are stacked and held together by weak van der Waals interactions (X. Li & Zhu, 2015; Tanyuan Wang et al., 2015). Among the three crystal phases exhibited by MoS_2, 2H and 3R phases are of trigonal prismatic symmetry while 1T possesses octahedral symmetry (Figure 1.7). The 3R phase is highly unstable and can easily be converted into 2H phase upon heating. The nature of different crystal phases in MoS_2 compounds is determined by the filling up of d orbitals of Mo, as the p orbitals of S are at much lower energy than the fermi level. The semiconducting behavior (2H) of MoS_2 materials is as a result of complete filling of d orbitals, while partial filling gives rise to metallic behaviour (1T). Thus, the different electronic properties of MoS_2 such as metal, semiconductor or insulator are results of variation in orbital occupancy (Sinha et al., 2018). Being a Gr

analogue and a layered material, in its nanoparticulate forms especially 2D forms, MoS_2 has been attracting great attention among researchers in recent years due to its peculiar properties which are different from those of the bulk MoS_2. Bulk 2H-MoS_2 possesses an indirect band gap which on exfoliation into monolayer thickness, exhibits direct electronic band gaps, for example, monolayer MoS_2 is a semiconductor with a direct bandgap of 1.8 eV, exploiting their significant role in energy conversion, storage, catalysis, sensing and electronic devices (X. Li & Zhu, 2015; Sinha et al., 2018). Properties such as semiconductivity with a direct bandgap, charge carrier transport properties, valley polarization, optical absorption, bright photoluminescence from monolayer MoS_2 etc. ensures the application of nanostructured MoS_2 in the fields of nanoelectronics and optoelectronics, as a promising catalyst towards hydrogen evolution reaction (HER) and oxygen reduction reaction as well as in the fields of energy conversion and storage. On account of unique properties such as novel electronic, optoelectronic and mechanical properties, 2D MoS_2 is now one of the most promising materials for flexible, transparent electronic device components also (Tanyuan Wang et al., 2015).

MoS_2 with its unique EC properties, large specific SA, structural flexibility and potentiality for surface modification imply that it can be applied in the field of EC sensing. The Gr like 2D structure of MoS_2 has propelled its use as a sensing electrode component for the chemical and biomolecular sensing devices at an unprecedented rate (Sinha et al., 2018; Tanyuan Wang et al., 2015). The large effective SA and structural anisotropy of MoS_2 provides a suitable matrix for the immobilization of different chemical and biological receptors and adsorption of target molecules at its surface to make it an advance recognition platform. Discussion of the EC properties of MoS_2 must include its electrode kinetics, a fundamental aspect in electrochemistry which represents the electron transfer reactions between the electrode surface and the inorganic redox probes in the solution.

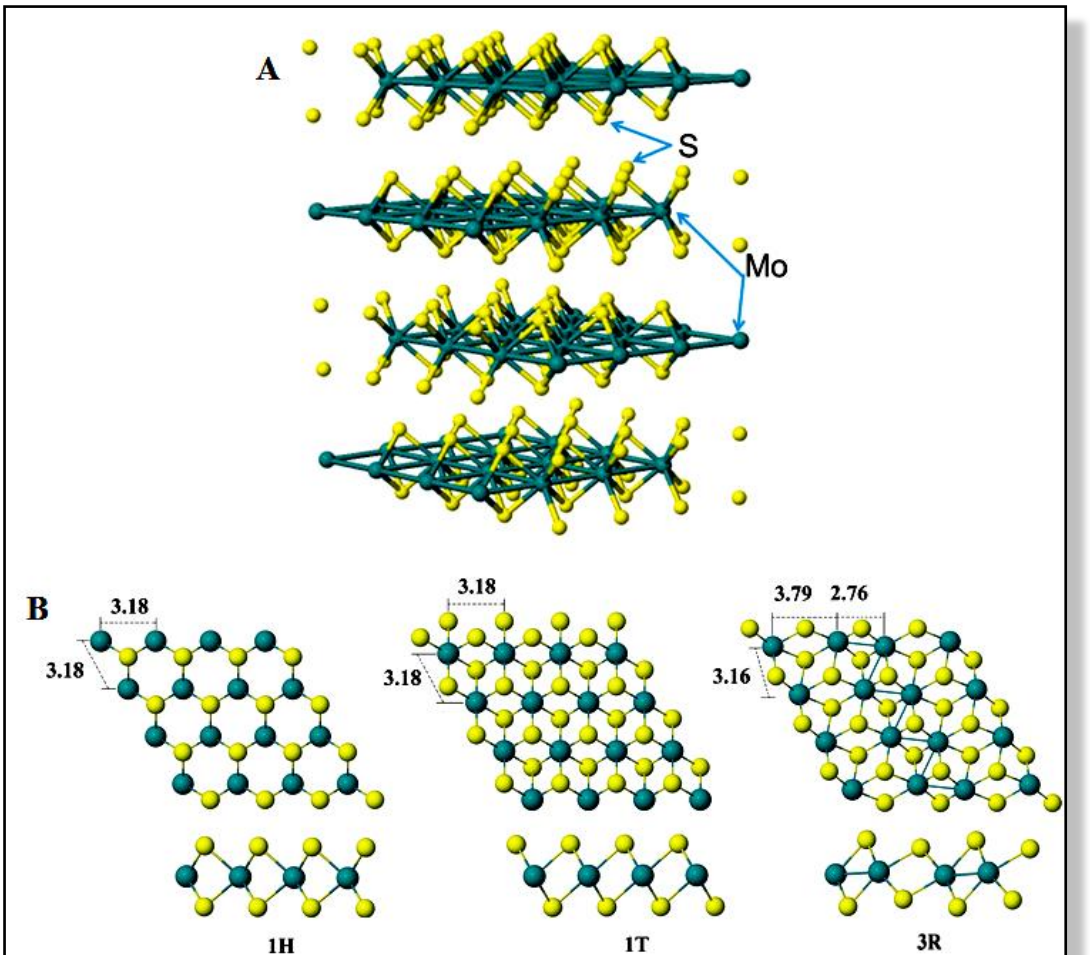

Figure 1.7. (A): The Crystal structure of MoS_2. (B): Three main types of atom arrangements of MoS_2 (2H-MoS_2, 1T-MoS_2 and 3R MoS_2) (X.-L. Fan et al., 2014; Tianyi Wang et al., 2017).

MoS_2 has been well investigated for its high heterogeneous electron transfer (HET) rate, which not only determines the kinetics of redox processes at the electrode but also governs its suitability for EC and bio sensing devices. An electrode material with intrinsically fast HET rate is preferable to lower the overpotential required for EC sensing and also to study the surface conformation of the electrode (Sinha et al., 2018), thus the properties make MoS_2 a suitable EC sensing platform.

1.4. A Brief Review on Gr and MoS_2 Based Materials in EC Sensing Applications

As mentioned earlier, the outstanding physical and chemical properties of Gr/Gr based materials such as large SA, high conductivity, abundant defect sites, superior electrocatalytic activity and fast electron transfer rate have led to its application in EC sensing of various chemical/ biological species. The Gr based EC sensors include modified electrodes with Gr/ functionalized Gr/ doped Gr, Gr-metal/ metal oxide/ metal chalcogenide, Gr-carbon, Gr-paper based, Gr-polymer Gr quantum dots (GQD) etc. in the last decade there have been enriched studies on various enzymatic and non-enzymatic biosensors based on this attractive material, and here we mention a couple of examples which are the most extensively studied and discussed. One of those kinds is the Gr-based glucose sensor, as the determination of glucose is highly important in the diagnosis of diabetes (Jang et al., 2012). To detect glucose enzymatically, the Gr-based electrode is usually modified by the enzyme glucose oxidase (GOD) in the final step of the electrode preparation, i.e. casting of the solution containing GOD onto the electrode. In addition to GOD, other enzymes may be immobilized onto Gr-based electrodes for construction of enzymatic sensors for various biomolecules (Wu et al., 2013). Enzymatic sensors possess several draw backs in terms of their lack of stability & reproducibility and high cost (Jackowska & Krysinski, 2013). These short comings were overcome with the emergence of non-enzymatic electrodes which are highly desirable since they offer better stability, reproducibility and is simple compared to the enzymatic sensors. Selective and simultaneous EC sensing of neurotransmitters, which constitute a series of compounds that have important physiological roles in the metabolic system of living bodies, such as dopamine (DA), ascorbic acid (AA) and uric acid (UA), is another important application of Gr-based electrodes for which a number of reports have been appeared in the literature (Ramachandran et al., 2018; Wu et al., 2013). Similarly, Gr-based electrodes have been fabricated as non-enzymatic sensors to detect other small biomolecules such as H_2O_2 (Q. Li et al., 2012), β-

nicotinamide adenine dinucleotide (NADH) (Longhua Tang et al., 2009) and many.

The application of Gr-based materials has been further explored for the detection of DNA and the single-nucleotide polymorphisms (SNPs) without any hybridization or labelling process since the electrode can detect each base in the oligonucleotides quantitatively (Wu et al., 2013). For example, Zhou et al. reported the chemically reduced GO-modified GCE to detect four free bases of DNA simultaneously, which was impossible to achieve on the GCE or graphite electrode (M. Zhou et al., 2009). Later, Gr-based EC immunosensors were achieved by immobilizing the antibodies to capture the corresponding antigens where the specific interaction between antibodies and antigens resulted in high selectivity and sensitivity (Wu et al., 2013). In addition to biomolecules, Gr-based electrodes have been employed for the detection of various chemicals; it can sensitively detect heavy metal ions, which include mercury (II) (Hg^{2+}) (Gong et al., 2010), cadmium (II) (Cd^{2+}), lead (II) (Pb^{2+}) (J. Li et al., 2009) but not limited to, hazardous chemicals/explosives such as trinitrotoluene (TNT) (Goh & Pumera, 2011), hydrazine (Lei et al., 2012), gas molecules (G. Lu et al., 2009), organic molecules (S.-j. Li et al., 2012) and so on, most of which are causing serious threat to the environment.

Similar to Gr, MoS_2 based materials are also emerging as attractive materials for EC applications recently, owing to their point defects, grain boundaries, amplified edge effects and enhanced surface to volume ratios, which offer several possibility of surface modification and chemical functionalization and because of its versatility to be made into MoS_2 nanostructures including MoS_2 nanoparticles (NPs), nanowires, nanoribbons, nanosheets and nanoflowers (Sinha et al., 2018). Based on their ORR activity, ultrasmall MoS_2 NPs has been reported with high sensitivity and selectivity as a H_2O_2 biosensor (T. Wang et al., 2013). Among the MoS_2 nanostructures, 2D MoS_2 nanosheets have been arousing more interest due to their peculiar structure and electronic properties (Tanyuan Wang et al., 2015). The electrochemistry of single-layer MoS_2 nanosheets was firstly

investigated by Zhang's group and revealed good conductivity, superior electron transfer rate and high EC activity of the electrochemically reduced MoS_2 ($rMoS_2$), which has been used for glucose detection and selective detection of DA in the presence of AA and UA (S. Wu et al., 2012).

MoS_2 nanostructures along with carbon materials, noble metals, metal oxides and polymers have been employed as an ideal strategy to improve and achieve the desired EC sensing properties. Moreover, various biohybrids of MoS_2 with enzymes, aptamers and antibodies hold promising sensing applications (Sinha et al., 2018). The main EC activity of MoS_2 occurs at its edge planes. Hence, creating defects in MoS_2 sheets will aid the introduction of electroactive electrocatalytic sites (Pumera & Loo, 2014). In view of this and as a kind of 2D nanomaterials, MoS_2 nanosheets can serve as a good sensing platform to support some NPs for constructing EC sensors. In recent times, various metal NPs such as Cu, Ni, Pt or Au decorated MoS_2 have been employed in the EC sensing of H_2O_2, glucose, DA, AA, UA, etc. (Tanyuan Wang et al., 2015) of which the Gold-NP-decorated MoS_2 nanocomposite ($AuNPs@MoS_2$) modified electrodes are the most discussed for their individual and simultaneous determination of AA, DA and UA (H. Sun et al., 2014). MoS_2 nanoflowers and chitosan-gold NPs composites modified electrode has been utilized for the EC detection of bisphenol A (K.-J. Huang, Y.-J. Liu, et al., 2014). Further, composite electrodes such as Au-MoS_2-PANI (K.-J. Huang, J.-Z. Zhang, et al., 2014), Ag-MoS_2/chitosan (Xia et al., 2014) etc. were also employed in the EC sensing of biomolecules such as DA, tryptophan etc. MoS_2-metal oxide composite electrodes were also reported for their selective and sensitive detection of analytes. For example, a MoS_2-Cu_2O nanohybrid sensor with MoS_2 nanoflowers and Cu_2O metal oxide has been reported for the non enzymatic amperometric detection of glucose in alkaline medium (Fang et al., 2017).

Apart from these, Gr-MoS_2 composites are gaining popularity in sensing, which can subsequently undergo functionalization with MoS_2 with band gap, resulting in synergistic effect and serve as an electrocatalyst with selective

reactivity upon exposure to various analytes (Pumera & Loo, 2014). The analyte molecules which have given excellent sensing responses to MoS_2/Gr nanohybrid sensors include H_2O_2 (H. Liu et al., 2014), acetaminophen (K.-J. Huang et al., 2013), other pharmaceutical samples etc. (Tanyuan Wang et al., 2015). MoS_2 based nanomaterials were used as a sensing platform for biomacromolecules, such as DNA due to their good biocompatibility. For example, in a recent report, MoS_2 nanostructures have been utilized as potential base for growth of ZnO nanosheets to form a notable biosensing platform for DNA detection (T. Yang et al., 2017). Moreover, MoS_2 based EC sensors are very recently employed in the effective and selective detection of various heavy metal ions such as Hg^{2+} (Aswathi & Sandhya, 2018), explosives such as TNT (T. Yang et al., 2016), inorganic ions/gases such as NO_2^- (Y. Zhang et al., 2017), H_2 (D. Zhang, C. Jiang, & Y. Zhang, 2017), NH_3 (D. Zhang, C. Jiang, & Y. e. Sun, 2017) exposing its applicability in versatile areas.

1.5. Energy Storage

Energy Storage is becoming one of the most imperative components of power generation, transmission and distribution, and consumption management. With the massive growth of clean, renewable energy sources, energy storage can play a substantial role to help create a sustainable society by displacing our current dependence on more problematic sources of power such as fossil fuel. Being motivated by these facts, we extended our works to utilize the energy storage possibilities of nanofunctional materials in an attempt to study the possibilities of nano Si-Gr based anodes in lithium ion secondary batteries.

1.5.1. Lithium ion batteries (LIBs)

Currently, the global energy use is growing dramatically due to steadily rising energy demand in society, where ~80% of the global energy consumption relies on the usage of non-renewable fossil fuel, which is non-sustainable and can cause serious environmental, climate and health problems (X. Su et al., 2014).

Accompanied with this scenario, cutting edge energy storage technologies with environmentally friendly and low cost features are desired for society in the future and can provide far-reaching benefits (Tianyi Wang et al., 2017). The research community is currently engaging in profuse efforts to achieve and to develop effective strategies/ devices and related materials for storing and producing electricity and thus for the replacement of fossil fuels and traditional energy sources (Goriparti et al., 2014). Meeting this aim of exploitation of alternative energy, while avoiding resource depletion and long-term damage to the environment, requires the development of high performance, low cost and environmentally benign energy systems (Hou et al., 2011). In this regard, LIBs can play a significantly important role due to their high gravimetric and volumetric energy (Figure 1.8), high power density, long cycle life and low self-discharge property. Furthermore, they have been proved as the most efficient energy storage strategy for a wide range of portable electronic devices such as cellular phones, laptops, medical microelectronic devices and other digital electronics. Nevertheless, there are still many critical challenges to be overcome for the employment of LIBs in high performance applications such as hybrid electric vehicles (HEV), plug in hybrid electric vehicles (PHEV) and pure electric vehicles (PEV), which need higher energy density than the present LIB technology can offer (150 Wh/kg) (Goriparti et al., 2014). These challenges include further increasing their energy and power densities, improving their safety, and lowering the cost (X. Su et al., 2014). To address these issues, the scientific community has focused in the development of new materials for electrodes and electrolytes and on demonstrating new designs where nanotechnology plays a dominant role (Lahiri & Choi, 2013). To understand more, the basic idea about the conventional LIB system is indeed necessary, which is briefed out in the coming section.

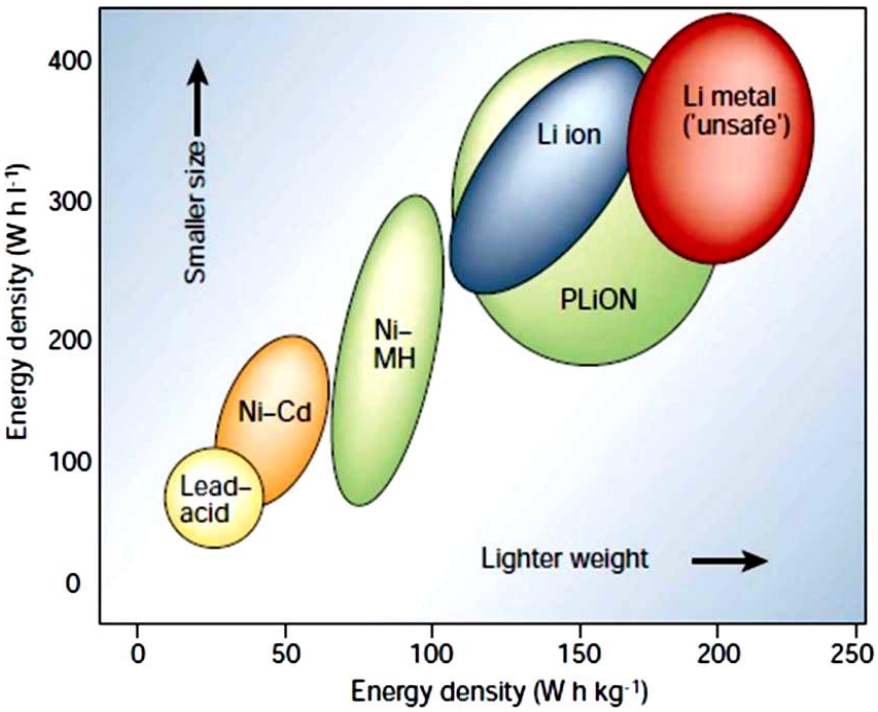

Figure 1.8. A comparison of different battery technologies based on their volumetric and gravimetric energy densities (Tarascon & Armand, 2001).

1.5.2. LIBs: Background and basics

The employment of Lithium (Li) in batteries has been motivated by its unique properties such as its high electropositivity (−3.04 V vs. hydrogen electrode) and lightest nature (density = 0.53 g/cm^3). Li is the lightest metal, known to mankind. These exciting EC and physical properties ensure high voltage, energy density and power density which constitute the key factors in the battery. LIBs with the graphitic anode, offers a nominal cell voltage in the range of 3.0–3.7 V, while other commercial secondary battery systems such as nickel-cadmium (Ni-Cd) and nickel metal hydride (Ni-MH) batteries show much lower voltage (1.2–1.5 V). These advantages of Li were appreciated in the early 1970s, although as a primary (non rechargeable) battery. However, the further development of this battery technology was hindered mainly by problems such as the dendritic growth of Li metal, leading to shorting of electrodes and finally, to thermal runaway. Later, Li metal was substituted by a Li insertion compound,

leading to the development of secondary rechargeable LIBs (Lahiri & Choi, 2013).

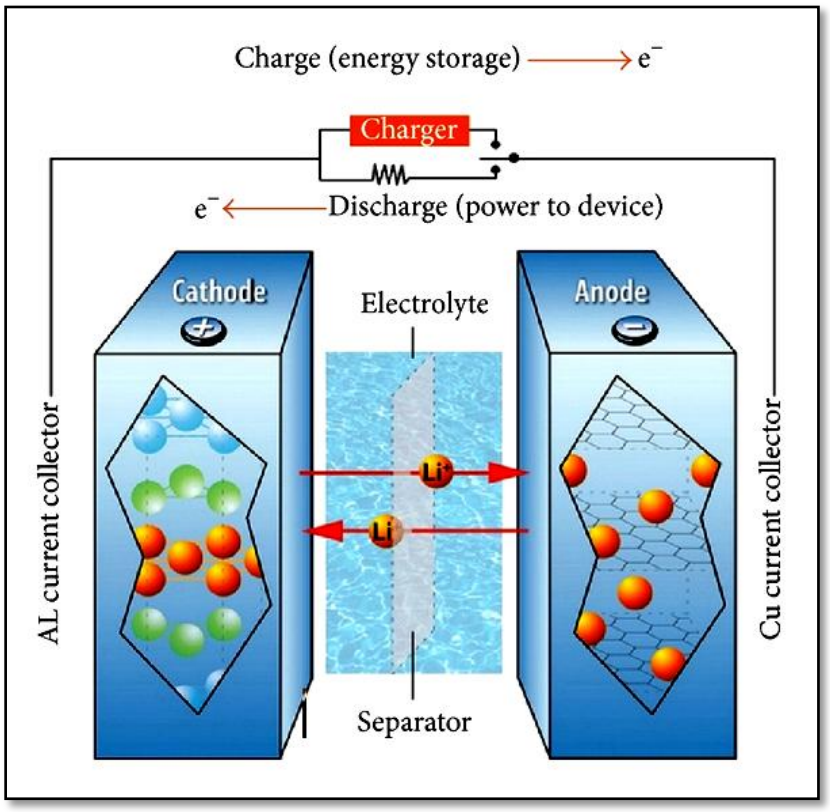

Figure 1.9. LIB schematic, showing ion and electron flows during charge and discharge (Mebarki et al., 2013).

A LIB system consists of a positive electrode (cathode), which serves as the source of Li^+ ion, a non aqueous liquid electrolyte, a polymeric separator, and a negative electrode (anode), which can accept Li^+ ions (Bruce et al., 2008). In the conventional LIBs, the most popular choices for cathode and anode are layered Lithium cobalt oxide ($LiCoO_2$) and graphite, respectively. Other choices of cathode materials for LIBs include Lithium manganese oxide ($LiMn_2O_4$), Lithium iron phosphate ($LiFePO_4$) etc. (Goriparti et al., 2014). The electrolyte used is generally an organic liquid containing lithium salt: mostly, 1M Lithium hexafluorophosphate ($LiPF_6$) dissolved in a mixture of ethylene carbonate-diethylene carbonate (EC-DEC) or ethylene carbonate dimethyl carbonate (EC-DMC). The polymeric separator ensures no direct contact between the electrodes,

by allowing ions but blocking the movement of electrons through it (Lahiri & Choi, 2013). During charging, Li^+ ions deintercalate from the source, which is a lithium- transition metal oxide, mostly $LiCoO_2$ structure, pass across the electrolyte to reach the anode, where they intercalate between the layers of graphite. Discharging reverses this process and electrons flow around the external circuit to perform electrical work (Bruce et al., 2008) (Figure 1.9). The EC reactions happening at the cathode and anode of a typical LIB along with the total reaction based on intercalation and de-intercalation of Li^+ ion, respectively, are given by Equations (1.6), (1.7) and (1.8) as follows,

$$LiCoO_2 \leftrightarrow Li_{1-x}\,CoO_2 + x\,Li^+ + x\,e^- \qquad (1.6)$$

$$C_n + x\,Li^+ + x\,e^- \leftrightarrow C_n\,Li_x \qquad (1.7)$$

$$LiCoO_2 + C_n \leftrightarrow Li_{1-x}\,CoO_2 + C_n\,Li_x \qquad (1.8)$$

Here in these reactions, forward direction represents charging and backward direction indicates discharging. The theoretical capacity of anode (here graphite) can be calculated by the following equation, Eq. (1.9) (Brousse et al., 1997),

$$Q_C = (x\,96500)/(3.6\,n\,M_C) \qquad (1.9)$$

Where Q_C is the theoretical specific capacity of "C" (graphite) in mAh/g and M_C is the molecular weight of "C". In both Equations (1.7), (1.8), and in (1.9), "C" can be replaced by any metal, which react with or intercalate Li^+ ions (Lahiri & Choi, 2013).

Corresponding to the formation of the intercalation compound LiC_6, the theoretical Li storage capacity (theoretical specific capacity) of a graphite anode for a LIB has been calculated to be 372 mAh/g, However, the practically achievable capacity from a graphite anode is still less (~300–310 mAh/g) (Endo et

al., 2000). With this limited capacity, graphite anode cannot conquer the energy demands of the upcoming markets of electric vehicles, of energy storage batteries for renewable energy sources, such as photovoltaic plants and/ or wind turbines and other KWh levels load, (Ma et al., 2014) as discussed in the previous section.

To further increase the energy and power densities of LIBs for the above-mentioned applications the research community has moved from the classical intercalation reaction to alloying reaction because the alloying reaction can store more Li compared to the intercalation reaction. For example, Li can react with Si to form $Li_{22}Si_5$ alloy, but with graphite, it can form LiC_6 only. Therefore, recently a number of alloy-type anodes have been intensively explored due to their high capacity, of which Si has been considered as one of the most attractive anode materials for LIBs, not only because of its high gravimetric (4,200 mAh g^{-1}) and volumetric capacity (2,400 mAh cm^{-3}), but also due to its abundance, cheapness, and environmentally benign property (Ma et al., 2014).

1.5.3. Si based anodes in LIBs: Advantages and challenges

Si has received a great deal of attention as a promising anode material for next generation LIBs which can successfully penetrate the markets of the previously mentioned applications, particularly because of its highest theoretical charge capacity (4200 $mAhg^{-1}$), which is ten times that of the currently used graphite anode (372 $mAhg^{-1}$), and low discharging potential (~ 0.2V vs. Li^+/Li), which is lower than most of the other alloy-type and metal oxide anodes. Such a low operation potential can lead to a high energy density of full cells using Si anodes (X. Su et al., 2014), furthermore, it is safer and stabler than graphite (lithiated silicon is more stable in typical electrolytes than lithiated graphite) (Ma et al., 2014). However, the increased number of lithium ion insertion/extraction results in a significant volume expansion of Si (~400%), which leads to structural pulverization and electrical disconnection between the active materials and the current collector, and finally rapid capacity fading which in turn leads to decreased cycling stability (Liang et al., 2014). Briefly, the failure mechanism of

Si anodes (see Figure 1.10) that resists their practical implementation can be described as follows,

- The huge change in the volume of Si anodes increases the internal resistance and loss of contact area between Si and conductive materials, which is considered to be the main reason for their rapid capacity loss. About 400% volume changes happen during cycling, by which the Si material tend to undergo pulverization. Most of the material loses contact with the current collector, resulting in poor transport of electrons, eventually capacity decay (Ma et al., 2014).
- Another factor which is responsible for the failure of the Si anode is the unstable solid electrolyte interphase (SEI) at the interface between the silicon and the liquid electrolyte. The SEI layer is formed due to the decomposition of organic electrolyte on the anode surface during battery discharging at the low potential. The SEI is formed as a thin layer over the Si anode in the lithiated and expanded state. During delithiation, when the Si particle shrinks, the SEI layer which is made of compounds of Si, Li and the electrolyte components, breaks down into pieces, and fresh Si surface is further exposed to the electrolyte. This results in the continuous formation of new SEI layers in the later cycles which is as an electronic insulator but a Li–ion conductor, further it consumes the active material. The electrically insulating nature of the SEI, as well as the long lithium diffusion distance through the thick SEI weakens the electrical contact between the current collector and anode material (Ma et al., 2014). Moreover, the electrode material degradation caused by mechanical stress from the thick SEI and the consumption of electrolyte, Si and lithium ions during continuous SEI formation lead to decrease of the electrode's EC activity. As discussed above, the large volume change and unstable SEI film formation are the main issues for the failure of Si anode.
- The electronic conductivity of Si is relatively low (~10^{-3} S cm^{-1}, which increases to ~10^{2} S cm^{-1} after lithiation) and,

- Lithium diffusion in Si materials is rather slow (diffusion coefficient between 10^{-14} and 10^{-13} cm^2 s^{-1}), which can significantly limit the utilization of its full capacity and hinder the rate performance of Si anodes (X. Su et al., 2014).

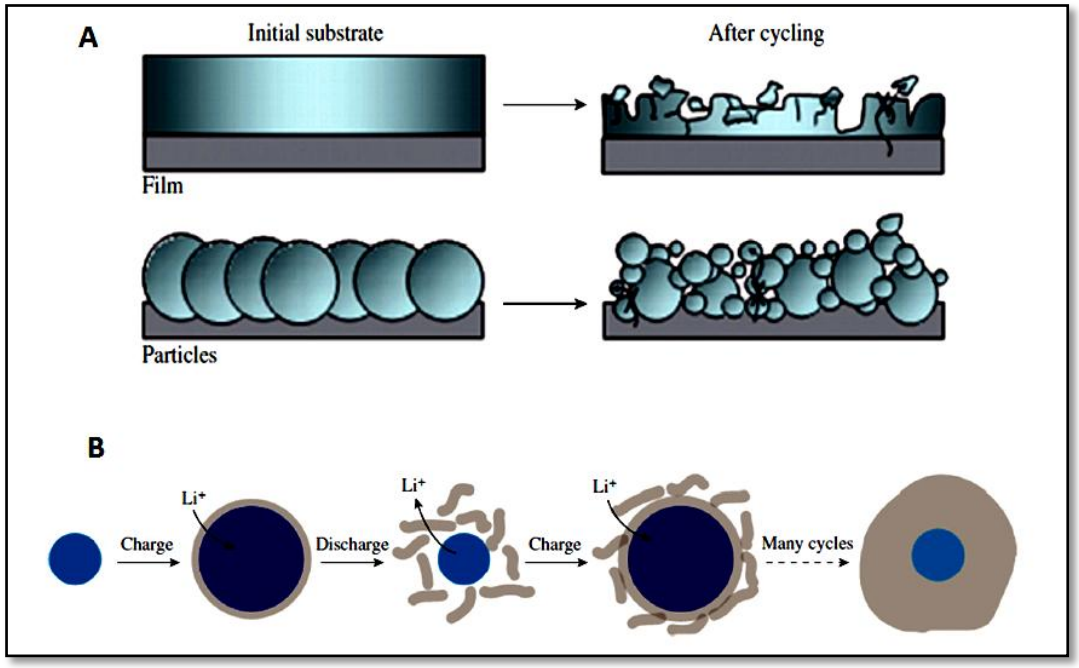

Figure 1.10. (A): Schematic of morphologic changes that occur in Si during electrochemical cycling (B): Schematic of SEI formation on Si surfaces (Chan et al., 2011; H. Wu et al., 2012)

1.5.4. Strategies to overcome the issues with Si anodes: A brief review

To overcome the issues discussed in the previous section and improve the EC performance of Si anodes, numerous strategies have been employed by researchers. One of the strategies is to reduce the size of bulk Si to the sub-micrometer scale in at least one dimension, such as nanowires and nanotubes, which can effectively avoid fracture (L.-F. Cui et al., 2008; Park et al., 2009). However, nanowires and nanotubes, are expensive and difficult to scale up and suffer from limited overall charge storage capacity due to the low mass fraction of the active component in the electrode (X. Zhao et al., 2011). Another approach is

the use of porous electrode frameworks made via sacrificial templates (H. Kim & Cho, 2008; H. Zhang et al., 2011), but the porous electrodes lack the mechanical strength and have reduced packing densities (X. Zhao et al., 2011). Dispersing Si NPs into carbon or other conducting matrices that can buffer the volume change and improve the electrical conductivity of Si active materials is another technique which has been well researched and found effective. Different materials have been studied as matrix for embedding Si NPs, of which carbon materials such as amorphous carbon (Datta et al., 2011; Z. Wen et al., 2011), graphite (W. Zhou et al., 2011), carbon nanotubes (Eom & Kwon, 2011; P. Gao et al., 2010), carbon nanofibers (P.-C. Chen et al., 2011; Gómez-Cámer et al., 2011), Gr (Ding et al., 2011; Lv et al., 2011; Z.-S. Wu et al., 2010; Zou & Wang, 2011) etc. have been extensively investigated and demonstrated to improve the cycling stability of Si anode material. Besides these composite materials, one of the more recent strategies is to use electrodes made from Si NPs using special polymer binders, such as polyacrylic acid (PAA) (Magasinski et al., 2010), carboxyl-methyl cellulose (CMC) (Bridel et al., 2009), alginate (Alg) (Kovalenko et al., 2011), CMC and PAA composite binder (Koo et al., 2012), or mussel-inspired adhesive binders (DA) (Ryou et al., 2013) which have been found to result in good cycle life performance.

1.5.5. Graphene as a matrix for Si NPs

From a brief survey, Gr may serve as an excellent carbon source for preparing carbon/Si hybrid anodes with respect to its outstanding physical and chemical properties which are briefly listed as follows (D. Chen et al., 2010; R. Hu et al., 2014),

- Superior electrical conductivity
- High specific surface area
- High surface-to-volume ratio
- Ultra-thin thickness which can shorten the diffusion distance of ions

- Efficient thermal conductivity leads to less resistive heating within the electrode.
- Inert basal surface
- Structural flexibility
- Unique two-dimensional structure renders itself a specific advantage of attaching Li-ions on both surfaces of the hexagonal C-ring based sheet.

These properties of Gr make it an excellent matrix for Si NPs to improve its EC properties. Nevertheless, for the Si-based anode materials, many difficulties still exist in the utilization of Gr/Gr based materials, which are discussed in chapter 7 in detail.

In our work, we have chosen a unique and novel strategy to improve the battery performance of Si anode, where a Si-Gr composite has been prepared in a core-shell manner, which has been discussed in chapter 7 in detail.

1.6. Objective and Scope of the Thesis

As mentioned, electrochemistry based analytical methods such as EC sensors have impacted multiple fields, including diagnostics, environmental analysis, food sciences, enzymatic kinetics and pharmacology (Govindhan et al., 2014). Recently, the assembly of miniaturized EC devices using various nano functional materials/ their composites has been demonstrated for the EC detection of several electroactive targets of importance in food analyses, environmental monitoring, and clinical diagnosis. The electrode materials play a critical role in the selectivity and sensitivity of EC sensing platforms for detecting target molecules through various analytical principles. Furthermore, in addition to the electrode materials property, making them nanosized can not only produce a synergic effect among catalytic activity, conductivity and biocompatibility to accelerate the signal transduction, but also amplify recognition events by specifically designed signal tags, leading to highly sensitive sensing (C. Zhu et al., 2014). Significantly, extensive research on the construction of functional

electrode materials, coupled with numerous EC methods, is advancing the wide applications of EC devices. Motivated by these, we tried to extend and explore the EC sensing applications of nano functional materials particularly focussing on Gr and MoS_2 based systems, for the reasons mentioned earlier.

For the successful EC sensing applications, there may exist a number of challenges associated with both the electrode material (here Gr and MoS_2 based) such as processability, ease of production, bulk preparation; and the analyte (biologically/environmentally important species) under consideration, which include the need for high sensitivity, selectivity, reproducibility etc. Hereby we attempted to address some of the challenges and explore the use of Gr and MoS_2 based materials for the highly sensitive and selective detection of various analyte species which are important either biologically/environmentally. The specific challenges and merits of the electrodes developed is been discussed for each work in detail. We identify the specific objectives of present research as,

- Development of Gr and MoS_2 based nanomaterials (as electrode materials) from the bulk
- Characterization, electrode modification and EC sensing studies of the developed materials
- Identification of biologically/environmentally important analytes and detection of them using selected electrode materials based on affinity/interactions between them
- Investigation of the underlying mechanism involved in the sensing

As a second part of our current research, we studied the EC storage possibilities of certain materials especially for developing anodes for LIBs. As discussed already, graphite is the traditional choice of anode material owing to its long cycle life, abundant material supply and relatively low cost. However, the graphite anode exhibits a low theoretical specific capacity of 372 mAh/g and is prone to catching fire when operated under the wrong conditions (Shukla & Kumar, 2008). Consequently, the investigation has been undertaken to develop

new anode materials with significantly improved performance in terms of capacity, energy density and rate capability. An ideal material under consideration is Si, as discussed before, which can accommodate around thirty times more Li-ions than the graphite during lithiation, forming $Li_{22}Si_5$, which corresponds to the highest known theoretical specific capacity for Li-ion intercalation over ten times higher than that of graphite. Despite its attractive features, such as abundance, inexpensive, sustainability etc., the practical use of Si is limited by the problems discussed in the previous section, such as severe volume change and unstable SEI formation during cycling which leads to its poor cycle performance. Though various strategies have been put forward to overcome these issues, which have been already discussed, we adopt a novel strategy where Gr is utilized as a matrix in a core-shell manner to accommodate the volume expansion and overcome the unstable SEI formation effectively. So the specific objectives are,

- Developing Si based anode materials with Gr based matrix in a core-shell design
- To overcome the huge volume expansion and unstable SEI
- Achieving higher specific capacity and cycle life.

1.7. Organization of the Thesis

This thesis describes the research work on the development of various Gr and MoS_2 based materials as EC sensors or EC energy storage materials, characterization of the materials, electrode modification and EC sensing or storage studies. The focus of our research is on identifying/selecting suitable electrodes materials for detecting biologically/environmentally important analytes based on the affinity/interaction between them so that better sensitivity and selectivity shall be achieved which is investigated by the systematic EC sensing studies. The underlying mechanisms involved in the sensing are studied and discussed based on the results. The final part of the thesis explores the energy

storage aspect of Gr as a matrix for Si NPs to improve the stability and cycle life of Si-Gr based anode for LIBs. The work focuses on the strategies to overcome the challenges with conventional Si-Gr based anode systems. The thesis is organized in eight chapters as given below.

Chapter 1 provides a detailed introduction to the the basics & fundamentals of electrochemistry, discusses about the various EC methods, and explains the back ground and basics of EC sensing, EC storage and LIBs. It provides a state-of-the-art literature survey on Gr and MoS_2 based materials in EC sensing. Further, it discusses Si based anodes in LIBs, challenges, strategies adopted, the role of Gr and our research problem &objectives.

Chapter 2 is the experimental section which describes the materials and methods used for the synthesis of various Gr and MoS_2 based materials, various EC procedures adopted for the preparation/modification of electrodes and other general procedures for systematic EC sensing studies. Various characterization techniques used are also discussed in this chapter.

Chapter 3 discusses a novel green method of synthesis of gold NP functionalized graphene (Au–Gr) from β-cyclodextrin functionalized Gr (CD–Gr), its characterization to confirm the structure and composition and its EC sensing studies towards biomolecules.

In **Chapter 4**, the synthesis of mechanically pulverized graphite (pGr) from graphite and the use of pGr as an electrode material for the EC sensing of certain biologically relevant analytes is described. In addition to that, the structure of pGr is proposed based on the sensing results and the mechanism for the selective and sensitive sensing is explained.

Chapter 5 explores the EC sensing properties of the solvent exfoliated MoS_2 towards mercury (II) ions (Hg^{2+}) detection. The mechanism of sensing is discussed and is confirmed using various characterization techniques.

Chapter 6 discusses a novel method of synthesis of nitrogen doped graphene quantum dots (N-GQD) from polyaniline. The EC behaviour of N-GQDs towards the detection of nitroaromatics is described and the mechanism is discussed.

In **Chapter 7**, a simple and effective strategy to achieve Si-Gr based anode with better stability and rate performances is discussed. The advantages of the structure and the possible reasons for better performance are also proposed.

Chapter 8 summarizes the highlights of the output of the research work and the future possibilities in this area.

CHAPTER 2

MATERIALS AND METHODS

This chapter gives a detailed description of the materials and the methods used for the synthesis of the Gr and MoS_2 based functional materials and mentions the various characterization instruments used for studying the structure and composition of the materials. Further, the methods used for the cleaning preparation/modification of the electrodes and the various electrochemical procedures adopted herein for the studies (both EC sensing and storage) along with the general procedures for reusability, reproducibility and stability studies of the developed EC sensors are detailed.

2.1. Materials

Graphite (21 μm particle size), beta cyclodextrins (CD) (97%, CD was recrystallized before use), hydrogen tetrachloroaurate (III) ($HAuCl_4$), dopamine (DA), acetyl choline (Ach), Molybdenum disulphide (MoS_2), 2,4,6-trinitrophenol (TNP) and 2,4 dinitrotoluene (DNT), $FeCl_3$, $FeCl_2$, $SnCl_4$, $SnCl_2$ and $CuSO_4$ were purchased from Sigma Aldrich India Co. Ltd. N,N dimethyl formamide (DMF), dimethyl sulphoxide (DMSO), potassium permanganate ($KMnO_4$), hydrogen peroxide (H_2O_2), hydrochloric acid (HCl), sulfuric acid (H_2SO_4), sodium hydroxide (NaOH), di-sodium hydrogen phosphate dihydrate, sodium dihydrogen phosphate monohydrate, glucose anhydrous and ascorbic acid (AA), hexane, Tetrahydrofuran (THF), uric acid (UA), aniline, ammonium peroxydisulfate (APS) and chloroform were purchased from Merck, India Ltd. graphite oxide (GO) was obtained from Anderlab Technologies Pvt. Ltd., rGO was prepared by chemical reduction using hydrazine hydrate. N-methyl pyrrolidone (NMP), Isopropanol (IPA), $HgCl_2$, $AgNO_3$, $CdCl_2$, $NiSO_4$, Zn $(NO_3)_2$, Co $(NO_3)_2$, $PbNO_3$ and $K_2Cr_2O_7$, were obtained from Spectrochem Pvt. Ltd. 2,4-dinitrophenol (DNP) was purchased from Sisco research laboratories Pvt. Ltd. 2-nitrophenol (NP) was

purchased from Otto Chemie Pvt. Ltd. Si NP with an average particle size of ~60 nm was purchased from American Elements Ltd. Distilled water was used in all the procedure unless specified otherwise. All the solvents and reagents used in this study were of analytical grade.

2.2. Characterization Techniques

Several techniques such as spectroscopic, microscopic and thermal are performed for the characterizations of synthesized materials. Fourier transform Infra-red (FTIR) spectra were recorded in a Perkin Elmer spectrum100 FTIR spectrophotometer. The range of FTIR spectra is 4500- 400 cm^{-1} with an optical resolution of 0.5 cm^{-1}. The sample was diluted with KBr pellet before doing the analyses.

Absorption spectra were recorded using CARY 100 Bio UV-Visible spectrophotometer. Photoluminescence (PL) spectra were recorded in Horiba FluoroMax-4 with the excitation and emission slits of 1 and 2 nm respectively. Raman spectroscopic measurements were carried out in Renishaw inVia Raman microscope with the excitation laser wavelength of 532 nm. Thermogravimetric Analysis (TGA) were done using TA Q50 instrument with the rate of 10°C/min either in the presence of air or nitrogen. X-ray diffraction (XRD) analyses were carried out on a Bruker D8 discover small angle X-ray diffractometer. The Cu Kα radiation (λ = 1.54 Å) was used as an excitation source. XRD pattern also allows estimating crystal size by Debye-Scherrer equation as given in equation 2.3. This equation gives the relationship between diffraction peak broadening (β) and crystallite size (D),

$$D = \frac{0.94\,\lambda}{\beta cos\theta} \qquad (2.1)$$

Scanning electron microscope (SEM) images were taken using Hitachi SU6600 variable pressure field emission (FE) SEM. High resolution transmission

electron microscopy (HRTEM) analyses were done using JOEL JEM 2100 electron microscope with an accelerating voltage of 200 kV. Brunauer-Emmett-Teller (BET) SA analyses were made in Tristar II micromeritics. X-ray photoelectron spectroscopy (XPS) analyses were carried out using Kratos analytical axis ultra X-ray photoelectron spectrometer with the excitation source of Al Kα. Agilent 5500 Scanning Probe Microscope Atomic force microscopy (AFM) with 9 μ scanner was used in tapping mode for AFM imaging. Scanning tunnelling microscope (STM) images were captured using nanoREV STM, Quazar Technologies Pvt. Ltd. Electrochemical Impedance Spectroscopy (EIS) studies were carried out between 100 mHz and 100 kHz at the open circuit voltage.

2.3. Methods

2.3.1. Electrochemical measurements

For EC sensing studies, all the EC measurements were carried out with potentiostat/ galvanostat PG 302N, AUT 83909 (Metrohm, Autolab, Netherlands) with three electrode system using glassy carbon electrode (GCE) with 3 mm diameter as working electrode, Pt wire as counter electrode and Ag(s)/ AgCl(s)/ Cl^{-1}(aq., saturated) as reference electrode. The voltammetric experiments were carried out using various techniques including CV, DPV, LSV etc. The voltammetric parameters in each technique, as well as the electrolytes vary with the sensor material as well as the analytes under consideration, which are discussed in each chapter in detail. Amperometric measurements, particularly pre-concentration studies were done by using chronoamperometry at required (specified) voltages.

The EC measurements adopted for battery studies are explained in chapter 7 in detail.

2.3.2. Electrode cleaning, preparations/modification

Prior to modification of GCE with the samples, they were mechanically polished with a wetted microcloth containing alumina powder (0.05 mm), and then carefully cleaned in distilled water and in acetone by ultra-sonication (2 minutes each). The dried GCEs were modified with the material samples by drop-dry casting method, the details are given in each chapter separately. In a general procedure, the electrode modification was done by dropcasting 20 µL of 0.5 mg ml^{-1} freshly ultrasonicated dispersions of the materials (in suitable solvents), to ensure that roughly the same amount of material is deposited onto the electrode surfaces. The drpcasted GCEs were dried under air or sometimes under the stream of nitrogen depending on the material behaviour. After each analysis, GCEs were cleaned by mechanical polishing followed by ultrasonication in the solvent, distilled water and in acetone.

2.3.3. Reusability, reproducibility and stability studies

In general, the reusability and storage stability of the developed sensor electrodes were evaluated using CV or DPV experiments by comparing the oxidation/reduction peak currents obtained in respective electrolytes containing a particular concentration of the respective analyte species immediately after washing, and after a period of 1 month respectively. The percentage of retention of the initial current responses were calculated and recorded. Measurements on five independently prepared electrodes were used to estimate the reproducibility, the relative standard deviations (% RSD) in the oxidation/reduction peak currents in CV/DPV for a particular analyte concentration were measured. RSDs were obtained by using the formula,

$$RSD = 100 \times {}^{s}/_{\bar{x}} \qquad (2.2)$$

Where s is the sample standard deviation and $\bar{x}$ is the sample mean.

2.3.4. Real sample analysis

2.3.4.1. Blood sample analysis

The general procedure adopted for real blood sample analysis involve spiking of real human blood sample via standard addition method, where known amounts of the analyte samples were added to the diluted blood sample (1000 times), analyzed electrochemically using CV/DPV methods and the recovery amounts were measured.

2.3.4.2. Water sample analysis

The real water sample analyses were carried out by extending the sensing studies to the samples such as sea, tap and ground water. The details are given in each chapter. In general, the samples were spiked with the analyte under study at different concentration levels, analyzed with the proposed EC method and the recovery amounts were calculated.

The recovery calculations were done using the formula,

$$\%\, Recovery = \left(\frac{C_{found} - C_{spiked}}{C_{spiked}} \times 100\right) + 100 \qquad (2.3)$$

Where C is the concentration of the analyte species under study. The high recovery values in real sample analysis are indicative of the successful applicability of the developed sensors in real environments.

CHAPTER 3

GREEN SYNTHESIS OF GOLD–GRAPHENE NANOCOMPOSITE FOR THE EFFICIENT NON-ENZYMATIC ELECTROCHEMICAL SENSING OF GLUCOSE AND ASCORBIC ACID

A new and green synthesis of gold nanoparticle functionalized graphene (Au–Gr) from β-cyclodextrin functionalized Gr (CD–Gr) is reported and its EC sensing property was investigated and discussed herein. The Au–Gr formation was confirmed by various characterization techniques such as UV-visible spectroscopy, electron microscopy, XRD and its formation mechanism was discussed. The EC sensing property of Au–Gr was evaluated using biomolecules such as glucose and ascorbic acid (AA). The Au-Gr yielded lowest LODs compared to the previous reports: 10 and 40 nM, for glucose and ascorbic acid, respectively. The possible reasons for the excellent sensing property of Au–Gr were evaluated and discussed.

3.1. Introduction

In constructing EC sensors, Gr is extensively employed recently, because of its exceptional properties as discussed in the introduction chapter. Similarly, metal NPs possess several advantages in terms of electroanalysis such as large specific SA, biocompatibility, catalysis and control over local microenvironment (Welch & Compton, 2006). Thus, the combination, metal NPs decorated Gr sheets have drawn the attention of researchers in the field of EC sensors as the metal NP–Gr composites can display a synergistic effect of the catalytic character of metal NPs and the high electrical conductivity of Gr (X. Wang & Zhang, 2013). Among the metal NPs, Au NPs are known for their unique optical and surface properties that attract a great deal of attention because of their potential

applications in catalysis, optics, sensing, nanobiotechnology etc. (C. Shen et al., 2008). The metal NP–Gr composites are usually obtained by in situ reduction of metallic salts on graphene oxide (GO) or modified Gr sheets (Goncalves et al., 2009; Xu et al., 2008; X. Zhou et al., 2009) in the presence of reducing or stabilizing agents or both. Muszynski et al. (Muszynski et al., 2008) have reported the synthesis of Gr sheets decorated with Au NPs by chemically reducing gold chloride ($AuCl_4^-$) with sodium borohydride ($NaBH_4$) in a Gr–octadecylamine suspension. Goncalves et al. (Goncalves et al., 2009) have reported the surface modification of Gr nanosheets with Au NPs based on the reduction of Au (III) complex by sodium citrate. These methods have the advantages of large-scale and high yield, but the use of excessive reducing agents will leave lots of chemical residues. Hence a simple and environmental friendly method for the synthesis of metal NP-Gr nanocomposites is preferable in terms of the final product and the environment. Recently, Tian et al. reported (Tian et al., 2012) the preparation of an AuNPs–β-cyclodextrin–Gr (AuNPs–CD–Gr) composite by an in situ thermal reduction of GO–CD and $HAuCl_4$ with NaOH. The AuNPs are known to electrochemically oxidize glucose in alkaline solutions (Pasta et al., 2010). The group have used the AuNPs–CD–Gr modified electrode for the simultaneous determination of AA, DA and UA by square wave voltammetry, whereas Kong et al. (Kong et al., 2012) reported a GO–thionine–Au nanostructure composite (GO–THi–Au/GCE) as a non-enzymatic glucose sensor with a detection limit of 0.05 mM.

In this chapter, we report the preparation of a AuNPs functionalized Gr nanocomposite, referred to as Au–Gr in aqueous medium using a simple, green synthesis method which utilizes the biocompatible, non-toxic compound, CD (K. Liu et al., 2008) as the reducing agent for Au (III) ions. Reduced graphene oxide (rGO) functionalized with CD molecules, named as CD–Gr (Aswathi et al., 2015), is used as the substrate to reduce and anchor Au (III) ions to form Au–Gr. Functionalization of rGO by CD renders CD-Gr, which is dispersible in water and its aqueous suspension yields individual Gr nanosheets of ~2 nm thickness. In addition to being a dispersing agent for the rGO in water, the CD molecules act as

reducing agent for the Au/Ag ions as well as capping agent to form the Au–Gr, silver NPs functionalized Gr (Ag–Gr) etc. (Bai et al., 2008; T. Huang et al., 2009; Manivannan & Ramaraj, 2011; Pushpa et al., 2013) and thus Au-Gr was made from CD-Gr without adding any external reducing agents. The results obtained for the EC sensing studies of the Au–Gr nanocomposite as a non-enzymatic electrode indicates that the Au–Gr possesses EC sensing properties better than the previously reported AuNPs–CD–Gr and is attributed to the usage of rGO which renders better conductivity. The non-enzymatic electrodes are highly desirable because it offers better stability, simplicity reproducibility and thus cost-effectiveness compared to the enzymatic counterparts. In this work, the Au–Gr was employed for sensing glucose and AA and the results indicate that the synergistic effect of Au NPs and Gr makes this nanocomposite an excellent electrode material for the sensing of the biomolecules. Our results show that the Au–Gr possesses the best LODs for glucose and AA, with 10 and 40 nM respectively, compared to that of the values reported in the previous literature.

3.2. Experimental

3.2.1. Preparation of GO, rGO and CD–Gr

The GO was synthesized according to modified Hummers' method (Venugopal et al., 2012). Preparation of rGO from GO was done using hydrazine hydrate reduction, which is described elsewhere (Stankovich et al., 2007). CD-Gr was synthesised by simple mechanical mixing of the rGO and CD, the procedure is as follows:

In a typical synthesis of CD–Gr, Gr (10 mg) and 100 mg of recrystallized CD were taken in an agate mortar and crushed by adding distilled water (1 ml) using a pestle for 3 hours. Distilled water was added in drops whenever the mixture became dry. After three hours of crushing, the powder obtained was dialysed in distilled water for 1–2 days and then centrifuged to remove water and dried in a vacuum oven at 60 ˚C overnight.

3.2.2. Preparation of Au–Gr

The Au-Gr was synthesized from the CD-Gr, in a typical synthesis of the Au–Gr nanocomposite, 10 ml of $HAuCl_4$ (1 mM) solution was heated to 100 ^oC and to the solution, 3–6 ml of 0.01% CD–Gr dispersion was added. The solution was heated at 100^oC for another 30 minutes, till a color change due to the formation of AuNPs was observed.

3.2.3. EC methods and preparation of electrodes

The EC behaviors of glucose and AA (in 0.1 M NaOH and 0.1 M phosphate buffer (PBS) solution respectively) were investigated at the three different electrodes: rGO, CD–Gr and Au–Gr modified electrodes, by CV. The electrodes were prepared by drop casting suspension (0.5 mg ml^{-1}) of each in DMF over the pre-treated GCEs. DMF was used as the solvent because it was able to disperse all the above mentioned samples. The electrodes were then allowed to dry for 24 hours at RT prior to the EC studies. The procedure for the preparation of electrodes is explained in detail in the Chapter 2.

3.3. Results and Discussion

3.3.1. Formation and characterization of CD–Gr from rGO

The formation of the CD–Gr from rGO, was confirmed by various techniques such as FTIR & Raman spectroscopy, TGA, SEM and AFM. The FTIR and Raman spectra of the GO, rGO and CD–Gr are given in Figure 3.1. The FTIR of CD-Gr (Figure 3.1A) shows peak at 3400 cm^{-1} corresponding to the –OH vibrations from CD, and in the regions below 1000 cm^{-1} similar to those seen in CD, suggesting the formation of the composite. The Raman spectra of GO, Gr and CD-Gr (Figure 3.1B and C) show three peaks for each, a disorder/defect peak D at 1360 cm^{-1}, a graphitic peak G at 1580 and a 2D peak at 2680-2800 cm^{-1}. The I_D/I_G is higher for the rGO which suggests that the defects are higher (due to the

hydrophilic functionalities present at the edges and other hydrophobic functionalities present in the basal plane) compared to that of the GO. The 2D peak of the powder samples of GO and rGO shows two peaks, one at 2680 and another at 2800 cm^{-1} while the 2D peak (2680 cm^{-1}) of the drop cast CD-Gr (from a dispersion), has higher intensity compared to that in GO and rGO, which is characteristic of fewer layers. This result suggests that the Gr sheets of few layers are present in the CD-Gr.

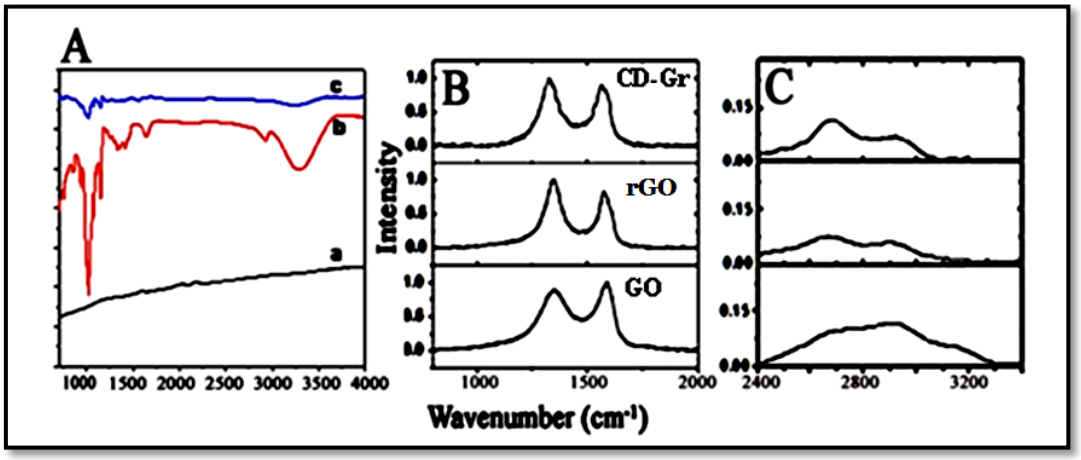

Figure 3.1. (A): The FTIR spectra of (a) rGO (b) CD and (c) CD-Gr; (B) and (C): Raman spectra of the powder samples of GO, rGO and dispersion of CD-Gr.

The thermograms of CD, CD-Gr and Au-Gr are provided in Figure 3.2 for comparison. The thermogram of CD-Gr confirms the presence of CD in the CD-Gr composites and that of the Au-Gr clearly shows the presence of Au in the composite, thus suggesting the formation of CD-Gr and Au-Gr. Further, the AFM images and height profiles of CD-Gr (Figure 3.3) show the presence of Gr sheets of ~2.0 nm thickness. Theoretically speaking, the thickness of a Gr sheet is 0.354 nm and the height of a CD molecule is 1.53 nm. Therefore the thickness of ~2.0 nm observed in the AFM analysis can be due to the presence of CD molecules on the individual Gr sheets which agrees with the previous report (Yujing Guo et al., 2010).

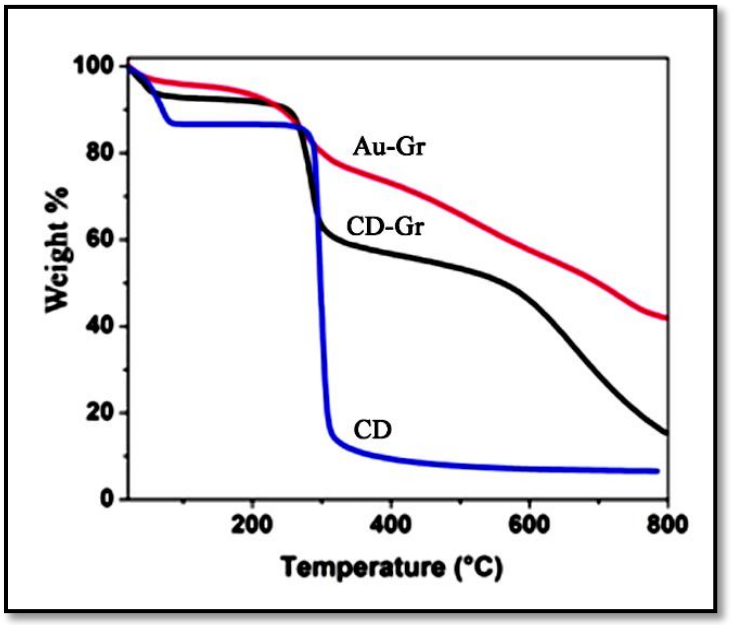

Figure 3.2. The thermograms of CD (blue), CD-Gr (black), and Au-Gr (red) done under N_2 atmosphere at the heating rate of 10 ^{o}C/minute.

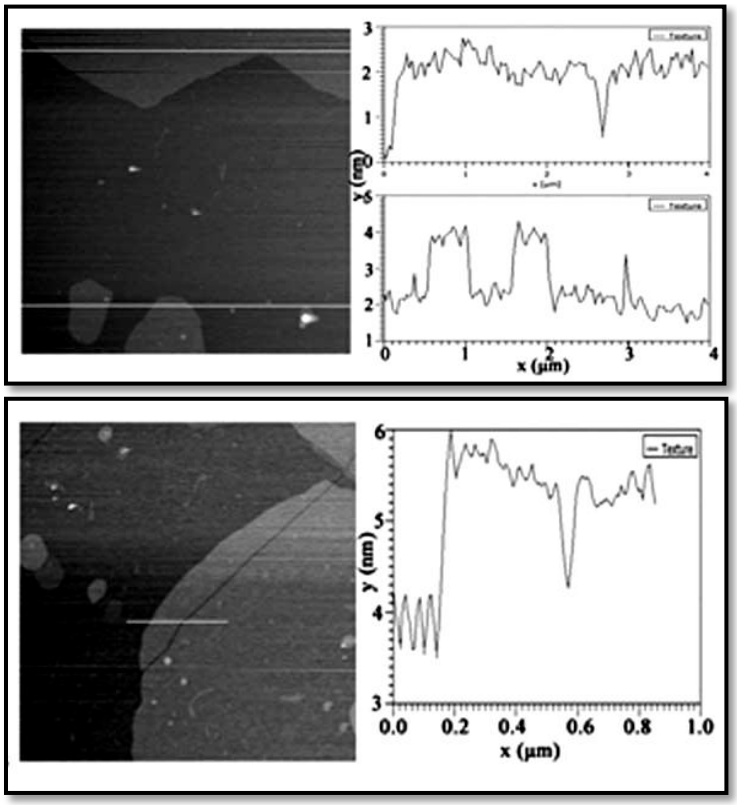

Figure 3.3. Tapping mode AFM images of CD-Gr showing Gr sheets of ~2 nm thickness

The Figure 3.4 shows the photographic images of the aqueous dispersion of CD-Gr in the presence of NaCl at different time intervals. It is seen that agglomeration of Gr nanosheets happens immediately after the addition of NaCl (Left) and complete settling happens within 24 hours (Right). The positive sodium ions compensate the negative charges of the hydroxyl groups of the CD molecules on the surface of the Gr and thus initiating the aggregation of Gr nanosheets.

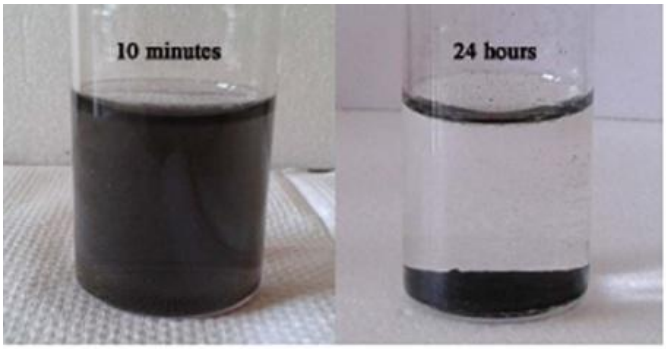

Figure 3.4. Photoimages of CD-Gr in water at ~10 minutes and 24 hours of addition of 1 % NaCl solution.

3.3.2. Formation and characterization of Au–Gr

The Au–Gr was prepared from the CD–Gr as explained in the experimental section. The schematic for the formation and the structure of the CD–Gr, and Au–Gr are illustrated in Figure 3.5.

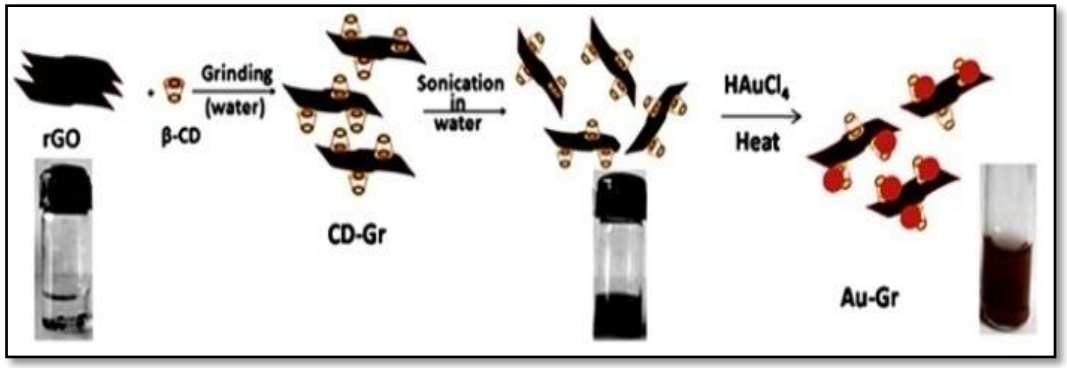

Figure 3.5. Schematic of the formation of CD-Gr, and Au-Gr from the CD-Gr. (Inset digital images of Gr, CD-Gr and Au-Gr in water)

The formation of the Au–Gr was confirmed by various techniques. The thermogram of the Au–Gr (Figure 3.2) showed an increase in the residual weight from that of the CD–Gr indicating the presence of Au in the Au–Gr. Further the SEM and TEM images (Figure 3.6) of the Au–Gr clearly showed the presence of Gr and Au NPs in the composite. The SEM images suggest that the Au NPs are attached to the Gr sheets and the images reveal that the Au NPs were not aggregated and are uniformly distributed throughout the Gr sheets (Figure 3.6B). Further, the TEM images agreed with this observation (Figure 3.6C). The non-aggregation of Au NPs might possibly be attributed to the presence of CD on the Gr sheets which reduces the Au (III) ions to Au NPs and thus creates a close contact with the Gr sheets and stabilizes the formed NPs. The TEM images of the Au–Gr revealed the presence of Gr nanosheets and Au NPs of 50–150 nm in size. The EDAX spectrum (Figure 3.6D) of the Au–Gr showed the presence of Au, carbon and oxygen in the Au–Gr and thus confirms the formation of Au–Gr.

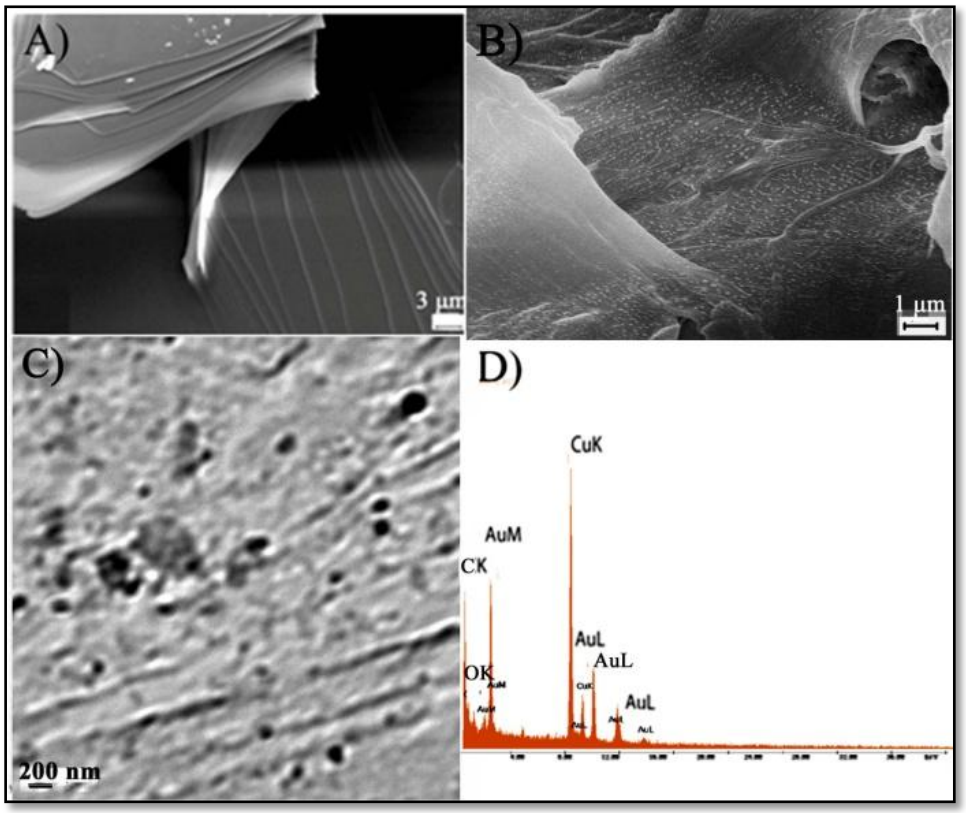

Figure 3.6. SEM image of (A): CD-Gr and (B): Au-Gr; (C) and (D): TEM image and the EDAX spectrum of the Au-Gr.

The Au–Gr was further characterized by XRD (Figure 3.7A) and the peaks corresponding to Au were present. The diffraction peaks at 2θ = 38.2◦, 44.4◦, 64.6◦ and 77.5◦ could be indexed to the (1 1 1), (2 0 0), (2 2 0) and (3 1 1) planes of a pure face-centered crystalline structure of Au (X. Feng et al., 2009). The thin Gr sheets as evident from the AFM images of the CD–Gr and from the TEM images of the Au–Gr, and the absence of the characteristic broad peak of rGO around 26˚ in the XRD suggest that the Gr sheets are well separated by the Au NPs in the Au–Gr. The results are indicating that in the Au–Gr nanocomposite, Gr sheets are attached with Au NPs through CD, and are not aggregated.

The UV-visible spectroscopy is an important tool for characterizing noble metal NPs and the spectrum of the Au–Gr showed the characteristic surface plasmon resonance (SPR) peak of Au NPs at around 550–560 nm, and thus confirmed the formation of Au NPs (Figure 3.7B). Thus, the characterization results undoubtedly confirm the formation of Au NP functionalized Gr nanocomposite from the CD–Gr. A control experiment of heating of $HAuCl_4$ in the presence of the physical mixture of Gr and CD resulted in a black precipitate, did not yield the color of Au NPs, and did not show the SPR peak corresponding to Au NPs. The result suggested that the mixture of CD and Gr did not form Au-Gr in the described structure, this might be due to the lack of stabilization of Gr sheets and the formed Au NPs by CD as in that of the Au-Gr, and hence undergoes aggregation, resulting in a non-dispersible black precipitate, which has no SPR peak. The mechanism of formation of the Au–Gr can be explained as follows: the Au (III) ions get attached to the –OH groups of CD, and the CD reduces the Au (III) ions to Au NPs, thus resulting in the formation of Au–Gr. The non-occurrence of the color of Au NP in the same conditions with Gr and CD mixture suggests that the functionalization of Gr by CD is crucial in the formation of the dispersible Au–Gr and to the contact between the Au and Gr.

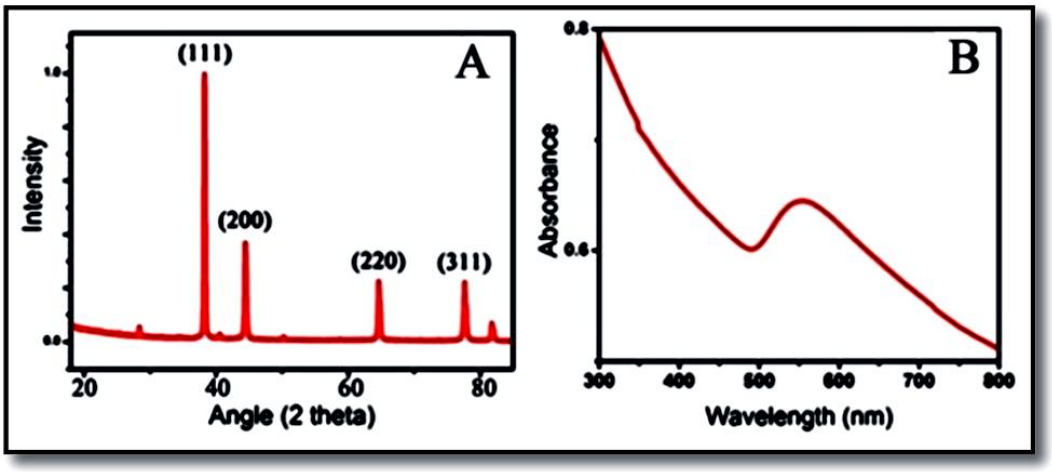

Figure 3.7. (A): XRD pattern and (B): UV-Visible spectrum of the Au-Gr

3.3.3. EC sensing properties

One of the potential applications of Au NPs functionalized Gr is the EC sensing of analytes. It has been reported that, Au NPs can electrochemically oxidize glucose in alkaline solution. However, there are challenges for Au NPs as an electrode, which are its aggregation on GCE and poor adsorption to the hydrophobic GCE (Pasta et al., 2010). Recently, Gr based materials have been extensively studied as electrode materials for sensing various analytes. Therefore, we investigated the EC sensing property of Au–Gr as a non-enzymatic electrode for sensing glucose and further extended it for the sensing of AA.

3.3.3.1. EC sensing of glucose

In an attempt to study the EC sensing properties of the electrodes, the EC oxidation of glucose in 0.1 M NaOH was investigated by CV at the three different electrodes: Gr coated GCE (Gr/GCE), CD–Gr coated GCE (CD–Gr/GCE) and Au–Gr coated GCE (Au–Gr/GCE) along with bare GCE. The results of the CV experiments are given in Figure 3.8 and Figure 3.9A. The CV curve of glucose at the Au–Gr/GCE exhibited three clear EC peaks in the anodic sweep and one in the cathodic return sweep. However, no redox peaks were observed for glucose at the GCE, Gr/GCE and CD–Gr/GCE for the same concentration (Figure 3.9A). The

first peak at around -0.02 V (Figure 3.8C, peak “a”) was attributed to the dehydrogenation of anomeric carbon (Pasta et al., 2010). A second oxidation peak was observed at around 0.2 V (Figure 3.8C, peak “b”) and was attributed to the formation of gluconate from glucose oxidation and the third peak around 0.45 V (Figure 3.8C, peak “c”) was due to the surface oxidation of Au (Pasta et al., 2010). The Au–O was then reduced at 0.1 V (Figure 3.8C, peak “d”) in the cathodic scan (Pasta et al., 2010). The interesting aspect of glucose on Au NP electrode is the oxidation peak of glucose (Figure 3.8C, peak “e”) during the cathodic scan which was obtained as soon as the oxide layer of Au was reduced (Hsiao et al., 1996; Jena & Raj, 2006; Xiang et al., 2003). The mechanism for the oxidation during the cathodic sweep was first proposed by Liu and Makovos: the oxide layer is reduced to generate free O^{2-} anions which react with glucose to give gluconic acid, and then the Au surface undergoes re-oxidation by OH^- in solution (Hsiao et al., 1996). The corresponding peaks were not detected at the Gr/GCE and CD–Gr/GCE electrodes even at 3 mM and a small peak was observed for glucose at both the electrodes (Gr/GCE and CD–Gr/GCE) from 3.2 mM onwards and this proves the inferior electroactivity of the electrodes towards the oxidation of glucose compared to that of the Au–Gr/GCE and the role of Au NPs in the electro catalytic oxidation of glucose. The response of the Au–Gr/GCE sensor for glucose was tested over the concentration range of 10 nM–10 mM. As shown in Figure 3.9B, excellent linearity was achieved (Linear dynamic range, LDR, R^2 = 0.994) throughout this concentration range, while such a response was absent with the other two electrodes (Gr/GCE and CD–Gr/GCE). As illustrated in Figure 3.9C, the observed LOD of glucose using the Au–Gr/GCE was 10 nM, where as the Gr/GCE and CD–Gr/ GCE did not show any glucose detection (see Figure 3.9A) in the nanomolar and micromolar range. The results clearly demonstrate the enhanced EC sensing behavior of the Au–Gr towards glucose biomolecule.

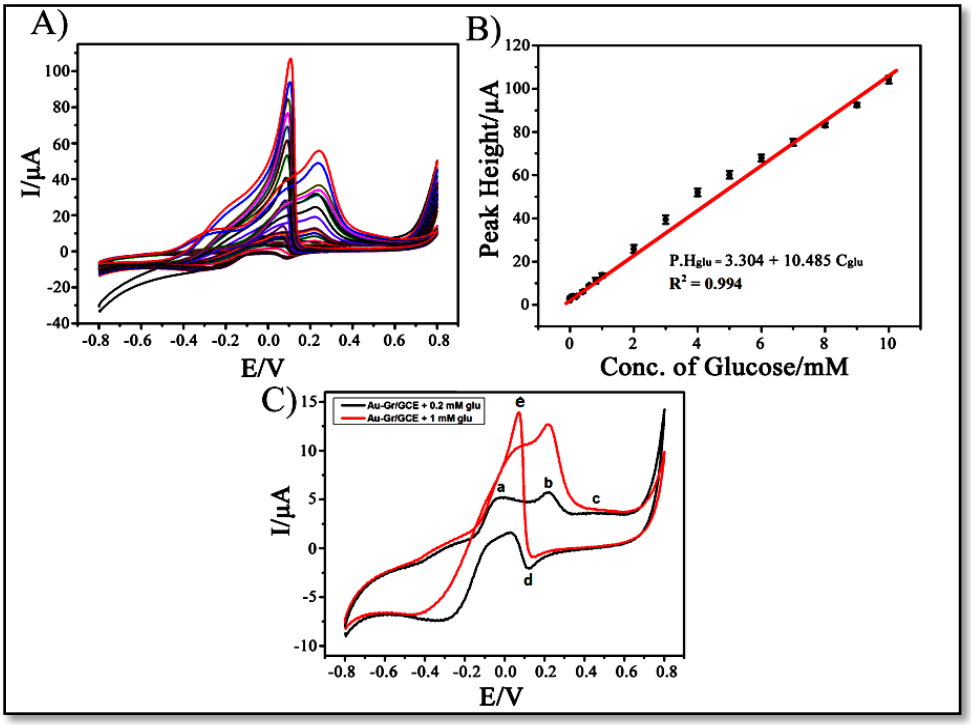

Figure 3.8. (A): The CV scans of glucose at the Au-Gr/GCE for the concentration range of 0 to 10 mM and (B): The corresponding linear relation between peak height and concentration from 10 nM to10 mM. (C): The CV scans of glucose using the Au-Gr/GCE in 0.1 M NaOH for two different concentrations (0.2 mM and 1 mM); the peaks a, b, c, d and e correspond to the formation of different EC oxidation and reduction products of glucose and Au.

Ideally, for Gr to exhibit its distinct properties, it should be narrowed to single or few-layer morphology (Artiles et al., 2011). Here, owing to the functionalization of CD, the Gr is restricted to one layer thickness, which might be a major reason for the higher sensitivity exhibited by the Au–Gr. However, it is well known that the Gr sheets tend to form irreversible agglomerates because of the van der Waals interactions and even restack to form multi layers over the electrode surface in the dry state (Baby et al., 2010). The prevention of restacking by the NPs as spacers will result in the increase in the SA and thereby enhancement in the performance. Thus, the increased sensitivity of Au– Gr might be due to the higher SA leading to high analyte loading (Artiles et al., 2011). Electrodes made from thin Gr sheets have significant uniform distribution of electrochemically active sites, and its entire volume is exposed to the surrounding due to its 2D structure, making it very efficient in detecting adsorbed molecules (Artiles et al., 2011), In addition, the improved catalytic and conducting properties

ensure remarkable EC sensing properties. Materials such as Au generally exhibit poor biomolecule adsorption, which results in the weak substrate– biomolecule coupling and high noise (Artiles et al., 2011). The Gr and CD in Au-Gr can assist the adhesion of biomolecules, due to its similarity to the biomolecules in terms of the carbon skeleton, functional groups and the ring structures which may promote the adsorption of the glucose biomolecules by stacking and H-bonding interactions. The NPs are known to increase the stability and maintain the activity of biomolecules, enhance the catalysis of EC reactions, decrease overpotentials, if any and enable the reversibility of redox reactions. The conductivity of NPs enhances the electron transfer between the active centres of biomolecules and electrodes so that the particles can act as electron transfer conduits or mediators. A major shortcoming of NPs is their lack of stability and tendency to aggregate. Immobilization of NPs is crucial for developing electrocatalytic devices (Artiles et al., 2011). The Au–Gr, can rise above these limitations because of the tethering of Au NPs to the Gr substrate through CD molecules thus enhancing the stability of the electrode. It is evident that the Au NPs are not aggregated in the Au–Gr from the SEM and TEM images of the Au–Gr. Bare Au NP on the GCE has limitations such as aggregation and lower adhesion to the electrode (GCE) which is of carbon (Pasta et al., 2010), whereas in the Au–Gr, the Gr provides improved adhesion to the GCE. This will prevent the easy loss of the sensor material from the surface of GCE, thus improving the stability of the electrode. Our studies show that the Au–Gr/GCE retains the 100% of the initial current response even after three weeks of storage at RT and the result proves the excellent stability of the non-enzymatic glucose sensor. Non-enzymatic glucose sensors based on the electrocatalytic oxidation of glucose is a subject of intense research interest, as it can avoid the poor stability of enzymatic sensors and the interference of certain electro-oxidizable species (H.-F. Cui et al., 2007). Our results show that the Au–Gr composite offers in addition to the excellent sensing property, stability as well. This is the first report of Au NP functionalized Gr, tested as a non-enzymatic sensor for the EC detection of glucose molecule, and the results show that the Au–Gr possesses excellent sensing properties, better than any other reported non-

enzymatic and enzymatic electrodes and is attributed to the synergistic effect of Au NP and Gr and the method of preparation.

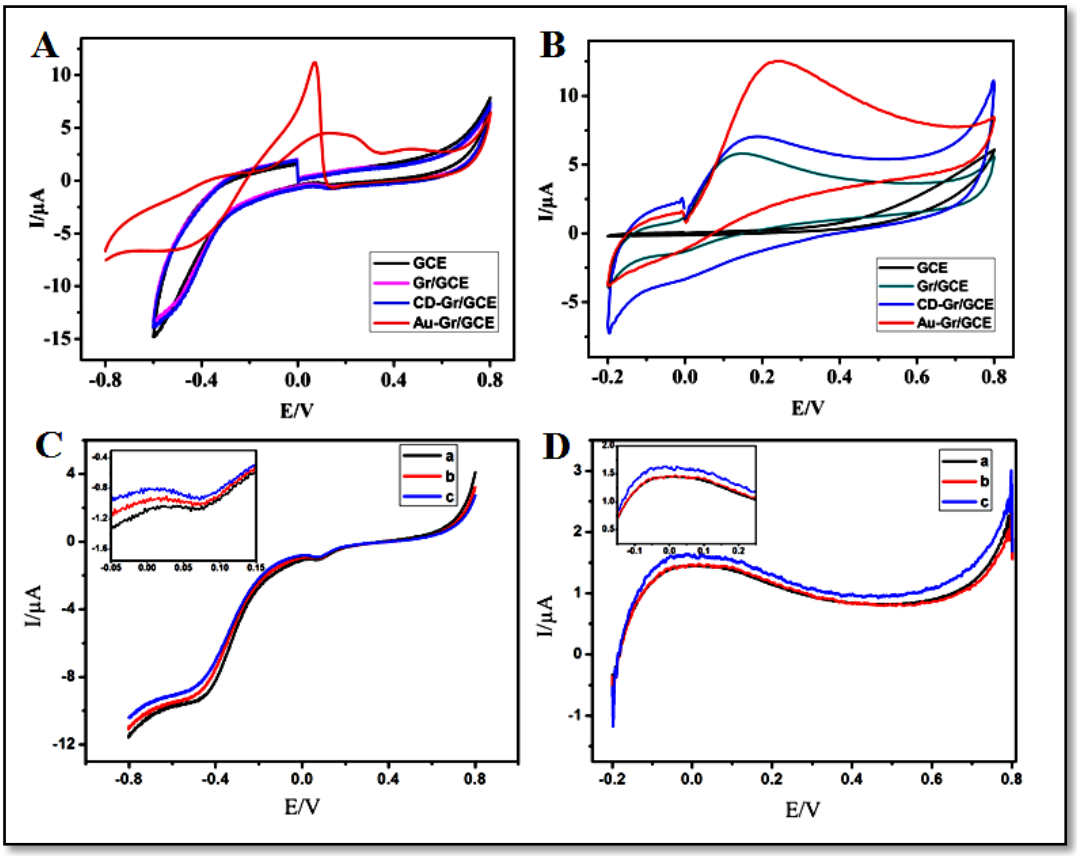

Figure 3.9. CV plots showing (A): Glucose sensing behaviour of GCE, Gr/GCE, CD-Gr/GCE and Au-Gr/GCE; (B): AA sensing behaviour of GCE, Gr/GCE, CD-Gr/GCE and Au-Gr/GCE; LSV plots showing LODs of Au-Gr/GCE for (C): glucose (a- 0 M, b- 10 nM , c- 20 nM) and (D): AA (a- 0 M, b- 30 nM, c- 40 nM).

A comparison of the reported glucose sensors to our results are given in Table 3.1. The result shows that the Au–Gr exhibits linearity in the physiological glucose level and has the best LOD compared to the reported values. The rate of electron transfer has been shown to be surface dependent. The creation of specific surface functional groups can increase this rate significantly (Artiles et al., 2011). The surface functional groups in the Au–Gr due to the CD molecules can possibly enhance the adsorption and desorption of molecules. The superior electrocatalytic property of the Au–Gr is attributed to the synergistic effect of the catalytic properties of nanocrystalline Au particles and the improved SA, adsorption and

conductivity offered by thin Gr sheets. The CD molecules mainly contribute to the atomic nature of Gr sheets, thus enhancing the conductivity, SA and electron transfer of Gr sheets and in addition, improve the adsorption of biomolecules. In order to see the potentiality and versatility of the Au–Gr as a non-enzymatic sensing electrode material, we investigated the EC sensing of the Au–Gr towards another important biomolecule, AA.

3.3.3.2. EC behavior of AA

The EC oxidation of AA was conducted in 0.1 M Phosphate buffer solution and investigated by CV. The experimental results show that the Au–Gr/GCE exhibits excellent EC sensing properties compared to that of the GCE, Gr/GCE and CD–Gr/GCE. (Figure 3.9B). The CV response of the Au–Gr/GCE sensor against increasing concentration of AA is illustrated in Figure 3.10A. The plot clearly showed the enhancement of the peak current, corresponding to the EC oxidation of AA, with increasing concentration of AA. As shown in Figure 3.10B, the Au–Gr/GCE gave an excellent LDR of 40 nM to 10 mM ($R^2 = 0.998$) for AA; the experimental range studied was 10 nM-10 mM. Moreover at lower concentration range (40 nM–1 mM) of AA, Au–Gr/GCE showed a remarkable enhancement in the current response and with good linearity as illustrated in Figure 3.10C. Such a good linear response was absent with the Gr/GCE and CD–Gr/ GCE sensors (Figure 3.11B). The LOD of the Au–Gr/GCE towards AA was found to be 40 nM, whereas those of the Gr/GCE and CD–Gr/GCE were 0.2 and 0.6 mM, respectively. The better performance of the Au–Gr/GCE towards AA molecule compared to that of the Gr/GCE and CD–Gr/GCE can be attributed to the synergistic effect of the catalytic activity of Au NPs (L. Zhang et al., 2011) and the excellent conductivity, better adsorption and higher SA of Gr in the composite as explained in the sensing of glucose section. The result is found to be one of the best when compared to other AA sensors reported previously (Table 3.2). The detection limit of AA for the previously reported Au NPs functionalized Gr through CD (Tian et al., 2012) was 10 μM whereas our value is 40 nM, which is 250 times lower.

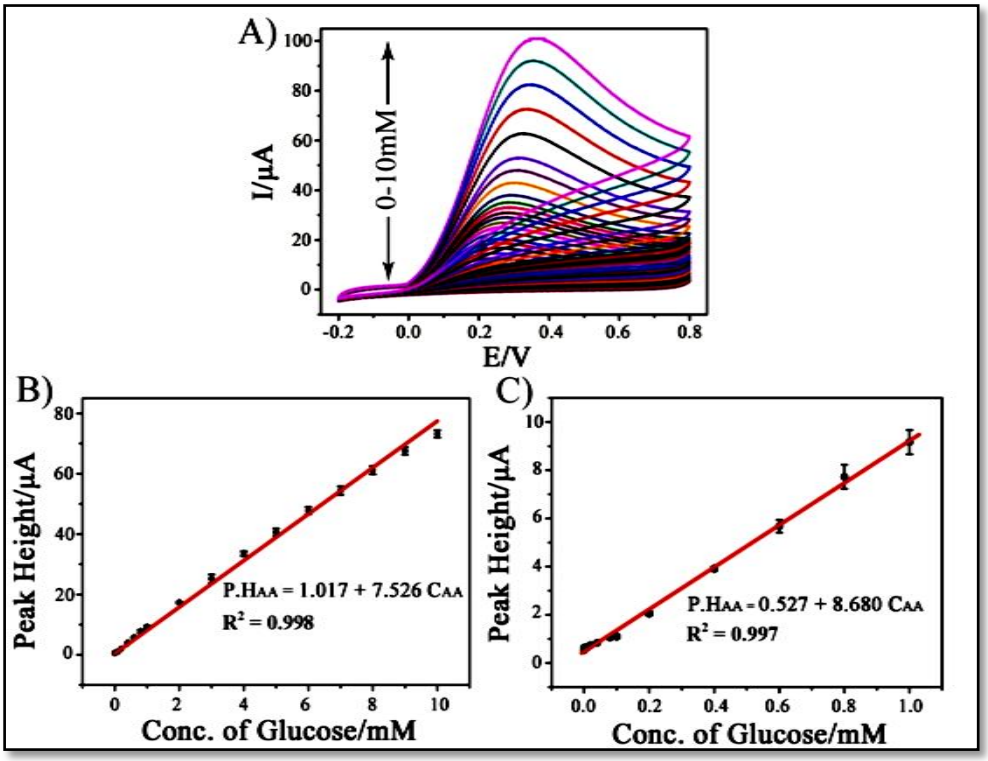

Figure 3.10. (A): CV scans of AA at the Au-Gr/GCE for the concentration range of 0 to 10 mM; (B) and (C): Corresponding linear relation between peak height and concentration for the concentration ranges, 40 nM to 10 mM and 40 nM to 1 mM (lower range linearity), respectively.

The results show that, the LODs obtained for glucose and AA are 10 and 40 nM, respectively, and were the best values reported. The better performance of the Au–Gr electrode towards AA when compared to the previously reported Au–CD–Gr (Tian et al., 2012) is possibly due to the improved conductivity offered by the Gr counterpart as rGO prepared by hydrazine hydrate reduction is used in our work, instead of the GO in their work. The low electrical resistance and atomic thickness of Gr, enhances the EC sensing (Artiles et al., 2011). The Nyquist plots obtained for the Au–Gr, CD–Gr and Gr are given in Figure 3.11B, which show that the interfacial charge resistance is minimal and the materials have good conductivity. Moreover, as the Au–Gr disperses well in water and DMF (Figure 3.5 inset) the homogeneity induced by the CD molecules may play a role in the improved sensing property. The anchoring of Au NPs through CD molecules might decrease the aggregation and increase the proximity of Au NPs to Gr and thus increases the electron transfer rates. Thus the enhanced current response

exhibited by the Au–Gr/GCE was assigned to the synergistic effects of Gr, CD and Au NPs (high conductivity, surface area, adsorption and catalytic activity). Zhang et al. reported (L. Zhang et al., 2011) that Au NPs may act as catalysts for AA oxidation. EC sensors based on Gr had been studied and proven as potential candidates for sensing many analytes due to their better conductivity and higher SA. Compared to the previous reports (Kong et al., 2012; Tian et al., 2012), the performance of the Au–Gr is far better in terms of sensing property and detection limit (10 and 40 nM respectively) towards glucose and AA. Figure 3.12 shows the schematic of the EC oxidation of glucose and AA on Au-Gr/GCE.

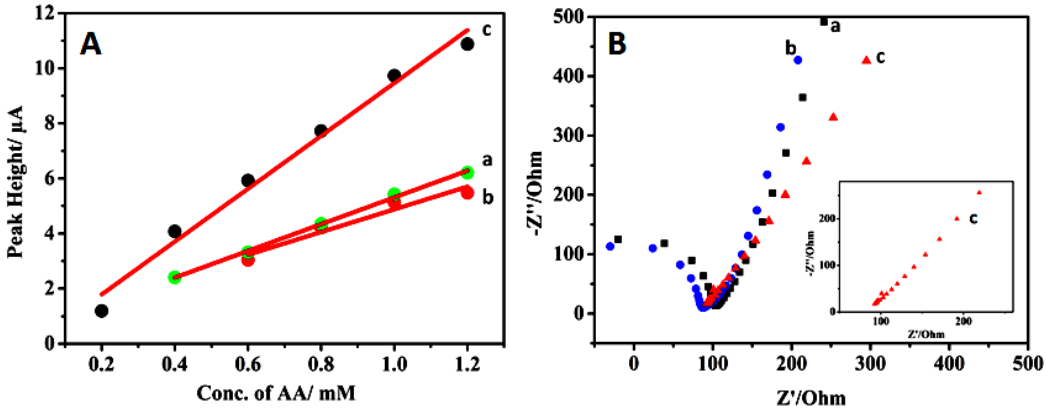

Figure 3.11. (A): Linear relation between peak height and concentration of AA and (B): EIS plots conducted in 0.1 M NaOH solution of (a): Gr/GCE; (b): CD-Gr/GCE and (c): Au-Gr/GCE.

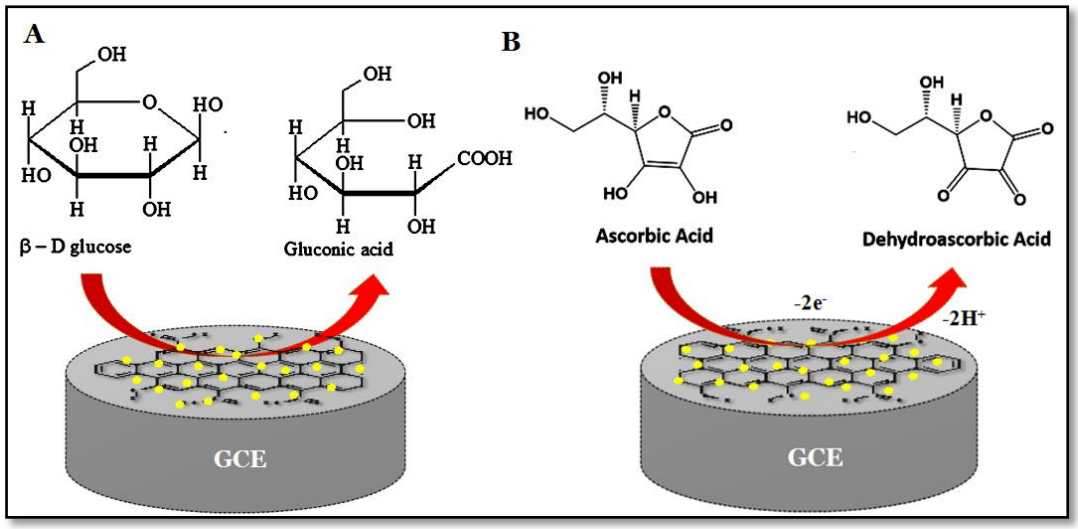

Figure 3.12. Schematic of the EC oxidation of (A): glucose and (B): AA on Au-Gr/GCE.

Table 3.1. The comparison of LDR and LOD of glucose by Au-Gr/GCE with other reported literature values of enzymatic and non-enzymatic sensors.

Type of electrode	LDR (mM)	LOD (μM)	Reference
Chitosan (CHI)–Au NPs / GCE	0.4-10.7	370	(D. Feng et al., 2009)
AuNPs/GCE	0.1 - 25	50	(Chang et al., 2014)
Au NW array electrode	0.5-14	30	(Cherevko & Chung, 2009)
GO–THi–Au/GCE	0.2 -13.4	0.05	(Kong et al., 2012)
Gr/AuNPs/GOD/ CHI (enzymatic)	2 - 10	180	(Shan et al., 2010)
Gr/nano-Au/GOD/GCE (enzymatic)	0.2-2 and 2-20	17	(X. Wang & Zhang, 2013)

3.3.4. Selectivity and interference studies of Au-Gr/GCE

The selectivity and interference studies of Au-Gr/GCE towards glucose detection was carried out in 0.1 M NaOH solution using the chronoamperometric technique at 0.1 V. The results are given in figure 3.13A. As it is clear from the figure, Au-Gr/GCE exhibits negligible current response towards AA, DA and UA in 0.1 M NaOH even at very high concentrations (double than that of glucose), whereas it shows great elevation in the current response for the addition of even small concentrations of glucose. This shows the greater selectivity of Au-Gr/GCE towards glucose and the lack of interference in sensing in the presence of other biomolecules of similar structure. Similarly, the studies were extended to see whether the sensing of AA by Au-Gr is selective and whether it is interfered by the presence of glucose, DA and UA. The studies were carried out in 0.1 M PBS at 0.2 V and the results are depicted in Figure 3.13B. The Au-Gr/GCE showed excellent selectivity towards AA in 0.1 M PBS as the addition of other analytes resulted almost in nil response in current, also it didn‘t varry the current response towards AA even in presence of these many analytes showing the lack of interference of other biomolecules in the sensing.

Table 3.2. The comparison of LDR and LOD of AA by Au-Gr/GCE with other reported literature values of enzymatic and non-enzymatic sensors.

Type of electrode	LDR (mM)	LOD (μM)	Reference
GC/GO1	0.1-10	-	(Stergiou et al., 2010)
Au NPs-L-cysteine	0.008–5.5	3	(G. Hu et al., 2008)
CHI-Gr/GCE	0.050–1.2	50	(Han et al., 2010)
Au NPs-CD-Gr/GCE	0.030–2	10	(Tian et al., 2012)
Gr–poly(3,4-ethylenedioxy-thiophene)/ ascorbate oxidase	0.005–0.48	2.0	(L. Lu et al., 2013)
Au-Gr/GCE	0.00004 -10	0.04	Our result (Aswathi et al., 2015)

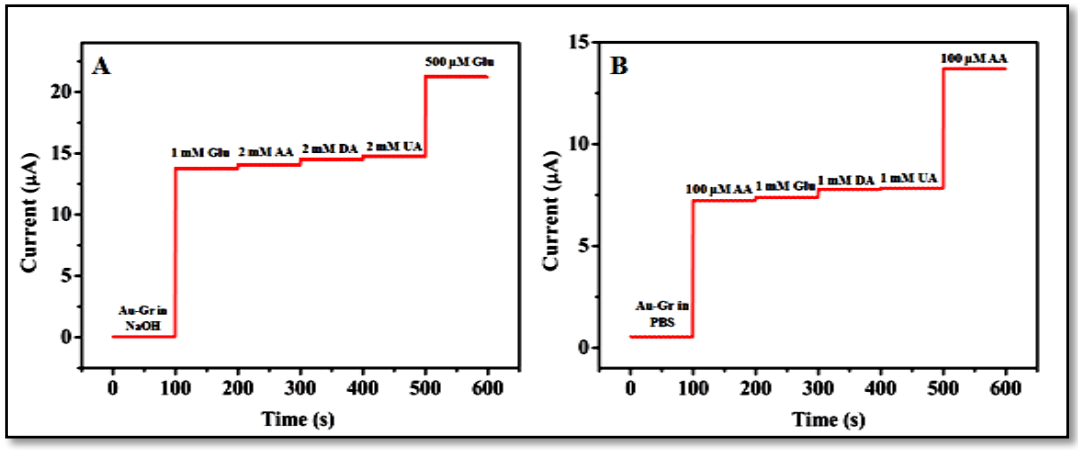

Figure 3.13. The selectivity and interference studies of Au-Gr/GCE in (A): 0.1 M NaOH at 0.1 V and (B): 0.1 M PBS at 0.2 V, for glucose and AA, respectively

3.3.5. Reproducibility, reusability and stability of Au-Gr/GCE

Measurements on five independently prepared electrodes were used to estimate the reproducibility of Au-Gr/GCE for the sensing of glucose and AA. The % RSD in the oxidation peak currents in CV for 1 mM glucose was found to

be 1.02%, and that for 1 mM AA was 1.22% indicating excellent reproducibility of the prepared electrode. Further, the storage stability of Au-Gr/GCE was evaluated separately for the sensing of glucose and AA. The Au-Gr/GCE retained 96.5 and 95.3 % of the initial current response of glucose and AA, respectively, after one month of storage. The results indicate the reproducibility and the remarkable stability of the sensor (Figure 3.14). The reproducibility and the temporal stability performances of Au-Gr/GCE can be assigned to the the better adsorption of Au-Gr to GCE and the synergistic effect of the catalytic activity, higher SA, adsorption and conductivity of Au NPs and Gr and the better adsorption and homogeneity induced by CD molecules.

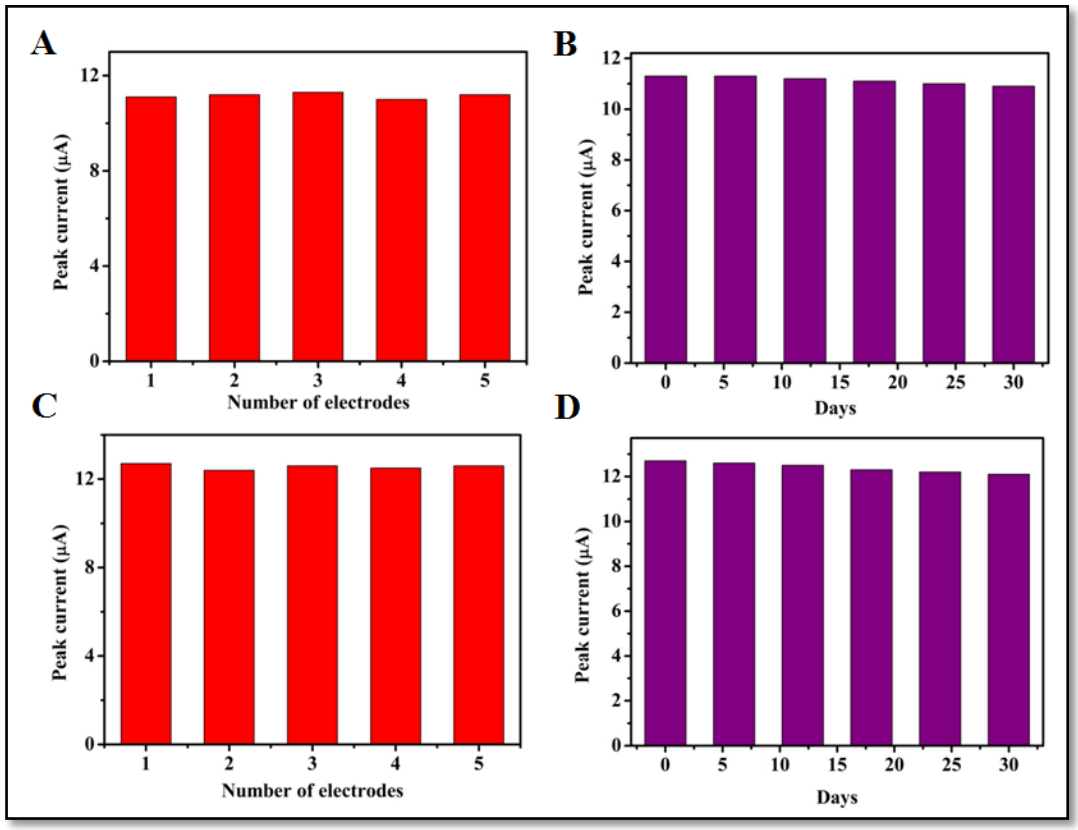

Figure 3.14. The reproducibility: (A) and (C); and temporal stability: (B) and (D) results of Au-Gr/GCE towards glucose and AA sensing respectively.

3.3.6. Real sample analysis

The Au-Gr/GCE was further applied for the detection of glucose and AA in human blood samples. The studies were carried out via standard addition method, where known amounts of glucose and AA were added to the diluted (1000 times) blood sample, to see whether the complex environment of blood samples interfere with the senssing peroperty of the electrode, and the recovery amounts were measured. The measurements are summarized in Table 3.3 and 3.4 respectively. The recovery calculated for the glucose detection was found to be in the range of 100.9–102.6% and that for AA detection in the range 99–102.2%. The near to 100 % recovery values indicate the successful applicability of the proposed electrode for the determination of glucose and AA in real biological samples.

Table 3.3. Determination and recovery test of glucose in human blood samples

Blood sample	Glucose Spiked (µM)	Glucose found (µM)	Recovery (%)
1	200	201.89	100.94
2	100	101.18	101.18
3	50	51.3	102.6

Table 3.4. Determination and recovery test of AA in human blood samples

Blood sample	AA Spiked (µM)	AA found (µM)	Recovery (%)
1	200	202.57	101.28
2	100	102.17	102.17
3	50	49.51	99.02

3.4. Conclusions

A successful green method for the preparation of Au–Gr from CD–Gr was reported. The CD–Gr in water yielded Gr nanosheets of ~2 nm thickness and the CD molecules act as stabilizing and reducing agent for the Au NPs. The method is environmental friendly. The Au–Gr exhibits excellent non-enzymatic EC sensing properties with the best detection limits towards glucose and AA molecule (10 and 40 nM, respectively), compared to the previous literature values. The better sensing of the Au–Gr towards AA compared to that of the previously reported Au–CD–Gr is assigned to the better conductivity of Gr, facilitated by the usage of rGO, instead of GO, made by hydrazine hydrate reduction. Moreover, the Au-Gr electrode exhibits excellent selectivity for both glucose and AA sensing and remarkable temporal stability. In addition, the developed sensor was able to extent the detection of glucose and AA in real biological samples. The better EC sensing properties of Au–Gr is attributed to the synergistic effect of better electron transfer and transport by the atomic thin Gr sheets, the catalytic properties of Au NPs along with the homogeneity induced by CD molecules. Further, the CD in Au-Gr can assist the adhesion of biomolecules, through ring stacking and H-bonding interactions. Thus, tethering of Au NPs to the Gr substrate through CD molecules enhances the stability and compatibility towards the analytes and makes it a potential candidate for sensing of biomolecules.

CHAPTER 4

PHYSIOLOGICAL LEVEL AND SELECTIVE ELECTROCHEMICAL SENSING OF DOPAMINE BY PULVERIZED GRAPHITE

This chapter discusses the preparation and characterization of mechanically pulverized graphite (pGr) from graphite and its utilization as an electrode material for the EC sensing of analytes such as DA and AA. The pGr was characterized by various techniques such as SEM, TEM, XRD, Raman spectroscopy etc. The pGr demonstrates selectivity towards DA in the presence of AA and is able to simultaneously detect DA, AA and UA. The enhanced and selective sensing of pGr towards DA is assigned to its intact aromatic basal plane structure which promotes the preferential adsorption of DA due to the similarities in their structures. Further, the reasons for the excellent sensing property of pGr were evaluated and discussed. The dispersibility of pGr in water and the formation of Gr nanosheets are explained by the hydrophilic edges. The results demonstrate the feasibility and the merits of pGr in the EC sensing applications and give insight to its structure.

4.1. Introduction

Gr, with its superior mechanical, electronic, EC/electro-catalytic properties and high SA fascinates the scientific communities as a potential candidate for many applications, and EC sensing application is no exception (Wu et al., 2013). However, in order to use Gr for EC applications effectively, it should have (i) processability (ii) better conductivity, i.e., lesser collateral damage to the honeycomb structure of the sheets and iii) methods to produce solution procesable Gr nanosheets in multi-gram scale. Chemical exfoliation method fails to produce

Gr with low collateral damage whereas mechanical (Scotch-tape) exfoliation though can yield Gr nanosheets with minimal damage, has a highly tedious procedure, thus is not a feasible method to produce Gr in large scale. Moreover, in both the cases the Gr obtained are not solution-processable.

Mechanical exfoliation and epitaxial growth even though can produce single or bilayer Gr sheets, the elaborate procedures make them unsuitable for mass production. Consequently, other alternatives for producing processable Gr should be exploited. Solid state mechanical ball-milling of graphite yields pulverized graphite (pGr), which is composed of graphite particles of controlled-sizes and a homogeneous structure (Ying Chen et al., 1999; JY Huang, 1999; Welham et al., 2003). The utilization of pGr had been limited to composite reinforcement for a long time, and recently has been extended to LIBs (C. Wang et al., 1998), double layer capacitors (Gomibuchi et al., 2006; H.-Q. Li et al., 2008), hydrogen storage (Awasthi et al., 2002; Imamura et al., 2003), Li-ion capacitors (Sivakkumar et al., 2011) etc. However, so far no studies have explored the possibility of utilization of pGr as EC sensing electrodes.

Here in this work, pGr was made by mechanical ball milling of graphite and was characterized for its structure and surprisingly found to be water dispersible. The pGr was utilized as a Gr source for the EC sensing of DA and AA and its sensing property has been compared with that of rGO, prepared by chemical exfoliation. Being a monoamine neurotransmitter, DA, is crucial for the function of brain, metabolic system of the human body (Han et al., 2010), cardiovascular, central nervous, renal, and hormonal systems (Heien et al., 2005) and the variation in the physiological concentration of DA (especially lowering) can lead to neurological disorders such as Schizophrenia, Huntington's disease, and Parkinson's disease (Wightman et al., 1988). Thus, the sensing of DA is important, however is rather difficult due to (i) its lower physiological concentration levels (~25-50 nM) and (ii) interferences from the structurally similar AA and uric acid (UA) which are present in fairly higher concentrations

(in mM), in biological tissues. Due to the structural similarities of DA, UA and AA, most of the conventional electrodes such as Au, Pt, and glassy carbon electrode (GCE) cannot differentiate between them (How et al., 2014; Y.-R. Kim et al., 2010). Therefore, various carbon materials, such as carbon nanotubes (CNT), boron-doped diamond, carbon nanofibers, rGO and graphite (Ying Wang et al., 2009) have been employed to elaborate the surface of the WE, however were not successful enough.

The EC sensing studies revealed the physiological level sensing property of pGr towards DA and AA and shows remarkable selectivity to DA and interestingly enough, the EC sensing results give insight in to the structure of pGr. Further, the pGr electrode (pGr/GCE) exhibited (i) selectivity towards DA in the presence of AA, (ii) simultaneous sensing of DA, AA and UA, and (iii) the lowest LOD for AA (in the absence of DA) and DA (in the absence and presence of AA) subjected to S/N=3 (Ramachandran et al., 2018), compared to that of the previously reported literature values. Comparison of the values with that of the control-rGO (SA 416 m^2/g), GO and other reported Gr based DA sensors ascertain the merit of pGr as an EC sensing electrode towards DA and AA. Further, the EC results give indication about the structure which agrees to the water dispersibility of pGr and the reason behind the excellent and selective sensing property of pGr towards DA.

4.2. Experimental

4.2.1. Pulverization, dispersibility and surface area studies

The mechanical pulverization was carried out by taking graphite (25 g) and zirconia balls (100 Nos.) in a container and ball milled for several hours. The SA and dispersibility of the pulverized samples were tested for every 150 hours interval. The dispersibility of pGr was studied in water, DMF, THF, Hexane, IPA and other solvents. The pGr (1mg) was taken in 1 ml of solvent and dispersed by probe ultrasonication for 30 minutes. The stability of the dispersion was noted by

observing for any settlement for one week. Degasification of the samples was done at 120 $^{\circ}$C overnight, prior to nitrogen (N_2) adsorption isotherm. The N_2 adsorption isotherms were carried out at 77 K using liquid N_2 as a coolant taken in the Dewar flask.

4.2.2. EC methods and preparation of electrodes

The pre-treatment and modification of GCE were done according to the procedure given in the experimental chapter. The samples (rGO or pGr) dispersed in DMF were drop cast (20 µL of a 0.5 mg ml^{-1} freshly ultrasonicated dispersions) over the pre-treated GCE carefully and then allowed to dry for 24 hours at RT. Though pGr is dispersible in water, DMF was chosen as the solvent because of the non-dispersibility of rGO (which is the control) in water. After each analysis, GCEs were cleaned by ultrasonicating in DMF and then distilled water. The EC measurements were carried out according to the procedure given in Chapter 2. The EC behaviors of DA, AA and AA (in 0.1 M PBS) on the electrodes were investigated using CV and DPV at RT. For DPV studies, an optimized scan rate of 50 mV/s and pulse amplitude of 25 mV were selected. EIS studies were carried out between 100 mHz and 100 kHz at the open circuit voltage.

4.3. Results and Discussion

4.3.1. Characterization of pGr

The digital images of graphite and pGr in powder form are given in Figure 4.1A&B, respectively. Unlike graphite, pGr had no metallic lustre, and was a black powder. The pGr samples of pulverization time ≥300 h were dispersible in water and it is evident from Figure 4.1C that the dispersibility improved with the pulverization time. Further, the pGr was found to be dispersible in organic solvents such as THF, DMF and NMP and the dispersibility was better in NMP and DMF (Figure 4.1D). The specific BET SA values of pGr at different intervals (Table 4.1) show that the SA of pGr increased with pulverization time and

reached an optimum value of ~500 m^2/g at ~1000 hours of ball milling. The SA of the control-rGO was 416 m^2/g. Other than the affinity/structure, the dispersibility and SA are two of the important factors which will influence the sensing performance of an electrode material. Since the pGr at 1000 h had comparatively higher SA, the sample was chosen for the EC sensing studies. Before that its comparatively superior sensing property was confirmed by testing the samples at the near lower and higher pulverization times; i.e, pGr samples at 450, 750, and 1200 h, to that of at 1000 h. The result (Figure 4.1E) clearly shows that the sample with the highest SA (i.e. 1000 h) exhibits the highest current response and thus the selection of 1000 h was justified.

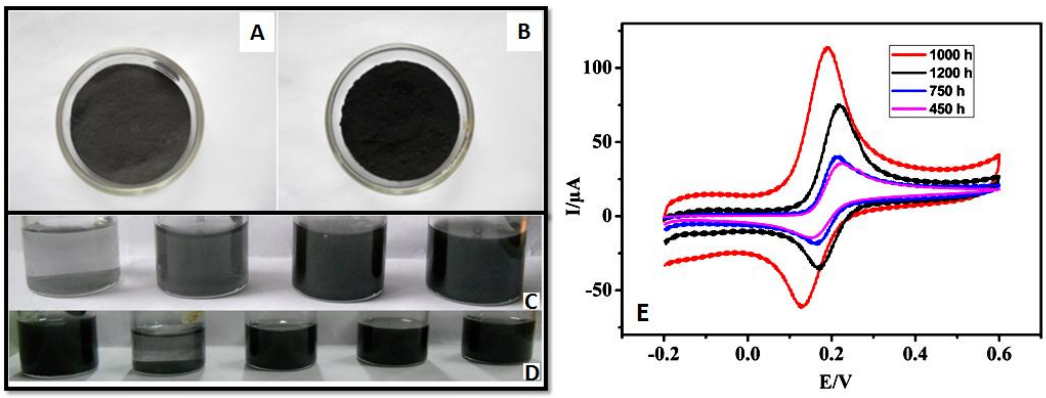

Figure 4.1. The digital images of (A): graphite; (B): pGr; (C): L to R: Water dispersions of graphite and pGr at different intervals of pulverization (~300 h, 600 h and 1000 h) demonstrates the improvement in dispersibility with time; (D): L to R: Dispersions of pGr (1000 h) in water, hexane, THF, DMF and NMP respectively. The figure clearly shows the better stability of pGr dispersions in DMF and NMP.(E) The CV study of pulverization time Vs sensing performance towards DA; CV response of different pGr/GCEs for 1 mM DA in 0.1 M PBS at a scan rate of 50 mVs^{-1}, revealing maximum current response for the pGr at 1000 h.

Table 4.1. BET SA and pore size values of PGr samples of different pulverization time.

Ball milling time (~hrs)	BET SA (m^2/g)	Pore size (Å)
0 (Graphite)	7.69	200.41
300	19.04	137.91
450	23.09	129.35
600	167.59	86.95
750	284.88	82.46
900	397.85	82.34
1000	510.87	82.77
1200	434.34	72.73

The FTIR spectra of the pGr, rGO (control) and graphite are given in Figure 4.2A. The peak at 3500 cm^{-1} in graphite is assigned to the moisture content, whereas in pGr and rGO, it is assigned to the –OH group of the edge functionalities (i.e. C-OH and –COOH) because of the presence of other corresponding peaks. The peak at ~1600 cm^{-1} is assigned to the aromatic C=C vibration. The spectrum of rGO has a peak at 1065 cm^{-1} and is assigned to the -C-O stretching of the epoxide linkages in the basal plane, whereas the peak is absent in pGr, indicating that the extent of oxidation of the basal plane is less or the nature of oxidation of pGr is different from that of the rGO. The HRTEM images of the pGr dispersion reveal thin and transparent Gr sheets (Figure 4.3A and C). The transparent Gr sheet in Figure 4.3C has single layer regions as suggested by the single crystalline pattern in the SAED (Figure 4.3D). The images show that the Gr sheets have certain roughness feature to it, which is assigned to the random partial removal of layers at the regions by mechanical exfoliation. Thus, the TEM images suggest that the pGr dispersion contains few layered Gr sheets with exposed mono layer regions and active edges which can improve its catalytic

activity. The AFM images (Figure 4.2B and C) show that the thicknesses of the sheets range from 2-10 nm. In addition, the variation of thickness from 2-10 nm in the same sheet confirms the roughness feature and agrees with the HRTEM images.

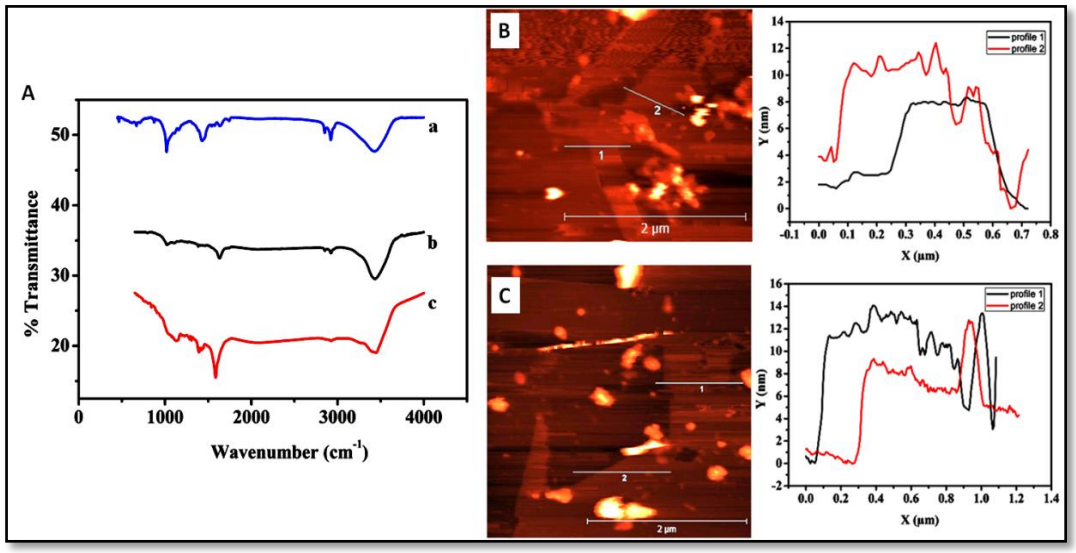

Figure 4.2. (A): The FTIR spectra of (a) rGO, (b) graphite and (c) PGr; (B) and (C): The AFM images of pGr dispersion and the corresponding height profiles of Gr sheets.

The Raman spectroscopy is considered to be an effective tool for the characterization of Gr nanosheets. In the Raman spectra (Figure 4.4), a major G band at ~1580 cm^{-1}, and a negligibly small D band at 1350 cm^{-1} was observed for graphite due to less defects. The spectrum of pGr (dispersion) was similar to that of rGO with D and G bands at 1350 and 1580 cm^{-1} respectively, and an I_D/I_G ratio of 1.29. Thus the Raman spectrum of pGr confirms the exfoliated nature of Gr sheets and the presence of defects in the Gr sheets due to the oxidation during pulverization. Besides the D and G bands, a 2D band was present at around 2700 cm^{-1}. The position and shape of the 2D band identify the presence and the number of layers of the Gr nanosheets, respectively (Chakrabarti et al., 2011). Few layered Gr has a characteristic Raman signature in the 2D-band. The 2D band in pGr was broader compared to that of the graphite, and can be split into more bands indicating the presence of few layered Gr nanosheets. Further, the shape of the 2D-band, more specifically the absence of a typical graphite shoulder at 2680

cm^{-1}, is characteristic of few layered Gr (Figure 4.4). Thus, TEM, AFM and the Raman results confirm that the pGr dispersion has few layered Gr sheets with certain degree of roughness and exposed mono-layer regions.

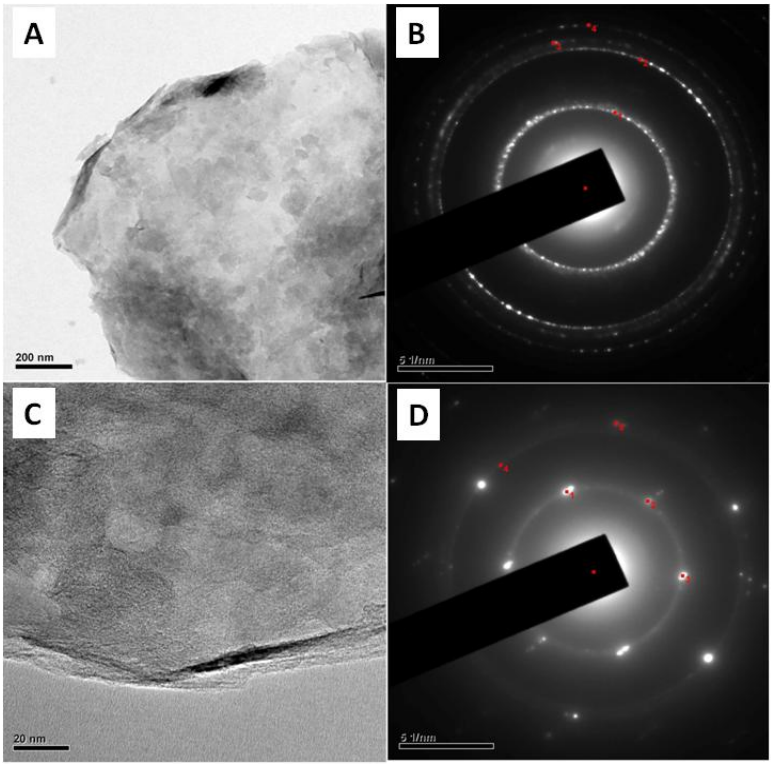

Figure 4.3. Characterization results of the pGr dispersion revealing the transparency and roughness: (A), (C): HRTEM images and (B), (D): the corresponding SAED patterns.

4.3.2. EC sensing studies

The non-enzymatic EC sensing property of pGr/GCE was investigated using DA, AA, UA and ACh as analytes (the chemical structures are given in Figure 4.5). The EC sensing of DA was done in the absence and the presence of physiological concentration ranges of AA. The sensing using other analytes was utilized to study the versatility and understand the relationship between the sensing property and the structure of pGr, if any. The sensing performance of pGr was compared with that of the control-rGO (SA-416 m^2/g) and GO.

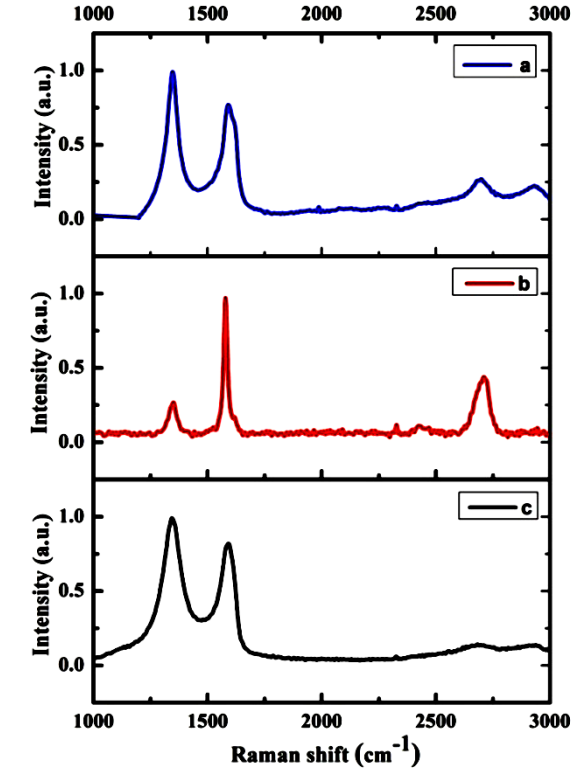

Figure 4.4. Raman spectrum of pGr revealing the few layer morphology and defects: Raman spectra of (a) pGr (b) graphite and (c) rGO

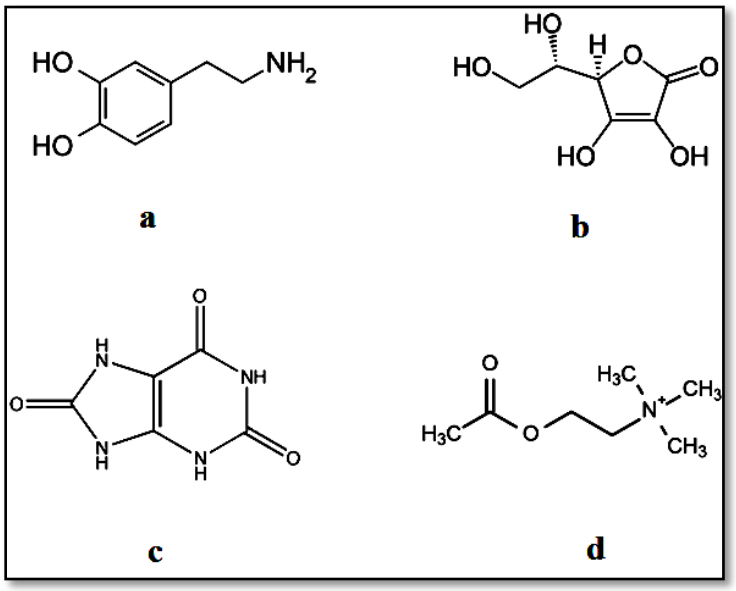

Figure 4.5. Chemical structure of the analytes used in the EC sensing studies of pGr; (a): DA (b): AA (c): UA (d): Ach

4.3.2.1. EC sensing of DA & AA individually

The CV curves obtained for the GCE, rGO/GCE and pGr/GCE (result for graphite/GCE electrode was similar to that of the bare GCE and hence not given) in the presence of 1 mM of DA are shown in Figure 4.7A. Compared to that of the bare GCE, rGO/GCE had a ~three-fold increase, while the pGr/GCE exhibited a much higher (~6.4-fold) increase in the current response. The peak potential for the oxidation of DA to dopamine quinone (DAQ) (Figure 4.6) at the pGr/GCE was lower (0.19 V) whereas the values of GCE and rGO/GCE were 0.37 and 0.20 V, respectively. The redox peak potential separation (ΔEp) values were 271, 93 and 66 mV for the GCE, rGO/GCE and pGr/GCE, respectively. Lower the ΔE_p between the redox peaks better is the electrode for the reaction. The higher current response and the lower ΔE_p & oxidation peak potential by pGr/GCE imply that the pGr has a better electrocatalytic oxidation behavior towards DA (Naik et al., 2009). The result clearly indicates that the pGr/GCE is a better electrode than the control-rGO/GCE and GCE.

Further, the sensing studies of pGr/GCE for the increasing concentrations of DA were conducted and the results are given in Figure 4.7B. The anodic peak current increased with the increase in the DA concentration and the obtained calibration graph (Figure 4.7C) covered a wide range of concentrations, from 10 nM to 6 mM, with three separate LDR: 10 nM–50 µM ($y = 478.22 x + 4.591$; $R^2 = 0.941$), 0.1–1 mM ($y = 58.612x + 37.613$; $R^2 = 0.962$) and 2–6 mM ($y = 18.525x + 92.94$; $R^2 = 0.967$). The LOD was found using DPV and was 1 nM (S/N=3) (Figure 4.8A), which is the lowest value, reported so far, for DA (Ramachandran et al., 2018).

The versatility and electrocatalytic activity of pGr as a sensing electrode was tested using AA as analyte and the CV responses obtained are provided in Figure 4.7D. The current increased linearly with the increasing concentrations of AA from 10 nM-10 mM (Figure 4.7F). The linear segment ($y = 3.46 + 13.95 x$)

corresponds to LDR from 10 nM-10 mM, with an R^2 = 0.994. The LOD of AA was obtained to be 1 nM (S/N=3) (Figure 4.8B). Our previous study (Aswathi et al., 2015) of EC sensing of AA by a modified rGO (Au-rGO-CD), yielded a LOD of ~40 nM, the lowest LOD then, compared to the literature reports, whereas the controls; CD modified rGO (rGO-CD) and rGO exhibited LOD values of 0.6 and 0.2 mM (Aswathi et al., 2015), respectively. Thus, the LOD of 1 nM for AA by pGr/GCE is the lowest and suggests that the pGr has remarkable electrocatalytic activity.

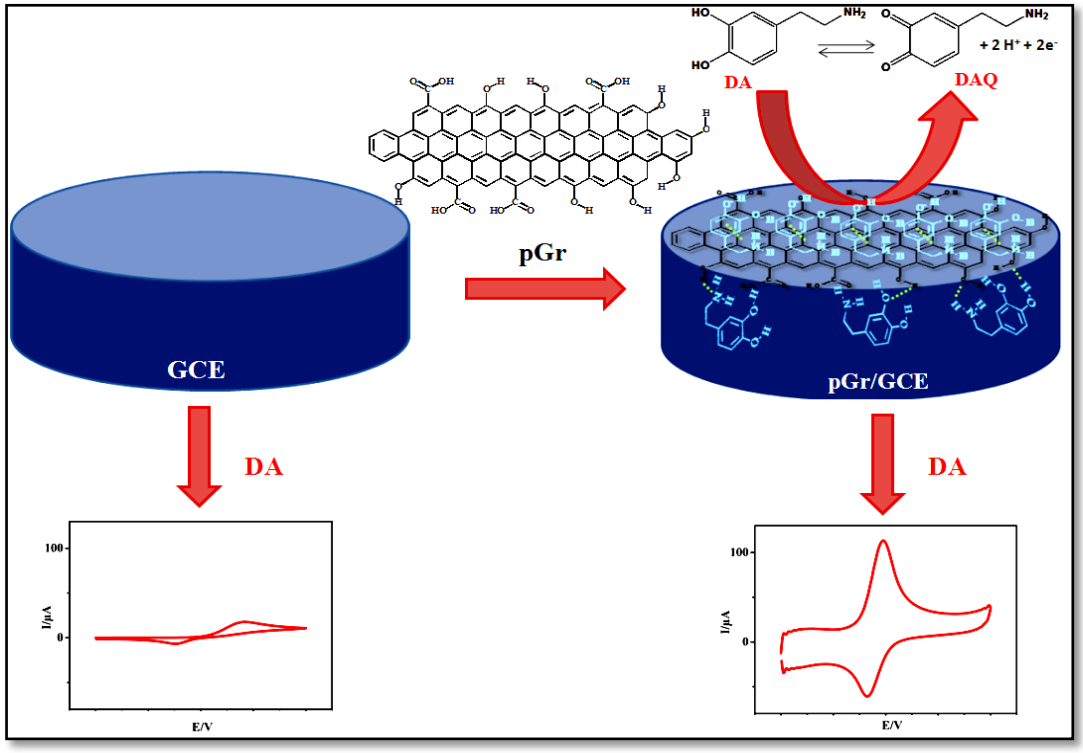

Figure 4.6. Schematic of the the enhanced current response by pGr as observed in CV for the electrocatalytic oxidation of DA to DAQ on pGr/GCE

4.3.2.2. Sensing of DA in the presence of AA at pGr/GCE

The selectivity of pGr/GCE was tested by the simultaneous detection of DA and AA. Generally, the detection of DA in the presence of AA, UA etc. has been challenged by the overlapping voltammetric responses at most of the electrodes, owing to their structural similarities.

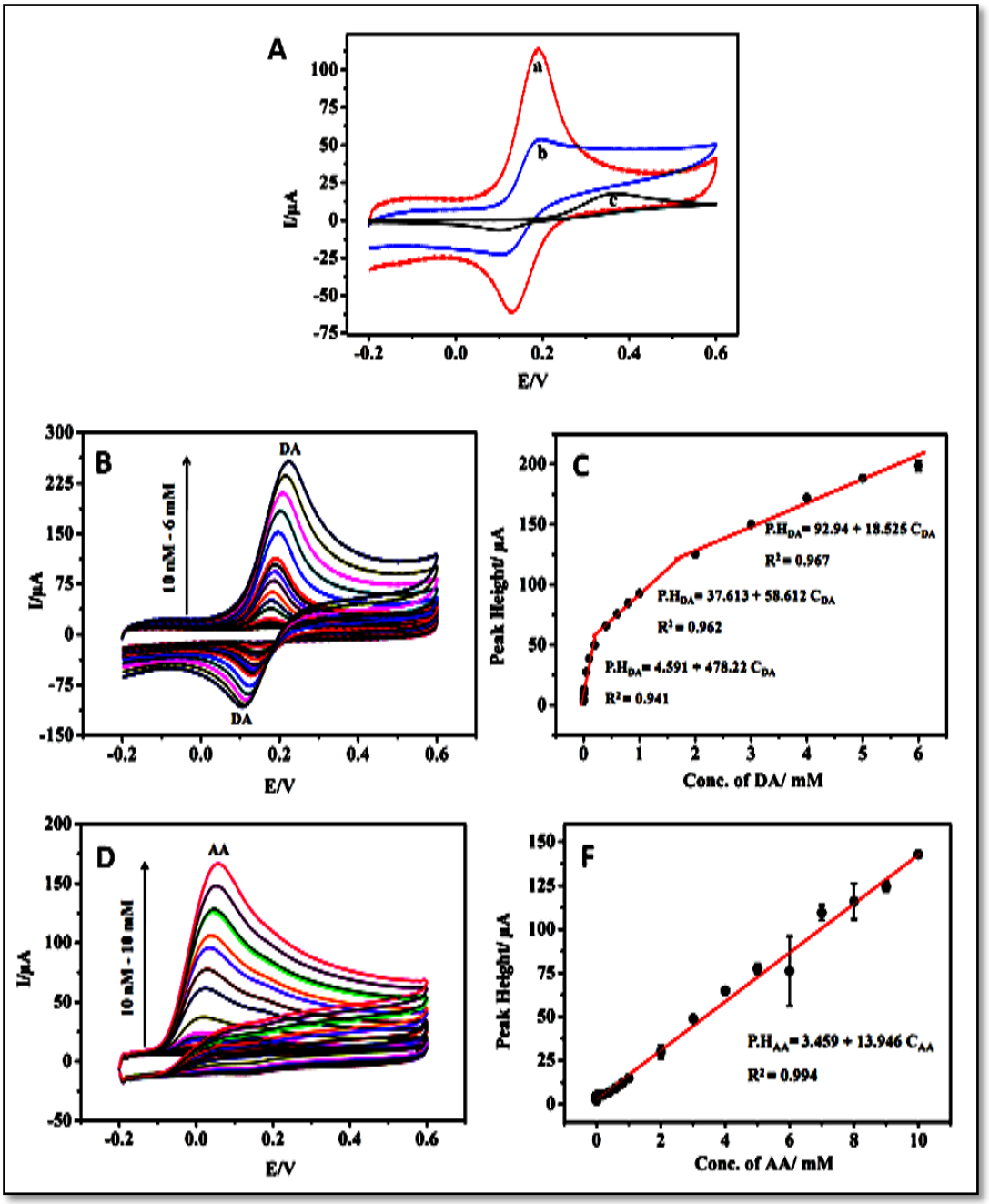

Figure 4.7. The CV results for the EC sensing of DA & AA individually: (A): CV scans obtained for 1 mM DA in 0.1 M PBS at (a) pGr/GCE; (b) rGO/GCE; and (c) GCE (c) at a scan rate of 50 mVs^{-1}; (B) and (D): the CV scans of DA and AA individually at the pGr/GCE for the concentration ranges of 0 to 6 mM and 0 to 10 mM, respectively; (C) and (F): The corresponding linear relation obtained between the peak height and the concentrations of AA and DA, respectively. (Ag(s)/ AgCl(s)/ Cl^{-1}(aq., saturated) was as the reference electrode)

The EC sensing of DA by pGr/GCE was conducted in 0.1 M PBS containing 1 mM AA (higher than the biological concentration of AA) by CV (Figure 4.8C) and DPV. The current response increased with the increasing concentrations of DA (Figure 4.9A) and three LDRs were observed for the concentration range of 5 nM to 200 µM (Figure 4.9B): from 5 nM- 1 µM (Figure 4.9C) ($y = 0.4598 + 3.6936\ x$; $R^2 = 0.997$); from 2 -40 µM ($y = 7.00 + 781.63\ x$; $R^2 = 0.960$) and from 60 -200 µM ($y = 35.72 + 154.15\ x$, $R^2 = 0.972$). The LOD of DA in the presence of AA was calculated as 1 nM (S/N=3), which was same as that of the LOD of DA in the absence of AA, indication of the absence of interference of AA in the DA sensing by pGr/GCE.

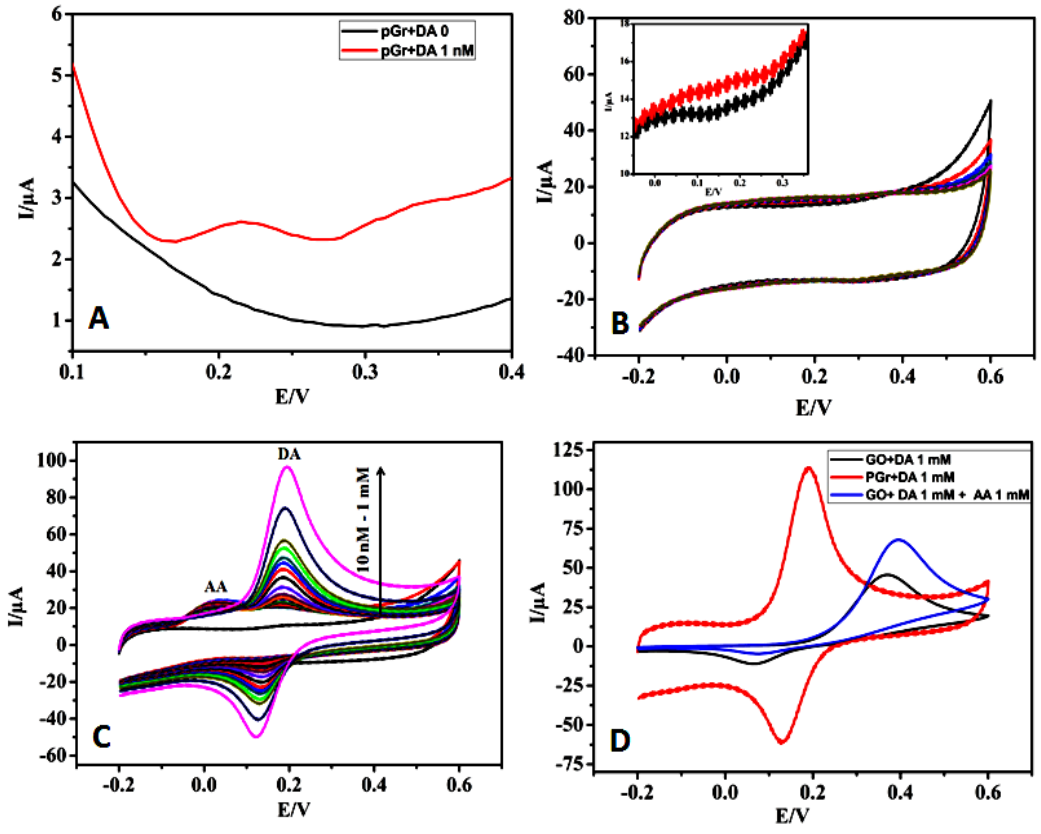

Figure 4.8. (A): The DPV responses of PGr/GCE towards nil concentration of DA (black) and 1 nM DA (red) which confirms the LOD as 1 nM; (B): the CV curves revealing the response of PGr/GCE towards the increasing concentration of AA from 1 to 5 nM (inset figure shows the curves for nil concentration of AA (black) and 1 nM AA (red) which confirms the LOD as 1 nM); (C): The CV curves revealing the response of PGr/GCE towards the increasing concentration of DA from 10 nM -1 mM in the presence of 1 mM AA; (D): Comparison of the CV responses of PGr/GCE with GO/GCE for 1 mM of DA.

Similar sensing experiments were conducted for AA in the presence of 100 μM DA and the CV responses towards the increasing concentrations of AA are given in Figure 4.9D. The response of AA was observed above 10 nM, and the peaks of DA and AA started merging at concentrations above 1 mM. Figure 4.9E reveals the corresponding calibration plot of the current versus concentration of AA. It was interesting to note that the current response of AA was decreased compared to that in the absence of DA, which suggests the interference of DA. Conversely, the peak potential value and the current response of DA were unaffected by the presence of AA, suggesting that the pGr has selectivity towards DA compared to that of AA. This means, there is possibly better and preferential interaction between the pGr and DA. Considering the structures (Figure 4.5) of DA and AA to that of pGr, both have double bonds, however, DA has an aromatic ring while AA does not. Therefore, the better interaction between DA and pGr may possibly due to the л–л or ring stacking interactions between DA and the aromatic domains of pGr. This result suggests that the structure of pGr may have larger and less oxidized aromatic domains to adsorb DA effectively. When, the LOD of AA in the presence of DA was increased to 10 nM from that of in the absence of DA (1 nM), the LOD of DA (1 nM) was unperturbed by the presence of AA. This is further evidence of the the selectivity of pGr towards DA. To find out whether the enhanced sensing of pGr towards DA and AA is due to their aromatic or double bond л-л interactions, the sensing study was carried out using an aliphatic neurotransmitter, ACh (Figure 4.5D). The response of pGr/GCE towards ACh was almost nil (Figure 4.9F) and suggests that the reason for the enhanced sensing of DA or AA by pGr is due to the similarities in terms, of double bonds, in their structures, which promotes closer interactions and thus better current response.

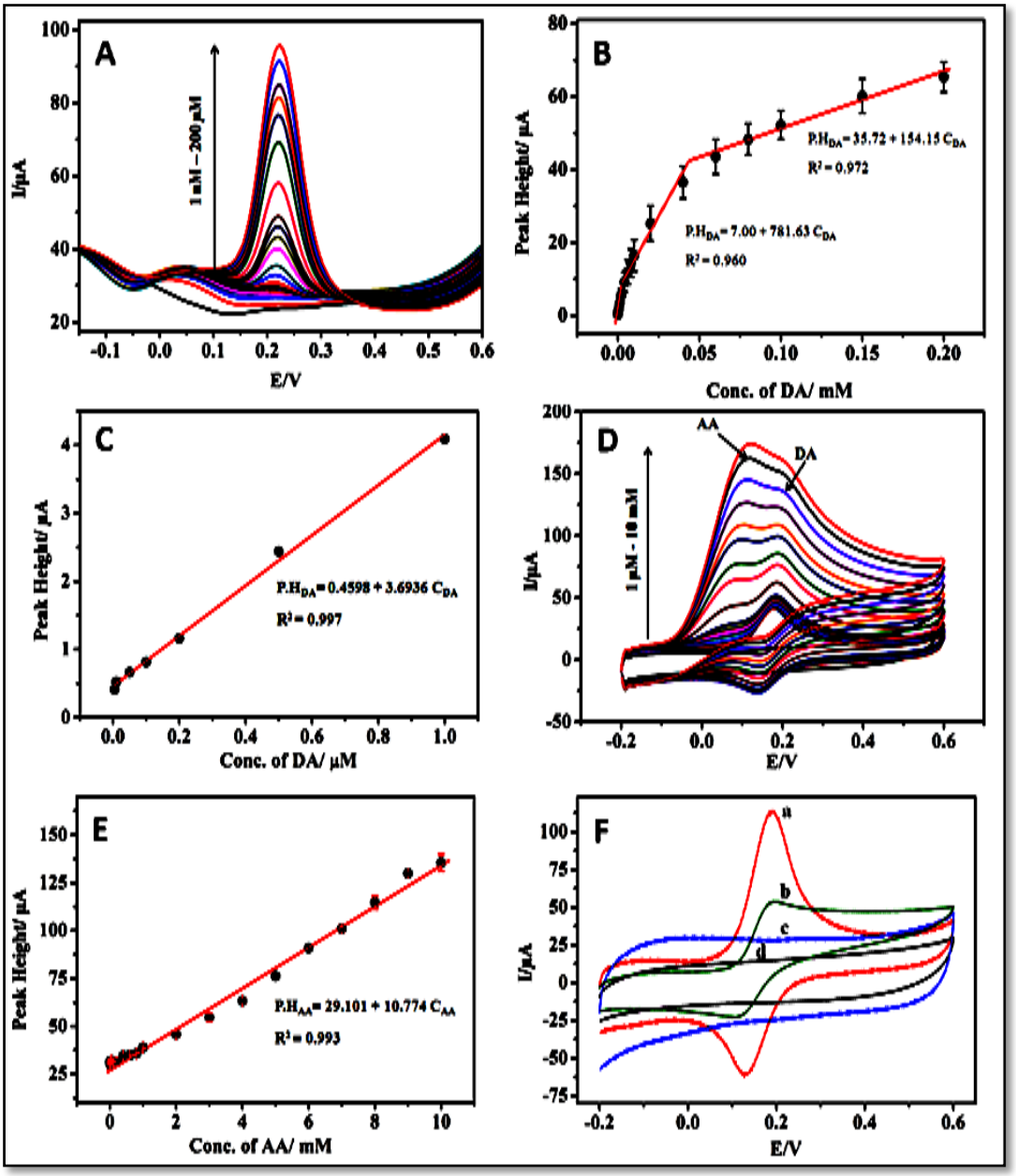

Figure 4.9. CV and DPV results for the EC sensing of DA in the presence of AA and vice versa (A): DPV scans of DA at the pGr/GCE for the concentration range of 1nM to 200 µM in the presence of 1mM AA and (B): The corresponding linear relation obtained between the peak height and the concentration between 5 nM to 0.2 mM; (C): expanded the lower range LDR from 5 nM-1 µM of B; (D): CV scans of AA at the pGr/GCE in the presence of 100 µM of DA and (E) Corresponding calibration curve showing the linear relation between the peak height and the concentration of AA from 10 nM to 10 mM; (F): CV for the oxidation of 1 mM DA on (a) pGr/ GCE and (b) rGO/ GCE; and that of 1 mM Ach on (c) rGO/ GCE and (d) pGr/ GCE. (Ag(s)/ AgCl(s)/ Cl^{-1}(aq., saturated) was as the reference electrode)

4.3.2.3. Comparison with rGO and GO

The sensing property of pGr was compared with the currently popular Gr based electrode materials such as rGO and GO and the results are given in Figure 4.7A and Figure 4.8D, respectively. The current response of pGr was higher than that of the rGO and GO (~2 and 2.5-fold respectively), suggesting a higher electrocatalytic activity of pGr/GCE towards DA oxidation. The peak of DA on rGO was broader and that on GO was at a higher potential (~0.35 V), than that of the pGr, thus demonstrating that the pGr is a better DA sensor. The enhanced sensing of DA by pGr is assigned to the greater interactions of DA with the pGr which promotes the faster charge transfer between them and the better electrocatalytic activity due to the active sites on the Gr surface as shown by TEM images. Since DA has H-bonding functional groups and an aromatic ring, the interactions between the electrodes and DA can be explained through the л-л and H-bonding interactions and in addition through the stacking of the aromatic rings.

4.3.3. Structure of pGr and the improved sensing towards DA and AA

To confirm the possible interactions between the pGr and DA, there should be a better knowledge about the structure of pGr. As one of the interactions between the analyte and the pGr is explained to be through their aromatic rings, the thermograms of pGr and rGO in N_2 atmosphere (Figure 4.10A) were compared to validate the comparatively better aromatic structure of pGr. Though the residual amount (~73%) of pGr and rGO were comparable, the profile of the thermogram of the pGr was entirely different from that of the rGO and was more similar to that of the graphite. In the case of rGO, degradation started just above 100°C and continued till 800°C, however, for pGr, besides the initial weight loss due to moisture at ~100°C, further weight loss till 400°C was negligible and the degradation started above 400°C only. The plateau region in the thermogram of pGr (similar to that of graphite) demonstrates the stability of the

aromatic domains of pGr and is an indication of the more or less intact honeycomb lattice structure with lesser oxidation sites. The similar residual amounts of pGr and rGO, suggest that the pGr is equally oxidized, which agrees with the water dispersibility of PGr, and is interesting. Therefore, it can be assumed that the oxidation sites of pGr are mainly located at the edges of the graphitic domain, formed by the size reduction of Gr sheets. The groups at the edges must be –COOH or –OH which are hydrophilic in nature, unlike the hydrophobic groups such as epoxy, which forms in the case of oxidation of the domains. This structure of pGr with larger and less oxidized aromatic domains and richly functionalized H-bonding edge groups agrees with the properties observed such as: dispersibility of pGr in solvents like water, THF, DMF and NMP (Figure 4.1D) and the better interactions with DA. Based on this structure, the improved and selective adsorption of DA on pGr to that of rGO is illustrated in Figure 4.10B. The proposed structure of pGr can explain the enhanced and selective sensing of DA as this structure can adsorb DA more effectively through the π-π bonding, ring stacking and/or H-bonding interactions compared to that of AA, which has no aromatic ring. While the synergy of these interactions in pGr favours the closer proximity of DA; rGO with relatively more number of oxidation sites in the aromatic domain will comparatively disrupt the adsorption of DA to the basal plane. Closer the analytes to the substrate, greater will be the possibility of electron transfer. This stronger adsorption of DA by pGr was further proved by DSC (Figure 4.11), which showed higher adsorption energy for the adsorption of DA on pGr compared to that of the rGO.

The study was further extended to the simultaneous detection of DA, AA, and UA, as UA too is a common interference in the sensing of DA on conventional electrodes. The responses of the electrodes for a mixture of AA (1 mM), DA (0.05 mM) and UA (0.1 mM) in 0.1 M PBS solution are shown in Figure 4.10C. The concentrations are equal or higher than the biological concentrations. The bare GCE produced only one peak which was weak and broad, demonstrating its poor selectivity and sensitivity. The

rGO/GCE, though exhibited three peaks; the responses for AA and DA were weak, with the signal of AA being more or less absent, the peaks of DA and UA were comparatively broader and the interference between these analytes, especially DA and UA, cannot be ruled out.

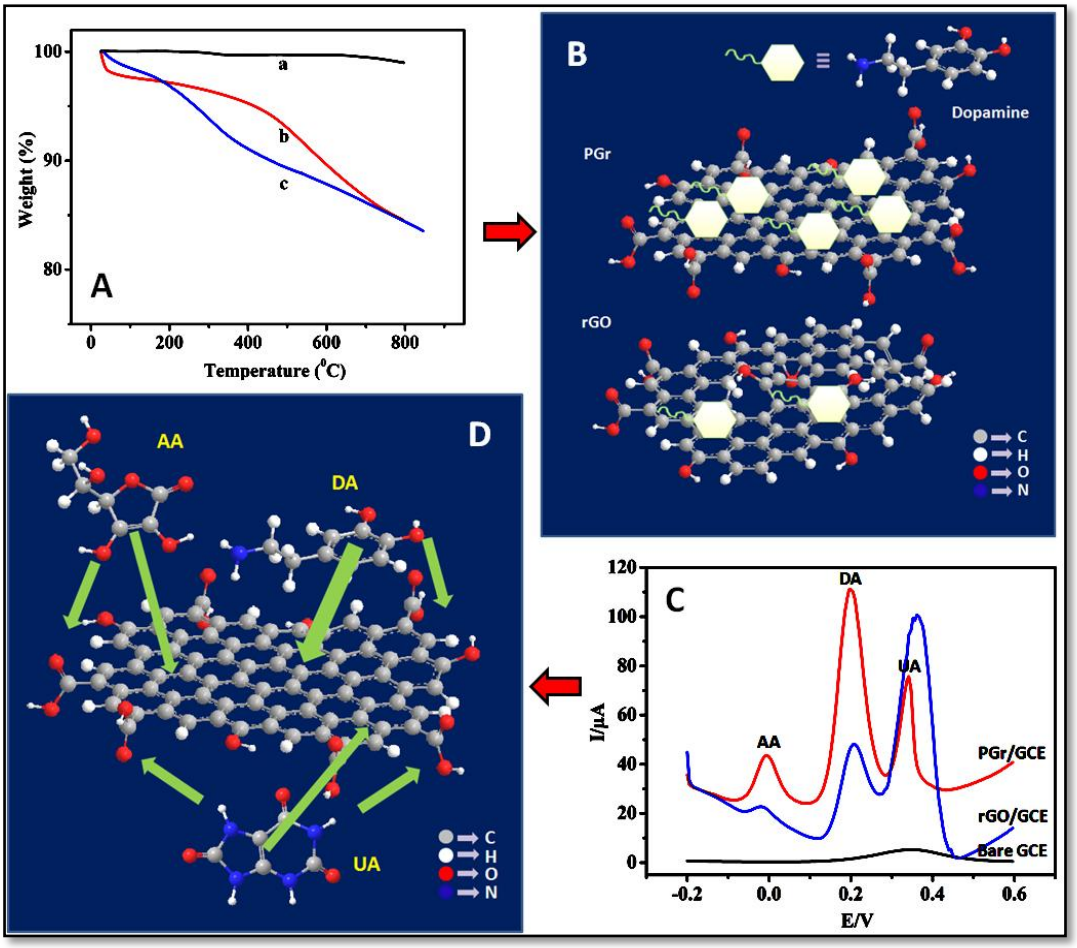

Figure 4.10. (A): Thermograms of (a) graphite, (b) pGr and (c) rGO in N_2 atmosphere; (B): Illustration of the honey comb structure (with lower oxidation sites) of pGr promoting selective and better adsorption of DA compared to that of the rGO; (C): DPV responses at the pGr/ GCE, rGO/ GCE and GCE for a mixture of 1 mM AA, 0.05 mM DA and 0.1 mM UA in 0.1 M PBS buffer solution; and (D): schematics of the structural aspects of pGr enabling the simultaneous detection of DA, AA and UA.

For GO/GCE, sensing was first tried with DA and AA (response peak of DA, appeared in the potential region of UA) and found that GO

could not differentiate between DA and AA itself (Figure 4.8D), which evidently supports the role of the better aromatic structure of pGr in DA sensing. Interestingly, with the pGr/GCE, three distinct and well-defined voltammetric peaks at -5, 200 and 342 mV were observed for AA, DA and UA, respectively. The ΔE_p values of AA-DA, DA-UA and AA-UA were found to be 205, 142 and 347 mV, respectively and were large enough for the simultaneous sensing. This suggests that the structure of pGr has different structural regions with different preferences of adsorption and the most being the structure which adsorbs DA. For the simultaneous detection, different regions of preferential adsorption for these molecules should exist in the substrate. Thus a scheme (Figure 4.10D) was proposed to illustrate the mechanism of simultaneous detection based on the proposed structure of pGr. The structure of pGr, with unique structural features such as highly aromatic (less oxidised) basal planes can favour the adsorption of DA through ring stacking, the л- л and H-bonding interactions, and the slightly oxidized sites of the basal planes interact with AA through the double bonds and the edges rich with functional groups facilitate the adsorption of UA via the H–bonds or vice versa. The selectivity to DA is explained by the larger area of the basal planes which prefers DA than AA or UA (Figure 4.10D). The higher electroactive surface sites and the numerous edge plane defects created by the exfoliation improve the catalytic activity of pGr for the oxidations of DA, AA, and UA. Consequently, the observed fast heterogeneous electron kinetics and electro catalytic behaviour of pGr can be attributed to its particular two dimensional honeycomb microstructure. The lower charge transfer resistance and the better electro-catalytic activity of pGr compared to that of the rGO was confirmed by the Nyquist plot (Figure 4.12) which shows comparatively smaller semicircle for pGr.

The capacity of electron transfer of pGr/GCE and rGO/GCE were compared using the electrochemical impedance spectroscopy in Figure 4.12. By fitting the data using an appropriate equivalent circuit, (Figure 4.12A) the values

of charge transfer resistance were determined and found that it is comparatively lesser for pGr (6.58 kΩ) when compared to rGO (7.9 KΩ), though both pGr and rGO produced the same equivalent circuit.

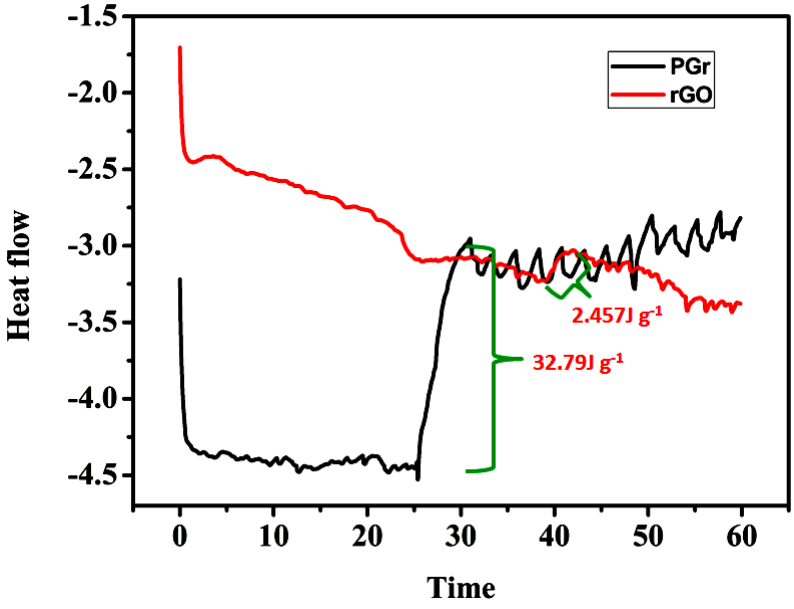

Figure 4.11. DSC thermogram showing the DA adsorption energies of PGr (black) and rGO (red).

The higher electrocatalytic behavior of pGr was confirmed by the reduced charge transfer resistance in the electrochemical impedance spectra. The interfacial capacitance in parallel was determined and found to be higher for pGr (1.84×10^{-2} µF) when compared to rGO (1.72×10^{-2} µF). The lower charge transfer resistance and higher interfacial capacitance of pGr is possibly due to its comparatively better graphitic basal plane compared to that of rGO, which will increase its conducting behaviour and thus in turn leads to faster electron transfer kinetics as the results suggested.

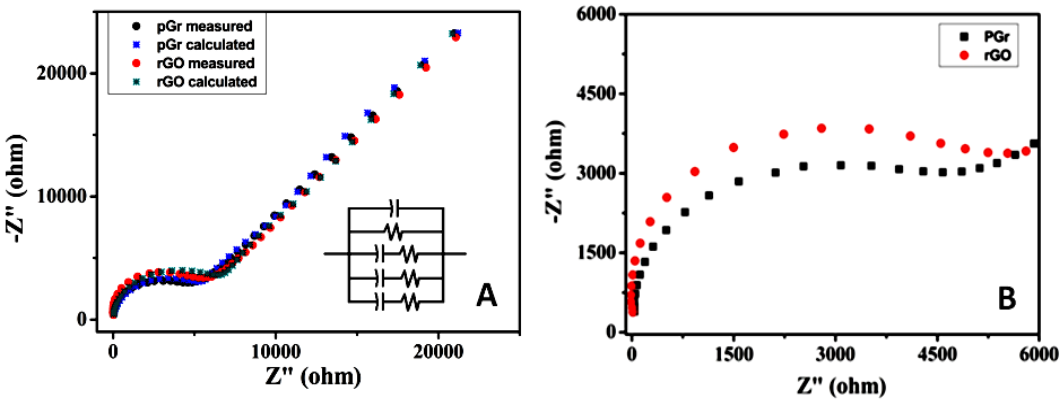

Figure 4.12. (A): Nyquist plots obtained for pGr/GCE and rGO/GCE in the presence of 0.1M $K_3[Fe(CN)_6]/K_4[Fe(CN)_6]$ (1:1) solution, along with their fitted data and the equivalent circuit; (B): Nyquist plot of pGr in comparison with rGO showing smaller semicircle.

4.3.4. Proof for the adsorption of DA by pGr via scan rate study

Scan rate studies were done to understand the reaction mechanism and the kinetics. The CV responses obtained for DA on pGr/GCE at different scan rates between 10 and 1000 mVs^{-1} are given in Figure 4.13A. As the scan rate increased, the redox peak current increased linearly, Figure 4.13B shows the linear relationship (R^2 = 0.983 and 0.986). A linear relationship between the peak currents and the scan rates is an indication of surface adsorption controlled mechanism (A. Yang et al., 2013), thus indicating that the EC oxidation of DA at the pGr/GCE is a typical surface adsorption controlled process. Furthermore, a linear correlation (Figure 4.13C) was obtained between the peak potentials (E_p) and the logarithm of the scan rates. For an adsorption-controlled process, the charge transfer coefficient (α) and the heterogeneous electron transfer rate constant (k_s) can be calculated from the variation of E_{pa} and E_{pc} with the logarithm of the scan rate, following the Laviron's model (Peik-See et al., 2014). A linear relationship was observed for the scan rates above 300 mVs^{-1} (Figure 4.13D). The slope of the linear equation is equal to $(-2.3RT/\alpha nF)$ and $(2.3RT/(1-\alpha)nF)$ corresponding to the cathodic and anodic peak respectively, which can be used to evaluate the cathodic and anodic electron transfer coefficients α_c and α_a. Here, the

α_a was found out to be 0.63. Meanwhile, the k_s was calculated to be 3.2 s^{-1} using the following Laviron's equation, Eq. (4.1) (Laviron, 1979):

$$\log k_s = \alpha \log (1-\alpha) + (1-\alpha) \log \alpha - \log (RT/nF\nu) - \alpha (1-\alpha) nF\Delta E_p/2.3\ RT \quad (4.1)$$

Where, ν is the scan rate; n is the number of transferred electrons; R and F are the gas and Faraday constant, respectively.

The calculated 'k_s' value was higher than the reported values (W. Sun et al., 2013; Sun et al., 2012; Z. Zhu et al., 2010), which usually had values between 2 to 3 s^{-1} and is evident of the fast electron transfer rate property of pGr/GCE for the EC oxidation of DA.

4.3.5. Reproducibility, reusability and stability of pGr/GCE

Measurements of five independently prepared electrodes were used to estimate the reproducibility, the relative standard deviations (% RSD) in the oxidation peak currents in DPV for 1 mM DA was found to be 2.23%, indicating excellent reproducibility. Further, the reusability and the storage stability of pGr/GCE were evaluated by comparing the oxidation peak currents of DA from a solution containing 200 µM DA immediately after washing, and after a period of 1 month respectively (Figure 4.14A and B). The pGr/GCE retained 90 and 89% of its initial current response, for immediate reuse and after a 30-day storage period, respectively. The results indicate the reproducibility and the remarkable stability of the sensor. The reproducibility, reusability and stability performances of pGr/GCE can be assigned to the stable, inert and biocompatible honeycomb basal plane of pGr with nil or minimal reactive functionalities which reduce the chances of surface fouling due to the impurities through adsorption of or unwanted surface reactions.

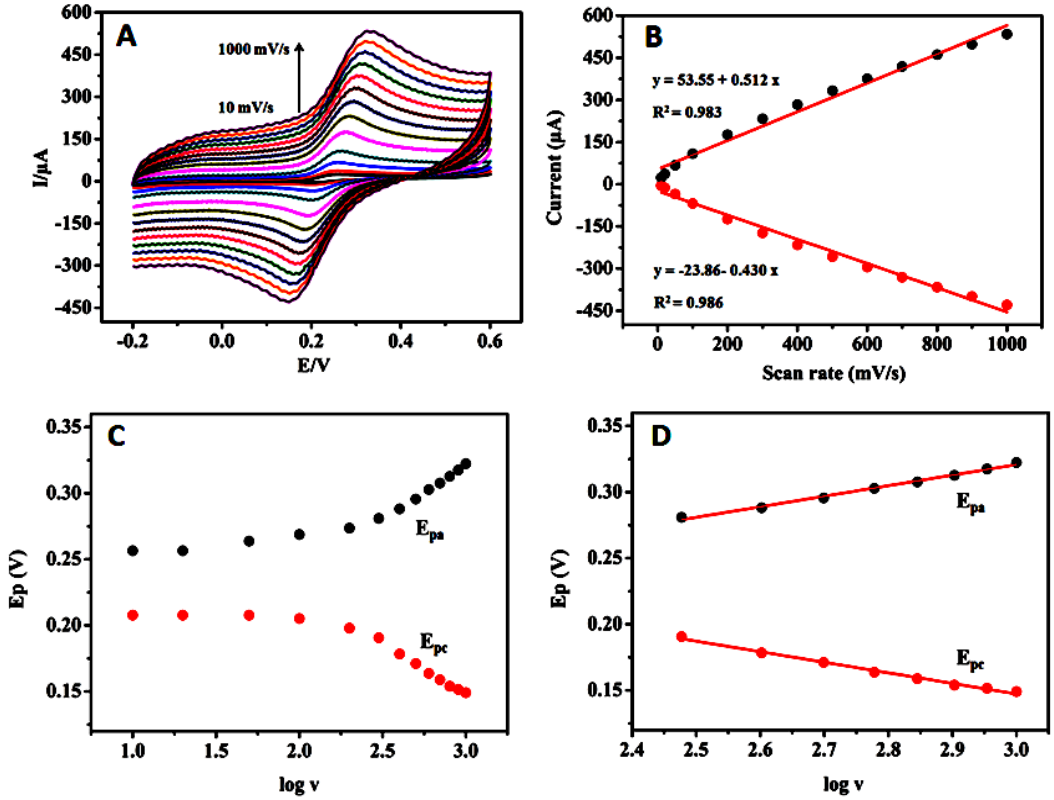

Figure 4.13. Scan rate study results of pGr/GCE: (A): CV obtained for pGr/ GCE in the presence of 0.5 mM DA in 0.1 M PBS with various scan rates from 10 to 1000 mVs^{-1}); (B): Calibration plots of cathodic and anodic peak current Vs. scan rates; (C): Plot of variation in the Ep values Vs. log v, with scan rates from 10–1000 mVs^{-1}; (D): Linear relationship between Ep values and log v for the scan rates from 300–1000 mVs^{-1}.

4.3.6. Real sample analysis

The pGr/GCE was further applied for the detection of DA in real human blood sample via standard addition method, where known amounts of DA was added to the diluted blood sample (1000 times) and the recovery amounts were measured. The measurements are summarized in Table 4.2, the DPV result is given in Figure 4.14C. The recovery calculated was found to be in the range of 99.9–103.4% with a relative standard derivation of 2.3 – 4.0%. The high recovery values indicate the successful applicability of the proposed electrode for the determination of DA in the real biological samples.

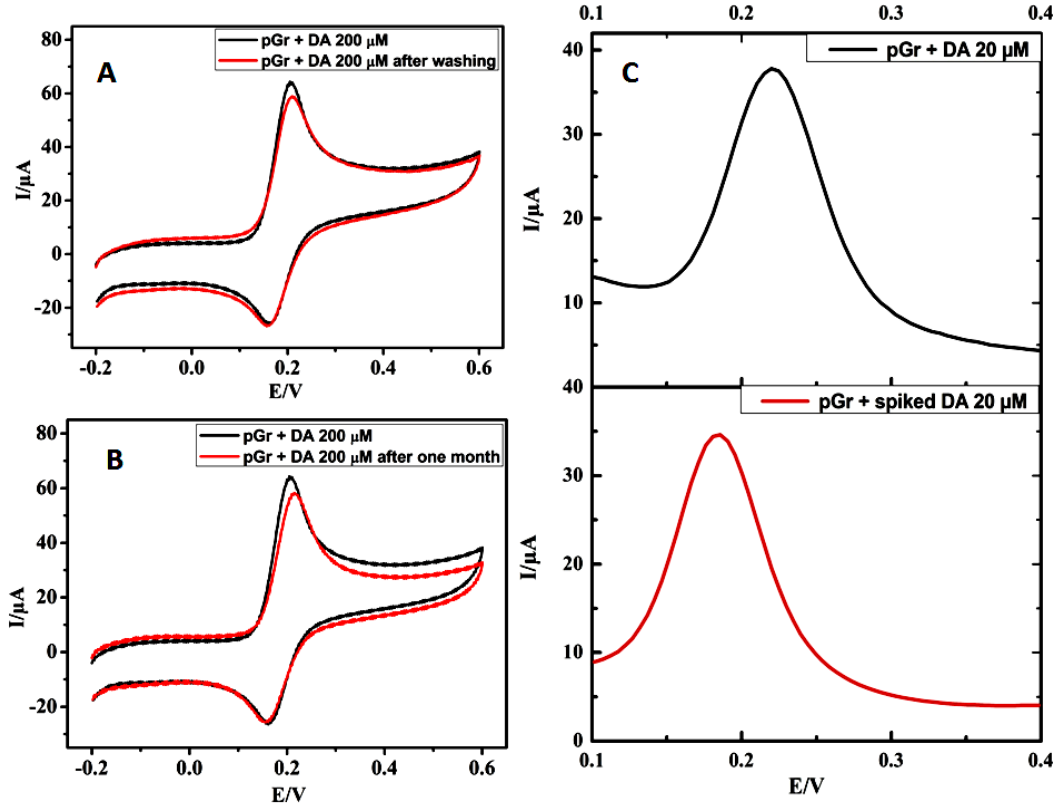

Figure 4.14. CV curves revealing (A): the reusability of pGr/GCE; and (B): stability of pGr/GCE after 1 month; (C): DPV curves showing the responses towards analyte DA sample (black) and DA spiked blood sample (red) respectively.

Table 4.2. Determination and recovery test of DA in human blood samples (n=3)

Blood sample	DA spiked (µM)	DA found (µM)	Recovery (%)	RSD (%)
1	12	12.408	103.40	4.01
2	20	20.404	102.02	3.93
3	50	49.932	99.86	2.34

4.3.7. Dispersibility of pGr in water and sensing properties using pGr/water dispersions

Since pGr was dispersible in water and found to form nanographene sheets, the sensing ability of pGr dispersion in water was studied using GCE modified with the aqueous dispersion of pGr (pGr-water/GCE) and the result is given in Figure 4.15. It can be seen that the current response of pGr-water/GCE is reasonably good (~70 μA) and the peak was sharp similar to that of pGr /GCE (from pGr dispersion in DMF) and the peak potential value was similar for both, which shows that pGr is dispersible in water though not to the extent that in DMF. The result of rGO-water/GCE is not shown due to the poor dispersibility of rGO in water. The result confirms the sensing ability of the water dispersed pGr and the water dispersibility of pGr and thus supports the proposed structure of pGr.

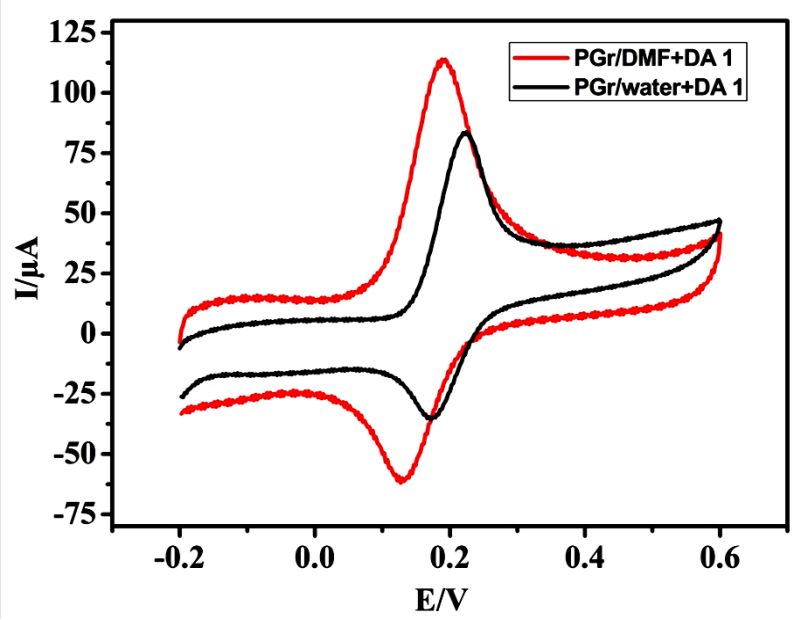

Figure 4.15. Comparison of CV responses of PGr/DMF modified GCE with pGr/water modified GCE for 1 mM of DA. (Ag(s)/ AgCl(s)/ Cl^{-1}(aq., saturated) was as the reference electrode)

Our results demonstrated that the pGr has superior and selective sensing properties for DA which is better than that of the rGO and GO. Further, the result was compared with other literature reports of DA sensors based on carbon nanomaterials. Table 4.3 and 4.4 provide the comparison of the performance of pGr/GCE with various relevant literature reports of non-modified and modified carbon nanomaterials DA sensors, respectively.

Table 4.3. Comparison of the LDR and LOD of pGr/GCE with various previously reported (non modified) Gr based DA sensors

Electrode	Fabrication method	LDR (μM)	LOD of DA in presence of AA (μM)	Reference
Gr	Chemical reduction	4 –100	2.64	(Y.-R. Kim et al., 2010)
ERGO (Electroche-mically reduced GO)	EC reaction	0.5 -60	50	(L. Yang et al., 2014)
pGr (Our Result)	Ball milling (Mechanical Pulverisation)	0.005-200	0.001 (1 nM)	Our result (Ramachandran et al., 2018)

The lowest reported LOD for DA is 10 nM by a SWCNT/Gr NS (X. Chen et al., 2012) while for pGr it is 1 nM. Most of the reported Gr based electrodes use supporting agents (S.-Q. Liu et al., 2012; Ying Wang et al., 2009) for achieving better selectivity and sensitivity, whereas the pGr was used without any modifications. Appreciable peak separation values between the analyte peaks add to the excellent performance of pGr/GCE as an EC sensor both in terms of selectivity and sensitivity. The results thus clearly suggest the merit of pGr as an EC sensor electrode for DA and AA and compounds of similar structures. The cost-effectiveness, solution processability, benign nature and the superior performance of pGr suggest that it is a promising material for the EC sensing of DA, AA and compounds of similar structure.

Table 4.4. Comparison of the LDR and LOD of pGr/GCE with the previously reported modified/functionalised Gr based DA sensors

Electrode	Fabrication method	LDR (µM)	LOD of DA in presence of AA (nM)	Reference
Gr -Chitosan (Gr-CS /GCE)	Chemical reduction	1 –15	270	(Ying Wang et al., 2009)
Gr Nanosheet paste	Chemical reduction	4 –52	600	(S.-Q. Liu et al., 2012)
CRGO/TCPP	Chemical reduction and ultrasonication	0.01 –70	22	(L. Wu et al., 2012)
Sulfonated- Gr	Chemical reduction	0.2 –20	40	(S.-J. Li et al., 2013)
Gr /Fc-NH_2	Chemical reduction	0.05 –200	50	(M. Liu et al., 2012)
AuNP@PSS–Gr	Chemical reduction	1 –60	20	(S. Liu et al., 2012)
AuNP–PS/RGO	Chemical reduction	0.05 –20	-----	(Qian et al., 2013a)
AuNP@Pd–rGO	Reduction	0.01 –100	24	(J. Jiang & Du, 2014)
rGO/Fe_3O_4	Reflux	0.01 –100.55	-----	(Salamon et al., 2015)
Cu_2O/Gr	Solvothermal	0.1 –10	-----	(F. Zhang et al., 2011)
RGO/PPy	In situ chemical oxidative polymerization	0.001 –8	-----	(Qian et al., 2013b)
RGO/carbon dots	Reduction	0.01 – 450	-----	(S. Hu et al., 2014)
SWCNT/Gr NS	Sonication	0.1–525	10 *	(X. Chen et al., 2012)
pGr (Our Result)	Ball milling (Mechanical Pulverisation)	0.005 –200	1	Our result (Ramachandran et al., 2018)

CRGO: chemically reduced graphene oxide; TCPP: meso-tetra(4-carboxyphenyl)porphine; Fc-ferrocene; PPy: polypyrrole; PS: polystyrene; PSS: polysodium4- styrenesulfonate; Pd: palladium NPs; SWCNT: single walled carbon nanotube.
*In the presence of Acetaminophen, (with AA is not available)

4.4. Conclusions

In summary, we have reported the EC sensing of a solution processable pGr obtained by mechanical ball milling of graphite with higher electrocatalytic activity and lowest LOD values for DA and AA. The pGr exhibited LDRs in their physiological concentration ranges. Selectivity was exhibited by the pGr/GCE towards DA and was attributed to its unique structure with different domains such as large aromatic domains with few oxidation sites and the edges rich with functional groups and/or defects. Owing to its structure, the pGr was able to simultaneously detect DA, AA and UA. Moreover, the structure explained the dipsersibility of pGr in water and other solvents and its better electrocatalytic properties. Our study has given a cost-effective, environmental friendly Gr material with interesting and remarkable EC sensing properties which can be produced in multi-gram scale. The study has given insight into the mechanism of the sensing of DA by pGr and the structure of pGr. The developed sensor was found to possess remarkable reproducibility, reusability and stability, moreover proves to be a successful material for the determination of DA in real biological samples.

CHAPTER 5

ULTRASENSITIVE AND SELECTIVE ELECTROCHEMICAL SENSING OF Hg (II) IONS IN NORMAL AND SEA WATER USING SOLVENT EXFOLIATED MoS_2: AFFINITY AND ELECTROCHEMISTRY MATTER

A solvent exfoliated molybdenum disulphide (MoS_2) has been employed for the EC sensing of Hg^{2+} ions to exploit the affinity of S^{2-} towards Hg^{2+}.The sensitivity and selectivity studies of MoS_2/GCE were carried out and the results were discussed. A mechanism for the enhanced and selective sensing of the MoS_2 towards Hg^{2+} has been proposed based on the evidences obtained for MoS_2-Hg interaction/affinity. The sensing studies were extended to real water samples such as tap and sea water to confirm the applicability of the sensor in real environmental samples.

5.1. Introduction

Development of sensors for detecting heavy metals in environmental bodies is of utmost importance because of the gravity of dangers posed by these toxic metals to the environmental and ecological system. Amongst these, mercury (Hg) is recognized widely as one of the most neurotoxic and hazardous environmental pollutants due to its persistent character. It is present in the environment in several forms; such as elemental Hg, inorganic Hg (Hg^{2+}) and methyl Hg (CH_3Hg^+). The ionic form, Hg^{2+}, is highly soluble and reactive, and can bind to various ligands in natural waters, particularly those having sulphur (S) functional group and is often accumulated through the food chain, thus posing a

serious threat to humans. The Hg^{2+} can cause serious damage to the heart, kidneys, lungs, brain development of foetus, and the immune system (Clarkson & Magos, 2006; Ratner & Mandler, 2015), the hazardous nature of Hg^{2+} has prompted researchers to develop methods to detect Hg^{2+} in environmental bodies which has resulted in atomic absorption spectrometry (Hatch & Ott, 1968), colorimetry (Lee et al., 2007) and cold vapour atomic fluorescence (Bloom & Fitzgerald, 1988). However, the environmental levels of Hg^{2+}, can be of as low as few parts per trillion (10^{-12} M), i.e. ppt. level, and hence highly sensitive and selective methods must be developed. In this context, EC sensing is an appealing method because of its high inherent sensitivity, low-cost, simple operation, fast analysis (Ratner & Mandler, 2015) and last but not least, portability. The research on the electrodes for the sensing of Hg^{2+} has been focused on materials containing Au or S because of the affinity between them and Hg. Earlier reports were based on ITO-AuNP/GCE (Ratner & Mandler, 2015), thymine-Au NP/GCE (Miao et al., 2009), and later on other materials such as hydroxyapatite nanoparticles/GCE (Kanchana et al., 2015), modified Gr based electrodes (Gong et al., 2010). Au was found to be a superior substrate to that of GCE in terms of sensitivity (Gong et al., 2010), because of its higher affinity towards Hg, however, had a major drawback in terms of reproducibility, due to the amalgam formation that necessitated complex EC and mechanical treatment (Kanchana et al., 2015). Therefore, GCE modified with suitable materials such as AuNP, Gr etc., gives better stability and reproducibility.

Interestingly, MoS_2, a layered semiconductor material made of covalently bound S-Mo-S layers stacked through weak Van der Waals interactions (Ramakrishna Matte et al., 2010), which has been explored already for its antibacterial applications (Yin et al., 2016), cancer therapy (Yin et al., 2014) etc. has the required properties as an EC electrode substrate and in addition has S in the form of sulphide (S^{2-}) groups which might possess affinity for Hg^{2+} and vice versa. MoS_2, in different forms, has been explored in the field of EC sensing for detecting analytes such as: H_2O_2 by MoS_2 NP (T. Wang et al., 2013),

acetaminophen by a layered MoS_2–Gr composites (K.-J. Huang et al., 2013), glucose and dopamine by an electrochemically reduced single-layer MoS_2 (S. Wu et al., 2012), cancer cells by in situ surface-functionalized MoS_2 nanosheets (Yulin Guo et al., 2017), microRNA-2 by Au NP-decorated MoS_2 nanosheet (S. Su et al., 2017) etc. Though, MoS_2 considering the presence of S^{2-} groups, can be a suitable electrode material for EC sensing of Hg^{2+}, to the best of our knowledge, has not been yet explored for the EC sensing of Hg^{2+}. Therefore, in this work, we have investigated the EC sensing of Hg^{2+} by solvent exfoliated MoS_2. Interestingly and not unexpectedly, the MoS_2/GCE exhibited remarkable sensitivity with a detection limit of $\leq$ 0.000001 nM (0.2 parts per quadrillion (ppq)) in addition to its remarkable selectivity (Aswathi & Sandhya, 2018). Other than Hg^{2+}, the only metal ion exhibited current response on MoS_2 was silver ion (Ag^+), however the current response of Ag^+ was lower and was at a higher potential. The EC sensing studies in saline solution showed that the performance of MoS_2 was not affected by the presence of NaCl which suggested the potentiality of application of the electrode in sea water, where the threat of Hg poisoning is significant. Moreover, the results of MoS_2 was compared with the currently popular and widely studied electrode materials such as rGO and GO and observed that undoubtedly MoS_2 is far superior than both rGO and GO in Hg^{2+} sensing, and is one of the best results so far obtained in terms of LOD and selectivity. Thus, in this work the potentiality of MoS_2 as an electrode material for sensing Hg^{2+} is demonstrated.

5.2. Experimental

5.2.1. Preparation of electrodes for sensing

MoS_2 (99%, 2 μm in size) was dispersed in DMF at a concentration of 0.5 mg mL^{-1} by probe sonication at RT for 30 minutes to form a suspension. This dispersion (20 μL) was used to modify the GCE. Prior to modification, each GCE was mechanically polished with wetted microcloth containing alumina powder for

about 15 minutes, and then carefully cleaned in distilled water and acetone by ultra-sonication for 2 minutes each. The sample dispersions in DMF were drop cast over the pre-treated GCE carefully and then allowed to dry for 24 hours at RT to achieve the modified electrodes. After each analysis, unless stated otherwise, cleaning of GCE was done by ultrasonicating in DMF followed by distilled water and acetone for 2 minutes each.

5.2.2. EC methods

The EC behaviours of various metal ions (Hg^{2+}, Ag^{+}, Cd^{2+}, Ni^{2+}, Zn^{2+}, Co^{2+}, Pb^{2+}) were investigated at the MoS_2/GCE using CV and DPV. For making the electrode, 0.5 mg ml^{-1} suspension of MoS_2 in DMF was drop cast on to a GCE. The EC measurements were carried out according to the procedure given in chapter 2. The electrolyte solutions used were 1 M HCl and 0.5 M HNO_3. DPV was applied for the successive determination of Hg^{2+} under optimal conditions. Mercury was deposited by the MoS_2 substrate in 1M HCl via the reduction of Hg^{2+} to Hg^{0}, while carrying out a CV scan from -0.2 to 0.4 V at a scan rate of 50 mV/s before the DPV scan. The DPV scans of deposited Hg^{0} were performed at the same voltage range as in the case of CV (-0.2 to 0.4 V) with optimized parameters (pulse amplitude 25mV). For pH studies, 0.1 M PBS was chosen as the electrolyte. The pH values were adjusted by adding ortho phosphoric acid and NaOH. All the experiments were performed at the RT, except for the temperature studies (5-50°C).

5.3. Results and Discussion

5.3.1. MoS_2 sample preparation and characterization

As this is the first time study of MoS_2 as an electrode substrate for the EC sensing of Hg^{2+}, solvent exfoliated commercial MoS_2 was chosen for the sensing studies. Ultrasonication in a solvent was proved to be an easy and efficient way to exfoliate layered materials, the commercial bulk MoS_2 was

ultrasonicated in DMF and the resultant dispersion was used for modifying GCE for preparing the sensing electrodes.

The MoS_2 dispersion was characterized using FESEM, AFM, STM and TEM techniques. Figure 5.1A and B depict the FESEM and the HRTEM images of the ultrasonicated MoS_2, respectively, which revealed exfoliated MoS_2 sheets with edges of the layers exposed. The AFM analysis (Figure 5.1C) further confirmed its exfoliated nature. The STM images and the corresponding height profile of the MoS_2 sample are given in Figure 5.1D and 5.1E respectively. The height of each exfoliated MoS_2 sheet ranged from 2 to 5 nm indicating that the exfoliated MoS_2 sheets consist of roughly 3-7 layers of MoS_2. The number of layers was further confirmed by Raman analysis and is discussed in a latter section. In addition, the exposure of S binding sites in the MoS_2 dispersion sample is confirmed by elemental mapping analysis. (Figure 5.1F-H).

5.3.2. EC Sensing studies of Hg^{2+} by MoS_2/GCE

5.3.2.1. Optimization of supporting electrolyte and concentration studies

According to the literature (Rajawat et al., 2012), the suitable supporting electrolytes for Hg determination are usually NaOH and HCl. However, reports of Hg^{2+} sensing at highly basic P^H values have resulted in lower peak current values and broader peak shapes which were attributed to the hydrolysis of Hg^{2+} (Kanchana et al., 2015). Before deciding on the electrolyte, the sensing studies of Hg^{2+} was conducted in various supporting electrolytes, such as 0.1 M Phosphate buffer, 0.1 M NaOH, 1 M HCl, and 0.05 M HNO_3 and from the results obtained (Figure 5.2) it was evident that the current response for Hg^{2+} is better in 1 M HCl compared to that of the other electrolytes, therefore, 1 M HCl was selected for further studies.

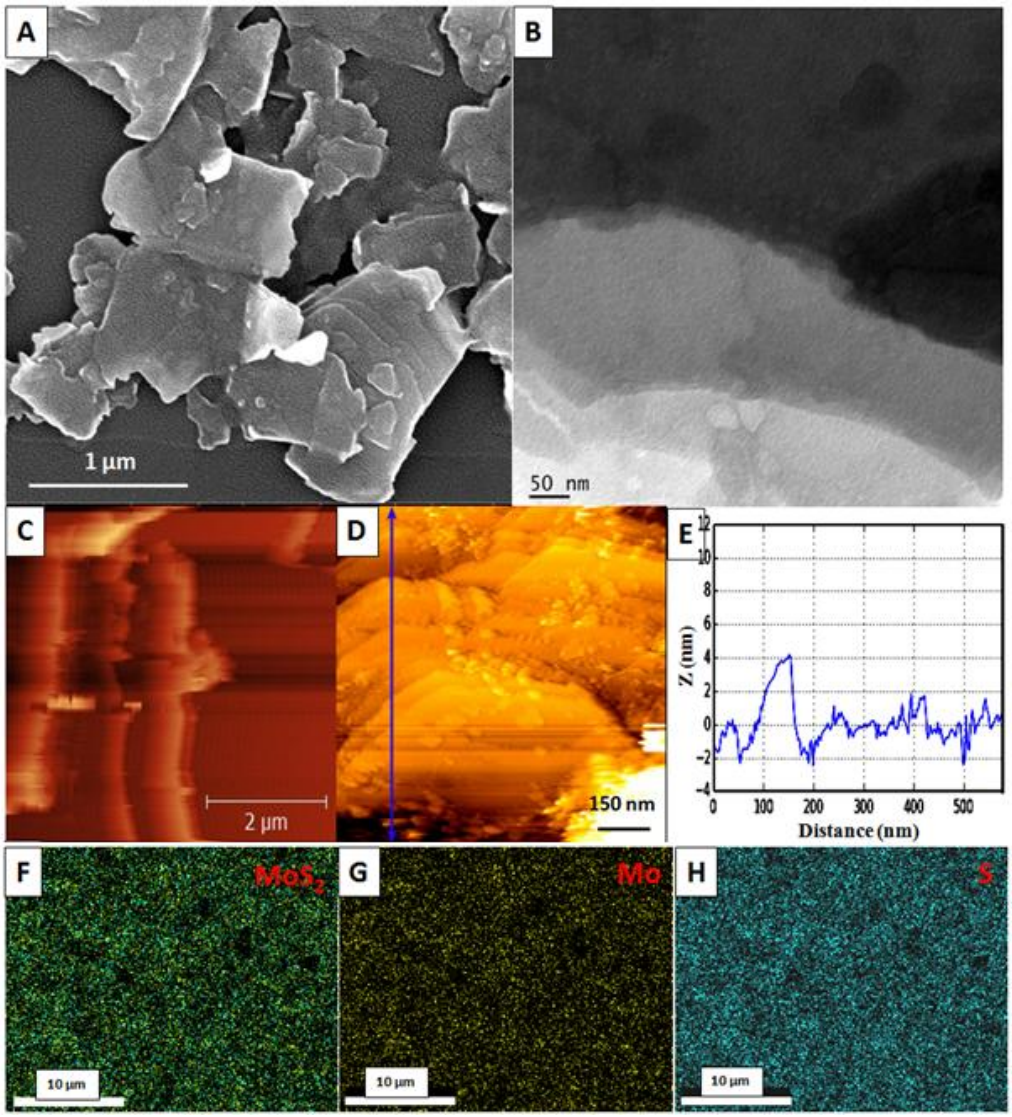

Figure. 5.1. (A): FESEM (B): HRTEM (C): AFM (D): STM images of ultrasonicated MoS_2 revealing its layered morphology, (E): height profile along the line in (D) and SEM-Mapping results of MoS_2 dispersion, (F): overlapped Mo and S G) Mo and (H): S, the result shows the ample (exposed) S binding sites in the exfoliated MoS_2.

The systematic investigation of EC sensing property of the modified electrode MoS_2/GCE towards Hg^{2+} was carried out using both CV and DPV techniques in 1 M HCl. The sensing property of MoS_2/GCE and that of bare GCE towards Hg^{2+} are depicted in Figure 5.3A, the MoS_2/GCE exhibits a 30-fold increase in the current response (~700 µA) from that of the bare GCE (~25 µA), indicating its suitability as an electrode material for the sensing of Hg^{2+}.

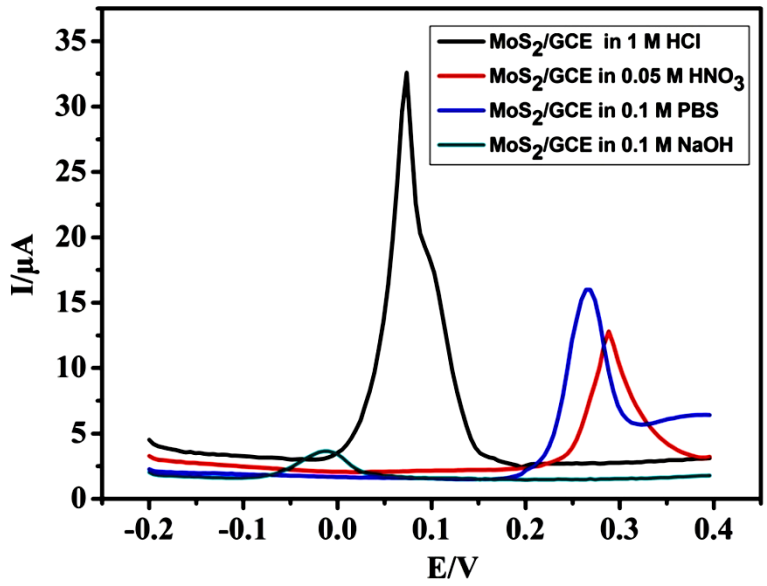

Figure 5.2. DPV responses of MoS_2/GCE for the same concentration of Hg^{2+} (10 µM) in various supporting electrolytes.

Further, the voltammetric responses for the increasing concentrations of Hg^{2+} were measured using CV and DPV and the plots obtained are shown in Figure 5.3B and 5.3C respectively. As expected, an increase in the anodic peak current was observed with the increase in the concentration and the measurements were conducted for concentrations up to 10 mM. The calibration graph (Figure 5.3D & E) obtained covered a wide range of concentrations from nM to mM, to be exact, 0.1 nM to 0.2 mM, with four separate linear segments corresponding to four different LDR: from 0.1–1 nM with an R^2 = 0.997, from 2–10 nM (R^2= 0.970), from 0.5-10 µM (R^2= 0.941) and from 0.06 - 0.2 mM (R^2= 0.980). The LOD of MoS_2 for Hg^{2+} was found out using DPV and was estimated as ~0.001 nM (Figure 5.3F). According to the US Environmental Protection Agency (EPA) maximum allowed limit of Hg^{2+} in drinkable water is 10 nM (2 ppb) (Miao et al., 2009). Therefore, a sensor with a LOD of 0.001 nM (1/10000th the concentration limit specified by EPA) should be considered highly efficient and sensitive for the detection of Hg^{2+}.

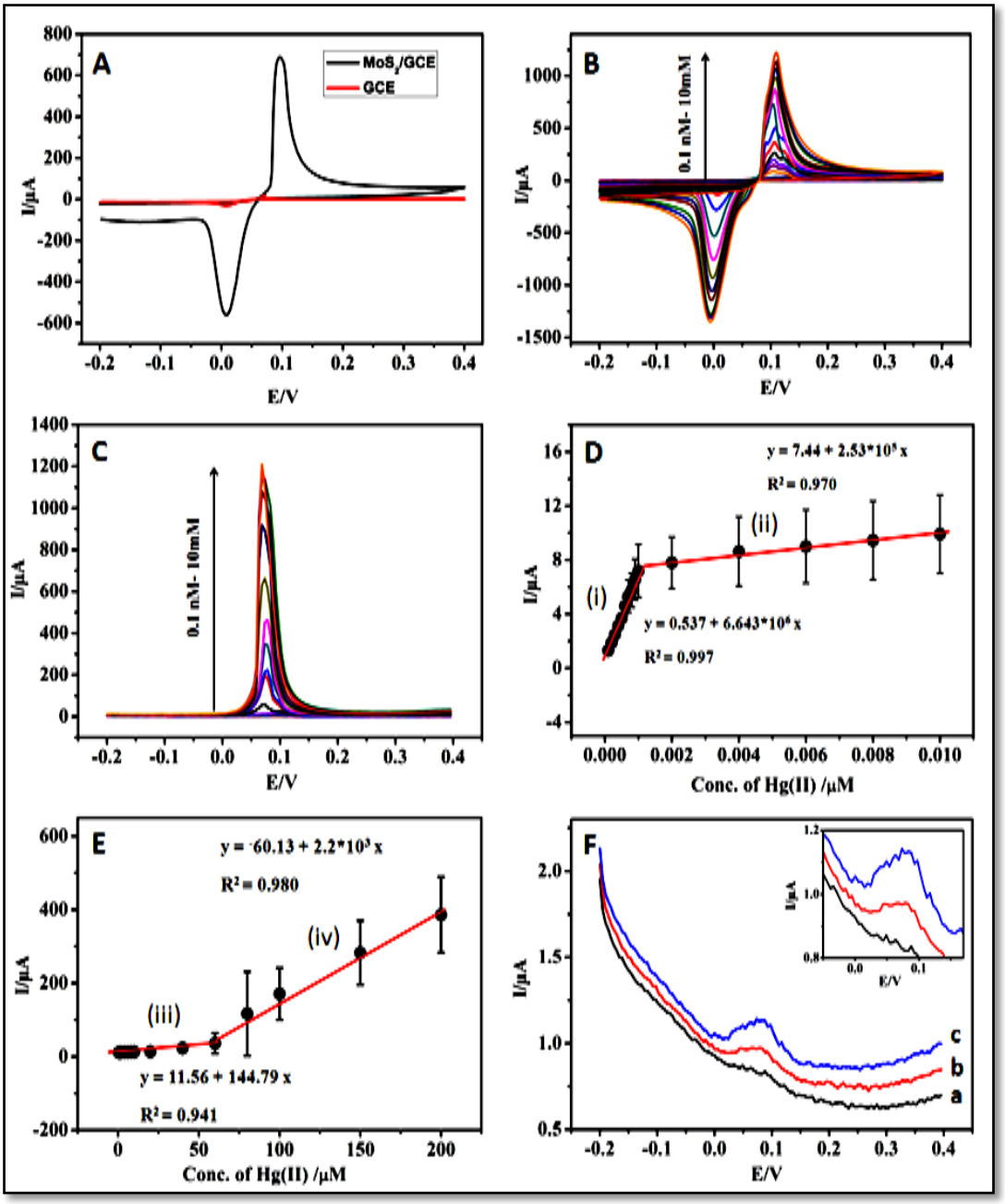

Figure 5.3 (A): CV response of MoS_2/GCE in comparison with bare GCE towards 1 mM Hg^{2+} in 1 M HCl at the scan rate of 50 mV/s. (B): CV and (C): DPV profiles at MoS_2/GCE with increasing concentration of Hg^{2+} (0.1 nM -10 mM) in 1M HCl at the scan rate of 50 mV/s. (D) and (E): The four different LDRs obtained for the sensing of Hg^{2+} on MoS_2/GCE; (D): LDRs between (i) 0.1- 1 nM and(ii) 2–10 nM; and (E): LDRs between (iii) 0.5-10 µM and iv) 0.02-0.2 mM. R^2 for the LDRs are ranging between 0.941- 0.997). (F): DPV response of MoS_2/GCE in 1M HCl (a) in the absence and (b) & (c) in the presence of 0.001 nM (LOD value) and 0.003 nM Hg^{2+}, respectively.

5.3.2.2. Interference studies and selective sensing of Hg^{2+} by MoS_2

Selectivity offered by an electrode towards the analyte is vital in determining its practical applicability. Therefore, further studies were carried out to find the selectivity of MoS_2 towards Hg^{2+}. The sensing performance of MoS_2/GCE towards various metal ions was tested using CV, and the results are depicted in Figure 5.4. Of the various ions tested (Hg^{2+}, Ag^{+}, Pb^{2+}, Fe^{2+}, Cd^{2+}, Co^{2+}, Ni^{2+}, Zn^{2+}, Sn^{2+}, Cu^{2+} and Cr^{6+}), Ag^{+} and Hg^{2+} showed measurable current response in the selected voltage regime of 0.2 to 0.8V. The response of Ag^{+} was lower, broader and was at a higher potential to that of Hg^{2+} with a difference (ΔE_p) of 0.4V. Both Hg and Ag ions possess affinity towards S containing groups such as thiols, sulphides and are well recorded. Thus, it is interesting to note that the current response of Ag^{+} was lower (almost one-third) and the peak potential was higher than that of the Hg^{2+}. This inferior response of Ag^{+} is evident of the preferentiality or selectivity of MoS_2 towards Hg^{2+}. Simultaneous sensing studies were carried out using Hg^{2+} and Ag^{+} as analytes and result (Figure 5.5A) exhibited two well separated peaks. Interference of the other metal ions on Hg^{2+} sensing was conducted, and the result is given in Figure 5.5B, measurable current response was observed only for Hg^{2+} and Ag^{+}. No other signals were observed and the current observed for Hg^{2+} and Ag^{+} were same as that obtained in the absence of the ions which confirms the absence of interference from the ions. It should be noted that, the metal ions which are known for their affinity for S namely Fe^{2+}, Cu^{2+} etc. did not show any significant current response, the result thus demonstrates the superior selectivity and preference of Hg^{2+} on MoS_2.

5.3.2.3. Comparison of MoS_2 with Gr based electrodes for the sensing of Hg^{2+}

Gr based electrodes are the most popular choices for EC sensing electrodes due to the excellent properties such as high theoretical surface area, conducting properties etc. Therefore the EC sensing of Hg^{2+} using Gr based materials such as GO and rGO were carried out for comparison, and the result is shown in Figure 5.6. It is evident from the result that MoS_2/GCE exhibited the

highest current response when compared to that of rGO/GCE and GO/GCE. The MoS_2/GCE exhibited a 30-fold increase in current response compared to that of bare GCE and GO/GCE and four times the current response of rGO/GCE. The responses of bare GCE and GO/GCE were negligible suggesting that they are not suitable for the sensing of Hg^{2+}. Even though, the structure of GO has many interaction sites, owing to its oxidized nature, the response for Hg^{2+} was negligible. The higher electronic conductivity and electron rich nature of rGO, which can reduce Hg^{2+} ions to Hg may possibly be the reason for the better response by rGO/GCE compared to that of GO/GCE.

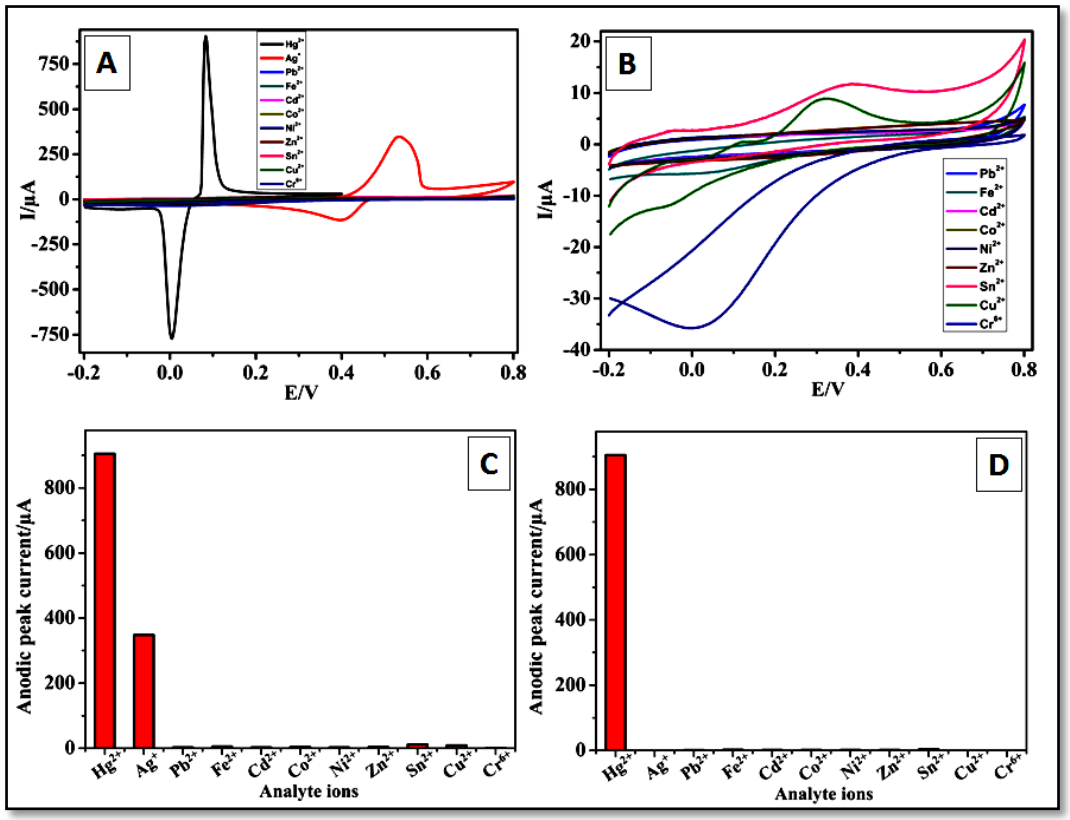

Figure. 5.4. (A): CV profiles at MoS_2/GCE in 1M HCl containing 1mM each of Ag^{+}, Pb^{2+}, Fe^{2+}, Cd^{2+}, Co^{2+}, Ni^{2+}, Zn^{2+}, Sn^{2+}, Cu^{2+} and Cr^{6+}; (B): Anodic current response of various analyte ions with respect to that of Hg^{2+} (C): CV response at MoS_2/GCE for the analyte ions other than Hg^{2+} and Ag^{+}; (D): Anodic peak current response of various analyte ions at the peak potential value of Hg^{2+}.

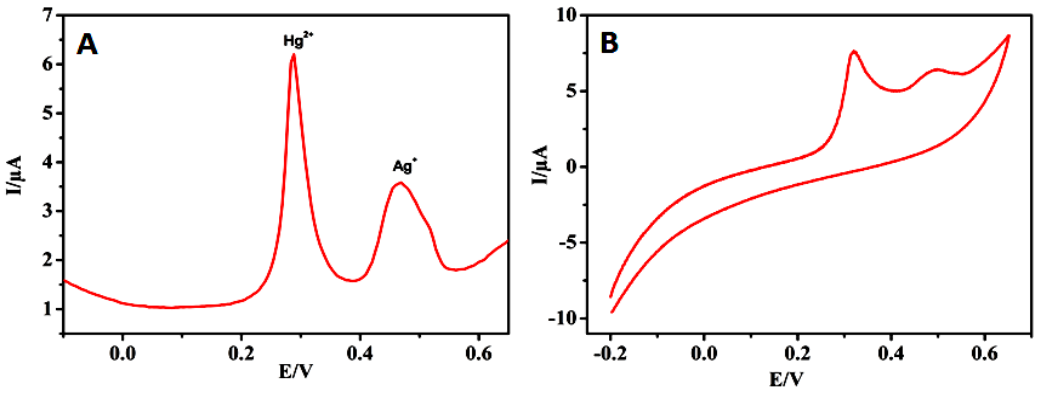

Figure 5.5. (A): DPV result showing the simultaneous sensing of Hg^{2+} and Ag^{+} by MoS_2/GCE in 0.05 M HNO_3 with concentration of Ag^{+} double that of the Hg^{2+}. (B): CV response of MoS_2/GCE in 0.05 M HNO_3 containing Hg^{2+}, Ag^{+}, Pb^{2+}, Fe^{2+}, Fe^{3+}, Cd^{2+}, Sn^{2+}, Ni^{2+}, Cu^{2+}, Cr^{6+}, Zn^{2+} and Co^{2+} with concentration of all ions double that of the Hg^{2+}.

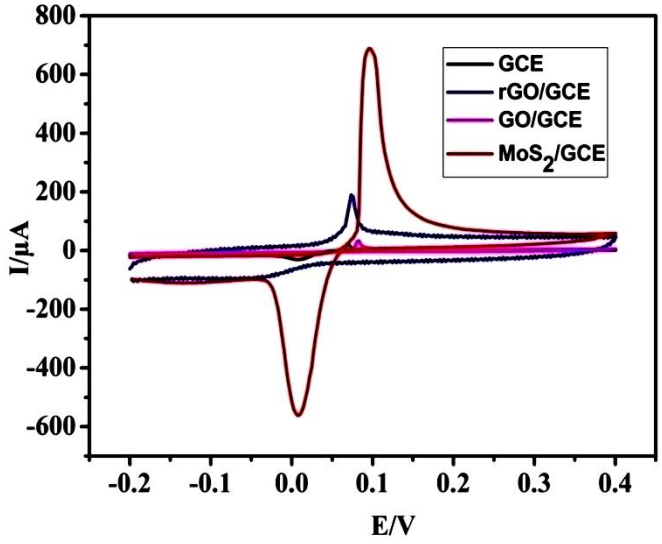

Figure 5.6. The CV responses of MoS_2 and Gr modified GCEs towards 1 mM Hg^{2+} in 1 M HCl at a scan rate of 50 mV/s.

5.3.2.4. Mechanism of the selective and enhanced sensing of Hg^{2+} by MoS_2

In most of the reports of heavy metal ion sensors, a pre-deposition step is conducted so that the target metal ion (in this case Hg^{2+}) adsorbed on the (modified) electrodes gets deposited in its reduced state (here as Hg^{0}, Eq. (5.1)) during the course of pre-deposition treatment, which subsequently undergoes oxidation on applying oxidation potential as described in (Eq. (5.2).

$$Hg^{2+} + 2e^- \rightarrow Hg^0 \qquad (5.1)$$

$$Hg^0 \rightarrow Hg^{2+} + 2e^- \qquad (5.2)$$

During the experiments using MoS_2 as electrode, it was observed that the pre-deposition/accumulation procedure was not required prior to the oxidation step, which implies that the reduction of Hg^{2+} to Hg^0 was happening spontaneously on MoS_2. This observation was interesting, and the reasons for this was thought to be the following: While Hg^{2+} is a strong oxidizing agent and electrophilic at RT, S^{2-} is a natural reducer and hence the S^{2-} group in MoS_2 can donate electrons to the adsorbed Hg^{2+} to form Hg^0 as described in Eq. (5.3) and Eq.(5.4) (Aswathi & Sandhya, 2018),

$$Hg^{2+} + 2e^- \rightarrow Hg^0 \; ; \; E^0_{red} = 0.851 \text{ V} \qquad (5.3)$$

$$S^{2-} - 2e^- \rightarrow S^0 \; ; \; E^0_{ox} = 0.476 \text{ V}^* \qquad (5.4)$$

$$\text{Net reaction: } Hg^{2+} + S^{2-} \rightarrow Hg^0 - S^0 \; (S \rightarrow Hg) \; ; \; E^0_T = 1.327 \text{ V} \qquad (5.5)$$

* pH changes alters the potential, lower pH makes the reduction potential of S^{2-} more positive.

The high positive cell potential $E^0{}_T$ for the overall reaction (Eq. (5.5)) indicates that it is thermodynamically favourable, at STP to a considerable extent. Note that the Hg and S may not actually separate out as the elements; Rather, the redox equation above suggests that, very strong S–>Hg coordinate covalent bonds are formed. So here, the S^{2-} anions in the MoS_2 itself act as the reducer to achieve Hg accumulation and hence a separate pre-deposition step was not required to achieve the mentioned results. The CV and DPV experiments were done simultaneously, and hence partial accumulation of Hg^0 might have taken place during the scan from -0.2 to 0.4 V. These enabled the determination of Hg^{2+} without requiring any pre-deposition step. The reason explains the no response by

GO/GCE for Hg^{2+} though GO was rich with functional groups which may act as binding sites. In the meantime, rGO seems to exhibit certain reducing ability through its redox potential; however, lower affinity between rGO and Hg^{2+} may be playing the spoilsport.

As explained above, the mechanism of EC sensing of Hg^{2+} is due to the spontaneous reduction of Hg^{2+} to Hg^0 on MoS_2, because of the higher reduction potential of Hg^{2+} ions compared to that of the S^{2-} ions, the Hg^0 subsequently undergoes oxidation on applying oxidation potential. Based on this electrochemistry, the selectivity of Hg^{2+} over the other analyte ions, which has similar affinity to S^{2-}, can be explained, say for example Pb^{2+}. When the two metal ions(Hg^{2+} and Pb^{2+}), both having affinity to S^{2-} ions are present in the medium, it is reasonable to believe that the ions of the metal with comparatively higher reduction potential will get preferably reduced on the surface of MoS_2 by the S^{2-} ions. Thus, Hg^{2+} with its higher standard reduction potential (0.85 V) is preferred over Pb^{2+} (-0.13 V), which has a lower standard reduction potential. Thus, the selectivity of Hg^{2+} is due to its higher positive reduction potential compared to that of the Pb^{2+} (The explanation agrees with the result obtained for Ag^+. The Ag^+ with its higher positive reduction potential (0.80 V), was spontaneously reduced by MoS_2 because of its higher standard reduction potential and yielded current response though lower compared to that of Hg^{2+}, which probably is because of its comparatively lower reduction potential). Therefore, thermodynamically speaking, in the presence of Hg^{2+}, Ag^+ and Pb^{2+} (and other analyte ions of lower reduction potential), Hg^{2+} will be favoured for reduction by MoS_2 which was confirmed by the CV and DPV experiments.

In addition to the affinity, the semiconducting nature of MoS_2 has been assumed to play a role in achieving the Hg^{2+} sensing. With the high surface area to volume ratio, the electronic properties of the atomically thin semiconductors can be readily modulated by their environment (S. Jiang et al., 2015). Hg^{2+} ions can strongly get adsorbed to MoS_2 layers due to the high binding affinity between Hg^{2+} and the S sites on the surface of MoS_2. It is reported that the Hg^{2+} can alter

the electronic transport properties of the few-layer MoS_2 in favour of its semiconducting properties (S. Jiang et al., 2015). Therefore, the semiconducting nature of MoS_2 may help/fasten the redox reactions happening over the electrode surface in the presence of Hg^{2+}.

5.3.2.5. Scan rate study

It is evident from the results that MoS_2 has preferential interaction towards Hg^{2+}, it is important to see whether it is governed by diffusion or adsorption controlled process. To investigate the mechanism of sensing, the influence of scan rates on the electrocatalytic response of MoS_2/GCE towards Hg^{2+} oxidation was examined and the CV response at different scan rates from 10 and 1000 mVs^{-1} are given in Figure 5.7A. The linear relationship (R^2 = 0.956 and 0.954) between the redox peak currents and the scan rates (Figure 5.7B) disclose that the EC reactions of Hg^{2+} on the MoS_2 surface is a typical surface adsorption controlled process (Ramachandran et al., 2018).

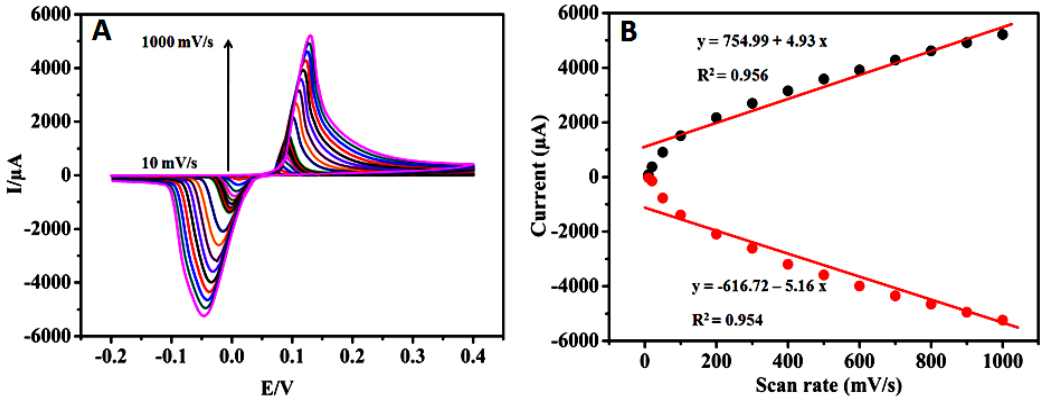

Figure 5.7. (A): CV profiles at MoS_2/ GCE in 1 M HCl containing 1 mM Hg^{2+} at various scan rates (10, 20, 30, 40, 50, 60, 70, 80, 90, 100, 200, 300, 400, 500, 600, 700, 800, 900 and 1000 mV). (B) Calibration plots of cathodic and anodic peak current vs. scan rate.

5.3.3. Evidences for the MoS_2-Hg affinity/interaction

The selective and preferential adsorption of Hg^{2+} over MoS_2/GCE was explained by the S-Hg interactions between Hg^{2+} and the S^{2-} groups of MoS_2.

Among the various elements, an S group is well known to bind tightly to Hg^{2+} and is well established, as the word 'mercaptan' (mercury capturer) implies. Though CV scans are clear evident of reduction of Hg^{2+} to Hg^0 by MoS_2, further evidence was sought to understand the interaction between MoS_2 and Hg^{2+}, for this the dispersion of MoS_2 was mixed with $HgCl_2$ solution and the product formed was washed well and dried. The as obtained MoS_2-Hg was analysed using FTIR, TGA, Raman spectroscopy, XRD and XPS. The FTIR spectra of the MoS_2-Hg and MoS_2 are given in Figure 5.8A. Though the spectra were similar for most parts, differences were observed in the region 1100-500 cm^{-1} (Inset of Figure 5.8A), which is the finger print region and is an indication of the interaction between the S^{2-} of MoS_2 and Hg^{2+}, which can alter the bond strengths of Mo-S and S-S due to the S–>Hg coordinate covalent bond formation. Thus, the FTIR analysis suggests an interaction between Hg^{2+} and MoS_2.

The thermogram of MoS_2 and MoS_2-Hg are shown in Figure 5.8B and it is clear from the thermograms that the MoS_2-Hg shows an entirely different thermal behaviour when compared to that of MoS_2. In the TGA curve of MoS_2, the first weight loss (<2 %) around 100°C, can be attributed to the loss of adsorbed water molecules. The weight loss from 350–500°C can be ascribed to the oxidation of MoS_2 to h-MoO_3 and finally phase transformation of h-MoO_3 to thermo-dynamically stable phase α-MoO_3, which is stable up to 670°C.The last stage sharp weight loss from 670 to 790°C is ascribed to the decomposition of the α-MoO_3 (Kumar et al., 2017). Whereas in that of MoS_2-Hg, the weight loss started just above 100°C and extended to 300°C, with ~30% loss, whereas it was a mere 2 % in MoS_2. This, may possibly due to the loss of S^0 and Hg^0 from MoS_2-Hg; S in the form of its oxides (SO_x) and Hg^0 due to its volatile nature (0.056 mg $h^{-1}cm^{-2}$ at 20°C) (Zhi et al., 2016), respectively (An isotherm at 100°C was carried out for 30 min. to confirm that the loss is not due to water molecules). The decomposition of S may probably caused by the weakening of Mo-S bonds because of the interaction with Hg^{2+} ions forming S–>Hg bonds. From 300-500°C it shows similar thermal behaviour to that of MoS_2, as the MoS_2 changes to α-MoO_3 phase. From 690 to 795°C it shows the similar sharp weight loss which is ascribed to the

decomposition of α -MoO_3, leaving a residual weight amount of 41%, while MoS_2 left a mere 4% of residue. As mentioned earlier the elemental Hg due to its volatile nature, will be vaporized and completely removed at temperatures above 500°C, since the vapor pressure of Hg is an appreciable value above this temperature (Collins et al., 1975). Therefore, it can be assumed that the residual weight at 800°C is due to Hg^{2+}, formed from the S–>Hg bonds during the loss of S as SO_x, combined with the strongly adsorbed Hg^{2+}. During the removal of S from the S–>Hg, there is a chance of Hg to return to Hg^{2+} or to a partially oxidized state. Interestingly, the TGA curve of MoS_2-Pb (which is prepared in the similar manner as that of MoS_2-Hg, replacing the Hg salt by Pb salt) is similar to that of MoS_2, does not show the changes that was observed in that of the MoS_2-Hg, other than an increase in the residual amount (~24%) from that of MoS_2, which can be attributed to the presence of Pb^{2+} (adsorbed) due to its affinity to S^{2-}. The thermal behaviour of MoS_2-Pb up to ~690°C showed no loss due to S, and thus ruling out any reduction of Pb^{2+} to Pb^0 by MoS_2. This result suggests that the S-Hg interaction and the electrochemistry between Hg^{2+} and MoS_2 are crucial in the sensing behaviour exhibited by MoS_2 towards Hg^{2+}.

The S-Hg interactions were further confirmed by XRD and Raman analysis. Figure 5.8C shows the normalized XRD pattern of MoS_2-Hg and MoS_2, all the diffraction peaks of bulk MoS_2 can be readily indexed to the hexagonal phase (JCPDS no. 37-1492). In comparison, MoS_2-Hg though basically retains the position of most of the diffraction peaks of MoS_2 (represented by # symbol), with lower intensity, though. In addition, MoS_2-Hg shows a very small (002) peak, indicating that the number of layers and the mean crystallite size and are much lower than those of the bulk MoS_2. This may be due to the incorporation of Hg^{2+} to the MoS_2 dispersion, and its interaction with S^{2-}, which disturbs the normal restacking of MoS_2 layers. Moreover, we can readily detect an equal number of extra peaks (represented by * symbol). On comparing the peaks obtained in the XRD of MoS_2-Hg with literature, it was found that the extra peaks are matching either with those of sulphur (S^0) or with the XRD patterns of Hg-S nanostructures. For example, the positions and intensities of the diffraction peaks at 2 theta =

28.32^0, 31.8^0, 40.5^0, 53.14^0 are in good agreement with the literature values for orthorhombic or α-phase S (Chaudhuri & Paria, 2014) in its elemental form (S^0). The diffraction peaks at 2theta = 46.44^0, 63.06^0, 69.07^0 can be indexed to the cubic phase HgS nanostructures (Sangsefidi et al., 2015). The presence of S^0 suggests the reduction of Hg^{2+} by MoS_2, to form Hg-S with partial Hg^0 and S^0 character, as explained in the mechanism part. Therefore, the result indicates the existence of S-Hg interaction sites with partial elemental character.

Further, the Raman spectra of MoS_2-Hg and MoS_2 (restacked from dispersion) were recorded (Figure 5.8D). The spectrum of MoS_2 reflects the two characteristic Raman modes, A_{1g} (out-of plane vibration of the S atoms) and $E_{2g}{}^1$ (in-plane vibration of Mo and S atoms) at ~380 and 405 cm^{-1}, respectively. In addition, an investigation of the A_{1g} - $E_{2g}{}^1$ frequency difference leads to a further clarification regarding the number of MoS_2 layers. It is interesting to note that the frequency difference of the as prepared MoS_2 (restacked from dispersion) is 25.1 cm^{-1}, proposes the thickness of MoS_2 film in the present work as ~5 layers (Plechinger et al., 2012). The Raman spectrum of MoS_2-Hg exhibits two major trends, as shown in Figure 5.8D (inset); i.e. after the Hg incorporation, a red shift of both the $E_{2g}{}^1$ and the A_{1g} mode was observed. The $E_{2g}{}^1$ mode represents the in-plane lattice vibration with the two S layers moving in the same direction collectively, opposed to the Mo movement. The metal has a very large dielectric constant and enhances the screening of the electron-electron interactions, thus weakening the planar inter-ionic interactions (Anandhakumar et al., 2012). The softening of the in-plane phonon mode causes the red shift of the $E_{2g}{}^1$ mode. So the red shift of $E_{2g}{}^1$ mode by 3.1 cm^{-1} can be ascribed to the result of in-plane strain introduced by S-Hg interactions in MoS_2-Hg. Similarly, the A_{1g} mode represents the out-of-plane lattice vibration with S atoms on both sides of Mo atoms moving in opposite directions. The red shift (2 cm^{-1}) in the A_{1g} mode of MoS_2-Hg indicates the tensile strain introduced by metal deposition (Yuan et al., 2015).

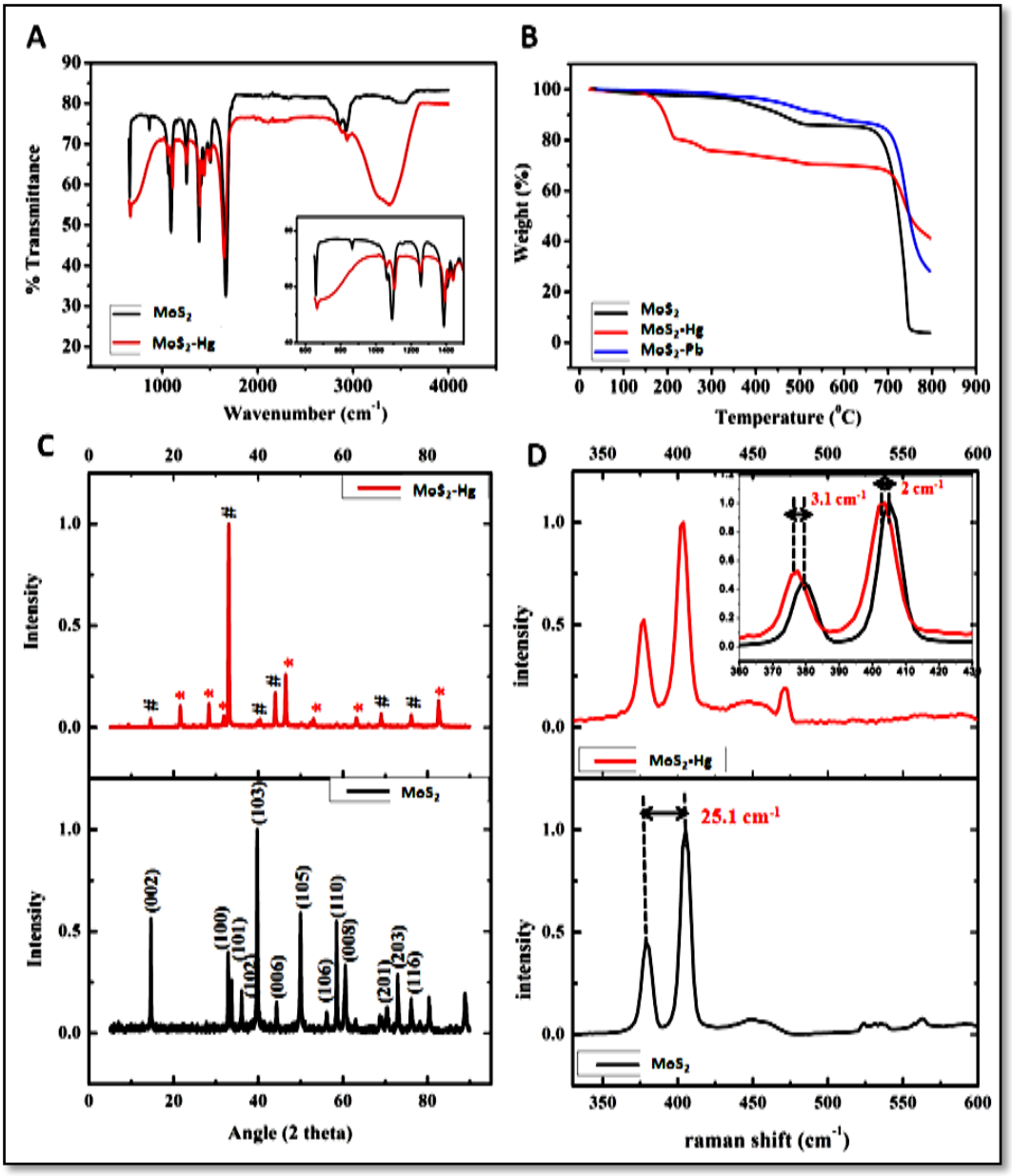

Figure. 5.8. Characterization results of MoS_2-Hg which shows S-Hg interactions: (A): FT-IR spectra (B): TGA plot (C): XRD and (D): Raman spectra of MoS_2 (restacked) and MoS_2-Hg (Inset plot shows the shift of characteristic E_{2g}^1 and A_{1g} bands of vibrations in MoS_2-Hg from MoS_2).

Castellanos-Gomez et al. studied the localized uniaxial strain influence on few-layered MoS_2 using Raman spectroscopy (Castellanos-Gomez et al., 2013) and observed that in few-layered (3~5 layers) MoS_2, both E_{2g}^1 and A_{1g} modes red-shifted with strain, and the shifts in E_{2g}^1 mode are larger, about 1.7 cm^{-1} per 1% strain. Therefore from the Raman results, it is clear that the strain inducing the

shifting of characteristic vibrational modes of MoS_2 in the MoS_2-Hg are undoubtedly arising from the S-Hg interactions. Thus, the results confirm the presence of the specific interactions of S^{2-} of MoS_2 and Hg^{2+}.

The XPS analysis of MoS_2-Hg further confirms the reduction of Hg^{2+} over the MoS_2 surface. While the XPS survey spectrum of the (exfoliated) MoS_2 shows only the Mo and S peaks, the survey spectrum of MoS_2-Hg (Figure 5.9A) displays the peaks of Mo, S and Hg, with the peaks of Hg correspond to the Hg 4f, Hg 4d and Hg 4p. The high-resolution XPS spectra of Mo (Figure 5.9B) in MoS_2-Hg displays two characteristic peaks of Mo $3d_{3/2}$ and Mo $3d_{5/2}$ centered at 232.5 and 229.3 eV, respectively, with a shift from those of the MoS_2 (232.25 and 229.05). The high resolution spectrum of S 2p (Figure 5.9C) of MoS_2-Hg shows peaks at 163.3 and 162.1 eV and are attributed to the S $2p_{1/2}$ and S $2p_{3/2}$ components, while that of MoS_2 are observed at lower binding energies (BE) (162.85 and 161.85). According to the literature (Smart et al., 1999), an increase in BE means increase in the oxidation number of the species, BE up to 163.2 eV are assigned to S^{2-} and above which are due to S^0, and hence the peak at 163. 3 eV of S 2p in the MoS_2-Hg is attributed to the presence of S^0 species (Hampton et al., 2011; Smart et al., 1999). Moreover, a peak belonging to S 2s that is clearly observed in the survey spectrum (Figure 5.9A) of MoS_2-Hg is absent in that of the MoS_2, and in the high resolution spectrum, an additional shoulder peak of S 2s with a slight higher BE was observed for MoS_2-Hg which was absent in MoS_2 (Figure 5.9B).

These results suggest the presence of higher oxidation state S in MoS_2-Hg compared to that of in MoS_2. Similarly, the high resolution spectrum of Hg in MoS_2-Hg, reveals the characteristic Hg 4f peaks at 101.2 and 105.2 eV (Figure 5.9D) corresponding to the Hg $4f_{7/2}$ and $4f_{5/2}$, respectively, which indicate the existence of Hg^0 (Zhi et al., 2016). Thus the results are clearly evident of the reduction of Hg^{2+} to Hg^0 by MoS_2. The schematic diagram shows the interactions of Hg^{2+} with MoS_2 is depicted in Figure 5.10. As mentioned earlier, MoS_2/GCE did not require a separate pre-reduction step prior to achieving the Hg^0 to Hg^{2+}

oxidation, as the S^{2-} anions in the MoS_2 itself act as the reducer to achieve Hg^0 accumulation; which is illustrated in the scheme. On the surface of MoS_2/GCE, the Hg^{2+} in contact with S^{2-} ions will undergo reduction to give Hg^0 which on EC application of potential results in the corresponding redox peaks.

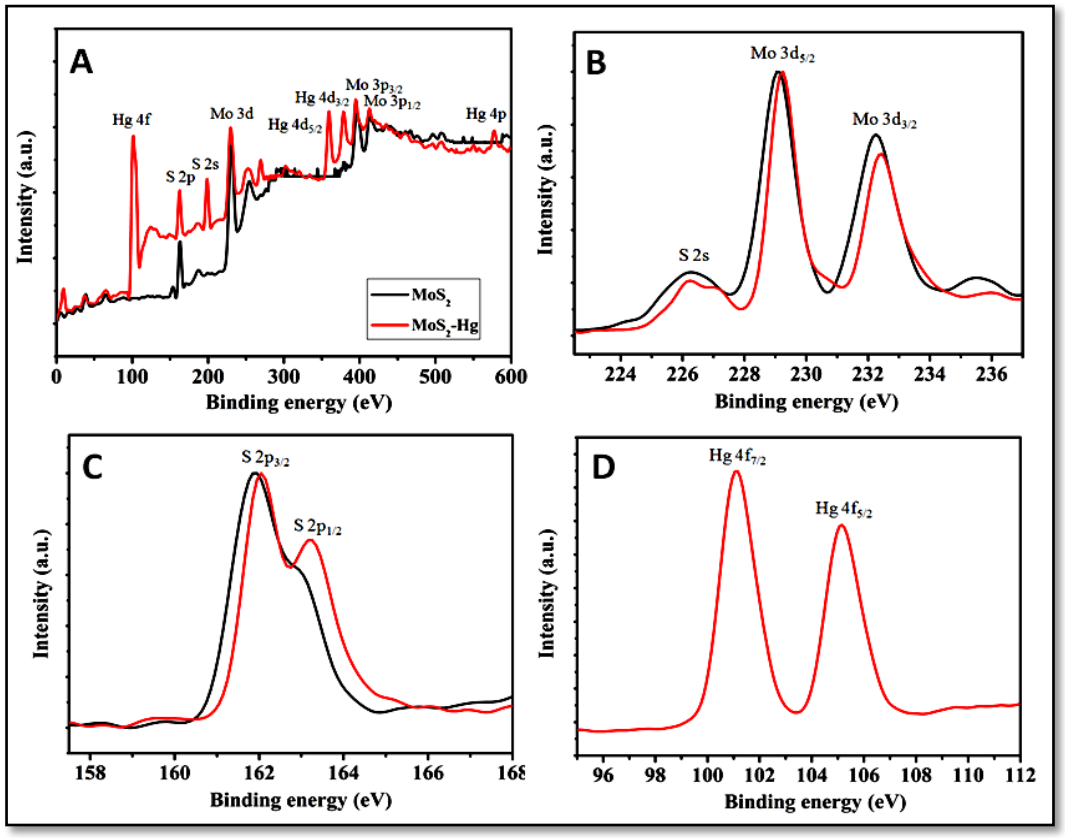

Figure. 5.9 (A): XPS survey spectrum of MoS_2 and MoS_2-Hg and high-resolution scans of (B): Mo 3d in MoS_2 and MoS_2-Hg, (C): S 2p in MoS_2 and MoS_2-Hg and (D): Hg 4f in MoS_2-Hg.

5.3.4. Determination of LOD and selectivity of MoS_2/GCE after pre-concentration

The LOD of 0.001 nM obtained by MoS_2 was without a pre-deposition procedure; however the reported LOD's in most of the literature are after pre-deposition step. Therefore, for comparison purpose, the LOD of MoS_2/GCE for Hg^{2+} was determined after the pre-deposition step. The pre-concentration was done at 0.005V for 5 minutes using the chronoamperometric method.

Interestingly, the LOD obtained after the pre-deposition step was ≤ 0.000001 nM and was 10^3 times lower than that obtained without the pre-reduction (Figure 5.11). The obtained LOD is in ppq level (0.2 ppq) and is equivalent to 0.0002 ng/L, which is indeed the lowest ever reported LOD for Hg^{2+} determination. The same procedure was repeated for interference studies to see whether the pre-concentration influences the current response of the other metal ions. The result obtained showed no significant change in the current response of other ions.

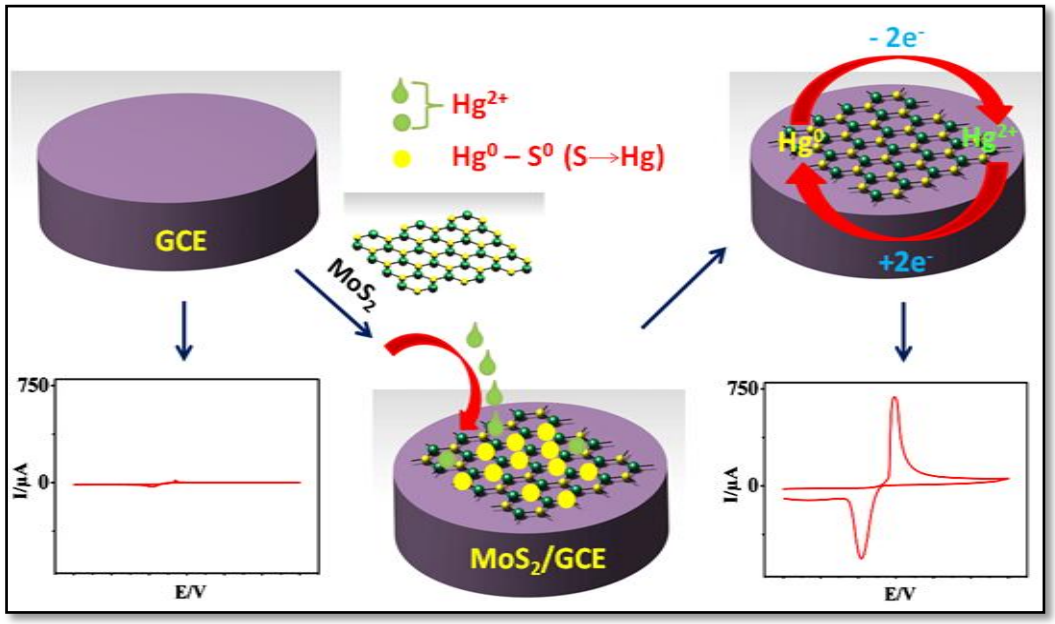

Figure 5.10. The schematic diagram showing the direct electrochemistry of Hg^{2+} at the MoS_2 modified GCE and the corresponding enhancement in the current response in CV.

The LOD values obtained for various modified electrodes using substrate like GCE, ITO, Au etc. which include Au-poly(3,4-ethylenedioxythiophene (Anandhakumar et al., 2012), chitosan modified carbon paste electrode (Marcolino-Junior et al., 2007), multiwalled carbon nanotubes (H. Yi, 2003), AuNP (Abollino et al., 2008), α-MnO_2 nanocrystals (Q.-X. Zhang et al., 2013), α- and β- cyclodextrins (Roa-Morales et al., 2005), SnO_2/rGO Nanocomposite (Wei et al., 2011) etc. are given in Table 5.1 along with our result (Aswathi & Sandhya, 2018) and the values demonstrate the merit of MoS_2 as an Hg^{2+} sensor. In addition, various DNA/Gr-DNA/oligonucleotide probe based Hg^{2+} sensors were reported with good LODs (D. Wu et al., 2010; Y. Zhang et al., 2013; Z.

Zhang et al., 2011; Zhuang et al., 2013), where a different approach like target-induced structure-switching was utilized. Other examples include DNA-based detection of Hg^{2+} with α-Hemolysin Nanopore (S. Wen et al., 2011), trace Hg^{2+} detection via induced circular dichroism of DNA-single-walled carbon nanotubes (X. Gao et al., 2008) etc. The previous lowest LOD attained by an electrode according to the literature is 0.15 ng/L which is equivalent to 0.00075 nM (Abollino et al., 2008) while the LOD of MoS_2 is 0.0002 ng/L which is equal to 0.000001 nM (0.2 ppq), and is the best reported, so far.

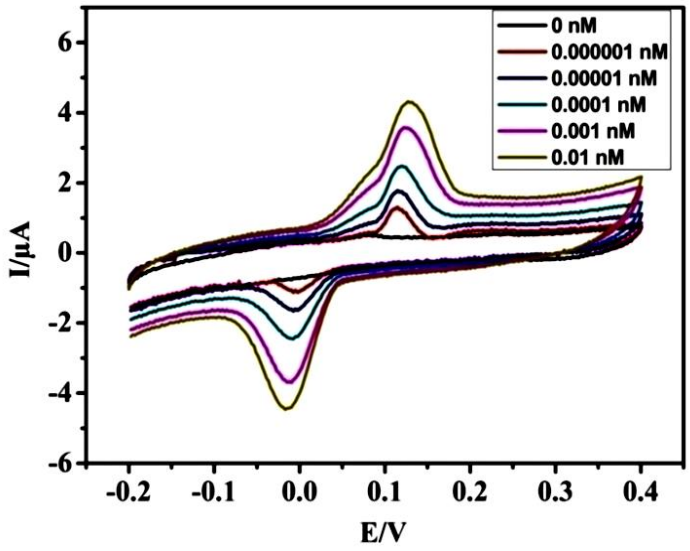

Figure 5.11. CV curves showing the LOD of MoS_2/GCE up to 10^{-6} nM after the pre-concentration step.

5.3.5. Reusability, reproducibility and stability of MoS_2/GCE

For a sensing electrode, reusability and reproducibility makes the whole process simple and cost-effective and hence are important. Stronger the interaction between the analyte and the substrate electrode, the reusability of the electrode gets affected, which is clearly evident in Au substrate for Hg sensing (Kanchana et al., 2015). The reusability and the storage stability were evaluated immediately after washing, and after a period of 1 month, respectively. Immediate reuse of the electrode after washing and the 30-day storage period, showed 99.6 and 88 % retention in the responses (Figure 5.12A and B), respectively. The result

demonstrates the remarkable reusability and stability of the sensor. The % RSD of the measurements from five independently prepared electrodes was 3.6% for 1 mM Hg^{2+}, indicating reproducibility of the electrode.

5.3.6. Sensing of Hg^{2+} in saline water samples

The Hg^{2+} concentrations found in non-anthropogenic sea waters are extremely low, about 10^{-11} M (2 ng/L). Therefore it is of great importance to have a sensing electrode of very high sensitivity and selectivity which can perform accurate analyses of Hg^{2+} in sea water samples (Gustavsson, 1986). There are numerous methods for the determination of Hg although very few are able to detect Hg^{2+} at the ppm to ppb levels in seawater (De Marco & Shackleton, 1999). First, the sensing studies were carried out in 0.6 M NaCl solution and the results are depicted in Figure 5.13A. Other than a shift in the peak potential and increase in the broadness of the redox peak, no change was observed in the current response in the saline medium when compared to that of the pure water. The slight shift in the peak positions observed may be due to the change in the amount of ions and pH in the electrolyte solution (1M HCl to 0.6 M NaCl). The result is evident of the ability of MoS_2/GCE to detect Hg^{2+} in saline water environment.

5.3.7. Sensing in real water samples

Inspired by the sensing results of MoS_2 in saline water, the sensing studies were extended to real water samples such as sea and tap water. The sea water samples (collected from the Arabian Sea near to Thiruvananthapuram) were spiked with Hg^{2+} at different concentration levels, analyzed with the proposed method and the recovery amounts were calculated. The recovery calculated was found to be in the range of 100.2–102.4%, which shows the excellent applicability of MoS_2/GCE in sea water (SW) sensing of Hg^{2+}. Further, tap water samples were evaluated using the same method. The recovery amounts calculated were ranging from 100.7–102.9 %. Both the measurements are summarized in Table 5.2; the CV responses are given in Figure 5.12C&D.

Table 5.1. Comparison of the LDR and LOD of MoS_2/GCE with the literature reports for Hg^{2+} sensing.

Electrode	LDR	LOD of Hg^{2+} (nM)	Reference
Hydroxyapatite (HA) nanoparticles /GCE)	0.2 - 210 µM	141 *	(Kanchana et al., 2015)
AuNPs-chi-graphene/GCE	0.025 -60 ppb	0.03 (6 ppt)	(Gong et al., 2010)
Gold-poly(3,4) ethylenedioxythiophene (Au-PEDOT)/ carbon paste electrode	10 -70 µM	0.005	(Anandhakumar et al., 2012)
chitosan modified carbon paste electrode	0.99 – 38.5 µM	628	(Marcolino-Junior et al., 2007)
multi-walled CNTs (MWCNT)/GCE	0.8 nM – 0.5 µM	0.2	(H. Yi, 2003)
AuNPs/GCE	0.01 to 50 µg/L	0.00075 (0.15 ng/L)	(Abollino et al., 2008)
carbon paste electrodes modified with β-CDs	0.2 - 4 µM	51	(Roa-Morales et al., 2005)
SnO_2/rGO Nanocomposite/GCE	0.2 - 0.6 µM	0.034	(Wei et al., 2011)
MoS_2/GCE (Our Result)	0.1 nM - 0.2 mM	With P.C : 0.000001 (0. 2 ppq) Without P.C : 0.001	Our result (Aswathi & Sandhya, 2018)

* The value is without the pre-reduction step. Except ref. (Kanchana et al., 2015) all other values are after pre-reduction step. The LOD for MoS_2 without pre-reduction was 0.001 nM, much lower than that of ref. (Kanchana et al., 2015). (P.C- Pre-concentration/pre-reduction)

The near to 100% recovery values indicate the successful applicability of the electrode for the determination of Hg in real water samples. In addition to the spiking and recovery analysis, the SW as such was taken as the electrolyte and the sensing studies were carried out by adding Hg^{2+} using two different SW samples collected from different localities. The current responses of Hg^{2+} in the SW samples (Figure 5.13B) matched with the original results, though the peak positions showed slight shifts, which may be due to the pH changes or to the complex environment due to the presence of different compounds in the sea

water. Interestingly, the same LOD value (0.001 nM) was obtained in SW (inset Figure 5.13B). The result is an indicative of the sensitivity and selectivity of the electrode towards Hg^{2+} sensing in complex environmental water samples where the presence of different organic compounds or species will make the sensing usually difficult. Notably, no other literature report has demonstrated the applicability of the electrodes in sea water for the sensing of Hg^{2+}.

Table 5.2. Determination and recovery test results of Hg^{2+} in real water samples

Sample number	Hg^{2+} spiked (µM)	Hg^{2+} found (µM)		Recovery (%)
1	0.5	Sea water	0.501	100.20
		Tap water	0.504	100.73
2	1	Sea water	1.018	101.80
		Tap water	1.015	101.50
3	2	Sea water	2.048	102.40
		Tap water	2.058	102.90

Further to verify the applicability of the MoS_2 sensor in the real environmental conditions, the studies have been extended to different pH and temperature conditions. For pH studies, 0.1 M PBS buffer was chosen as the electrolyte, to keep the pH stable during the experiments. The studies show the variations in the current response with pH from 3-11 (Figure 5.14A), it can be seen that there is a measurable current response at all pH values in the studied electrolyte conditions.

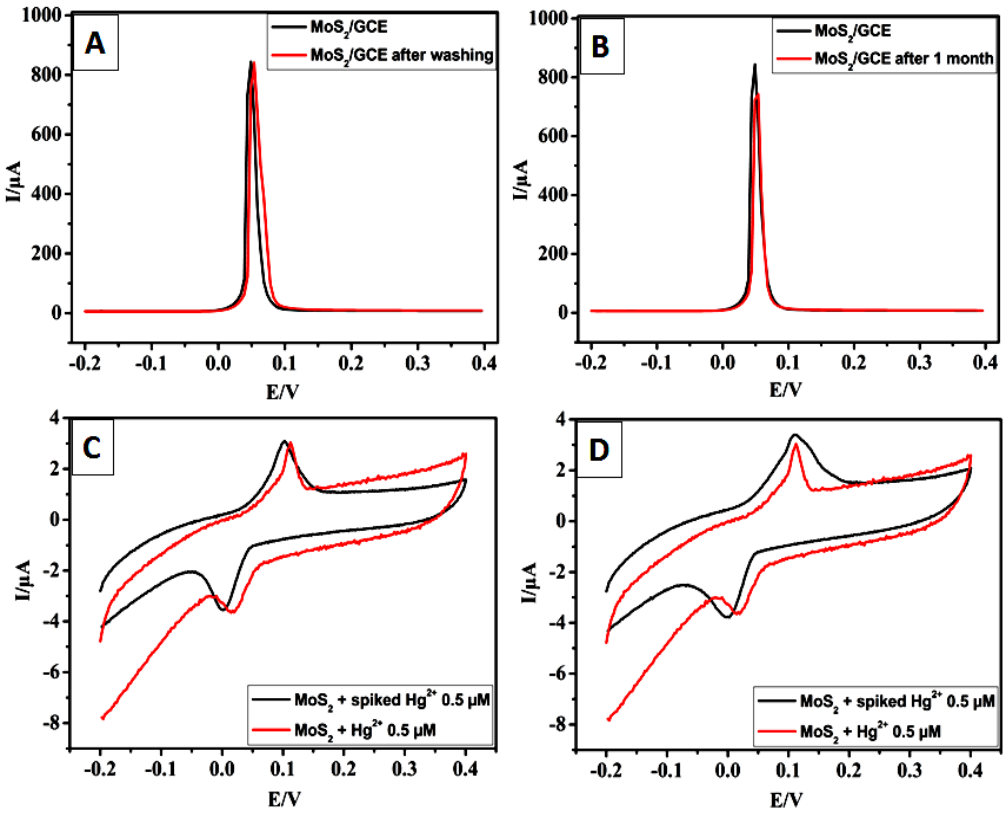

Figure 5.12. DPV profiles revealing (A): the reusability; and (B): stability after 1 month of MoS_2/GCE; (C) and (D): CV profiles at MoS_2/GCE comparing the response of Hg^{2+} in pure sample and (C): sea water and (D): tap water samples spiked with Hg^{2+}, respectively, showing similar current responses.

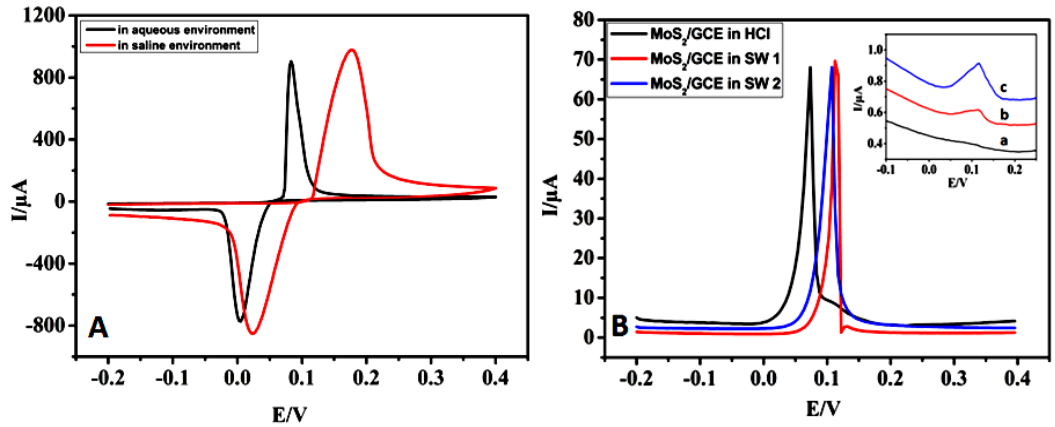

Figure 5.13. (A): Comparison of CV responses of MoS_2/GCE for Hg^{2+} sensing in aqueous and saline medium. (B): DPV response of MoS_2/GCE in 1 M HCl, SW1 and SW2, each containing 20 µL of Hg^{2+}. Inset figure shows the DPV response of MoS_2/GCE in SW environment (a) in the absence and (b) & (c) in the presence of 0.001 nM and 0.002 nM Hg^{2+}, respectively.

Similarly, the response of MoS_2/GCE for different temperatures of testing solution (5-50^{0}C) was recorded. The current response was observed even at temperature as low as 5^{0}C and it increased from 5 to 20^{0}C with a higher slope and the increase was mild beyond 20^{0}C (Figure 5.14B). The current increase observed with the increase in the temperature shall be ascribed to the increase in the reaction rate with temperature and due to the increase in the mobility of ions. Thus, the results show that the sensing of Hg^{2+} by MoS_2 is feasible at all pH and at temperature as low as 5^{0}C and at higher temperature of 50 ^{0}C and beyond, thus showing its applicability in the environmental conditions. Therefore, Considering the remarkable selectivity, the lowest LOD (in ppq) and the successful applicability in real water samples and real environmental conditions, MoS_2 stands out as an electrode for Hg^{2+} sensing.

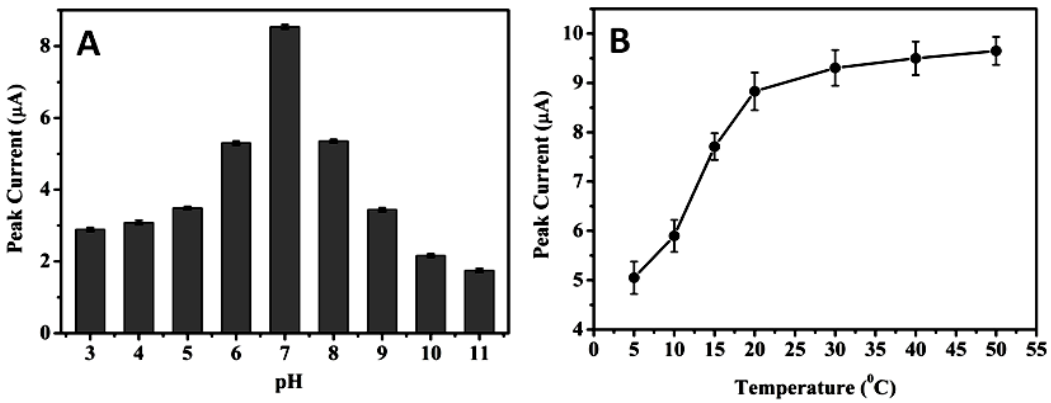

Figure 5.14. The dependence of Hg^{2+} oxidation peak current (by MoS_2/GCE) on (A): buffer pH and (B): Temperature of the electrolyte solution

5.4. Conclusions

Here in this work, , for the first time, the merits of solvent exfoliated MoS_2 for EC sensing of Hg^{2+} was successfully demonstrated and interestingly it can detect up to ppq (10^{-15} M) level and in addition, has excellent selectivity for Hg^{2+}. Moreover, MoS_2/GCE was able to detect Hg^{2+} in environmental water

samples. The reason for the remarkable selectivity and sensitivity was assigned to the affinity between the S^{2-} groups of MoS_2 and Hg^{2+} and the spontaneous redox reactions which were confirmed by various characterization techniques. The preparation of the electrode is simple as it involves only a solvent exfoliation step via ultrasonication, and is environmentally benign. Moreover, the electrode exhibits excellent reusability, reproducibility and stability. Thus, in this work, a simple and cost-effective electrode for the sensing of Hg^{2+} is reported, which according to the results is indeed a promising electrode for detecting Hg^{2+} ions in complex environmental samples which can be extended to sea water.

CHAPTER 6

POLYANILINE DERIVED NITROGEN-DOPED GRAPHENE QUANTUM DOTS FOR THE ULTRA TRACE LEVEL ELECTROCHEMICAL DETECTION OF TRINITROPHENOL AND THE EFFECTIVE DIFFERENTIATION OF NITROAROMATICS: STRUCTURE MATTERS

This chapter discusses a novel method of synthesis of nitrogen doped graphene quantum dots (N-GQD) from polyaniline (PANI) and its EC sensing applications. The prepared N-GQD has been characterized thoroughly using various characterization techniques which include FT-IR, UV-Visible, HRTEM, SEM-Mapping, XRD, XPS etc. The EC sensing property of N-GQD was evaluated by taking nitroaromatics as the analytes. The N-GQD modified electrode demonstrates unparalleled EC sensing properties towards nitroaromatics and greater sensitivity towards trinitrophenol (TNP). It effectively distinguishes between different nitroaromatics and extends the remarkable sensing property in real water samples as well. The possible structure of N-GQD was proposed and the reasons behind its exceptional EC sensing property were evaluated and discussed.

6.1. Introduction

In recent years, GQDs, the luminescent nano-materials consisting of Gr sheets of lateral dimensions less than 100 nm, have ignited tremendous research interest (Dong, Li, et al., 2012; L. Fan et al., 2012; H. Sun, L. Wu, et al., 2013; Van Tam et al., 2014; F. Wang et al., 2014) due to the extraordinary chemical/physical properties such as high specific SA, good electrical

conductivity, high mobility, strong and tunable PL, slow hot-carrier relaxation and good dispersion in various solvents (Z. Li et al., 2015; W. Liu et al., 2013; Razmi & Mohammad-Rezaei, 2013). In addition, the unique and combination of properties such as low cytotoxicity, bio-compatibility, stable and tunable PL, tunable properties by pronounced quantum confinement, edge effects, doping etc. along with the catalytic, conductivity, and better surface grafting properties, make them highly promising materials for the construction of various novel devices such as bio-imaging devices (S. Zhu et al., 2011), biosensors (Razmi & Mohammad-Rezaei, 2013; J. Zhao et al., 2011), photovoltaic devices (Y. Li et al., 2011), fuel cells and light-emitting diodes (Y. Li et al., 2012; Libin Tang et al., 2012). Recently, it was observed that heteroatom doping of GQD is highly effective in modulating its band gap to achieve new properties for device applications (Y. Li et al., 2009; H. Liu et al., 2011). The presence of heteroatom such as nitrogen (N) in GQD's lattice can significantly modulate the chemical and electronic properties and offer more active sites, thus leading to unexpected and better properties which could be applied in various fields (Y. Li et al., 2009; H. Liu et al., 2011).

N-GQDs were synthesized through hydrothermal or EC strategies which are based on breaking/cutting down of carbon (nano) materials such as graphite (M. Zhang et al., 2012), GO (L. L. Li et al., 2012; Pan et al., 2010; J. Shen et al., 2011), Gr film (Y. Li et al., 2011; Zhuo et al., 2012), carbon nanotubes (Minati et al., 2012), amorphous carbons (Dong, Chen, et al., 2012; Peng et al., 2012) fullerene (J. Lu et al., 2011) and biomass (Z. Wang et al., 2016) in the presence of N-containing molecules/N-precursor. The procedure with GO or allied materials (ref. given above whichever is applicable), requires lots of strong chemical acid, oxidant and water for washing (Van Tam et al., 2014). Moreover, the N-doping in the aromatic lattice would result in an N-GQD with defects in the aromatic structure due to N-doping and with lower percent of lattice N-doping due to the stability of aromatic structure. The bottom-up methods, had been from biomolecules such as, CD (Mohamed Mukthar Ali & Sandhya, 2017), glucose (Libin Tang et al., 2012), citric acid (Dong et al., 2013; Dong, Shao, et al., 2012)

etc, which are aliphatic in nature, in the presence of N-precursors; for example, citric acid in the presence of dicyandiamide (Ju et al., 2014), GO in presence of ammonia (C. Hu et al., 2013), GQD with hydrazine (Ju & Chen, 2014) and strong acid treatment of N-doped Gr (M. Li et al., 2012).

Herein, we report a new and simple fool-proof approach for obtaining a better N-doped GQD, in terms of aromatic structure and percent N-doping. With this in mind, we chose polyaniline (PANI), which is a N containing organic polymer as the precursor, and synthesized N-GQD using hydrothermal method (Lin et al., 2015) and further have explored the possibilities of the N-GQD as an EC sensor for nitrocompounds. In this method, the N containing aromatic species formed during the hydrothermal treatment of PANI was expected to undergo ring closure to form N-containing pyridinic structure, thus forming an almost perfect N-GQD, with N in the aromatic lattice. In addition to the effective N-doping, this approach thus can yield N-GQD, with pyridinic, pyrrolic and graphitic N rings, which are aromatic in nature and thus is expected to influence and enhance its electronic and hence the sensing properties significantly (The possible structure of N-GQD is given in the discussion part, see Figure 6.5).

The heteroatom doping in GQD was found to be effective for achieving the properties which favour the EC sensing applications such as selectivity and efficiency, as it can effectually tune the physical and chemical properties of the GQD (Cai et al., 2015). Owing to the structural similarities and the properties arising from the *insitu* N-doping, the N-GQD from PANI was investigated as an EC sensor for the detection of nitroaromatic compounds. Nitroaromatics/ Nitrophenols, are widely used in the production of dyes, pesticides, pharmaceuticals, explosives, forensic investigations, military industries etc., and can accumulate in natural waters over the long-term, during their testing, usage, storage, and dumping (Rong et al., 2015). They contaminate the environment extensively, including soil and water bodies such as lakes, rivers, ground water etc. (Z. Li et al., 2015). Of this, 2, 4, 6-trinitrophenol (TNP) is particularly important, because it is an environmentally deleterious substance and is an

intermediate in the manufacture of explosives. TNP with the phenolic and nitro functionalities is poorly biodegradable, explosive and toxic, and can cause health problems for humans, such as skin irritation, anaemia, abnormal liver functioning and damage to respiratory organs on inhaling, and can be absorbed through skin. It has been recognized as an environmental contaminant and a human carcinogen (Lin et al., 2015). Being an explosive component and a contaminant, detection of TNP is crucial and hence demands a field-portable tool capable of sensitive and selective detection in a faster, simpler, and reliable manner. Therefore, we have investigated the PANI derived N-GQD, for the aforementioned reasons, as an EC sensing platform for the selective and sensitive detection of TNP. To the best of our knowledge, this is the first time report of the synthesis of N-GQD from an *insitu* N containing aromatic carbon source and the EC sensing of TNP using N-GQD. Previous reports of EC determination of TNP/picrates have been mainly using ion-selective electrodes (Hadjiioannou & Diamandis, 1977) based on the classical ion exchange, their inherent selectivity pattern might cause interference problems from lipophilic anions, which is a limitation of the method (X.-G. Wang & Fan, 2009); or surfactant (cetyl pyridinium chloride) modified electrodes (X.-G. Wang & Fan, 2009) which possess impracticability in terms of the sensitivity, reproducibility and stability. Recent reports on the EC sensing of TNP based on the metal ion/NP based materials and/or metal based electrodes such as N- doped rGO and copper sulfide NPs sensor (Giribabu et al., 2016) suffers from a poor sensitivity; bulk bismuth based TNP sensor (Prchal et al., 2010) causes radioactive and toxic issues and thus can cause serious environmental pollution; polished Ag solid amalgam composite electrode (Vyskočil et al., 2011) has the disadvantage of Hg contamination; copper electrode (Junqueira et al., 2013) and Au microelectrode (J. Huang et al., 2014), both of which have poor LOD. Mahyari et al. fabricated a Pt NPs-rGO nanocomposite modified electrode (Mahyari, 2016), Pt being a noble metal, leads to a relatively higher cost. A recent report of a TNP sensor (Yong Wang et al., 2018) based on copper (II) electrodeposited on electroreduced graphene oxide (ERGO) placed on GCE has a LOD in micromolar concentration (0.1 μM). Therefore, it is imperative to explore a low-cost, simple, and sensitive EC sensing platform for the TNP detection. The

N-GQD reported herein was investigated for its EC sensing properties and was found to effectively detect TNP with the lowest LOD value of 0.2 ppb, and in addition was able to distinguish between different nitroaromatics such as TNP, 2,4-dinitrophenol (DNP), 4- nitrophenol (NP) and 2,4-dinitrotoluene (DNT) (2,4,6-Trinitrotoluene (TNT) was not tested due to its unavailability). Further, the N-GQD electrode demonstrated excellent reproducibility and stability properties and extended the sensing to real water samples.

6.2. Experimental

6.2.1. Synthesis of PANI

PANI was prepared by an interfacial polymerization procedure as reported elsewhere (Jiaxing Huang & Kaner, 2004) with modifications. Typically the interfacial reaction was performed in a 50 mL beaker in which 3 ml of aniline was dissolved in the organic phase (10 mL) chloroform. APS (1.5 g) was dissolved in 10 mL of 1 M HCl solution and added to the organic phase containing aniline keeping the temperature below 20 ^{0}C. After mixing, the beaker was kept at RT for about 12 hrs, for the polymerization reaction to complete. The product was filtered using millipore filtration and washed well with distilled water until it became neutral. The obtained PANI was dried in an air oven at 70^{0}C overnight.

6.2.2. Synthesis of N-GQD

N-GQD was prepared by a simple hydrothermal route using PANI as the source material, as follows: In a typical synthesis, 50 mg of the above prepared PANI was dispersed in 10 ml distilled water by ultrasonication for 1 hr. Then 2 drops of NaOH (2M) was added to the dispersion and was transferred into a 20 ml teflon lined autoclave and kept at 220°C for 12 hours. Afterthat, the solution was naturally brought down to RT and subsequently the supernatant light wine coloured liquid containing N-GQD was collected and the unreacted PANI at the

bottom was discarded. The solution was diluted 2 times for characterizations and EC sensing studies.

6.2.3. Preparation of electrodes for sensing and EC methods

Prior to modification of GCEs with the samples, they were mechanically polished with a wetted microcloth containing alumina powder, and then carefully cleaned in distilled water by ultra-sonication (2 minutes). After each analysis, GCEs were polished as described above and cleaned by ultrasonicating in distilled water and then in acetone. The N-GQD sample was drop casted over the cleaned GCE carefully and then allowed to dry for 24 hours at RT. The EC behaviors of TNP, DNP, NP, DNT etc. (in 0.1 M PBS) were investigated by CVand DPV at RT. For DPV studies, an optimized scan rate of 50 mV/s and pulse amplitude of 25 mV was opted. For making the electrodes, 20 μL of N-GQD solution (after 2 times dilution) was drop cast on to a GCE.

6.3. Results and Discussion

6.3.1. Synthesis and formation of N-GQD

The synthesis of N-GQD was done, as described in the experimental part, using a single precursor (PANI) which contains insitu N, by a facile and simple hydrothermal approach. The approach, as mentioned previously, is expected to deliver a N-GQD with higher N content and a better (N-containing) aromatic structure which might positively influence the electronic property of the N-GQD. The schematic of the synthesis of N-GQD is illustrated in Figure 6.1. The formation of GQD was analyzed by the HRTEM (Figure 6.2), the uniform sized nano dots in the TEM images confirm the formation of GQD from PANI.

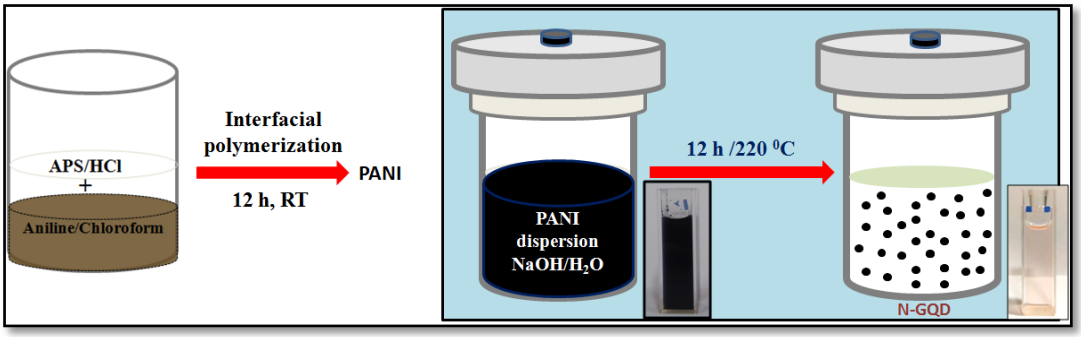

Figure 6.1. Schematic of the synthesis of N-GQD as described.

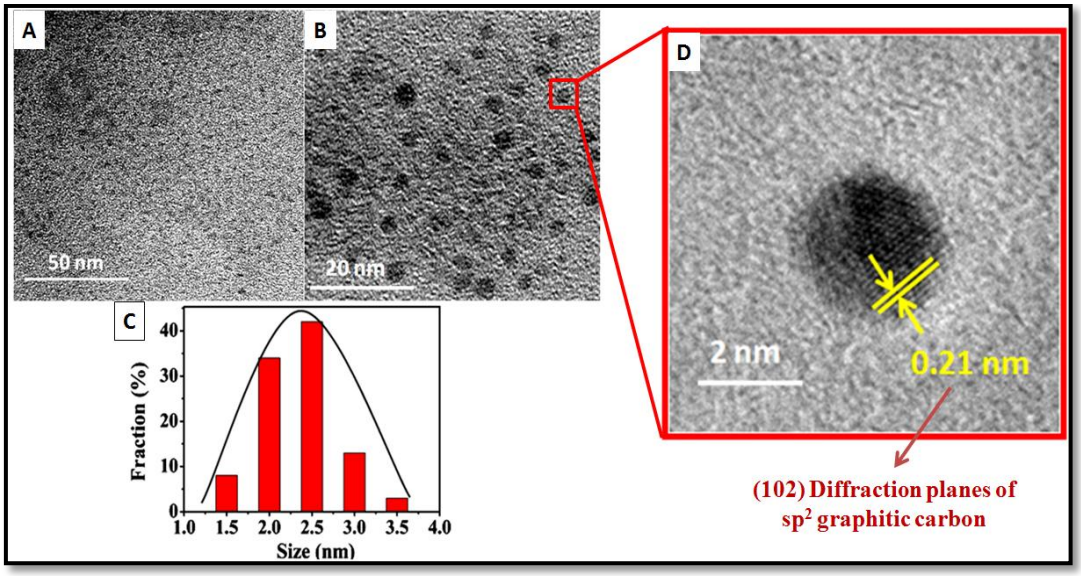

Figure 6.2. (A) and (B): The HRTEM images of the synthesized N-GQD. (C): the size distribution of the synthesized N-GQD as obtained from HRTEM. (D): HRTEM image revealing the crystallinity of N-GQD.

6.3.2. Structure, size and the properties of N-GQD

The TEM images of the as-synthesized N-GQD confirm that they have a fairly uniform and narrow size distribution (Figure 6.2A and B) ranging from 2 to 3 nm. (Figure 6.2C). The high-resolution image shows a round shape for the N-GQD, with visible crystalline lattice fringes (Figure 6.2D) having an interlayer spacing of 0.21 nm which corresponds to the (102) diffraction planes of sp^2 graphitic carbon (H. Sun, N. Gao, et al., 2013), which indicates the crystalline nature of GQD. Further it was characterized by FTIR, XPS, XRD, SEM-elemental

mapping and EDAX to confirm the N-doping and the nature and degree of N in N-GQD and the crystalline nature.

The FTIR spectra of N-GQD and PANI are given in Figure 6.3A. In the spectrum of PANI, the peaks at 3435 cm^{-1} (N-H stretching), 2860 cm^{-1}, 2925 cm^{-1} (C–H stretching), 1595 cm^{-1} (C-C stretching of benzenoid ring), 1494 cm^{-1} (C-C stretching of quinonoid ring), 1404 cm^{-1}, 1451 cm^{-1} (C=C stretching), 1080 cm^{-1} (C-N stretching) and 825 cm^{-1} (C-H out of plane bending), agrees to that of reported for PANI in the literature (Alam et al., 2013). In N-GQD, a broad band was observed near 3400 cm^{-1} which has a shoulder, is assigned to the -N-H stretching vibrations (along with –O-H stretching) and the aromatic –C-H stretching, respectively. The presence of the stretching vibrations of -NH (near 3400 cm^{-1}) and C-NH- C at 1350 cm^{-1} along with C-N in plane bending vibration at 1020 cm^{-1} confirmed the N-doping in N-GQD. The peak at around 1564 cm^{-1}, can be assigned to sp^2 bonded C–N. In addition, the vibration peaks at 1645 cm^{-1}, 1786 cm^{-1}, 1411 cm^{-1}, 2815 cm^{-1} and 1120 cm^{-1} could be ascribed to C=O vibration (aromatic), C=C stretching (aromatic), -COO vibration C-H stretching and -C-OH stretching, which confirms the aromatic C-ring structure of N-GQD with edge hydrophilic functional groups. The presence of –NH and –C-N peaks along with the aromatic –C=C- suggests the retention of PANI aromatic ring structure (Figure 6.5) in the N-GQD and indicates the presence of N in the lattice.

The XRD pattern of the N-GQD (Figure 6.3B) revealed rather sharp peaks indicative of the crystalline nature of the N-GQD, at around $2\theta = 23.5^{\circ}$, 43° and 44° corresponding to the reflections of graphitic planes (002), (100) and (101), respectively (Gavrilov et al., 2012; Z. Zhou et al., 2014). The sharp peaks and the d-spacing values (Figure 6.3B) confirm the presence of nearly perfect Gr skeleton which shall be assigned to the N-precursor, PANI. The XPS analysis was carried out to understand the structure of N-GQD mainly in terms of the degree and configuration of N-doping. Figure 6.3C depicts the survey scan spectrum of the N-GQD, which revealed the C1s peak at ~284.5 eV, O1s peak at ~530.5 eV and a pronounced N1s peak at ~400.5 eV, which confirms the presence of N in the

N-GQD. Figure 6.3D shows the high resolution N1s spectrum which gives more detailed information about N functional groups present in the N-GQD. The deconvolution of the N1s peak indicates the presence of pyridinic (~398.7 eV), pyrrolic (~400.2 eV) graphitic (~400.7 eV) and oxidised pyridinic (~402.3 eV) N species, with comparatively higher proportion of graphitic-N, which agrees to the proposed structure of N-GQD in Figure 6.5. The high-resolution C1s spectrum of the N-GQD (Figure 6.3E) revealed the presence of C-C/C=C (284.7 eV), C-O (286.4 eV), C=O (287.9 eV) and O-C=O (290 eV) functional groups (Lin et al., 2015). The high intensity peak at 284.7 eV can be ascribed to the graphitic carbon.

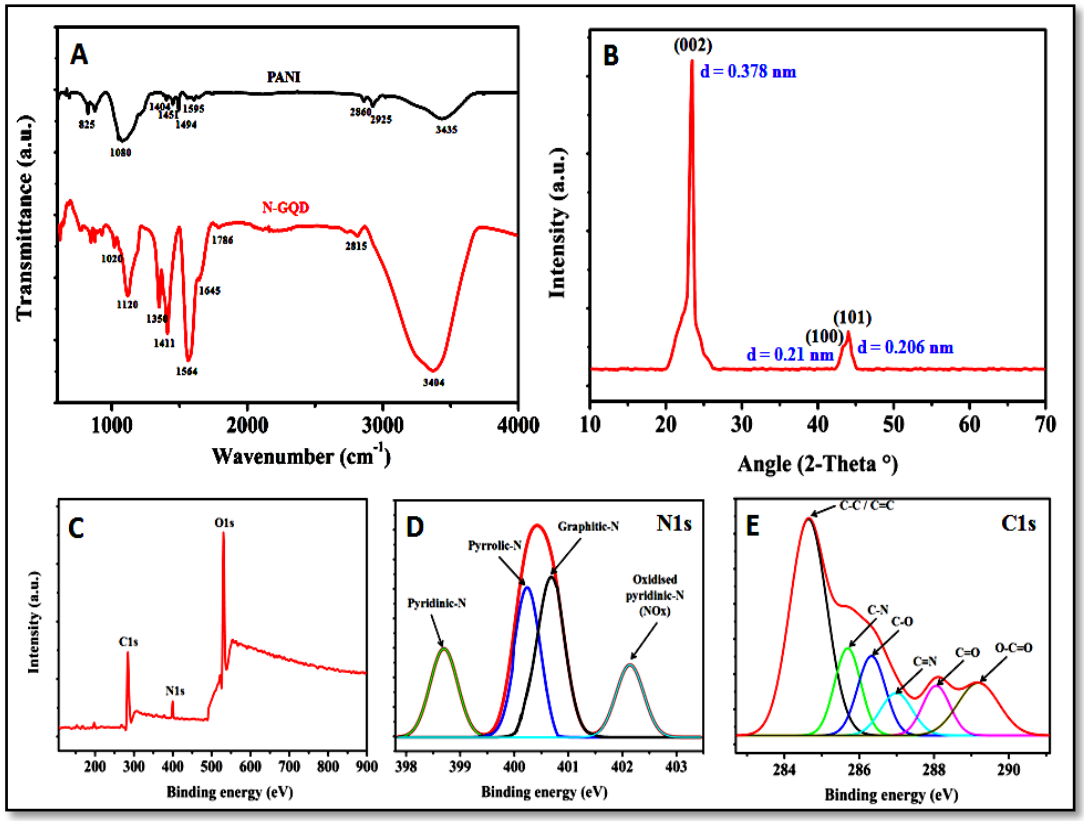

Figure 6.3. (A): The FTIR spectra of N-GQD and PANI; (B) and (C): the XRD and XPS spectrum of N-GQD; (D) and (E): High resolution XPS spectra of the N1s and C1s of N-GQD, respectively, and their related curve-fitted components.

In addition to the oxygen functionalities, the C⁻N peak (~285.8 eV) and C=N peak (287 eV) can be certainly identified which further indicates the aromatic structure of N-GQD with a number of side functionalities and the successful in situ N-doping in its lattice (Cai et al., 2015).

The presence of N in N-GQD was further confirmed by the SEM elemental mapping analysis and EDAX analysis. Figure 6.4A shows the SEM image of N-GQD and the corresponding elemental mapping results with the C, O and N elemental distribution in Figure 6.4B, 6.4C, 6.4E & 6.4F, respectively. The mapping results show ~10 % N in N-GQD, which is one of the highest percentage doping by hydrothermal strategy, reported so far. Further the EDAX spectrum (Figure 6.4D) confirms the presence and the uniform distribution of N in N-GQD. Thus the characterisation results clearly confirm the formation of N-GQD with its crystalline and Gr structure containing aromatic rings with pyrridinic, pyrrolic and graphitic N in the lattice and the edge groups, ensuring a considerable amount of N-doping. Based on the informations obtained from the characterization studies, a representative structure of the N-GQD is proposed which is given in Figure 6.5. The structure consist of aromatic basal plane enriched with N atoms, in the form of graphitic-N, pyrrolic-N, pyridinic-N and oxidised pyridinic-N (NO_x) rings, in addition as side functional groups such as amino ($-NH_2$). Apart from N, the structure encompasses a number of hydrophilic oxygen rich functionalities such as –OH, -COOH etc., which along with the aromatic N-heterocyclic basal plane, is expected to promote and enhance the electrocatalytic behaviour. The graphitic N is supposed to give better conductivity and electronic properties (Matsoso et al., 2016), which is abundant in the N-GQD formed. The degree and the configuration of N-doping in the N-GQD are dependent on the concentration of the N-precursor material (Matsoso et al., 2016) and hence we shall attribute the vivid and enriched N-doped structure of N-GQD to the N-precursor, PANI.

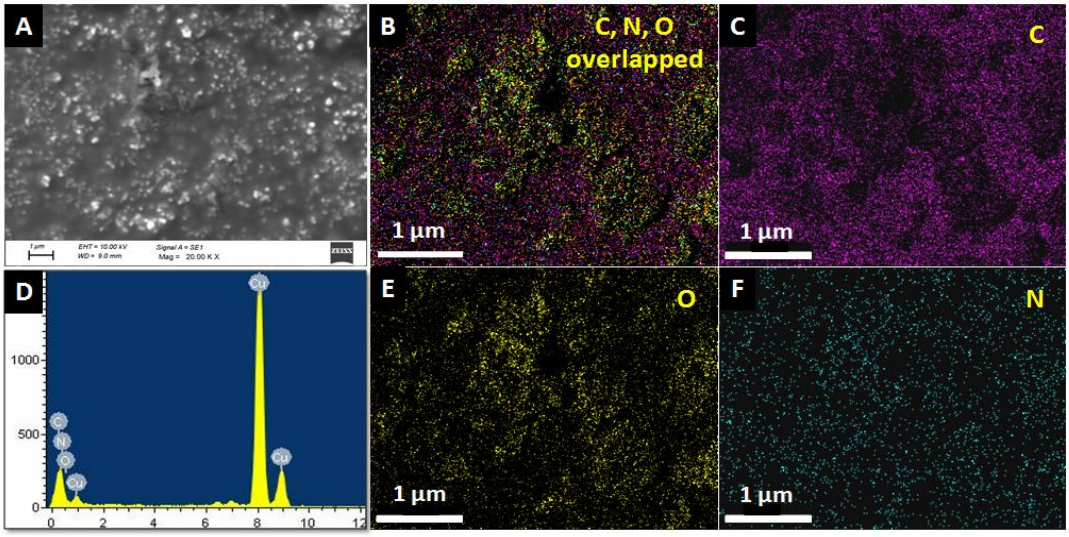

Figure 6.4. (A): SEM image of N-GQD; (B), (C), (E-F): SEM elemental mapping results overlapped, C, O and N, respectively; and (D): EDAX spectrum confirming the rich presence and uniform distribution of N in N-GQD.

The UV-Vis spectrum and the optical images of the photoluminscence of N-GQD in comparison with that of PANI are shown in Figure 6.6A. The spectrum of PANI reflects characteristic absorption band at 341 nm, and a broad band beyond 550 nm attributed to the polaron π*, and π polaron transitions, respectively (Alam et al., 2013). On the other hand, the UV–vis absorption spectrum of N-GQD had a typical absorption of graphene derivatives in the UV region (200–300nm) with a peak at ~260nm which was assigned to the π–π* transition of aromatic sp^2 domains. In addition to these, an absorption peak centered at ~512 nm was observed and is assigned to an n–π* transition which is indicative of N doping in Gr. Inset images of Figure 6.6A include photographs of the aqueous solutions of N-GQD taken under normal light and under irradiation by a 365 nm lamp. It is observed that the N-GQD exhibits a light greenish blue fluorescence color.

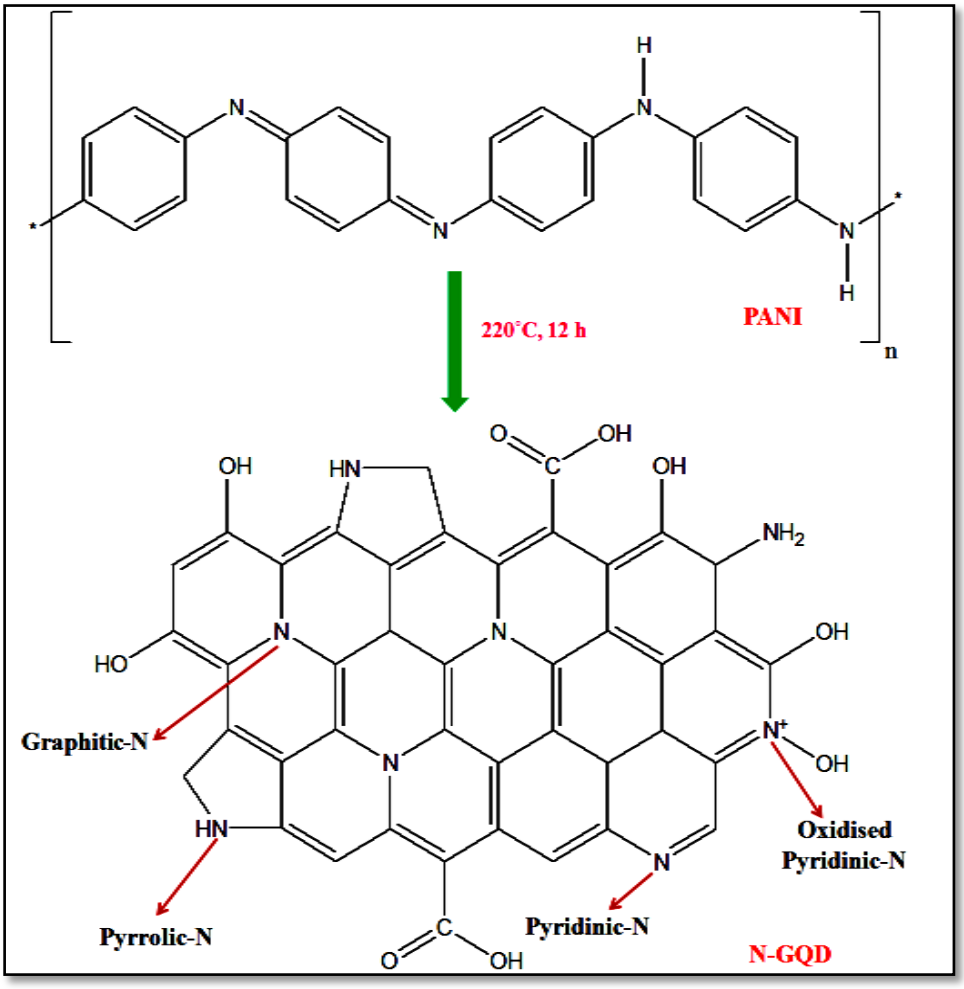

Figure 6.5. The proposed structure of N-GQD prepared from PANI with enriched N-doping and the possible different N-configurations

To further explore the optical properties of N-GQD, the PL characterization was used. The PL emission of N-GQD was observed to be excitation wavelength-dependent (Figure 6.6B). On excitation with 320 nm, the PL spectrum exhibited a strong peak at ~420 nm with a Stokes shift of 100 nm, corresponding to a blue emission and with longer excitation wavelengths (from 340 to 380 nm, the PL peak shifts to longer wavelengths with a rapid decrease in intensity, which are consistent with the previous reports of N-GQDs (Cai et al., 2015; Pan et al., 2010; Van Tam et al., 2014). From 400 nm excitation wavelength onwards another strong emission band started dominating corresponding to a green emission, centred at ~520 nm reaches a maximum intensity at 420 nm, and showed similar trend of wavelength shift and intensity decrease with longer

excitation wavelengths (420 to 580 nm). According to the previous reports, the isolated sp^2-hybridized clusters with a size of ~3 nm within the carbon-oxygen matrix can yield band gaps consistent with blue emission owing to the localization of electron-hole pairs (Eda et al., 2010; Y. Li et al., 2012). Therefore, from the experimental results described above, it can be assumed that the oxygen-rich groups and the doping of N atoms with strong electron-withdrawing ability is the reason to the observed blue shift in the PL emission of N-GQD. The green emission regions may arise from the less doped GQD matrix where N could be part of amine functionalities. Thus, the result further confirms the formation and the structure of N-GQD.

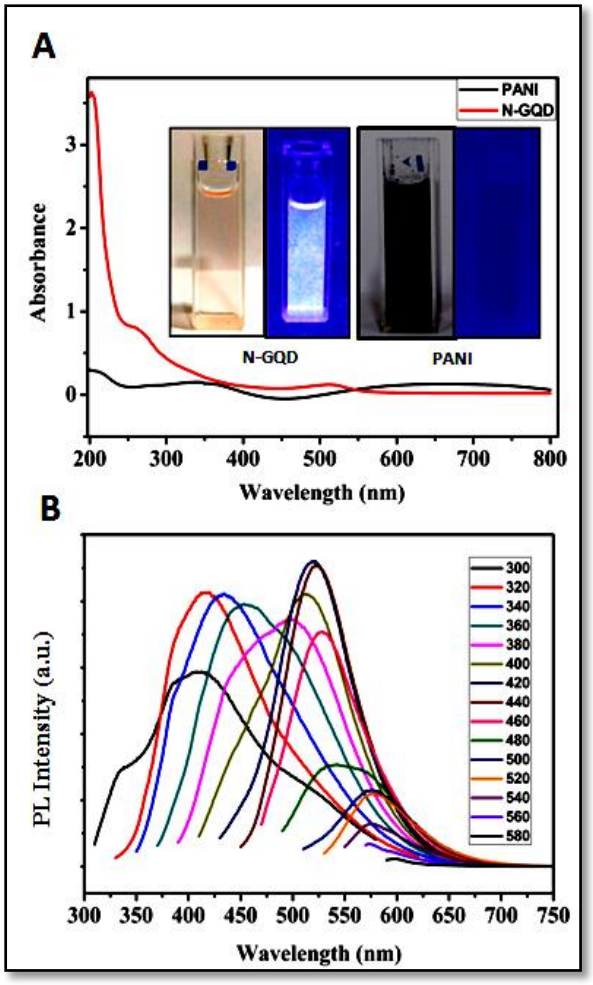

Figure 6.6. (A): The UV-Vis spectra of PANI and N-GQD; (B): The excitation wavelength dependent PL spectra of N-GQD. The inset in (A) shows the digital images of PL of the N-GQD (left) and PANI (right) under normal light and under 365 nm UV irradiation.

6.3.3. EC sensing studies

The N-GQD/GCE was tested as electrode for EC sensing and differentiation of nitroaromatic compounds, such as TNP, DNP, NP, and DNT, the sensing of TNP by N-GQD was studied in detail because of its importance and the results obtained are discussed. Further, the sensing of N-GQD was compared with that of an undoped GQD/GCE and the bare GCE.

6.3.3.1. Electrocatalytic reduction of TNP by N-GQD/GCE

The DPV of TNP on N-GQD/GCE was performed to study the electrocatalytic activity of the N-GQD for the TNP reduction. The DPV response was recorded from –0.1 to –0.9 V at an optimized scan rate of 50 mV/s and a pulse amplitude of 25 mV. The DPV results of N-GQD/GCE for TNP (100 µM) along with that of GCE and GQD/GCE are given in Figure 6.7A for comparison. While there are no recognizable peaks for TNP on bare GCE, the GQD/GCE, showed a slightly better response compared to that of the bare GCE, with two reduction peaks which were barely recognizable indicating the poor electrocatalytic behaviours of the bare GCE and GQD/GCE towards the TNP reduction. On the other hand, three well defined reduction peaks were observed at –0.19, –0.65, and –0.78 V in the DPV of TNP on N-GQD/GCE. The peak at -0.65 V, corresponding to the reduction of the nitro ($-NO_2$) group in the 4^{th} position of TNP, showed ~6-fold and ~4-fold increase from that of the GCE and GQD/GCE, respectively. Moreover, among the three studied, the N-GQD/GCE was the only electrode which produced three well defined reduction peaks, which are assigned to the stepwise reduction of $–NO_2$ groups in the TNP molecule to the hydroxylamine and finally to amine (Cai et al., 2015), confirming the higher and effective electrocatalytic property of the N-GQD.

The comparitively higher electrocatalytic activity of the N-GQD towards TNP to that of the GQD is ascribed to the improved electronic characteristics of N-GQD imparted by the highly N-doped structure containing more of graphitic N

(Matsoso et al., 2016) along with various configurations of N. N-doping can alter the energy gap of HOMO–LUMO (H–L gap) of the N-GQD, which can in turn alter the barrier to electron transfer (Cai et al., 2015) positively. Upon doping with N, the H–L gap decreases and the electrons are more easily excited from the valence bands to the conduction bands. A lower H–L gap for the N-GQD results in an improvement of the conductivity of N-GQD. Therefore the enhanced conductivity and the improved electron transfer ability of the N-GQD together result in significant increase in its electrocatalytic reactivity and in turn in the enhanced TNP detection. In addition to the graphitic N, the better the N-doping which means incorporation of N-doping in the aromatic lattice without disrupting the honeycomb structure may have a significant role in the enhanced catalytic activity. It has been reported that the presence of graphitic N can preserve the high mobility of charge carriers in N-doped Gr and can enhance the catalytic behaviour as it provides extra electron density to the graphitic basal plane (Matsoso et al., 2016; Pollack et al., 2017). Similarly the incorporation of the pyrrolic N into Gr can introduce defects and strong disorders which will enhance the adsorption properties (towards the analyte) (J. Zhang et al., 2016). Hence the structure of N-GQD with dominant proportions of graphitic-N and pyrrolic-N, as deduced from the characterization results, can effectively enhance its sensing performance. In addition, the sensing behaviour of N-GQD/GCE could have been further enhanced by (i) the molecular interactions between the N-GQD and the analyte molecules such as ring stacking and л-л interactions due to the aromatic structures and (ii) electrostatic and hydrogen bonding interactions promoted by the hydroxyl (−OH) and the edge groups such as -NH, and $-NH_2$ on the N-GQD towards nitrophenols. Schematic which represents the enhanced sensing property towards TNP in DPV upon modification of GCE to N-GQD/GCE is given in Figure 6.8.

6.3.3.2. Sensitive EC detection of TNP by N-GQD/GCE

The sensitivity and concentration dependency of N-GQD/GCE towards the EC detection of TNP was evaluated by recording the DPV responses starting from low concentration level of 1 nM (ppt levels). Figure 6.7B shows the DPV

response of the N-GQD/GCE with the increasing concentration of the TNP in 0.1 M PBS electrolyte. The reduction current gradually increased with the increasing concentration of TNP. Since there are three peaks, the cathodic peak at –0.65 V was selected as the assay signal, which exhibited linear response towards TNP for a wide concentration range from 1nM to 100 µM (Figure 6.7C). Two separate linear dynamic ranges (LDR) were obtained: from 1 nM to 1 µM with a correlation coefficient (R^2) of 0.994 and from 1 µM to 100 µM with a R^2 value of 0.998. The LOD obtained was 1 nM, i.e. 0.2 ppb (S/N=3), which is further confirmed by the chronoamperometric analysis (Figure 6.7D).

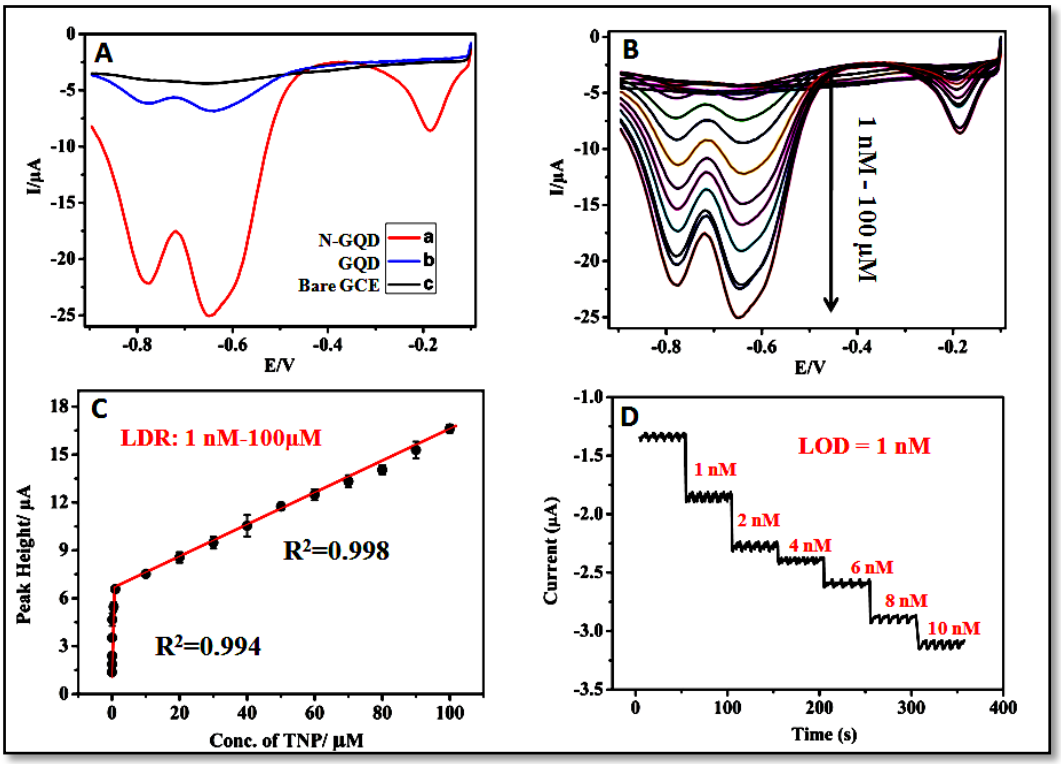

Figure 6.7. (A): DPV scans obtained for 100 µM TNP in 0.1 M PBS on (a) N-GQD/GCE; (b) GQD/GCE; and (c) GCE. (B) The DPV response of TNP on N-GQD /GCE for the concentration range of 1nM to 100 µM; (C): The corresponding linear relation obtained between the peak height and the concentration of TNP; (D): Chronoamperometric response of N-GQD/GCE for the increasing concentration of TNP from 0-10 nM at a potential of -0.6 V.

The comparison of LOD values obtained for various TNP sensors (relevant) reported in the literature with that of the N-GQD electrode is given in Table 6.1. From the Table it is clear that the achieved LOD is the lowest reported

for TNP so far by any sensing method. To the best of our knowledge, the lowest LOD reported for TNP is 1.69 ppb, by a fluorescent platform using a metal organic framework (MOF) system (Asha et al., 2016). Therefore the LOD value of 0.2 ppb reported in the present study is the lowest and is fit enough for the practical detection of TNP in water.

Table 6.1. Comparison of the LOD of N-GQD/GCE with the literature reports for TNP sensing.

Materials/Electrodes	Sensing method	LOD (ppb)	Reference
MOF	Fluorescence	1.69 ppb	(Asha et al., 2016)
N-GQD	Fluorescence	300 nM (~ 68 ppb)	(Lin et al., 2015)
GQD	Fluorescence	91 nM (~ 21 ppb)	(Z. Li et al., 2015)
Graphitic Carbon Nitride	Fluorescence	8.2 nM (~ 1.9 ppb)	(Rong et al., 2015)
N-rGO/CuS/GCE	EC	69 nM (~ 16 ppb)	(Giribabu et al., 2016)
Bismuth bulk electrode electrode (BiBE)	EC	200 nM (~ 46 ppb)	(Prchal et al., 2010)
Polished Ag solid amalgam composite electrode (p-AgSA-CE)	EC	1 µM (~ 230 ppb)	(Vyskočil et al., 2011)
Copper electrode (CuE)	EC	6.0 µM (~ 1380 ppb)	(Junqueira et al., 2013)
1-pyrenebutyl-amino-β-CD and rGO modified Au microelectrode (PyCD-rGO/AuME)	EC	0.54 µM (~ 124 ppb)	(J. Huang et al., 2014)
PtNPs–rGO/GCE	EC	1 µM (~ 230 ppb)	(Mahyari, 2016)
Copper(II)-1,3,5-benzenetricarboxylic acid (Cu-BTC)/ ERGO/GCE	EC	0.1 µM (~ 23 ppb)	(Yong Wang et al., 2018)
Surfactant (cetyl pyridinium chloride)/GCE	EC	190 nM (~ 44 ppb)	(X.-G. Wang & Fan, 2009)
N-GQD/GCE	EC	1 nM (~ 0.2 ppb)	Present study

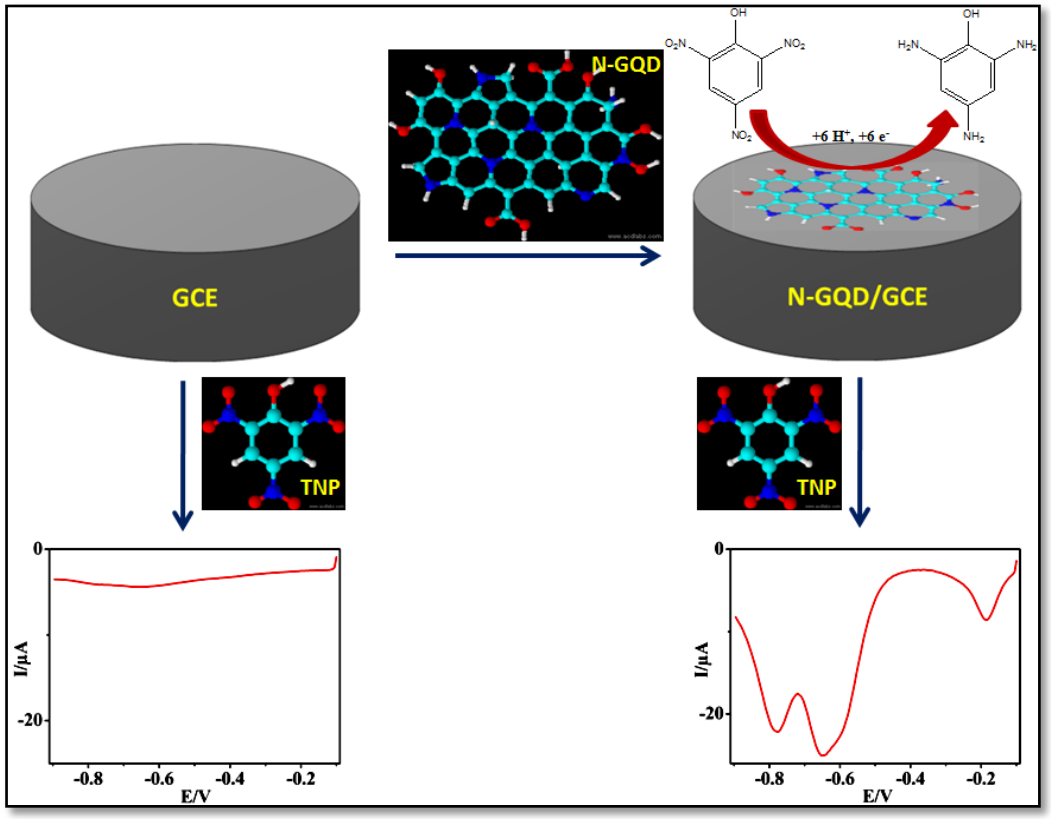

Figure 6.8. The schematic diagram showing the modification of GCE with the N-GQD and the resultant enhanced sensing of TNP in DPV.

6.3.3.3. Selectivity and interference studies of N-GQD/GCE

In order to evaluate the practical applicability of an electrode, selectivity and interference studies are crucial. Therefore, sensing of N-GQD towards various other possible contaminant species/metal ions was tested using CV, and the results are depicted in Figure 6.9A. Of the various ions tested (Hg^{2+}, Ag^{+}, Pb^{2+}, Fe^{2+}, Co^{2+}, Ni^{2+}, Zn^{2+}, Sn^{4+}, Cu^{2+} and Cr^{6+}), Ag^{+} and Hg^{2+} showed measurable current response, though much smaller compared to that of TNP along with other nitroaromatics DNP, NP and DNT which showed measurable responses. Therefore, further the interference studies were carried out using chronoamperometric technique (Figure 6.9B) at a selected voltage of –0.65 V. While Ag^{+} and Hg^{2+} showed very small responses though at concentrations more than 10 times that of TNP which is in accordance with the selectivity studies, nil interference was observed with the other ions at this higher concentration levels.

The results thus demonstrate the superior and preferetial selectivity of TNP on N-GQD and the absence of interference in the TNP sensing.

6.3.3.4. Detection and differentiation between various nitroaromatics by N-GQD/GCE

To evaluate the applicability of the N-GQD/GCE for the effective differentiation of nitroaromatics, we recorded the EC response of compounds such as 2-NP, 2,4-DNP, and 2,4-DNT at the N-GQD/GCE (Figure 6.8). Even with their similar structures, it is clear from the result that they can be clearly distinguished using the DPV profiles (peak numbers and positions vary for each and thus create a different profile). While 2, 4-DNP exhibited two reduction peaks (–0.61 and –0.76 V) (Figure 6.9D), 2-NP showed only one reduction peak (–0.61 V) (Figure 6.9C) corresponding to the number of the $–NO_2$ groups present. Similarly, 2,4-DNT displayed two reduction peaks (Figure 6.9F) in the DPV similar to that of 2, 4-DNP, however, the shape, positions and the potentials of the peaks were different (–0.54 and –0.69 V) from that of the latter. Whereas in TNP, three peaks corresponding to the three NO_2 groups were observed at the potentials of –0.19, –0.65, and –0.78 V (Figure 6.9E), thus suggesting the capability of N-GQD to differentiate between them whereas GQD/GCE and GCE were not able to differentiate between them as demonstrated in Figure 6.7. The number of the reduction peaks obtained for the nitroaromatics on N-GQD/GCE is equivalent to the number of NO_2 groups in the molecule, indicating the potentiality of the N-GQD to differentiate between the molecules with different number of $–NO_2$ groups such as NP, DNP and TNP which is usually tough to achieve because of their similarity in the structure and properties. In addition, the N-GQD can differentiate between the aromatic compounds with the same number of $–NO_2$ groups but having different substituent groups (eg; DNP and DNT) using the different peak profiles in the DPV (Figure 6.9). The result is an indication of the effectiveness of N-GQD in the EC sensing of nitroaromatics and shall be assigned to its effectively N-doped aromatic structure. Correspondingly, the result reveals the capability of N-GQD to differentiate between TNP and 2,4,6-trinitrotoluene

(TNT) as they are expected to exhibit different DPV profiles because of the difference in their substituents, (analysis of TNT was not done due to the unavailability of the compound because of the restrictions on the material). The ability to differentiate between the nitrophenols and nitrotoluenes by N-GQD and the enhanced sensing exhibited by N-GQD towards the nitroaromatics is attributed to the synergistic effect of the different types of N- rings such as graphitic, pyrrolic and pyridinic in an aromatic structure along with the edge groups such as –OH, -NH, $-NH_2$ which can interact with nitrophenols differently from that of the nitrotoluenes. These N-heterocycles can give rise to domains which are able to differentially interact with the analytes even with highly similar structure and thus create different profiles. Further the better electronic conductivity, adsorption properties due to defects and catalytic properties enhance the sensing activity of N-GQD. From our result, it is evident that this is possible only on a suitable electrode such as N-GQD as evident in Figure 6.7 where GQD and GCE fails to even come close to the sensing performance and hence are unable to differentiate between the nitroaromatic compounds.

6.3.3.5. Deduction of the role of aromatic nature of analyte in the sensing performance of N-GQD

In order to confirm whether the aromatic nature of the analyte has importance in the EC sensing performance of N-GQD, the sensing studies were conducted with different analytes like phenol, nitrobenzene and the aliphatic nitromethane in comparison with that of TNP. The studies carried out using chronoamperometry at the potential of -0.65 (Figure 6.10B) exhibited nearly nil current response for phenol (an aromatic alcohol without the $–NO_2$ group) and nitromethane (an aliphatic nitrocompound), where as the aromatic nitrocompound, nitrobenzene showed a significantly greater current response, however, when compared to that of TNP, the response was much lower. This indicates that the aromatic nitrocompounds are more preferentially sensed by N-GQD than that of aliphatic nitro compounds. To verify that there are no other peaks for nitromethane in the DPV profile we conducted the experiment and found that no

peaks (Figure 6.10A) were found in the experimental voltage window, instead a peak was observed to start appearing at a much higher potential which confirms the role of aromatic structure.

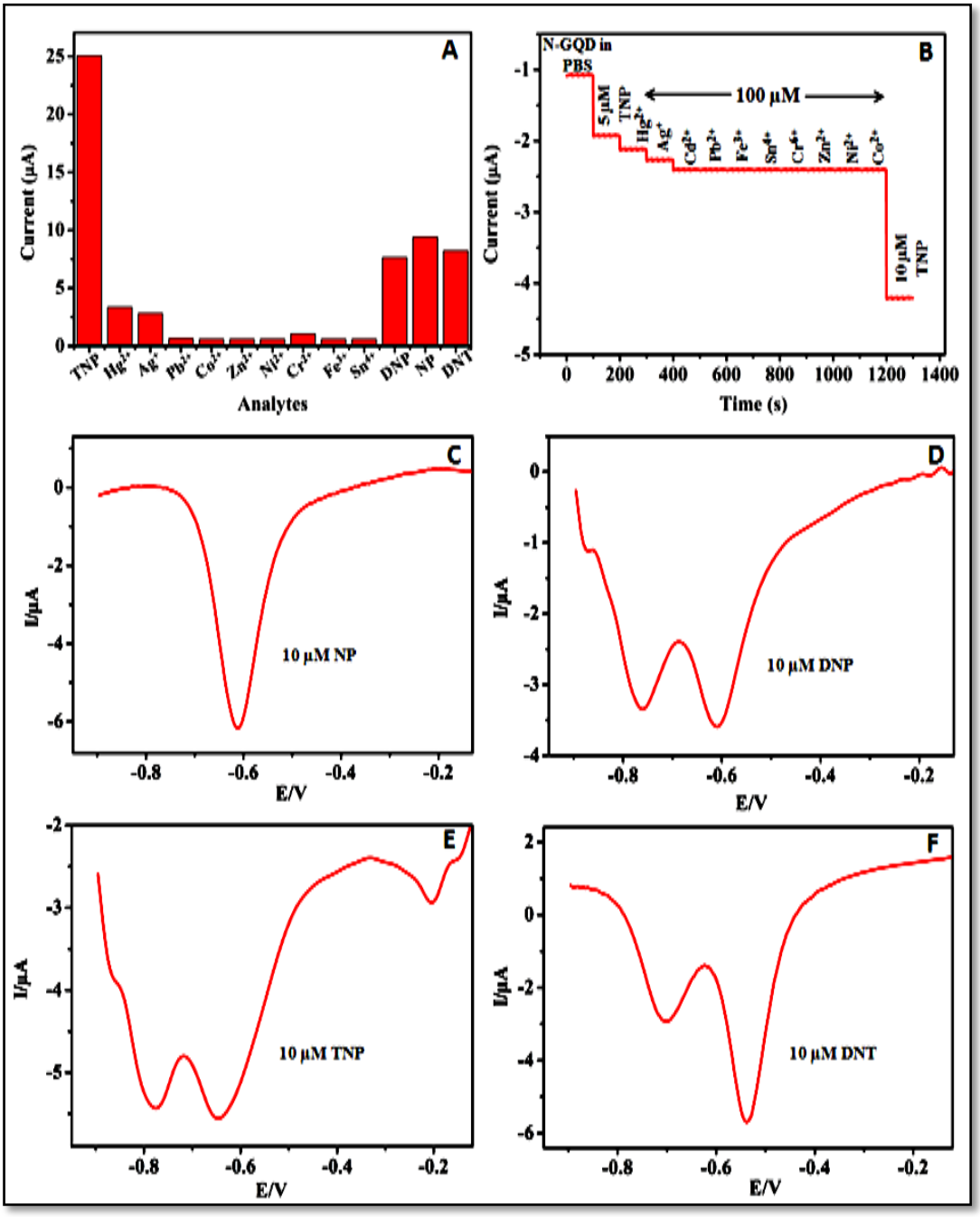

Figure 6.9. (A): Selectivity studies of N-GQD/GCE with various analyte species; (B): Interference studies of N-GQD/GCE for the detection of TNP; DPV scans obtained for (C): 10 µM 2-NP; (D): 10 µM 2, 4-DNP; (E): 10 µM 2, 4, 6-TNP and (F): 10 µM 2, 4-DNT in 0.1 M PBS at N-GQD/GCE.

Therefore from these results along with the previous selectivity and interference results, it can be concluded that the EC sensing behaviour of the N-GQD for nitrocompounds is of the order; aromatic nitrophenols ≥ aromatic nitrotoluenes > aromatic nitrocompounds > aliphatic nitrocompounds. A synergistic effect was observed for the presence of a $–NO_2$ group along with a phenol shall be attributed to the combined presence of the N-doped aromatic structure and the edge groups which promote H-bonds, whereas $–NO_2$ attached to the aromatic moiety resulted in better performance than that of an aliphatic nitro, indicative of the aromatic structure of the N-GQD, as the aromatic structures of the analytes and N-GQD can bring about л-л stacking and electrostatic interactions which lead to better adsorption and better EC sensing performance.

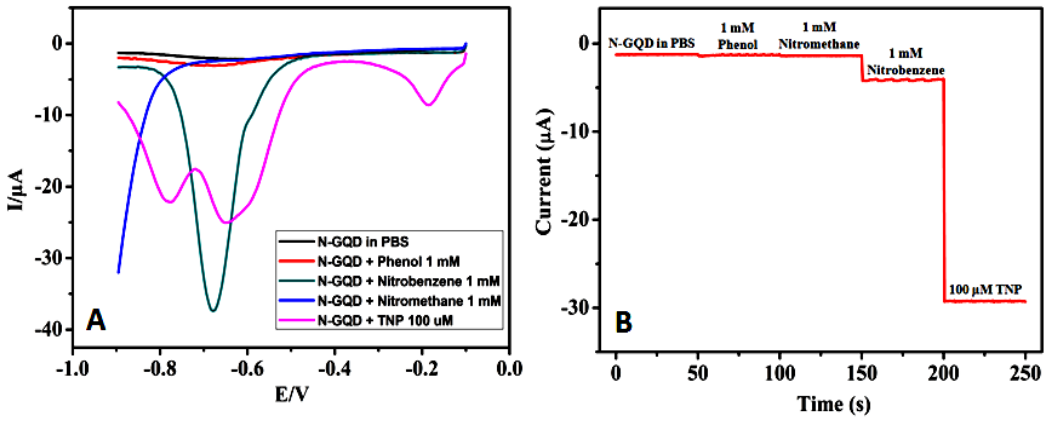

Figure 6.10. The comparison of current response of the N-GQD towards the sensing of phenol, nitrobenzene, nitromethane (1 mM each) with that of TNP (100 μM) using (A): DPV and (B): Chronoamperometry at the selected voltage of -0.65 V.

6.3.4. Reproducibility, reusability and stability of N-GQD/GCE

The reusability and the storage stability of the N-GQD/GCE was evaluated by comparing the reduction peak currents for 100 μM TNP immediately after washing, and after a period of 1 month, respectively, with the initial current response (Figure 6.11A and B). The N-GQD/GCE retained 94.5 and 91.5% of the initial current response, indicating the reusability of the sensor and the remarkable stability. Further, the relative standard deviations (% RSD) in the reduction peak

currents estimation from five independently prepared electrodes in DPV for 100 µM TNP was found to be 1.14% (Figure 6.11C), indicating excellent reproducibility.

6.3.4. Real water analysis

Inspired by the excellent sensing performances of N-GQD, the sensing studies were extended to real water samples such as tap and ground water. The tap water samples were spiked with TNP at different concentration levels (2, 5 and 10 µM), analyzed with the proposed method and the recovery amounts were calculated. The recovery calculated was found to be in the range of 100.78–101.45%, which shows the excellent applicability of N-GQD/GCE in real water sensing of TNP. Further, ground water samples were also evaluated using the same method. The recovery amounts calculated were ranging from 98.92–99.49 %. Both the measurements are summarized in Table 6.2. The DPV response for one of the tap water analysis is given in Figure 6.11D.

Table 6.2. Determination and recovery test results of TNP in real water samples

Water sample	TNP Spiked (µM)	TNP found (µM)		Recovery (%)
1	2	Ground water	1.985	99.23
		Tap water	2.016	100.78
2	5	Ground water	4.974	99.49
		Tap water	5.072	101.45
3	10	Ground water	9.892	98.92
		Tap water	10.093	100.93

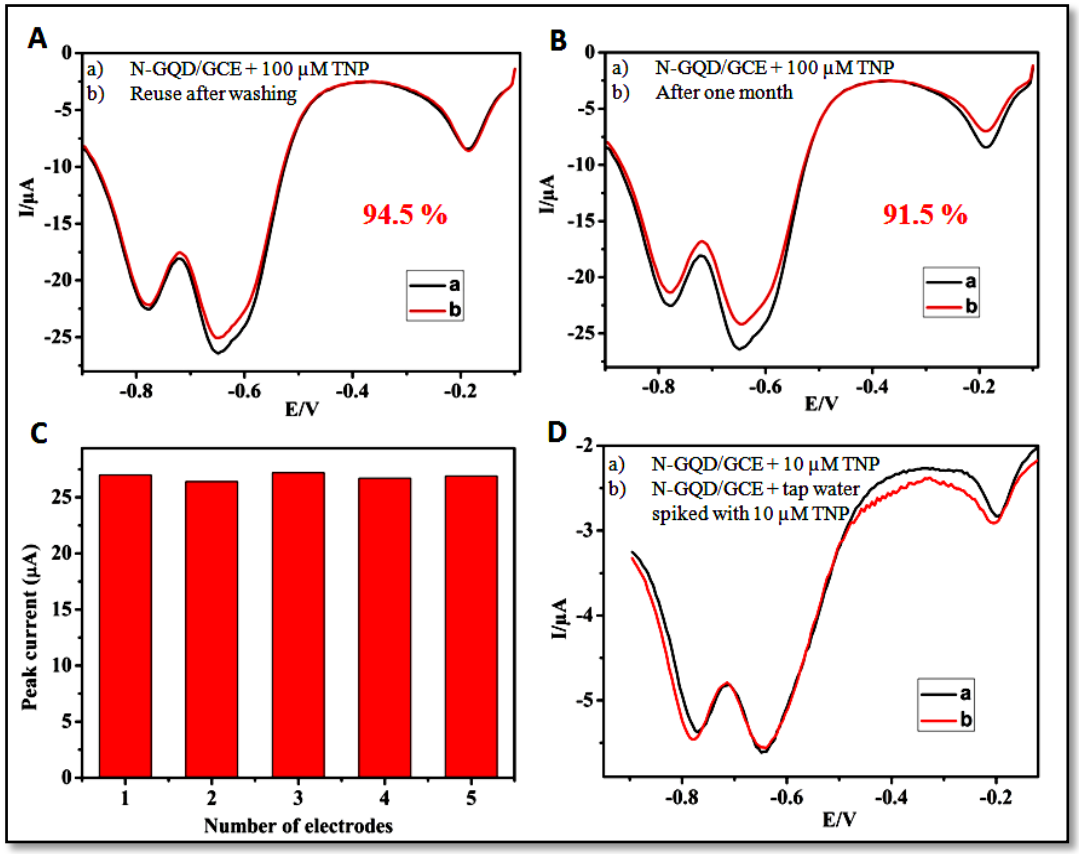

Figure 6.11. DPV scans obtained for 100 µM 2, 4, 6-TNP on N-GQD/GCE (A): after immediate washing showing the reusability; (B): before and after 1 month of time showing the stability and (C): The peak current of five independently coated electrodes showing reproducibility of N-GQD/GCE.D) DPV scan obtained for tap water spiked with 10 µM 2, 4, 6-TNP on N-GQD/GCE in comparison with the actual result.

6.4. Conclusions

Here in this work, we have demonstrated a simple and novel hydrothermal strategy for the synthesis of N-GQD for the first time from an aromatic N-containing polymer, PANI without using any external doping agent and have verified the merit of the N-GQD/GCE as an EC sensor for TNP and nitroaromatics. Interestingly, it could detect up to 0.2 ppb levels of TNP showing excellent sensitivity and in addition, could effectually distinguish between different nitroaromatic explosives. The electrode shows excellent selectivity for TNP and was able to extend the detection to real (tap and ground) water samples. The reason for the remarkable electrocatalytic reactivity was assigned to the

possible electrostatic, H-bonding, ring stacking and л-л interactions between the aromatic TNP and the N-GQD enriched with O-rich hydrophilic side functionalities and aromatic N-hetero cycles in the basal plane. Moreover, the low H–L gap, the enhanced conductivity and improved electron transfer ability of N-GQD resulted from the effective N-doping without tampering the aromatic ring shall contribute to its exceptional EC sensing properties. The electrode exhibited excellent reusability, reproducibility and stability. Thus, a simple and cost-effective electrode for the preparation of N-GQD which can be used as an EC sensing platform for TNP is reported, which according to the results is indeed promising for the detection and differentiation of nitroaromatics, and for detecting TNP in complex environmental samples.

CHAPTER 7

NANO GRAPHENE SHELL FOR SILICON NANOPARTICLES: A NOVEL STRATEGY FOR A HIGH STABILITY ANODE FOR LITHIUM ION BATTERY

This chapter discusses a simple strategy to achieve Si-Gr based anode of a core-shell structure different than that of the conventional intercalated structure of Si-Gr, which is expected to provide better stability to the anode. The greater specific capacity and cycle life properties of this core-shell structure, referred to as Si-nanographene oxide (Si-nGO), is discussed in comparison with the intercalated Si-graphene oxide (Si-GO). It was observed that the change in the structure of Si-Gr based anode to the core-shell has improved the stability remarkably and shows that it is a promising strategy towards achieving electrode material for advanced lithium ion batteries.

7.1. Introduction

The increasing demand for advanced energy storage materials for electric powered vehicles (EVs) and other applications has driven intense research on high-capacity anode and cathode materials to realize advanced LIBs. As explained in the introduction chapter, Si has attracted the most attention among the various anode materials, due to its highest theoretical charge capacity (4200 $mAhg^{-1}$), ten times that of the currently used graphite anode (372 $mAhg^{-1}$), and low Li uptake potential (< 0.5V vs. Li^+/Li) (D. Wang et al., 2013). However, the practical application of Si as an anode material is challenged by its lack of stability due to the significant volume change (> 300 %) during the lithiation and delithiation process, which leads to the destruction of the initial particle morphology. This in turn results in losing the electrical contact and to lower electrical conductivity,

rapid consumption of active material (AM) due to the formation of fresh SEI, in total resulting in rapid capacity fading (Evanoff et al., 2011; Nguyen et al., 2011; Oumellal et al., 2011).

To overcome the volume change and the formation of fresh SEI on Si anodes, numerous strategies have been employed by researchers, which are already discussed in the introduction chapter (Section 1.1.4.4). Majority of the reports were successful in attaining stability at lower AM mass loading capacities, some as low as ≤ 0.1 mg cm^{-2}. However, the stability values at these lower AM mass loading does not guarantee stability at higher mass loading values (≥ 3 mg cm^{-2}), which is crucial for real application. In this context, we have conducted the studies with electrodes having higher AM mass loading values ~ 2.0 mg cm^{-2}. The particle level structural stability is crucial in order to withstand stress and electrode level cracking and to achieve stability at higher mass loadings (N. Liu et al., 2014). Therefore we have chosen Gr material as the shell for superior performance as it can provide high mechanical strength and flexibility (X. Zhou, Yin, Cao, et al., 2012).

Recently, Gr materials have been intensively used as flexible carbonaceous coatings to construct different dimensions of Si-based electrode materials using various strategies (R. Hu et al., 2014). Gr with its excellent properties and superior mechanical flexibility is becoming more and more appealing, as it can accommodate the large volumetric changes of the Si NPs during charge/discharge cycling. Moreover, it can enhance the conductivity of Si NPs with its exceptionally high electrical conductivity (X. Zhou, Yin, Wan, et al., 2012), and its large surface area, in principle, can accommodate higher amount of Si NPs compared to amorphous carbon and other carbon nanomaterials or other materials studied such as TiO_2 (Jia et al., 2011; Novoselov et al., 2004; H. Wang et al., 2011; X.-L. Wang & Han, 2010). However, so far, the reports of Gr-based Si electrode materials are focused on the intercalated structure of Si-Gr (R. Hu et al., 2014; H.-i. Kim et al., 2012; X. Li et al., 2012; N. Liu et al., 2014; X. Zhou, Cao, et al., 2012), which is expected to mitigate the volume expansion. This

approach however has the limitation of restricting the volume expansion mainly in the stacking direction (assume it as Z-direction) and not in the other two directions (X and Y direction). Further the electrolyte can seep in between the layers and make contact with the Si NPs to form the SEI which is unstable because of the contraction and expansion and gradually lead to the loss of AM. Thus the NPs eventually will get consumed or lose its structural integrity. This is evident from the reports of Si-Gr composite of intercalated structures with an average cycling stability of ~100-200 cycles at the mass loading values of ≤0.1 - 1.5 mg cm^{-2}.

Therefore, we looked at the core-shell design for making Si-Gr anode, as this design can limit the volume expansion of Si NPs in all the direction and further can protect Si from SEI formation. The micron sized sheets of Gr or GO if mixed with Si NPs, by default, forms the sandwiched structure of Si-Gr, therefore, to attain the core-shell structure, the size of GO was decreased by oxidation which yielded smaller (≤ 300 nm) sized sheets hereafter referred to as nGO (H.-i. Kim et al., 2012). The core-shell type -Si-nGO structure was achieved by a simple mixing of the aqueous dispersions of Si NPs and nGO. The formation of the core-shell nanostructure of the composite was confirmed by various characterization techniques. Our results show that the Si-nGO core-shell structure exhibited a stability of ~250 cycles, at a mass loading of ~1.5 mg cm^{-2}, with an initial specific capacity of 1960 $mAhg^{-1}$ at a current rate of 657 mAg^{-1}. The Si-nGO anode retained 80 % of the initial capacity at 250 cycles. A higher mass loading of 1.93 mg cm^{-2} was tested and achieved a stability of ~160 cycles. Although there are literature reports (de Guzman et al., 2013; R. Hu et al., 2014; X. Zhou, Cao, et al., 2012) with up to ~1000 cycles life for modified Si anodes, the areal mass loadings of the AM are as low as ≤ 0.2 mg cm^{-2}, which significantly reduces the overall energy density of the anodes (De Volder et al., 2013; N. Liu et al., 2014), and does not necessarily extrapolate to the stability at higher mass loading values. The best so far reported Si-C is a of a pomegranate inspired structure (N. Liu et al., 2014) designed to avoid the formation of SEI on Si NPs and , has reported to achieve 150-160 cycles at a mass loading of ~1.9 mg cm^{-2}. Our results indicate that the

core-shell Si-nGO is superior in terms of cycling stability and specific capacity compared to the sandwiched Si-GO structure.

7.2. Experimental

7.2.1. Synthesis of nGO

The nGO was synthesized by the oxidation of commercially available GO using $KMnO_4$ as an oxidant in acidic medium as described elsewhere (H.-i. Kim et al., 2012) with slight modification. The resulting nanosized graphite oxides yielded nGOs on ultra sonication. The detailed procedure is as follows. Graphite oxide (0.5 g) was added into a concentrated H_2SO_4 solution (500 mL), and then $KMnO_4$ 1.5 g (300 wt % of graphite oxide) was slowly added to the above solution with vigorous stirring to produce nGO. Stirring was continued for 2.5 hours at 45 °C. The resulting mixture was cooled down in an ice bath, and 1 L of H_2O_2 solution (950 mL of water + 50 mL of 30 wt % H_2O_2) was then added very slowly and stirred over 1 h. The resultant mixture solution was filtered and washed with 5% HCl solution, followed by distilled water until became neutral and then dried in a vacuum oven at 80°C to get the solid nanosized graphite oxide product. It was then ultrasonicated for 30-60 min. in order to obtain exfoliated nGOs from nanosized graphite oxides. The resultant nGO was used to prepare the Si-nGO composites.

7.2.2. Synthesis of Si-nGO composite

In a typical synthesis of Si-nGO composite, about 100 mg of Si nanopowder was dispersed in 200 ml of distilled water by ultrasonication for 1-2 hours, this homogeneous suspension was mixed with 1 mg/ml aqueous dispersion of nGO prepared by ultrasonication. The volume of nGO dispersion depended on the amount of nGO required. The mixture was stirred at room temperature for 2 days and then filtered to get the product. Similarly, Si-GO composites were prepared by following the same synthetic procedure replacing nGO with GO.

7.2.3. EC measurements

Coin cells (CR 2032) were fabricated using a slurry containing: 85 wt% of the active composite material, 10 wt% Y-50 A as a conductive material, and 5% polyvinylidene fluoride (PVDF) (Alfa aesar) as binder. Lithium metal (Sigma Aldrich) was used as a counter/reference electrode. The electrolyte was a 1 M $LiPF_6$ solution with a mixture of Ethylene Carbonate (EC)/Diethyl Carbonate (DEC) (1:1) (Toda Corporation) as a solvent, with no additives. The electrodes were separated by a PP/PE/PP membrane (39% porosity, 20 µm micro porous, Celgard 2320, USA) and assembled in an argon-filled glove box (MBRAUN UNILAB, USA).

7.3. Results and Discussion

7.3.1. Formation of Si-nGO core-shell nanostructure

The conventional Si-Gr based composites reported are essentially of a sandwiched structure where Si NPs are intercalated between Gr or GO sheets of large (micron sizes) lateral dimensions. This structure (i) can allow the expansion of Si NPs in the X-Y directions (considering stacking of Gr sheets is in the Z-axis) and thus can gradually degrade the integrity of Si NPs, (ii) will allow the contact of electrolytes with Si NPs and thus the SEI formation on the Si NPs gradually, which will reduce the capacity and thus the stability. On the other hand a core-shell structure in principle, will limit the expansion of Si NPs in all the directions and thus expected to provide better cycling stability, and can avoid the formation of unstable SEI on the Si NPs due to the protective Gr based shell. For attaining the core-shell structure, instead of the sandwich, the size of GO sheets were decreased from micron to nano sizes (≤ 300 nm) by oxidation of GO (H.-i. Kim et al., 2012). The reduction in the dimension of the GO to form nGO sheets is evident from the AFM images (Figure 7.1), which display sheets of ~300 nm in nGO while micron sized sheets in GO. Figures 7.2 & 7.3 provide the FT-IR, TGA and XRD spectra of the composite and nGO. The XRD of nGO shows broadening

of the characteristic (sharp) peak of GO at ~11^{o} and a new peak centred around 24^{o}, suggesting changes in the GO sheets. The Figure 7.3B shows the spectrum of Si-nGO, where the peak of the nGO at 11° is disappearing or getting broader which suggests the disruption of the (random) layered structure of nGO in the composite due to the formation of the core-shell structure.

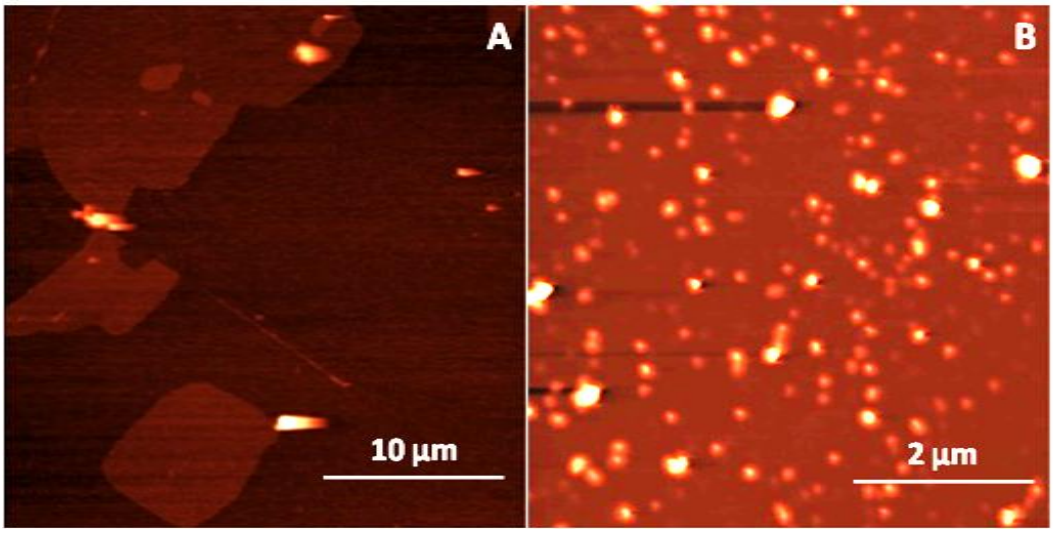

Figure 7.1. AFM image of (A): GO and (B): nGO

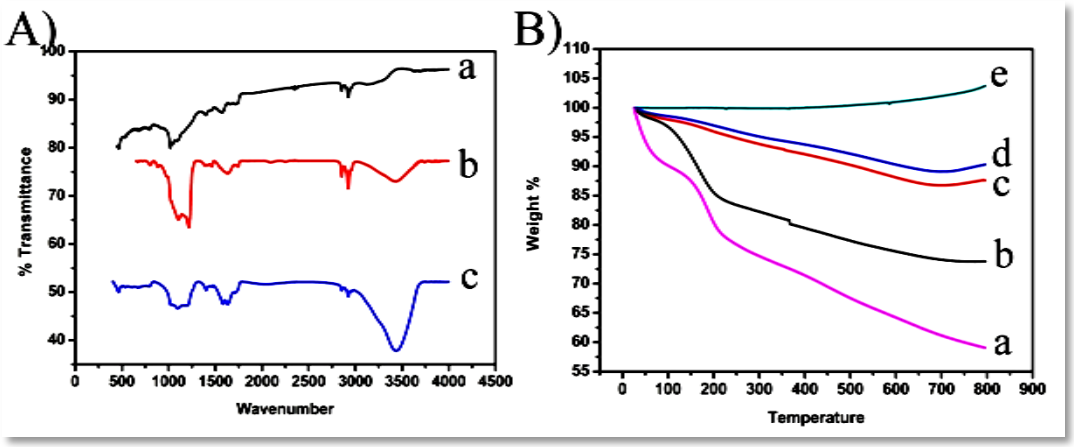

Figure 7.2. (A): FT-IR spectra of a) nGO, b) Si NP and c) Si-nGO (B): TGA of Si-nGO composites of varying composition of Si NPs in comparison with that of bare Si NP: a-nGO, b-40% Si NP, c- 67% Si NP, d- 75% Si NP, e- Si NP.

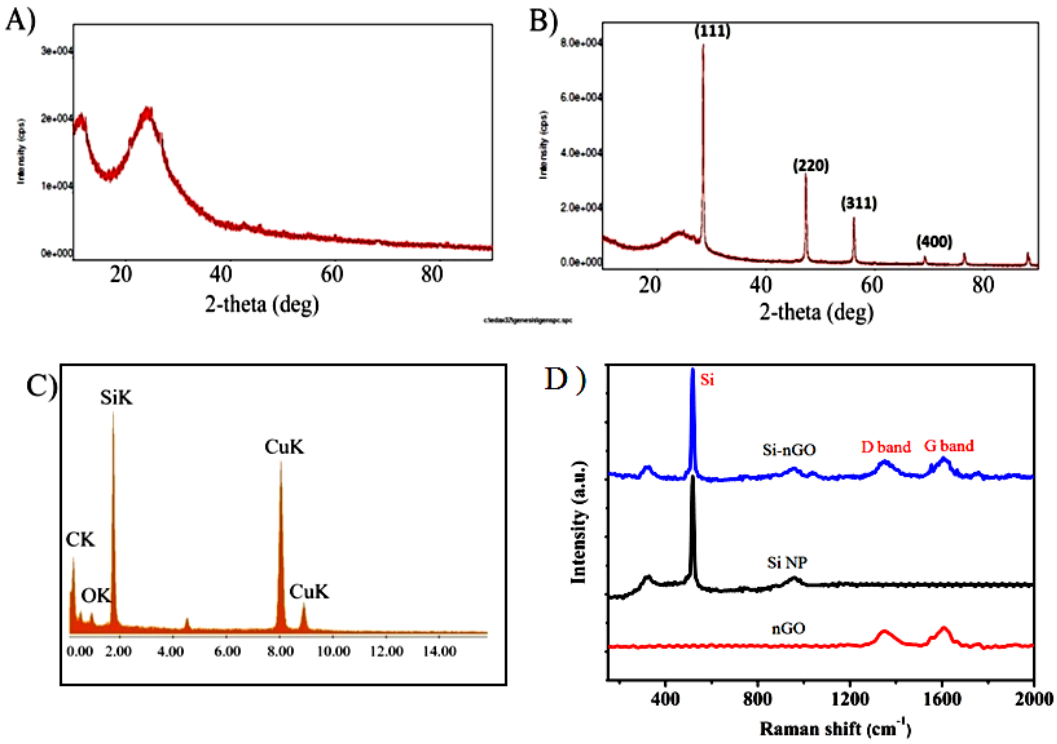

Figure 7.3. XRD of (A): nGO and (B): Si-nGO (C): EDAX of Si-nGO and (D): Raman spectra of nGO, Si NP, Si-nGO

The formation of the Si-nGO core-shell type composite was initially studied by the zeta potential (ZP) measurement. The surface –OH groups of Si NPs, due to the oxidized layer may make it negative and thus might restrict the effective wrapping of the Si NPs by nGO. Therefore, we examined the surface charges of the starting materials: aqueous dispersions of the Si NPs and the nGO. While the ZP of nGO was negative (-10.63 mV) which is assigned to the functional groups such as carboxylic acid and phenolic hydroxy groups that are located on the nGO sheets, the ZP of the Si NP was positive (+ 3.1 mV). The ZP values indicating that the mutual electrostatic attractions of the oppositely charged Si NP and nGO can act as the trigger for the formation of Si-nGO core shell structure. And the product Si-nGO on analysis exhibited a ZP of -33.16 mV, confirming negative value indicating the formation of a core-shell Si-nGO with Si NPs as core and nGO as shell. The increase in the zeta potential of the Si-nGO might possibly be due to the structural change of nGO from sheets to nearly spherical (which changes the calculation, as the ZP measurements assume any

shape to be spherical). Thus, the results suggest the formation of Si-nGO core-shell structure. The schematic of the formation of the proposed structure is given in Figure 7.4.

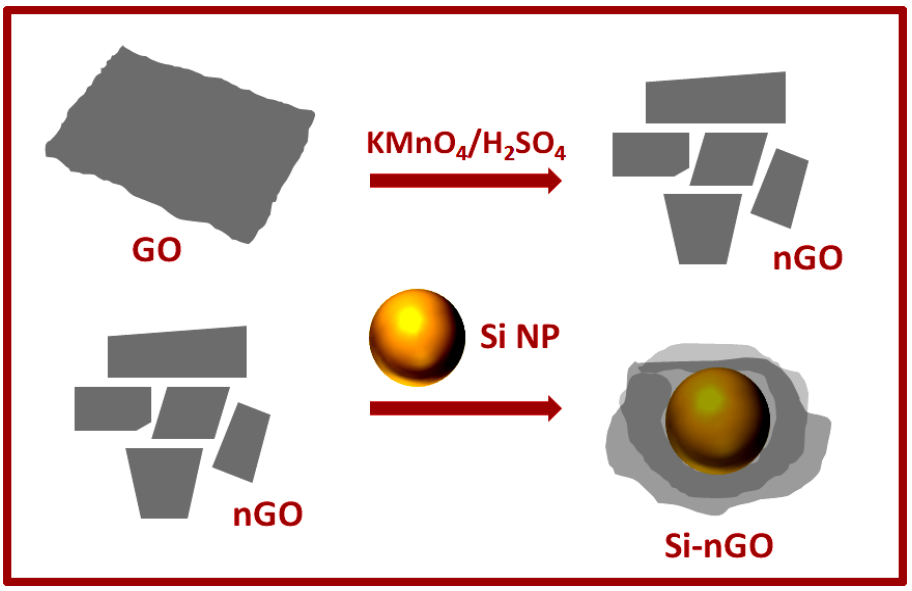

Figure 7.4. Schematic for the formation of Si-nGO composite. The edges need not be sharp as shown

The morphology and composition of the Si-nGO composite was characterized by HRTEM, FESEM and EDAX. The HRTEM images (Figure 7.5A-D) in accord to the proposed core-shell structure showed Si NPs wrapped by thin, almost transparent nGO sheets to form a core-shell Si-nGO structure. Figure 7.5G-I confirm the core-shell morphology of each Si-nGO system. Moreover, the images show that in some cases spaces are formed between the Si NP core and the nGO shell due to the folding of nGO sheets around the Si NP's, which is an advantage to the electrode.

The space formation between core and the shell is preferable as it can accommodate the volume change of the Si NPs during lithiation/delithiation processes and thus further protects the shell from damaging easily (X. Li et al., 2012; N. Liu et al., 2014). Besides that, the nearly transparent nGO sheets in the

images suggest that the shell is made of single to few layered nGO sheets, which essentially improves the insertion and desertion of Li^+ ions.

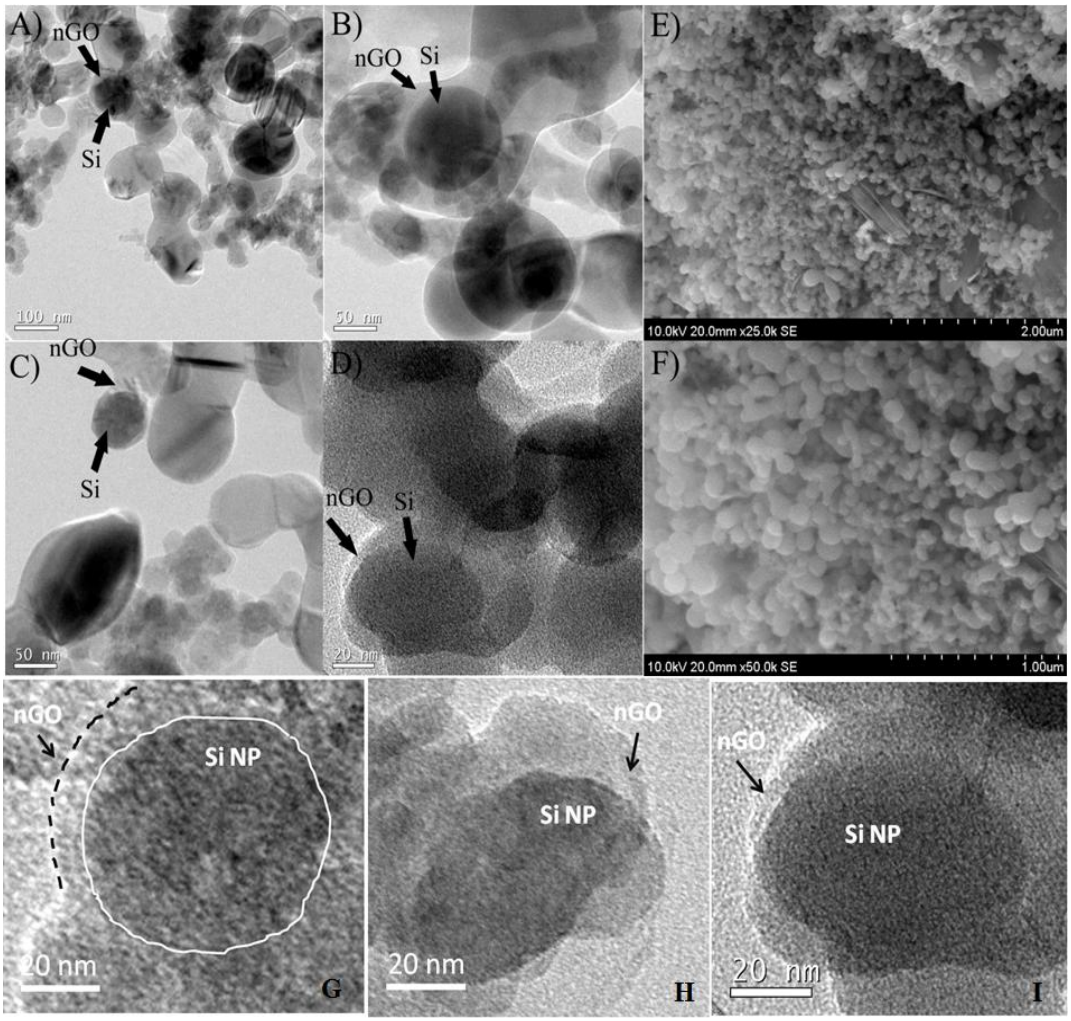

Figure 7.5. Morphology characterisation of Si-nGO conforming to a core-shell structure: (A-D): HRTEM images and (E), (F): FESEM images of Si-nGO composite (G)-(I): High resolution images of single Si NP-nGO core-shells.

Thus, a core–shell structure of Si-nGO was obtained, which combines the benefits of thin flexible and robust nGO sheets as a shell/matrix to restrict the volume expansion and improve the conductivity of electron and Li^+ ions. Unlike the intercalated structure, the core-shell structure can protect the Si NPs in a better way from the unstable SEI formation during the cycling process. The HRTEM images (Figure. 7.5) do not show any micron sized GO sheets in the images confirming the formation of nGO sheets. The HRTEM and FESEM images

obtained for Si-GO are given in Figure 7.6 and it clearly shows a different structure from that of the Si-nGO with bigger sized GO sheets (marked by arrows) with number of Si NPs on it, which is characteristic of an intercalated structure. The FESEM images of Si-nGO (Figure 7.5E and 7.5F) show the presence of Si and nGO and that the sizes of the Si NPs range from 60-100 nm and confirm the absence of big micron sized GO sheets.

The EDAX spectrum (Figure 7.3C) confirms the presence of Si, C and O in the composite, confirming the presence of both the Si and nGO. The Si-nGO composite was further characterized by XRD (Figure 7.3B). Apparently, the diffraction peaks of the Si-nGO nanocomposite perfectly overlapped with those of the Si NPs, indicating that the crystalline nature of Si NPs did not alter in the process of preparation, which is as expected, as there are no such conditions in the procedure. Figure 7.3D presents the Raman spectrum of the Si-nGO composite, with that of Si and nGO shown for comparison. For Si-nGO composite, a main peak at about 520 cm^{-1} is in agreement with the data in the spectrum of Si NPs, while the peaks at 1350 and 1596 cm^{-1} correspond to the D band and the G band, respectively, which are characteristic Raman peaks for carbon materials, indicating the presence of nGO. The intensity of the D band is comparable to that of the G band in the Si-nGO composites, which may be due to (1) a decrease in the average size of the new or more sp^2 domains during the cutting down of GO to nGO and (2) the presence of a few defect sites or oxygen moieties that is formed after the size reduction of GO to nGO. Thus our characterization results confirm the formation of Si-nGO core shell structure from Si NP and nGO dispersions.

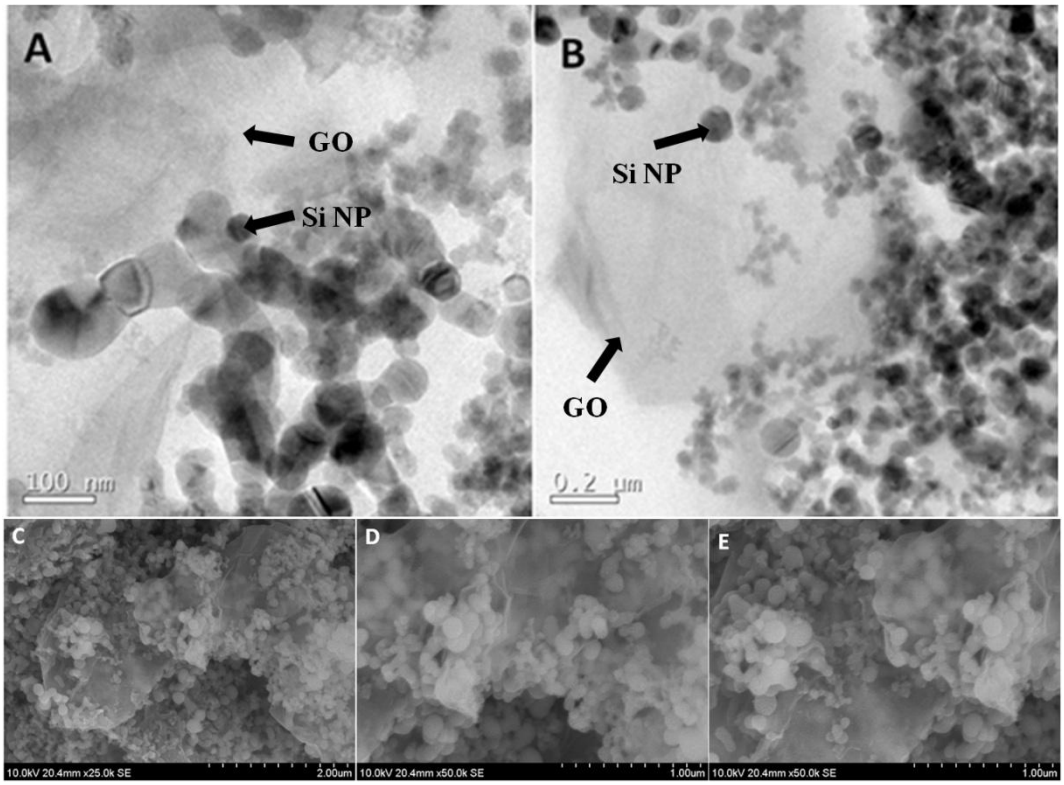

Figure 7.6. (A): and (B): HRTEM images and (C)-(E): FESEM images of Si-GO composite showing large micron sized GO sheets covering Si NP forming an intercalated structure

7.3.2. EC Evaluation

The electrochemical characterizations as well as the galvanostatic charge-discharge studies were carried out for the Si-nGO composite. The specific capacities as well as the coulombic efficiency trends of Si-nGO anodes were recorded for a charge-discharge rate of C/3 (657 mAg^{-1}) and are given in Figure 7.7A. Figure 7.7B displays the representative discharge–charge profiles of a 1^{st}, 50^{th} and 100^{th} cycles between the voltage limits 0.05 and 0.5 V vs. Li/Li^+.(The voltage values are limited to 0.5 V as the full charge capacity was achieved within the voltage). As shown in Figure 7.7B, Si-nGO composite has an irreversible capacity of 984 $mAhg^{-1}$ in the first cycle and an initial coulombic efficiency of ~50%. The irreversible capacity loss in the initial cycle can be ascribed to the electrolyte decomposition and formation of SEI on the surface of nGO sheets, which has relatively higher SA considering the wrapping of Si NPs with nGO

sheets. After the first cycle, the coulombic efficiency has stabilized to ~99% and then ranges from 98–100% in the subsequent cycles which indicates the stability of the SEI's formed on nGO. The Si-nGO anode was tested at 1.5 and 1.93 mg cm^{-2} AM (Si-nGO) mass loading values. At the areal mass loading of 1.5 mg cm^{-2}, Si-nGO anode exhibits a large initial discharge capacity of 1960 $mAhg^{-1}$ and stability for more than 250 cycles with 80 % capacity retention at a current rate of 657 mAg^{-1} with ≥ 98% coulombic efficiency. The reversible capacity of Si-nGO electrode retains as high as 1560 $mAhg^{-1}$ even after 250 cycles. The specific discharge capacities are calculated with respect to the mass of Si in the composite). The cycling performance of bare Si NPs anode was carried out under the same testing conditions, and similar mass loading (~1.5 mg cm^{-2}), was ≤ 25 cycles at a specific capacity of ~1150 $mAhg^{-1}$. The inferior stability of Si NP anode is attributed to the large volume changes of Si NPs leading to fresh SEI formation which destroys the structural integrity of the electrode resulting in rapid capacity decay and hence lower stability.

The discharge/charge profiles of the 50^{th} and 100^{th} cycles given in Figure 7.7B, confirm the reversibility of the reactions of the Si-nGO electrode. This reversibility is attributed to the enhanced structural stability imparted by the core-shell morphology of the Si-nGO and the improved electronic and Li^+ conductivity of the electrodes resulting from the thin nGO sheets which promotes easy Li^+ transport. The decrease in the charge transfer resistance of Si-nGO electrode compared to that of the Si NPs was demonstrated by the Nyquist plots (Figure 7.8) and is attributed to the thin nGO sheets which remarkably improve the electronic conductivity of the composite.

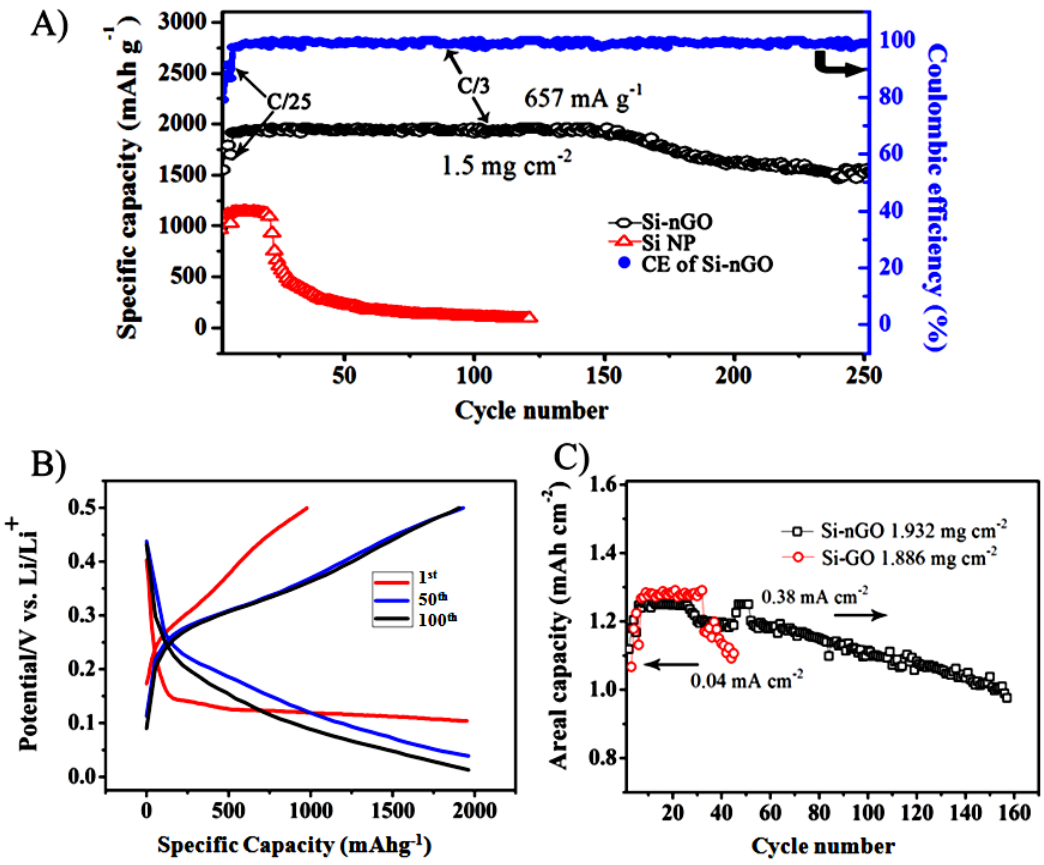

Figure 7.7. Specific capacity and cycling stability trends of Si-nGO: (A): Cycling performance of Si-nGO anode with an AM loading of 1.5 mg cm^{-2} at a current rate of 657 mAh g^{-1} in comaparison with that of bare Si NPs (B): Galvanostatic discharge/charge profiles of a few representative cycles of Si-nGO and (C): The comparison of cycling stability of Si-nGO and Si-GO at comparable AM loading.

Further, we investigated the electrochemical performance of Si-GO anode, in order to verify whether the core-shell strategy has, in practice, improved the performance of the anode from that of the conventional sandwich structure. For comparison, the cycling stability of Si-nGO and Si-GO anodes at the mass loading values of 1.93 and 1.89 mg cm^{-2}, respectively, were done and the results obtained are given in Figure 7.7C. The result shows that while the Si-GO exhibits a poor stability of ~50 cycles, the Si-nGO is stable for ~160 cycles which is more than 3-fold times the stability of that of the Si-GO anode. Stable cycling at high mass loading values can only be achieved if the electrode materials possess remarkable structural stability at the (nano) particle level, because even small changes in particle morphology could accumulate across the thickness of the

electrode and cause electrode-level cracking and failure (N. Liu et al., 2014). Thus, the result clearly suggests that, the core-shell structure has indeed enhanced the stability at the nanoparticles level, i.e., the Si-nGO core shell protects Si NP better compared to that of the sandwiched Si-GO structure. Therefore, we attribute the enhanced stability of Si-nGO to its core-shell morphology which prevents the formation of the unstable SEI on the Si NP and thus ensures the stability of the NPs.

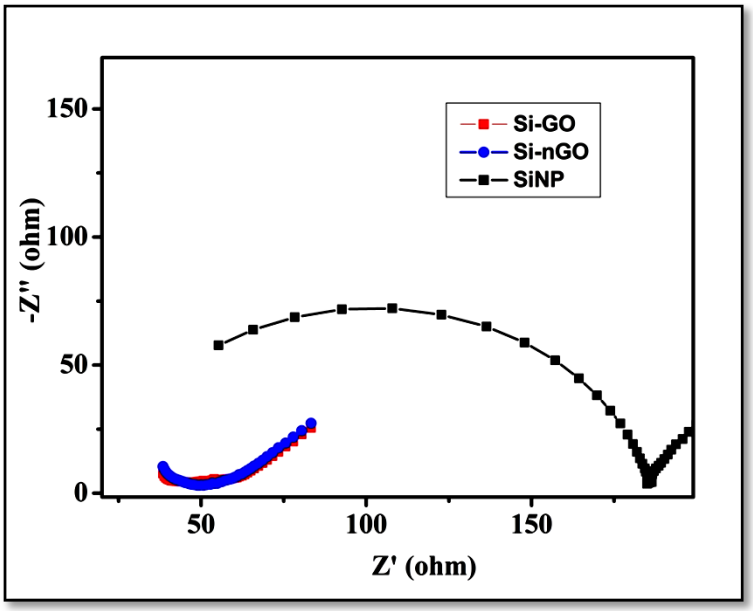

Figure 7.8. FRA of Si NP (black), Si-GO (red) and Si-nGO (blue)

Stability at higher discharge rates is considered significant for an electrode material. Therefore, the high rate cycling trends of Si-nGO and Si-GO anodes were studied and the results are given in Figure 7.9. The result shows that the Si-nGO is highly stable till 2C rate with a capacity retention of 100% and ~80, 70 and 50% capacity retentions were observed at 3C, 5C and 10C rates, respectively and the 100% initial capacity was restored when the current rate was changed to the initial C/10 value after cycling at 10C rate (Figure 7.9B), which indicates that the stability of the matrix and the anode. This result verifies the superior high-rate capability of the Si-nGO electrode due to the buffering of the volumetric change of the active Si NPs offered by the thin nGO matrix.

Meanwhile the Si-GO anode was able to retain the initial capacity for 1C only and the capacity degraded to ~90, to 25% at 2C, to 5C rate, respectively. (10C study was not shown for Si-GO anode due to complete capacity degradation).

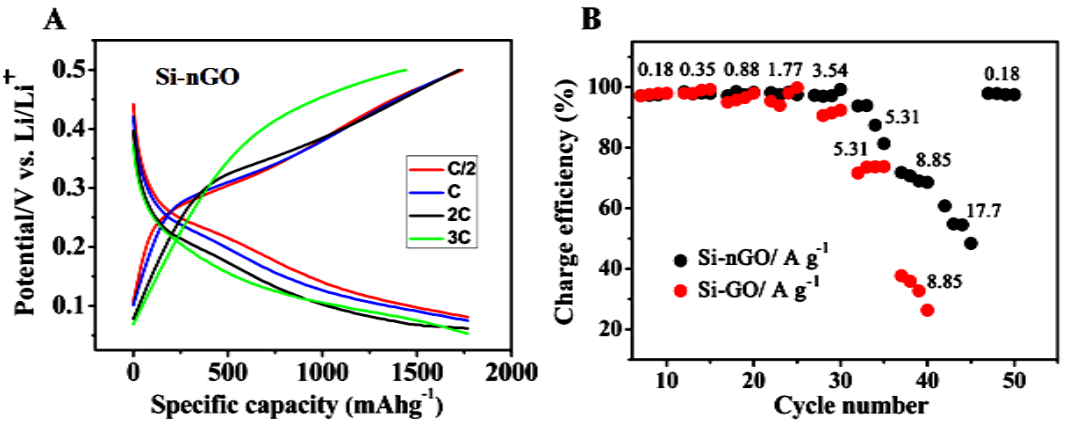

Figure 7.9. (A): Rate capability plots of Si-nGO: The galavanostatic charge-discharge curves at different C rates (1C = 1.77 A g^{-1}) and (B): High rate cycling performance (discharge) of Si-nGO.

Thus, the result clearly suggests the core-shell structure to be effective in improving the electrochemical rate performance for the anode compared to that of the sandwiched structure. Among the Si-Gr based materials, Si-nGO is superior in terms of the cycling stability also. The stability of the nGO matrix after the 10C rate was analyzed using the HRTEM and is given in Figure 7.10A and B. The figure shows the presence of many intact nGO matrices over the Si NP cores without being destroyed after the cycling process. On the other hand, the images of Si-GO samples after cycling (Figure 7.10C and D) describe the damaged matrix and the pulverized Si NPs which confirm the inadequateness of the GO matrix to stop the electrolyte contact with the Si NPs and thus the pulverization. The differences in the image may be due to the conducting material and binder remaining in the electrode.

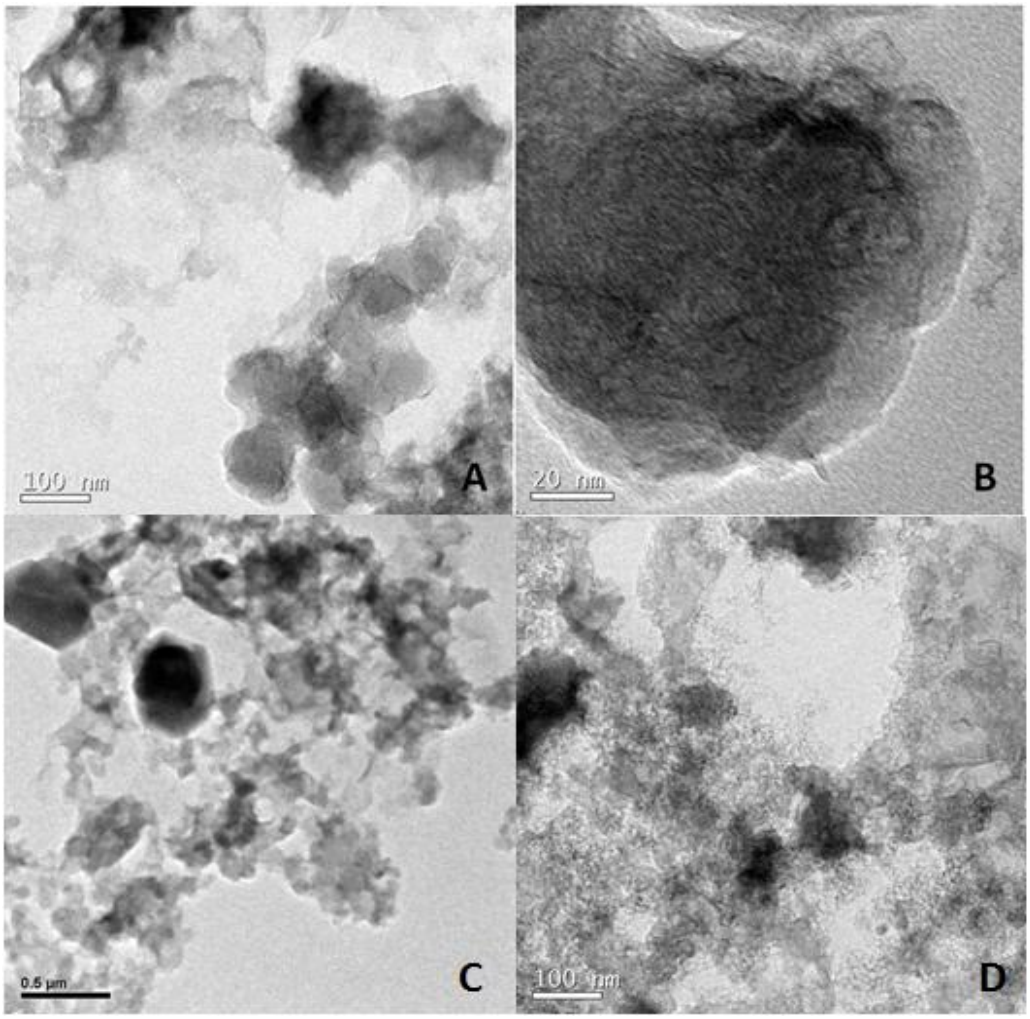

Figure 7.10. HRTEM images after cycling; (A) and (B): of the Si-nGO sample showing the intact matrix after cycling. (C) and (D): of the Si-GO sample showing the decayed matrix and pulverized Si NPs.

The schematic is given in Figure 7.11 (cross-sectional view) to explain the advantages of Si-nGO structure compared to the Si-GO during charge-discharge processes over cycles which results in the better cycling stability. Figure 7.11A demonstrates the case of bare Si NPs, where the lack of a matrix results in the total exposure of the particles to the electrolyte which results in an unstable and repeated SEI formation during charge-discharge cycles resulting in the consumption and degradation of Si. In the case of Si-GO, i.e. the sandwiched structure; the Si NPs are vulnerable to the exposure of electrolyte more so in the edges of the sandwich structure and thus result in the SEI formation on the

surfaces of Si NPs (Figure 7.11B). The repeated shrinkage and expansion of Si NPS will lead to the formation of fresh SEI and thus leads to the consumption of the Si NPs which in turn causes capacity decay as evident from the results. Whereas, in the core-shell Si-nGO anode with the active Si NP being in the inner side with an outer shell of nGO (Figure 7.11C), the exposure of the Si NPs to the electrolyte is minimal thus the formation of fresh SEI during each cycle is restricted and thus minimizes the capacity decay and improves the stability of the electrode. The TEM images, show hollow spaces in between the core and the shell in most places, this allows the Si core to expand without hurting the shell matrix. During delithiation, the inner surface of the Si core shrinks back. Overall, the interface with the electrolyte remains the same i.e. the nGO surface.

In case of the SEI formation and stability, the nGO sheets play an important role. It facilitates the formation of a stable SEI film by nGO coating, resulting in reduced impedance caused by the SEI film. In addition, the flexibility and availability of the nano spaces provided by thin nGO sheets can accommodate to an extent the volume changes of Si NPs. A report on hollow core–shell structured Si-C nanocomposites containing void spaces is able to accommodate the volume expansion for 100 cycles with ~80% capacity retention at an initial specific capacity of 760mAhg^{-1} (based on the entire electrode weight) (X. Li et al., 2012), whereas Si-nGO showed >250 cycles at this conditions, which demonstrates the superior strength of Gr as the matrix/shell compared to the amorphous carbon. A Si-Gr nanocomposite, by Hu et al., containing Si NPs individually wrapped and connected by Gr nanosheets, delivered a stability of 200 cycles for a discharge capacity of 1732 mAhg^{-1} (based on the Si loading) at a rate of ~280 mAg^{-1} where the electrode mass loading is reported to be between 1.12 and 1.44 mg cm^{-2} (R. Hu et al., 2014). The comparatively better stability of Si-nGO anode is assigned to the synergistic effect of the flexible and mechanically robust nGO shell which helps the Si NPs to withstand the deformation pressure from Li–Si alloying and dealloying processes, the core-shell structure, the void spaces in the Si-nGO and the thin nGO sheets which improve both the electronic and Li^+ conductivity of Si-nGO. Our study shows that a minor alteration in the

strategy of preparation of electrode materials can remarkably improve the stability of the electrode material.

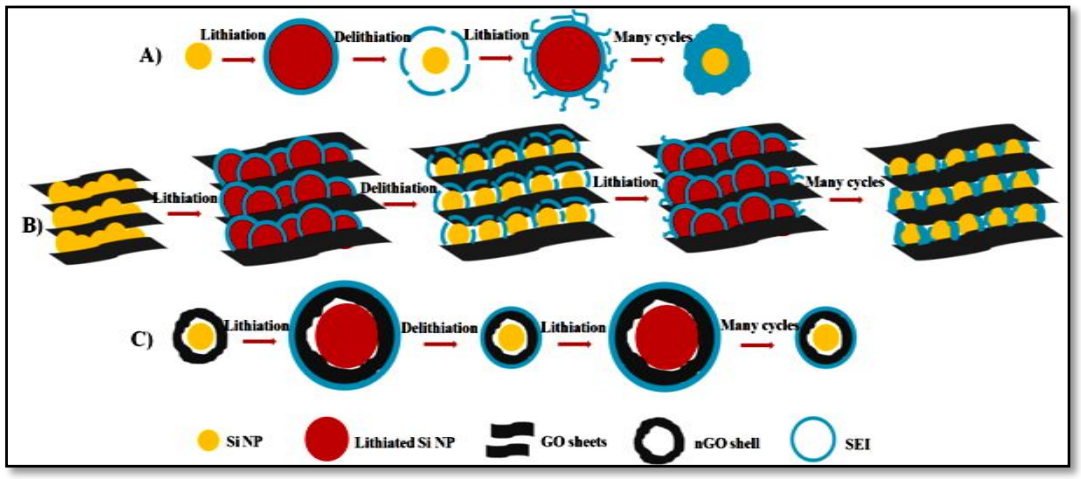

Figure 7.11. Schematic (cross sectional view) showing the formation and stability of SEI during charge-discharge cycles for: (A): Si NP alone (B): Si-GO intercalated structure and (C): Si-nGO core-shell structure. (Both A & B illustrate the unstable and repeated SEI formation over Si NPs during charge-discharge cycles and C illustrates the SEI stability during charge-discharge cycles due to the presence of nGO shell over Si NPs)

Comparing the rate performance of Si-nGO anode to the literature reports of modified Si based anodes; most of the systems fail during higher current rate cycling beyond a limit. For example, Sun et al., proposed an amine functionalized Si NP-GO intercalated structure (C. Sun et al., 2014) whose capacity degraded to 27% of the initial capacity at a current rate of 4.2 Ag^{-1}. The Si-pomegranate anode reported by Liu et al. exhibited < 30% capacity retention cycled at 8.4 Ag^{-1} current rate (N. Liu et al., 2014). Similarly, the Si-Gr composite anode prepared by Hu et al., showed 28% capacity retention at ~1.4 Ag^{-1} current rate (R. Hu et al., 2014). A hollow core–shell structured Si-C nanocomposite anode proposed by Liu et al. exhibited ~30% capacity retention at 8 Ag^{-1} (X. Li et al., 2012). One of the best reported in this context is a Si-polymer composite by Chen et al. (Yao Chen et al., 2014) which retained ~50% capacity retention at the rate of 16 Ag^{-1} and the stability was attributed the performance to its superior Li^{+} conductivity (a point to note is, this result probably might have achieved with a low mass loading value, the mass loading values are not mentioned in the report). In comparison, our Si-

nGO electrode exhibited 50 % capacity retention at the current rate of 18 Ag^{-1}. The better rate performance of Si-nGO anode at elevated rates can be attributed mainly to the thin and flexible nGO shell which improves the electronic conductivity and provide an easy platform for rapid Li^+ ion intake and release and thereby making the charging and discharging process easier.

The result clearly demonstrates the superior transport of Li^+ ions by the Si-nGO electrode which significantly improved the higher rate performance of the anode. The superior cycling and rate performances of the core-shell structured Si-nGO composite is attributed to the following reasons. The limiting of the volume expansion in all the directions by the thin highly flexible and robust nGO sheets due to its remarkable mechanical strength and flexibility, the ease of the transport of Li^+ ions and electrons to the Si NPs due to the core-shell structure, and most importantly avoids the formation of unstable SEI due to the core-shell structure and in addition the presence of certain extend of nano spaces between the Si NPs and nGO possibly contribute to the improved stability of the shell matrix by accommodating the volume changes occurring during charge–discharge cycles, thus improving the cycling stability.

It is a well known fact that lower mass loading of AM in the electrodes will give higher cycling stability and is not suitable for real battery electrodes. In reports, it is usual to show the stability of lower mass loading electrodes. The comparison of the cycling stability of battery electrode materials without mentioning the mass loading of AM in the electrodes is incomplete and will give a misleading picture of the stability of the electrode. Therefore, it is important to mention the mass loading of the AM when discussing the stability of electrodes. The practical view of the battery performance that could be delivered by an anode can be well understood by the amount of AM used per cm^{-2} in the battery electrode. Higher areal mass loading ($\geq$3 mg cm^{-2}) is needed to realize battery electrodes for practical applications (De Volder et al., 2013; N. Liu et al., 2014). In our electrodes, the loading of AM is in a range ~1.5-2.0 mg cm^{-2} and is closer to the practical applications value, though not the same. Most of the reported

literatures on battery electrode materials have values ranging from ≤ 0.1 to 1.5 mg cm^{-2} (de Guzman et al., 2013; R. Hu et al., 2014; X. Zhou, Cao, et al., 2012). To the best of our knowledge, high capacity and stable cycling at a mass loading level of 2.0 mg cm^{-2} and above is rarely been reported for Si based anodes. One of the best reported stability at higher mass loadings on Si anodes is by Liu et al. of a Si pomegranate anode with a stable cyclability of 150-160 cycles at the mass loading values of 1.93 mg cm^{-2} (N. Liu et al., 2014); with the same mass loading of 1.93 mg cm^{-2}, our Si-nGO anode shows similar cycle life (~160 cycles). The addition of CNT has helped to improve the stability of their electrodes, which is evident from the better stability achieved by electrodes containing 5 and 30% CNT (in the place of PVDF) compared to the electrodes without CNT, whereas, our Si-nGO electrodes were prepared using PVDF binder (15 %) alone. The better performance of Si-nGO with PVDF binder alone compared to that of the pomegranate structure is attributed to the nGO sheets which promote better conductivity compared to the amorphous carbon in the case of the pomegranate structure. There are reports showing excellent performance of Si-Gr composite anodes where the performance was achieved with particular binders like polyacrylonitrile (PAN) (Hassan et al., 2015), poly(acrylic acid) (PAA) (R. Yi et al., 2014) etc. It is simple logic that if the battery electrode can yield performance with PVDF, that means it will give better performance with other more compatible binders. Even with PVDF binder, Si-nGO showed good performance, because of the core-shell structure of the Si-nGO composite and the better conductivity and flexibility of nGO sheets as discussed earlier.

The excellent performance of Si-nGO cells at higher mass loading indicates successful achievement of a core-shell structure. Moreover, the procedure adapted in our method avoids the use of hazardous chemicals, multi step reactions and heavy reaction conditions, thus is simpler and environmental friendly. Further on, in order to check the reproducibility of the results, a second batch of experiments was carried out, and the comparison of cycle life performances of the two batches of the Si-nGO electrodes are depicted in Figure 7.12. As seen from the result, the coin cells prepared in both the batches followed

exactly the same path in their cycle life Vs. Coulombic efficiency curves. The results show that Si-Gr core-shell structure is a promising anode material for advanced LIBs. Furthermore, the Si-nGO can be reduced to Si-nrGO which might improve the electrochemical performance of the anode as it can improve the conductivity of the matrix. As an extension, we intend to study the performance of Si-nrGO as anode material for LIBs.

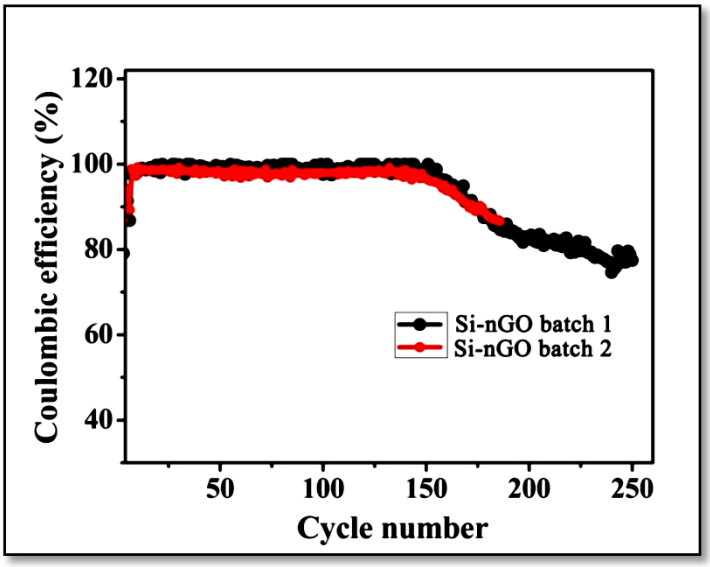

Figure 7.12. Comparison of cycle life performances of two batches of the Si-nGO electrodes prepared

Table 7.1 compares Si-nGO results and other literature reports of Si based anodes with reasonable stability and rate performance. The comparison of performances demonstrates that the synergistic effect of the core-shell structure and the Gr matrix improved the stability and rate performance of the Si-nGO anode to a greater extend that it can indeed be a promising electrode material for next generation LIBs.

Table 7.1. Comparison of Si-nGO anode with other literature reports of Si based anodes with reasonable stability and rate performance.

Name of anode	Structure and Materials	A.M. mass loading (mg cm^{-2})	Stability at the mentioned A.M. loading	Higher rate and Capacity retention	Reference
Si-amorphous carbon	Pomegranate, Amorphous carbon	1.93	150-160 cycles	8.4 Ag^{-1}, <30%	(N. Liu et al., 2014)
Si–wolfram carbide (WC)/Gr	Core (Si) - shell (WC)-shell (Gr)	1.12 and 1.44	200 cycles	~1.4 Ag^{-1}, 28%	(R. Hu et al., 2014)
Si@NH_2/GO	Intercalated	~1.5	400 cycles	4.2 Ag^{-1}, 27%	(C. Sun et al., 2014)
Si–amorphous carbon	Hollow core (Si) – shell (amorphous carbon)	…….	100 cycles	8 Ag^{-1}, ~30%	(X. Li et al., 2012)
Si-conductive polymer	Core (Si)-shell (polymer)	…….	400 cycles	16 Ag^{-1}, ~50%	(Yao Chen et al., 2014)
Si-GO	Intercalated	1.89	~50 cycles	8.85 Ag^{-1}, 25%	Our results
Si-nGO	Core (Si)-shell (nGO)	~1.5 and 2.0	250 and 150	18 Ag^{-1}, 50 %	Our results

7.4. Conclusions

In this work, a simple and environmental friendly strategy to prepare a Si-Gr based nanocomposite, for the first time in a core-shell structure with nGO material as the shell which remarkably improves the electrochemical performance of the anode material compared to the conventional sandwiched Si-Gr based structure. The prepared Si-nGO, exhibited superior electrochemical properties compared to that of the Si-GO structure. At the areal AM loading ~2.0 mg cm^{-2}, it showed 3-fold cycling stability compared to that of Si-GO, which implies the effect of the core-shell structure. The higher current rate performance was much superior to its intercalated counterpart. The excellent electrochemical properties of

the Si-nGO anode are attributed to the core-shell structure which limits the volume expansion of the Si NPs in all the directions, improved flexibility, robustness and conductivity offered by the thin nGO sheet matrix, the nano-spaces between the core and the shell which can accommodate the volume changes, and superior mechanical property of nGO sheets which improves the stability of the matrix and most importantly, unlike the sandwiched structure, the structure effectively minimizes the formation of unstable SEI (on the Si NPs), thus imparting stability to the anode.

CHAPTER 8

SUMMARY AND HIGHLIGHTS

8.1. Summary

EC sensors are the largest and the oldest group of chemical sensors due to the simplicity of the procedures and instrumentation required, and are easy to miniaturize and integrate into automatic systems, without compromising analytical characteristics (Antuña-Jiménez et al., 2012). However, for an EC sensor to hyphenate its possibilities to the advanced clinical and environmental monitoring devices, sensitivity, selectivity, stability and reproducibility characteristics are of immense importance. Hence, herein, we have included the designing and development of various Gr/MoS_2 based nanofunctional materials with all the studies mentioned, to meet the advance/future requirements of EC sensors in the objectives of our present study. We have developed four different EC sensing systems, characterized the materials thoroughly for their structure, composition, morphology etc., rationally chosen the analytes for each system and achieved the best EC sensing results in terms of sensitivity, selectivity, stability, reproducibility, real sample analysis etc. The mechanism underlined in each sensing system was analysed meticulously, even by the aid of various characterization techniques, explained in detail and a few conclusions were drawn.

The developed systems include the following, (i) Au-Gr/GCE for the effective nanomolar detection of biomolecules glucose and AA non-enzymatically; (ii) PGr/GCE as the physiological level and selective EC sensing platform for DA; (iii) MoS_2/GCE for the ultra trace/ ppq level detection of Hg^{2+}; and (iv) N-GQD/GCE for the sensitive EC sensing of TNP and the effective differentiation of nitrocompounds. The major findings and contributions of the study are listed in the latter section of this chapter.

Developing advanced LIBs which satisfy the demands of large scale energy storage applications, such as in electrical vehicles, smart grid, and renewable power stations require systems with substantially enhanced energy density, safety and cycle life. Si and Si composites, widely considered as promising alternative anode materials for next-generation LIBs, can satisfy these requirements provided they should surmount the pulverization and low cycle life problems. Aiming at these concerns, we have designed and developed a core-shell Si/Gr composite, Si-nGO, characterized systematically and battery performance was analyzed. The studies ended up with satisfactory cycle life and capacity results and the possible reasons were analysed and explained.

Here in this chapter we are listing out the highlights, summary and future perspectives of the work.

8.2. Major Outcomes of the Thesis

The major contributions of the present thesis are,

- A green synthesis method for Au-Gr nanocompositewas developed and applied successfully for sensing biomolecules.
- First time, Au NP functionalized Gr was tested as a non-enzymatic electrochemical sensor for glucose.
- Obtained the lowest LOD compared to the previous reports for both glucose and AA as low as 10 and 40 nM, respectively.
- The synergistic effect of Gr's catalytic activity, higher conductivity & specific SA and the EC mechanism of Au NPs, along with the higher adsorption due to the CD molecules are observed. The better dispersion and homogeneity induced by CD enhances the electrochemical performance of the Au–Gr and makes it a potential candidate for sensing applications.

- Simple mechanical ball milling method was employed to obtain solution processable Gr nanosheets in bulk (gram level).
- Lowest LOD values, compared to the literature, were reported, for DA and AA, which were as low as 1 nM. Selectivity was exhibited by the pGr/GCE towards DA and was possibly due to the unique structure of the pGr which has large aromatic domains with fewer oxidation sites and the edges rich with functional groups and/or defects. Owing to its structure, the pGr was able to simultaneously detect DA, AA and UA. Moreover, the presence of functional group rich edges was able to explain the dipsersibility of pGr in water and other polar solvents and its better electrocatalytic properties.
- For the first time, the merits of a solvent exfoliated MoS_2 for the EC sensing of Hg^{2+} was investigated and reported.
- Ultra sensitivity for Hg^{2+} was achieved with a LOD up to 10^{-15} M level (0.2 ppq).
- MoS_2/GCE was able to detect Hg^{2+} in real (tap and sea) water samples. The reason for the remarkable selectivity and sensitivity was assigned to the possible interactions between the S^{2-} groups of MoS_2 and Hg^{2+} which was confirmed by various characterization techniques. Further it was found that the electrochemistry, i.e. reduction of Hg^{2+} to Hg^0 plays a major role in the selective and enhanced sensing activity of MoS_2.
- N-doped GQD was synthesized from (PANI) as the precursor material for the first time.
- The EC sensing of TNP by N-GQD/GCE was investigated for the first time.
- The N-GQD/GCE exhibited high selectivity for nitroaromatics and was able to effectively distinguish between various nitrocompounds.
- Excellent sensitivity for TNP with a LOD of 1 nM (0.2 ppb) was obtained. The higher sensing activity can be ascribed to the higher electrocatalytic activity of the N-GQD because of the improved electronic characteristics of

N-GQD due to the *insitu* N-doping and the effective molecular interactions between the N-rich aromatic N-GQD and the aromatic nitrocompounds.

- A Si-Gr composite material was prepared, Si-nGO, for the first time in a core-shell architecture which exhibited superior electrochemical properties with a high specific capacity, cycle life, rate capability etc.

8.3. Future Perspectives

- To explore the possibilities of modified MoS_2 based nano architectures for enhanced Hg (II) sensing
- N-GQD/ Functionalized N-GQD as electrode for the EC sensing of other bio-molecules based on affinity/interaction
- Explore the possibility of N-GQD as a fluorescent sensing platform.
- Other Gr/MoS_2 based materials as matrices for Si anodes

REFERENCES

1. Abollino, O., Giacomino, A., Malandrino, M., Piscionieri, G., and Mentasti, E. (2008). Determination of mercury by anodic stripping voltammetry with a gold nanoparticle-modified glassy carbon electrode. *Electroanalysis: An International Journal Devoted to Fundamental and Practical Aspects of Electroanalysis, 20*(1): 75-83.

2. Aized, T., Khan, M. B., Raza, H., and Ilyas, M. (2017). Production routes, electromechanical properties and potential application of layered nanomaterials and 2D nanopolymeric composites—a review. *The International Journal of Advanced Manufacturing Technology, 93*(9-12): 3449-3459.

3. Alam, M., Alandis, N. M., Ansari, A. A., and Shaik, M. R. (2013). Optical and electrical studies of polyaniline/ZnO nanocomposite. *Journal of Nanomaterials, 2013*(147): 1-5.

4. Ambrosi, A. (2007). *The application of nanomaterials in electrochemical sensors and biosensors.* Dublin City University.

5. Anandhakumar, S., Mathiyarasu, J., and Phani, K. (2012). Anodic stripping voltammetric detection of mercury (ii) using Au-PEDOT modified carbon paste electrode. *Analytical Methods, 4*(8): 2486-2489.

6. Antuña-Jiménez, D., Díaz-Díaz, G., Blanco-López, M. C., Lobo-Castañón, M. J., Miranda-Ordieres, A. J., and Tuñón-Blanco, P. (2012). Molecularly imprinted electrochemical sensors: Past, Present, and Future *Molecularly Imprinted Sensors* (pp. 1-34): Elsevier.

7. Aoki, K., Osteryoung, J., and Osteryoung, R. A. (1980). Differential normal pulse voltammetry-theory. *Journal of Electroanalytical Chemistry and Interfacial Electrochemistry, 110*(1-3): 1-18.

8. Artiles, M. S., Rout, C. S., and Fisher, T. S. (2011). Graphene-based hybrid materials and devices for biosensing. *Advanced drug delivery reviews, 63*(14-15): 1352-1360.

9. Asha, K., Vaisakhan, G., and Mandal, S. (2016). Picogram sensing of trinitrophenol in aqueous medium through a water stable nanoscale coordination polymer. *Nanoscale, 8*(23): 11782-11786.

10. Aswathi, R., Ali, M. M., Shukla, A., and Sandhya, K. Y. (2015). A green method to gold–graphene nanocomposite from cyclodextrin functionalized graphene for efficient non-enzymatic electrochemical sensing applications. *RSC Advances, 5*(40): 32027-32033.

11. Aswathi, R., and Sandhya, K. Y. (2018). Ultrasensitive and selective electrochemical sensing of Hg (ii) ions in normal and sea water using solvent exfoliated MoS_2: affinity matters. *Journal of Materials Chemistry A*, *6*(30): 14602–14613.

12. Awasthi, K., Kamalakaran, R., Singh, A., and Srivastava, O. (2002). Ball-milled carbon and hydrogen storage. *International Journal of Hydrogen Energy, 27*(4): 425-432.

13. Baby, T. T., Aravind, S. J., Arockiadoss, T., Rakhi, R., and Ramaprabhu, S. (2010). Metal decorated graphene nanosheets as immobilization matrix for amperometric glucose biosensor. *Sensors and Actuators B: Chemical, 145*(1): 71-77.

14. Bai, J., Yang, Q., Li, M., Wang, S., Zhang, C., and Li, Y. (2008). Preparation of composite nanofibers containing gold nanoparticles by using poly (N-vinylpyrrolidone) and β-cyclodextrin. *Materials Chemistry and Physics, 111*(2-3): 205-208.

15. Bard, A. J. (1983). Chemical modification of electrodes. *Journal of Chemical Education, 60*(4): 302-304.

16. Bard, A. J., and Faulkner, L. R. (2000). *Electrochemical Methods: Fundamentals and Applications*: Wiley.

17. Bloom, N., and Fitzgerald, W. F. (1988). Determination of volatile mercury species at the picogram level by low-temperature gas chromatography with cold-vapour atomic fluorescence detection. *Analytica chimica acta, 208*(1): 151-161.

18. Bridel, J.-S., Azais, T., Morcrette, M., Tarascon, J.-M., and Larcher, D. (2009). Key parameters governing the reversibility of Si/carbon/CMC electrodes for Li-ion batteries. *Chemistry of materials, 22*(3): 1229-1241.

19. Brousse, T., Defives, D., Pasquereau, L., Lee, S., Herterich, U., and Schleich, D. (1997). Metal oxide anodes for Li-ion batteries. *Ionics, 3*(5-6): 332-337.

20. Brownson, D. (2013). *Graphene electrochemistry: fundamentals through to electroanalytical applications.* Manchester Metropolitan University.

21. Bruce, P. G., Scrosati, B., and Tarascon, J. M. (2008). Nanomaterials for rechargeable lithium batteries. *Angewandte Chemie International Edition, 47*(16): 2930-2946.

22. Cai, Z., Li, F., Wu, P., Ji, L., Zhang, H., Cai, C., et al. (2015). Synthesis of nitrogen-doped graphene quantum dots at low temperature for electrochemical sensing trinitrotoluene. *Analytical chemistry, 87*(23): 11803-11811.

23. Castellanos-Gomez, A., Roldán, R., Cappelluti, E., Buscema, M., Guinea, F., van der Zant, H. S., et al. (2013). Local strain engineering in atomically thin MoS_2. *Nano letters, 13*(11): 5361-5366.

24. Cazes, J. (2004). *Analytical instrumentation handbook*: CRC Press.

25. Chakrabarti, A., Lu, J., Skrabutenas, J. C., Xu, T., Xiao, Z., Maguire, J. A., et al. (2011). Conversion of carbon dioxide to few-layer graphene. *Journal of Materials Chemistry, 21*(26): 9491-9493.

26. Chan, C. K., Peng, H., Liu, G., McIlwrath, K., Zhang, X. F., Huggins, R. A., et al. (2011). High-performance lithium battery anodes using silicon nanowires. *Materials for Sustainable Energy: A Collection of Peer-Reviewed Research and Review Articles from Nature Publishing Group* (pp. 187-191): World Scientific.

27. Chang, G., Shu, H., Ji, K., Oyama, M., Liu, X., and He, Y. (2014). Gold nanoparticles directly modified glassy carbon electrode for non-enzymatic detection of glucose. *Applied Surface Science, 288*(1): 524-529.

28. Chaudhuri, R. G., and Paria, S. (2014). Visible light induced photocatalytic activity of sulfur doped hollow TiO_2 nanoparticles, synthesized via a novel route. *Dalton Transactions, 43*(14): 5526-5534.

29. Chen, D., Tang, L., and Li, J. (2010). Graphene-based materials in electrochemistry. *Chemical Society Reviews, 39*(8): 3157-3180.

30. Chen, P.-C., Xu, J., Chen, H., and Zhou, C. (2011). Hybrid silicon-carbon nanostructured composites as superior anodes for lithium ion batteries. *Nano Research, 4*(3): 290-296.

31. Chen, X., Zhu, J., Xi, Q., and Yang, W. (2012). A high performance electrochemical sensor for acetaminophen based on single-walled carbon nanotube–graphene nanosheet hybrid films. *Sensors and Actuators B: Chemical, 161*(1): 648-654.

32. Chen, Y., Fitz Gerald, J., Chadderton, L. T., and Chaffron, L. (1999). Nanoporous carbon produced by ball milling. *Applied physics letters, 74*(19): 2782-2784.

33. Chen, Y., Zeng, S., Qian, J., Wang, Y., Cao, Y., Yang, H., et al. (2014). Li^+-conductive polymer-embedded nano-Si particles as anode material for advanced Li-ion batteries. *ACS applied materials and interfaces, 6*(5): 3508-3512.

34. Cherevko, S., and Chung, C.-H. (2009). Gold nanowire array electrode for non-enzymatic voltammetric and amperometric glucose detection. *Sensors and Actuators B: Chemical, 142*(1): 216-223.

35. Clarkson, T. W., and Magos, L. (2006). The toxicology of mercury and its chemical compounds. *Critical reviews in toxicology, 36*(8): 609-662.

36. Collins, L. W., Gibson, E., and Wendlandt, W. (1975). The thermal properties of inorganic compounds: II. Evolved gas studies of some mercury (I) and (II) compounds. *Thermochimica Acta, 11*(2): 177-185.

37. Cui, H.-F., Ye, J.-S., Zhang, W.-D., Li, C.-M., Luong, J. H., and Sheu, F.-S. (2007). Selective and sensitive electrochemical detection of glucose in neutral solution using platinum–lead alloy nanoparticle/carbon nanotube nanocomposites. *Analytica chimica acta, 594*(2): 175-183.

38. Cui, L.-F., Ruffo, R., Chan, C. K., Peng, H., and Cui, Y. (2008). Crystalline-amorphous core−shell silicon nanowires for high capacity and high current battery electrodes. *Nano letters, 9*(1): 491-495.

39. Datta, M. K., Maranchi, J., Chung, S. J., Epur, R., Kadakia, K., Jampani, P., et al. (2011). Amorphous silicon–carbon based nano-scale thin film anode materials for lithium ion batteries. *Electrochimica Acta, 56*(13): 4717-4723.

40. de Guzman, R. C., Yang, J., Cheng, M. M.-C., Salley, S. O., and Ng, K. S. (2013). A silicon nanoparticle/reduced graphene oxide composite anode with excellent nanoparticle dispersion to improve lithium ion battery performance. *Journal of Materials Science, 48*(14): 4823-4833.

41. De Marco, R., and Shackleton, J. (1999). Calibration of the Hg chalcogenide glass membrane ion-selective electrode in seawater media. *Talanta, 49*(2): 385-391.

42. De Volder, M. F., Tawfick, S. H., Baughman, R. H., and Hart, A. J. (2013). Carbon nanotubes: present and future commercial applications. *Science, 339*(6119): 535-539.

43. Ding, S., Luan, D., Boey, F. Y. C., Chen, J. S., and Lou, X. W. D. (2011). SnO_2 nanosheets grown on graphene sheets with enhanced lithium storage properties. *Chemical Communications, 47*(25): 7155-7157.

44. Dong, Y., Chen, C., Zheng, X., Gao, L., Cui, Z., Yang, H., et al. (2012). One-step and high yield simultaneous preparation of single-and multi-layer graphene quantum dots from CX-72 carbon black. *Journal of Materials Chemistry, 22*(18): 8764-8766.

45. Dong, Y., Li, G., Zhou, N., Wang, R., Chi, Y., and Chen, G. (2012). Graphene quantum dot as a green and facile sensor for free chlorine in drinking water. *Analytical chemistry, 84*(19): 8378-8382.

46. Dong, Y., Pang, H., Yang, H. B., Guo, C., Shao, J., Chi, Y., et al. (2013). Carbon-based dots co-doped with nitrogen and sulfur for high quantum yield and excitation-independent emission. *Angewandte Chemie, 125*(30): 7954-7958.

47. Dong, Y., Shao, J., Chen, C., Li, H., Wang, R., Chi, Y., et al. (2012). Blue luminescent graphene quantum dots and graphene oxide prepared by tuning the carbonization degree of citric acid. *Carbon, 50*(12): 4738-4743.

48. Eda, G., Lin, Y. Y., Mattevi, C., Yamaguchi, H., Chen, H. A., Chen, I. S., et al. (2010). Blue photoluminescence from chemically derived graphene oxide. *Advanced materials, 22*(4): 505-509.

49. Endo, M., Kim, C., Nishimura, K., Fujino, T., and Miyashita, K. (2000). Recent development of carbon materials for Li ion batteries. *Carbon, 38*(2): 183-197.

50. Eom, J.-Y., and Kwon, H.-S. (2011). Preparation of single-walled carbon nanotube/silicon composites and their lithium storage properties. *ACS applied materials and interfaces, 3*(4): 1015-1021.

51. Evanoff, K., Magasinski, A., Yang, J., and Yushin, G. (2011). Nanosilicon-coated graphene granules as anodes for Li-ion batteries. *Advanced Energy Materials, 1*(4): 495-498.

52. Fan, L., Hu, Y., Wang, X., Zhang, L., Li, F., Han, D., et al. (2012). Fluorescence resonance energy transfer quenching at the surface of graphene quantum dots for ultrasensitive detection of TNT. *Talanta, 101*(11): 192-197.

53. Fan, X.-L., Yang, Y., Xiao, P., and Lau, W.-M. (2014). Site-specific catalytic activity in exfoliated MoS_2 single-layer polytypes for hydrogen evolution: basal plane and edges. *Journal of Materials Chemistry A, 2*(48): 20545-20551.

54. Fang, L., Wang, F., Chen, Z., Qiu, Y., Zhai, T., Hu, M., et al. (2017). Flower-like MoS_2 decorated with Cu_2O nanoparticles for non-enzymatic amperometric sensing of glucose. *Talanta, 167*(5): 593-599.

55. Faridbod, F., Gupta, V. K., and Zamani, H. A. (2011). Electrochemical sensors and biosensors. *International Journal of Electrochemistry, 2011*, Article ID 352546.

56. Feng, D., Wang, F., and Chen, Z. (2009). Electrochemical glucose sensor based on one-step construction of gold nanoparticle–chitosan composite film. *Sensors and Actuators B: Chemical, 138*(2): 539-544.

57. Feng, X., Hu, J., Chen, X., Xie, J., and Liu, Y. (2009). FAST TRACK COMMUNICATION: Synthesis and electron transfer property of sulfhydryl-containing multi-walled carbon nanotube/gold nanoparticle heterojunctions. *Journal of Physics D Applied Physics, 42*(4): 042001.

58. Gao, P., Nuli, Y., He, Y.-S., Wang, J., Minett, A. I., Yang, J., et al. (2010). Direct scattered growth of MWNT on Si for high performance anode material in Li-ion batteries. *Chemical Communications, 46*(48): 9149-9151.

59. Gao, X., Xing, G., Yang, Y., Shi, X., Liu, R., Chu, W., et al. (2008). Detection of trace Hg^{2+} via induced circular dichroism of DNA wrapped around single-walled carbon nanotubes. *Journal of the American Chemical Society, 130*(29): 9190-9191.

60. Garry, L. M. (2013). *The Electrochemical Characterisation of Carbon-based Nanomaterials and their Application in the Detection of Heavy Metal Ions.* National University of Ireland Maynooth.

61. Gavrilov, N., Pašti, I. A., Mitrić, M., Travas-Sejdić, J., Ćirić-Marjanović, G., and Mentus, S. V. (2012). Electrocatalysis of oxygen reduction reaction on polyaniline-derived nitrogen-doped carbon nanoparticle surfaces in alkaline media. *Journal of Power Sources, 220*(12): 306-316.

62. Giribabu, K., Oh, S. Y., Suresh, R., Kumar, S. P., Manigandan, R., Munusamy, S., et al. (2016). Sensing of picric acid with a glassy carbon electrode modified with CuS nanoparticles deposited on nitrogen-doped reduced graphene oxide. *Microchimica Acta, 183*(8): 2421-2430.

63. Goh, M. S., and Pumera, M. (2011). Graphene-based electrochemical sensor for detection of 2, 4, 6-trinitrotoluene (TNT) in seawater: the comparison of single-, few-, and multilayer graphene nanoribbons and graphite microparticles. *Analytical and bioanalytical chemistry, 399*(1): 127-131.

64. Gómez-Cámer, J. L., Morales, J., and Sánchez, L. (2011). Anchoring Si nanoparticles to carbon nanofibers: an efficient procedure for improving Si performance in Li batteries. *Journal of Materials Chemistry, 21*(3): 811-818.

65. Gomibuchi, E., Ichikawa, T., Kimura, K., Isobe, S., Nabeta, K., and Fujii, H. (2006). Electrode properties of a double layer capacitor of nano-structured graphite produced by ball milling under a hydrogen atmosphere. *Carbon, 44*(5): 983-988.

66. Goncalves, G., Marques, P. A., Granadeiro, C. M., Nogueira, H. I., Singh, M., and Gracio, J. (2009). Surface modification of graphene nanosheets with gold nanoparticles: the role of oxygen moieties at graphene surface on gold nucleation and growth. *Chemistry of materials, 21*(20): 4796-4802.

67. Gong, J., Zhou, T., Song, D., and Zhang, L. (2010). Monodispersed Au nanoparticles decorated graphene as an enhanced sensing platform for ultrasensitive stripping voltammetric detection of mercury (II). *Sensors and Actuators B: Chemical, 150*(2): 491-497.

68. Goriparti, S., Miele, E., De Angelis, F., Di Fabrizio, E., Zaccaria, R. P., and Capiglia, C. (2014). Review on recent progress of nanostructured anode materials for Li-ion batteries. *Journal of Power Sources, 257*(7): 421-443.

69. Govindhan, M., Adhikari, B.-R., and Chen, A. (2014). Nanomaterials-based electrochemical detection of chemical contaminants. *RSC Advances, 4*(109): 63741-63760.

70. Guo, Y., Guo, S., Ren, J., Zhai, Y., Dong, S., and Wang, E. (2010). Cyclodextrin functionalized graphene nanosheets with high supramolecular recognition capability: synthesis and host-guest inclusion for enhanced electrochemical performance. *ACS nano, 4*(7): 4001-4010.

71. Guo, Y., Shu, Y., Li, A., Li, B., Pi, J., Cai, J., et al. (2017). Efficient electrochemical detection of cancer cells on in situ surface-functionalized MoS_2 nanosheets. *Journal of Materials Chemistry B, 5*(28): 5532-5538.

72. Gustavsson, I. (1986). Determination of mercury in sea water by stripping voltammetry. *Journal of Electroanalytical Chemistry and Interfacial Electrochemistry, 214*(1-2): 31-36.

73. Hadjiioannou, T., and Diamandis, E. (1977). Analytical study of a new picrate-selective membrane electrode. *Analytica chimica acta, 94*(2): 443-447.

74. Hampton, M. A., Plackowski, C., and Nguyen, A. V. (2011). Physical and chemical analysis of elemental sulfur formation during galena surface oxidation. *Langmuir, 27*(7): 4190-4201.

75. Han, D., Han, T., Shan, C., Ivaska, A., and Niu, L. (2010). Simultaneous determination of ascorbic acid, dopamine and uric acid with chitosan-graphene modified electrode. *Electroanalysis, 22*(17-18): 2001-2008.

76. Hassan, F. M., Batmaz, R., Li, J., Wang, X., Xiao, X., Yu, A., et al. (2015). Evidence of covalent synergy in silicon–sulfur–graphene yielding highly efficient and long-life lithium-ion batteries. *Nature communications, 6*(8597): 1-11.

77. Hatch, W. R., and Ott, W. L. (1968). Determination of submicrogram quantities of mercury by atomic absorption spectrophotometry. *Analytical chemistry, 40*(14): 2085-2087.

78. Heien, M. L., Khan, A. S., Ariansen, J. L., Cheer, J. F., Phillips, P. E., Wassum, K. M., et al. (2005). Real-time measurement of dopamine fluctuations after cocaine in the brain of behaving rats. *Proceedings of the National Academy of Sciences, 102*(29): 10023-10028.

79. Hou, J., Shao, Y., Ellis, M. W., Moore, R. B., and Yi, B. (2011). Graphene-based electrochemical energy conversion and storage: fuel cells, supercapacitors and lithium ion batteries. *Physical Chemistry Chemical Physics, 13*(34): 15384-15402.

80. How, G. T. S., Pandikumar, A., Ming, H. N., and Ngee, L. H. (2014). Highly exposed {001} facets of titanium dioxide modified with reduced graphene oxide for dopamine sensing. *Scientific reports, 4*(5044): 1-8.

81. Hsiao, M., Adžić, R., and Yeager, E. (1996). Electrochemical oxidation of glucose on single crystal and polycrystalline gold surfaces in phosphate buffer. *Journal of The Electrochemical Society, 143*(3): 759-767.

82. Hu, C., Liu, Y., Yang, Y., Cui, J., Huang, Z., Wang, Y., et al. (2013). One-step preparation of nitrogen-doped graphene quantum dots from oxidized debris of graphene oxide. *Journal of Materials Chemistry B, 1*(1): 39-42.

83. Hu, G., Ma, Y., Guo, Y., and Shao, S. (2008). Electrocatalytic oxidation and simultaneous determination of uric acid and ascorbic acid on the gold nanoparticles-modified glassy carbon electrode. *Electrochimica Acta, 53*(22: 6610-6615.

84. Hu, R., Sun, W., Chen, Y., Zeng, M., and Zhu, M. (2014). Silicon/graphene based nanocomposite anode: large-scale production and stable high capacity for lithium ion batteries. *Journal of Materials Chemistry A, 2*(24): 9118-9125.

85. Hu, S., Huang, Q., Lin, Y., Wei, C., Zhang, H., Zhang, W., et al. (2014). Reduced graphene oxide-carbon dots composite as an enhanced material for electrochemical determination of dopamine. *Electrochimica Acta, 130*(6): 805-809.

86. Huang, J. (1999). HRTEM and EELS studies of defects structure and amorphous-like graphite induced by ball-milling. *Acta materialia, 47*(6): 1801-1808.

87. Huang, J., and Kaner, R. B. (2004). A general chemical route to polyaniline nanofibers. *Journal of the American Chemical Society, 126*(3): 851-855.

88. Huang, J., Wang, L., Shi, C., Dai, Y., Gu, C., and Liu, J. (2014). Selective detection of picric acid using functionalized reduced graphene oxide sensor device. *Sensors and Actuators B: Chemical, 196*(6): 567-573.

89. Huang, K.-J., Liu, Y.-J., Liu, Y.-M., and Wang, L.-L. (2014). Molybdenum disulfide nanoflower-chitosan-Au nanoparticles composites based electrochemical sensing platform for bisphenol A determination. *Journal of hazardous materials, 276*(7): 207-215.

90. Huang, K.-J., Wang, L., Li, J., and Liu, Y.-M. (2013). Electrochemical sensing based on layered MoS_2–graphene composites. *Sensors and Actuators B: Chemical, 178*(3): 671-677.

91. Huang, K.-J., Zhang, J.-Z., Liu, Y.-J., and Wang, L.-L. (2014). Novel electrochemical sensing platform based on molybdenum disulfide nanosheets-polyaniline composites and Au nanoparticles. *Sensors and Actuators B: Chemical, 194*(4): 303-310.

92. Huang, T., Meng, F., and Qi, L. (2009). Facile synthesis and one-dimensional assembly of cyclodextrin-capped gold nanoparticles and their applications in catalysis and surface-enhanced Raman scattering. *The Journal of Physical Chemistry C, 113*(31): 13636-13642.

93. Imamura, H., Kusuhara, M., Minami, S., Matsumoto, M., Masanari, K., Sakata, Y., et al. (2003). Carbon nanocomposites synthesized by high-energy mechanical milling of graphite and magnesium for hydrogen storage. *Acta materialia, 51*(20): 6407-6414.

94. Jackowska, K., and Krysinski, P. (2013). New trends in the electrochemical sensing of dopamine. *Analytical and bioanalytical chemistry, 405*(11): 3753-3771.

95. Jang, H. D., Kim, S. K., Chang, H., Roh, K.-M., Choi, J.-W., and Huang, J. (2012). A glucose biosensor based on TiO_2–graphene composite. *Biosensors and Bioelectronics, 38*(1): 184-188.

96. Jena, B. K., and Raj, C. R. (2006). Enzyme-free amperometric sensing of glucose by using gold nanoparticles. *Chemistry–A European Journal, 12*(10): 2702-2708.

97. Jia, H., Gao, P., Yang, J., Wang, J., Nuli, Y., and Yang, Z. (2011). Novel three-dimensional mesoporous silicon for high power lithium-ion battery anode material. *Advanced Energy Materials, 1*(6): 1036-1039.

98. Jiang, J., and Du, X. (2014). Sensitive electrochemical sensors for simultaneous determination of ascorbic acid, dopamine, and uric acid based on Au@Pd-reduced graphene oxide nanocomposites. *Nanoscale, 6*(19): 11303-11309.

99. Jiang, S., Cheng, R., Ng, R., Huang, Y., and Duan, X. (2015). Highly sensitive detection of mercury (II) ions with few-layer molybdenum disulfide. *Nano Research, 8*(1): 257-262.

100. Ju, J., and Chen, W. (2014). Synthesis of highly fluorescent nitrogen-doped graphene quantum dots for sensitive, label-free detection of Fe (III) in aqueous media. *Biosensors and Bioelectronics, 58*(8): 219-225.

101. Ju, J., Zhang, R., He, S., and Chen, W. (2014). Nitrogen-doped graphene quantum dots-based fluorescent probe for the sensitive turn-on detection of glutathione and its cellular imaging. *RSC Advances, 4*(94): 52583-52589.

102. Junqueira, J. R., de Araujo, W. R., Salles, M. O., and Paixão, T. R. (2013). Flow injection analysis of picric acid explosive using a copper electrode as electrochemical detector. *Talanta, 104*(1): 162-168.

103. Kaifer, A. E., and Gómez-Kaifer, M. (1999). *Supramolecular electrochemistry*: John Wiley and Sons.

104. Kanchana, P., Sudhan, N., Anandhakumar, S., Mathiyarasu, J., Manisankar, P., and Sekar, C. (2015). Electrochemical detection of mercury using biosynthesized hydroxyapatite nanoparticles modified glassy carbon electrodes without preconcentration. *RSC Advances, 5*(84): 68587-68594.

105. Kim, H.-i., Moon, G.-h., Monllor-Satoca, D., Park, Y., and Choi, W. (2012). Solar photoconversion using graphene/TiO_2 composites: nanographene shell on TiO_2 core versus TiO_2 nanoparticles on graphene sheet. *The Journal of Physical Chemistry C, 116*(1): 1535-1543.

106. Kim, H., and Cho, J. (2008). Superior lithium electroactive mesoporous Si@ Carbon core-shell nanowires for lithium battery anode material. *Nano letters, 8*(11): 3688-3691.

107. Kim, Y.-R., Bong, S., Kang, Y.-J., Yang, Y., Mahajan, R. K., Kim, J. S., et al. (2010). Electrochemical detection of dopamine in the presence of ascorbic acid using graphene modified electrodes. *Biosensors and Bioelectronics, 25*(10): 2366-2369.

108. Kong, F.-Y., Li, X.-R., Zhao, W.-W., Xu, J.-J., and Chen, H.-Y. (2012). Graphene oxide–thionine–Au nanostructure composites: preparation and applications in non-enzymatic glucose sensing. *Electrochemistry Communications, 14*(1): 59-62.

109. Koo, B., Kim, H., Cho, Y., Lee, K. T., Choi, N. S., and Cho, J. (2012). A highly cross-linked polymeric binder for high-performance silicon negative electrodes in lithium ion batteries. *Angewandte Chemie, 124*(35): 8892-8897.

110. Kounaves, S. P. (1997). Voltammetric techniques (pp. 709-726): Prentice Hall, Upper Saddle River, NJ, USA.

111. Kovalenko, I., Zdyrko, B., Magasinski, A., Hertzberg, B., Milicev, Z., Burtovyy, R., et al. (2011). A major constituent of brown algae for use in high-capacity Li-ion batteries. *Science*, 1209150.

112. Kumar, N., George, B. P. A., Abrahamse, H., Parashar, V., and Ngila, J. C. (2017). Sustainable one-step synthesis of hierarchical microspheres of PEGylated MoS2 nanosheets and MoO_3 nanorods: Their cytotoxicity towards lung and breast cancer cells. *Applied Surface Science, 396*(2), 8-18.

113. Kurkina, T. (2012). Label-free electrical biosensing based on electrochemically functionalized carbon nanostructures.

114. Lahiri, I., and Choi, W. (2013). Carbon nanostructures in lithium ion batteries: past, present, and future. *Critical Reviews in Solid State and Materials Sciences, 38*(2): 128-166.

115. Laina, A., and Girish Kumar, K. (2013). *Voltammetric Sensors for the Determination of Pharmaceuticals.* Cochin University of Science And Technology.

116. Laviron, E. (1979). General expression of the linear potential sweep voltammogram in the case of diffusionless electrochemical systems. *Journal of Electroanalytical Chemistry and Interfacial Electrochemistry, 101*(1): 19-28.

117. Lee, J. S., Han, M. S., and Mirkin, C. A. (2007). Colorimetric detection of mercuric ion (Hg^{2+}) in aqueous media using DNA-functionalized gold nanoparticles. *Angewandte Chemie International Edition, 46*(22): 4093-4096.

118. Lei, J., Lu, X., Wang, W., Bian, X., Xue, Y., Wang, C., et al. (2012). Fabrication of MnO_2/graphene oxide composite nanosheets and their application in hydrazine detection. *RSC Advances, 2*(6): 2541-2544.

119. Li, H.-Q., Wang, Y.-G., Wang, C.-X., and Xia, Y.-Y. (2008). A competitive candidate material for aqueous supercapacitors: High surface-area graphite. *Journal of Power Sources, 185*(2): 1557-1562.

120. Li, J., Guo, S., Zhai, Y., and Wang, E. (2009). High-sensitivity determination of lead and cadmium based on the Nafion-graphene composite film. *Analytica chimica acta, 649*(2): 196-201.

121. Li, L. L., Ji, J., Fei, R., Wang, C. Z., Lu, Q., Zhang, J. R., et al. (2012). A facile microwave avenue to electrochemiluminescent two-color graphene quantum dots. *Advanced Functional Materials, 22*(14): 2971-2979.

122. Li, M., Wu, W., Ren, W., Cheng, H.-M., Tang, N., Zhong, W., et al. (2012). Synthesis and upconversion luminescence of N-doped graphene quantum dots. *Applied physics letters, 101*(10): 103107.

123. Li, Q., Qin, X., Luo, Y., Lu, W., Chang, G., Asiri, A. M., et al. (2012). One-pot synthesis of Ag nanoparticles/reduced graphene oxide nanocomposites and their application for nonenzymatic H_2O_2 detection. *Electrochimica Acta, 83*(11): 283-287.

124. Li, S.-j., Deng, D.-H., Pang, H., Liu, L., Xing, Y., and Liu, S.-R. (2012). Preparation of electrochemically reduced graphene oxide-modified electrode and its application for determination of p-aminophenol. *Journal of Solid State Electrochemistry, 16*(9): 2883-2889.

125. Li, S.-J., He, J.-Z., Zhang, M.-J., Zhang, R.-X., Lv, X.-L., Li, S.-H., et al. (2013). Electrochemical detection of dopamine using water-soluble sulfonated graphene. *Electrochimica Acta, 102*(7): 58-65.

126. Li, X., Meduri, P., Chen, X., Qi, W., Engelhard, M. H., Xu, W., et al. (2012). Hollow core–shell structured porous Si–C nanocomposites for Li-ion battery anodes. *Journal of Materials Chemistry, 22*(22): 11014-11017.

127. Li, X., and Zhu, H. (2015). Two-dimensional MoS_2: Properties, preparation, and applications. *Journal of Materiomics, 1*(1): 33-44.

128. Li, Y., Hu, Y., Zhao, Y., Shi, G., Deng, L., Hou, Y., et al. (2011). An electrochemical avenue to green-luminescent graphene quantum dots as potential electron-acceptors for photovoltaics. *Advanced materials, 23*(6): 776-780.

129. Li, Y., Zhao, Y., Cheng, H., Hu, Y., Shi, G., Dai, L., et al. (2012). Nitrogen-doped graphene quantum dots with oxygen-rich functional groups. *Journal of the American Chemical Society, 134*(1): 15-18.

130. Li, Y., Zhou, Z., Shen, P., and Chen, Z. (2009). Spin gapless semiconductor−metal−half-metal properties in nitrogen-doped zigzag graphene nanoribbons. *ACS nano, 3*(7): 1952-1958.

131. Li, Z., Wang, Y., Ni, Y., and Kokot, S. (2015). A sensor based on blue luminescent graphene quantum dots for analysis of a common explosive

substance and an industrial intermediate, 2, 4, 6-trinitrophenol. *Spectrochimica Acta Part A: Molecular and Biomolecular Spectroscopy, 137*(2): 1213-1221.

132. Liang, B., Liu, Y., and Xu, Y. (2014). Silicon-based materials as high capacity anodes for next generation lithium ion batteries. *Journal of Power Sources, 267*(12): 469-490.

133. Lin, L., Rong, M., Lu, S., Song, X., Zhong, Y., Yan, J., et al. (2015). A facile synthesis of highly luminescent nitrogen-doped graphene quantum dots for the detection of 2, 4, 6-trinitrophenol in aqueous solution. *Nanoscale, 7*(5): 1872-1878.

134. Liu, H., Liu, Y., and Zhu, D. (2011). Chemical doping of graphene. *Journal of Materials Chemistry, 21*(10): 3335-3345.

135. Liu, H., Su, X., Duan, C., Dong, X., and Zhu, Z. (2014). A novel hydrogen peroxide biosensor based on immobilized hemoglobin in 3D flower-like MoS_2 microspheres structure. *Materials Letters, 122*(5): 182-185.

136. Liu, K., Fu, H., Xie, Y., Zhang, L., Pan, K., and Zhou, W. (2008). Assembly of β-cyclodextrins acting as molecular bricks onto multiwall carbon nanotubes. *The Journal of Physical Chemistry C, 112*(4): 951-957.

137. Liu, M., Wang, L., Deng, J., Chen, Q., Li, Y., Zhang, Y., et al. (2012). Highly sensitive and selective dopamine biosensor based on a phenylethynyl ferrocene/graphene nanocomposite modified electrode. *Analyst, 137*(19): 4577-4583.

138. Liu, N., Lu, Z., Zhao, J., McDowell, M. T., Lee, H.-W., Zhao, W., et al. (2014). A pomegranate-inspired nanoscale design for large-volume-change lithium battery anodes. *Nature nanotechnology, 9*(3): 187-192.

139. Liu, S.-Q., Sun, W.-H., and Hu, F.-T. (2012). Graphene nano sheet-fabricated electrochemical sensor for the determination of dopamine in the presence of ascorbic acid using cetyltrimethylammonium bromide as the discriminating agent. *Sensors and Actuators B: Chemical, 173(*10): 497-504.

140. Liu, S., Yan, J., He, G., Zhong, D., Chen, J., Shi, L., et al. (2012). Layer-by-layer assembled multilayer films of reduced graphene oxide/gold nanoparticles for the electrochemical detection of dopamine. *Journal of Electroanalytical Chemistry, 672*(5): 40-44.

141. Liu, W., Yan, X., Chen, J., Feng, Y., and Xue, Q. (2013). Novel and high-performance asymmetric micro-supercapacitors based on graphene quantum dots and polyaniline nanofibers. *Nanoscale, 5*(13): 6053-6062.

142. Lu, G., Ocola, L. E., and Chen, J. (2009). Reduced graphene oxide for room-temperature gas sensors. *Nanotechnology, 20*(44): 445502.

143. Lu, J., Yeo, P. S. E., Gan, C. K., Wu, P., and Loh, K. P. (2011). Transforming C 60 molecules into graphene quantum dots. *Nature nanotechnology, 6*(4): 247-252.

144. Lu, L., Zhang, O., Xu, J., Wen, Y., Duan, X., Yu, H., et al. (2013). A facile one-step redox route for the synthesis of graphene/poly (3, 4-ethylenedioxythiophene) nanocomposite and their applications in biosensing. *Sensors and Actuators B: Chemical, 181*(5): 567-574.

145. Lv, W., Sun, F., Tang, D.-M., Fang, H.-T., Liu, C., Yang, Q.-H., et al. (2011). A sandwich structure of graphene and nickel oxide with excellent supercapacitive performance. *Journal of Materials Chemistry, 21*(25): 9014-9019.

146. Ma, D., Cao, Z., and Hu, A. (2014). Si-based anode materials for Li-ion batteries: a mini review. *Nano-Micro Letters, 6*(4): 347-358.

147. Magasinski, A., Zdyrko, B., Kovalenko, I., Hertzberg, B., Burtovyy, R., Huebner, C. F., et al. (2010). Toward efficient binders for Li-ion battery Si-based anodes: polyacrylic acid. *ACS applied materials and interfaces, 2*(11): 3004-3010.

148. Mahyari, M. (2016). Electrochemical determination of picric acid based on platinum nanoparticles–reduced graphene oxide composite. *International journal of environmental analytical chemistry, 96*(15): 1455-1468.

149. Manivannan, S., and Ramaraj, R. (2011). Polymer-embedded gold and gold/silver nanoparticle-modified electrodes and their applications in catalysis and sensors. *Pure and Applied Chemistry, 83*(11): 2041-2053.

150. Marcolino-Junior, L. H., Janegitz, B. C., Lourençao, B. C., and Fatibello-Filho, O. (2007). Anodic stripping voltammetric determination of mercury in water using a chitosan-modified carbon paste electrode. *Analytical Letters, 40*(16): 3119-3128.

151. Matsoso, B. J., Ranganathan, K., Mutuma, B. K., Lerotholi, T., Jones, G., and Coville, N. J. (2016). Time-dependent evolution of the nitrogen

configurations in N-doped graphene films. *RSC Advances, 6*(108): 106914-106920.

152. Mebarki, B., Draoui, B., Allaou, B., Rahmani, L., and Benachour, E. (2013). Impact of the air-conditioning system on the power consumption of an electric vehicle powered by lithium-ion battery. *Modelling and Simulation in Engineering, 2013*, Article No. 26.

153. Miao, P., Liu, L., Li, Y., and Li, G. (2009). A novel electrochemical method to detect mercury (II) ions. *Electrochemistry Communications, 11*(10): 1904-1907.

154. Minati, L., Torrengo, S., Maniglio, D., Migliaresi, C., and Speranza, G. (2012). Luminescent graphene quantum dots from oxidized multi-walled carbon nanotubes. *Materials Chemistry and Physics, 137*(1): 12-16.

155. Mohamed Mukthar Ali, and Sandhya, K. Y. (2017). A novel approach for P25-carbon dot composite and the reactive oxygen species involved in the visible light photocatalytic mineralization of rhodamine B. *ChemistrySelect, 2*(35): 11840-11845.

156. Muszynski, R., Seger, B., and Kamat, P. V. (2008). Decorating graphene sheets with gold nanoparticles. *The Journal of Physical Chemistry C, 112*(14): 5263-5266.

157. Naik, R. R., Swamy, B. K., Chandra, U., Niranjana, E., Sherigara, B., and Jayadevappa, H. (2009). Separation of ascorbic acid, dopamine and uric acid by acetone/water modified carbon paste electrode: a cyclic voltammetric study. *Int. J. Electrochem. Sci, 4*(6): 855-862.

158. Nguyen, H. T., Yao, F., Zamfir, M. R., Biswas, C., So, K. P., Lee, Y. H., et al. (2011). Highly interconnected Si nanowires for improved stability Li-ion battery anodes. *Advanced Energy Materials, 1*(6): 1154-1161.

159. Novoselov, K. S., Geim, A. K., Morozov, S. V., Jiang, D., Zhang, Y., Dubonos, S. V., et al. (2004). Electric field effect in atomically thin carbon films. *Science, 306*(5696): 666-669.

160. Oumellal, Y., Delpuech, N., Mazouzi, D., Dupre, N., Gaubicher, J., Moreau, P., et al. (2011). The failure mechanism of nano-sized Si-based negative electrodes for lithium ion batteries. *Journal of Materials Chemistry, 21*(17): 6201-6208.

161. Pan, D., Zhang, J., Li, Z., and Wu, M. (2010). Hydrothermal route for cutting graphene sheets into blue-luminescent graphene quantum dots. *Advanced materials, 22*(6): 734-738.

162. Park, M.-H., Kim, M. G., Joo, J., Kim, K., Kim, J., Ahn, S., et al. (2009). Silicon nanotube battery anodes. *Nano letters, 9*(11): 3844-3847.

163. Pasta, M., Ruffo, R., Falletta, E., Mari, C., and Della Pina, C. (2010). Alkaline glucose oxidation on nanostructured gold electrodes. *Gold Bulletin, 43*(1): 57-64.

164. Patey, T. J. (2009). *Oxide nanoparticles for electrodes in lithium-ion batteries.* ETH Zurich.

165. Peik-See, T., Pandikumar, A., Nay-Ming, H., Hong-Ngee, L., and Sulaiman, Y. (2014). Simultaneous electrochemical detection of dopamine and ascorbic acid using an iron oxide/reduced graphene oxide modified glassy carbon electrode. *Sensors, 14*(8): 15227-15243.

166. Peng, J., Gao, W., Gupta, B. K., Liu, Z., Romero-Aburto, R., Ge, L., et al. (2012). Graphene quantum dots derived from carbon fibers. *Nano letters, 12*(2): 844-849.

167. Pérez López, B. (2009). *Carbon nanotubes for electrochemical (bio) sensing*: Universitat Autònoma de Barcelona.

168. Pillay, J. (2009). *Electrochemical properties of self-assembled films of single-walled carbon nanotubes, monolayer-protected clusters of gold nanoparticles and iron (II) phthalocyanines at gold electrodes.* University of Pretoria.

169. Plechinger, G., Heydrich, S., Eroms, J., Weiss, D., Schüller, C., and Korn, T. (2012). Raman spectroscopy of the interlayer shear mode in few-layer MoS 2 flakes. *Applied physics letters, 101*(10): 101906.

170. Pollack, B., Holmberg, S., George, D., Tran, I., Madou, M., and Ghazinejad, M. (2017). Nitrogen-rich polyacrylonitrile-based graphitic carbons for hydrogen peroxide sensing. *Sensors, 17*(10): 2407.

171. Prchal, V., Vyskocil, V., and Barek, J. (2010). Voltammetric determination of environmental pollutant 2, 4, 6-Trinitrophenol using a bismuth bulk electrode. *J Electrochem Soc, 164*: H316-H320.

172. Pumera, M., and Loo, A. H. (2014). Layered transition-metal dichalcogenides (MoS2 and WS2) for sensing and biosensing. *TrAC Trends in Analytical Chemistry, 61*(10): 49-53.

173. Pushpa, R., Annaselvi, A., and Subramaniam, P. (2013). Synthesis and characterization of β-cyclodextrin capped silver nanoparticles. *International Journal of Nanomaterials and Biostructures, 3*(1): 26-30.

174. Qian, T., Yu, C., Wu, S., and Shen, J. (2013a). Gold nanoparticles coated polystyrene/reduced graphite oxide microspheres with improved dispersibility and electrical conductivity for dopamine detection. *Colloids and Surfaces B: Biointerfaces, 112*(12): 310-314.

175. Qian, T., Yu, C., Wu, S., and Shen, J. (2013b). In situ polymerization of highly dispersed polypyrrole on reduced graphite oxide for dopamine detection. *Biosensors and Bioelectronics, 50*(12): 157-160.

176. Rajawat, D. S., Srivastava, S., and Satsangee, S. P. (2012). Electrochemical determination of mercury at trace levels using eichhornia crassipes modified carbon paste electrode. *Int. J. Electrochem. Sci, 7*(11): 11456-11469.

177. Ramachandran, A., Panda, S., and Yesodha, S. K. (2018). Physiological level and selective electrochemical sensing of dopamine by a solution processable graphene and its enhanced sensing property in general. *Sensors and Actuators B: Chemical, 256*(3): 488-497.

178. Ramakrishna Matte, H., Gomathi, A., Manna, A. K., Late, D. J., Datta, R., Pati, S. K., et al. (2010). MoS2 and WS2 analogues of graphene. *Angewandte Chemie International Edition, 49*(24): 4059-4062.

179. Ratner, N., and Mandler, D. (2015). Electrochemical detection of low concentrations of mercury in water using gold nanoparticles. *Analytical chemistry, 87*(10): 5148-5155.

180. Razmi, H., and Mohammad-Rezaei, R. (2013). Graphene quantum dots as a new substrate for immobilization and direct electrochemistry of glucose oxidase: application to sensitive glucose determination. *Biosensors and Bioelectronics, 41*(3): 498-504.

181. Roa-Morales, G., Ramírez-Silva, M., Gonzalez, R. L., Galicia, L., and Romero-Romo, M. (2005). Electrochemical characterization and determination of mercury using carbon paste electrodes modified with cyclodextrins. *Electroanalysis: An International Journal Devoted to Fundamental and Practical Aspects of Electroanalysis, 17*(8): 694-700.

182. Rong, M., Lin, L., Song, X., Zhao, T., Zhong, Y., Yan, J., et al. (2015). A label-free fluorescence sensing approach for selective and sensitive detection of 2, 4, 6-trinitrophenol (TNP) in aqueous solution using graphitic carbon nitride nanosheets. *Analytical chemistry, 87*(2): 1288-1296.

183. Ryou, M. H., Kim, J., Lee, I., Kim, S., Jeong, Y. K., Hong, S., et al. (2013). Mussel-inspired adhesive binders for high-performance silicon nanoparticle anodes in lithium-ion batteries. *Advanced materials, 25*(11): 1571-1576.

184. Salamon, J., Sathishkumar, Y., Ramachandran, K., Lee, Y. S., Yoo, D. J., and Kim, A. R. (2015). One-pot synthesis of magnetite nanorods/graphene composites and its catalytic activity toward electrochemical detection of dopamine. *Biosensors and Bioelectronics, 64*(2): 269-276.

185. Sangsefidi, F. S., Esmaeili-Zare, M., and Salavati-Niasari, M. (2015). Hydrothermal synthesis and characterization of HgS nanostructures assisted by inorganic precursor. *Journal of Industrial and Engineering Chemistry, 28*(8): 197-201.

186. Shan, C., Yang, H., Han, D., Zhang, Q., Ivaska, A., and Niu, L. (2010). Graphene/AuNPs/chitosan nanocomposites film for glucose biosensing. *Biosensors and Bioelectronics, 25*(5): 1070-1074.

187. Shen, C., Hui, C., Yang, T., Xiao, C., Tian, J., Bao, L., et al. (2008). Monodisperse noble-metal nanoparticles and their surface enhanced Raman scattering properties. *Chemistry of materials, 20*(22): 6939-6944.

188. Shen, J., Zhu, Y., Chen, C., Yang, X., and Li, C. (2011). Facile preparation and upconversion luminescence of graphene quantum dots. *Chemical Communications, 47*(9): 2580-2582.

189. Shenderova, O., Zhirnov, V., and Brenner, D. (2002). Carbon nanostructures. *Critical Reviews in Solid State and Material Sciences, 27*(3-4): 227-356.

190. Shukla, A., and Kumar, T. P. (2008). Materials for next-generation lithium batteries. *Current science, 94*(3): 314-331.

191. Sindhu, I., and Girish Kumar, K. (2011). *Fabrication of Electrochemical Sensors for the Determination of Pharmaceuticals.* Cochin University of Science and Technology.

192. Sinha, A., Tan, B., Huang, Y., Zhao, H., Dang, X., Chen, J., et al. (2018). MoS_2 nanostructures for electrochemical sensing of multidisciplinary targets: A Review. *TrAC Trends in Analytical Chemistry, 102*(5): 75-90.

193. Sivakkumar, S., Milev, A. S., and Pandolfo, A. (2011). Effect of ball-milling on the rate and cycle-life performance of graphite as negative electrodes in lithium-ion capacitors. *Electrochimica Acta, 56*(27): 9700-9706.

194. Skoog, D. A., Holler, F. J., and Nieman, T. A. (1998). *Principles of Instrumental Analysis*: Saunders College Pub.

195. Smart, R. S. C., Skinner, W. M., and Gerson, A. R. (1999). XPS of sulphide mineral surfaces: metal-deficient, polysulphides, defects and elemental sulphur. *Surface and Interface Analysis: An International Journal devoted to the development and application of techniques for the analysis of surfaces, interfaces and thin films, 28*(1): 101-105.

196. Stankovich, S., Dikin, D. A., Piner, R. D., Kohlhaas, K. A., Kleinhammes, A., Jia, Y., et al. (2007). Synthesis of graphene-based nanosheets via chemical reduction of exfoliated graphite oxide. *Carbon, 45*(7): 1558-1565.

197. Stergiou, D. V., Diamanti, E. K., Gournis, D., and Prodromidis, M. I. (2010). Comparative study of different types of graphenes as electrocatalysts for ascorbic acid. *Electrochemistry Communications, 12*(10): 1307-1309.

198. Stradiotto, N. R., Yamanaka, H., and Zanoni, M. V. B. (2003). Electrochemical sensors: a powerful tool in analytical chemistry. *Journal of the Brazilian Chemical Society, 14*(2): 159-173.

199. Su, S., Cao, W., Liu, W., Lu, Z., Zhu, D., Chao, J., et al. (2017). Dual-mode electrochemical analysis of microRNA-21 using gold nanoparticle-decorated MoS_2 nanosheet. *Biosensors and Bioelectronics, 94*(8): 552-559.

200. Su, X., Wu, Q., Li, J., Xiao, X., Lott, A., Lu, W., et al. (2014). Silicon-based nanomaterials for lithium-ion batteries: a review. *Advanced Energy Materials, 4*(1): 1300882.

201. Sun, C., Deng, Y., Wan, L., Qin, X., and Chen, G. (2014). Graphene oxide-immobilized NH2-terminated silicon nanoparticles by cross-linked interactions for highly stable silicon negative electrodes. *ACS applied materials and interfaces, 6*(14): 11277-11285.

202. Sun, H., Chao, J., Zuo, X., Su, S., Liu, X., Yuwen, L., et al. (2014). Gold nanoparticle-decorated MoS_2 nanosheets for simultaneous detection of ascorbic acid, dopamine and uric acid. *RSC Advances, 4*(52): 27625-27629.

203. Sun, H., Gao, N., Wu, L., Ren, J., Wei, W., and Qu, X. (2013). Highly photoluminescent amino-functionalized graphene quantum dots used for sensing copper ions. *Chemistry–A European Journal, 19*(40): 13362-13368.

204. Sun, H., Wu, L., Wei, W., and Qu, X. (2013). Recent advances in graphene quantum dots for sensing. *Materials Today, 16*(11): 433-442.

205. Sun, W., Wang, X., Wang, Y., Ju, X., Xu, L., Li, G., et al. (2013). Application of graphene–SnO2 nanocomposite modified electrode for the sensitive electrochemical detection of dopamine. *Electrochimica Acta, 87*(1): 317-322.

206. Sun, W., Wang, Y., Zhang, Y., Ju, X., Li, G., and Sun, Z. (2012). Poly (methylene blue) functionalized graphene modified carbon ionic liquid electrode for the electrochemical detection of dopamine. *Analytica chimica acta, 751*(11): 59-65.

207. Tang, L., Ji, R., Cao, X., Lin, J., Jiang, H., Li, X., et al. (2012). Deep ultraviolet photoluminescence of water-soluble self-passivated graphene quantum dots. *ACS nano, 6*(6): 5102-5110.

208. Tang, L., Wang, Y., Li, Y., Feng, H., Lu, J., and Li, J. (2009). Preparation, structure, and electrochemical properties of reduced graphene sheet films. *Advanced Functional Materials, 19*(17): 2782-2789.

209. Tarascon, J. M., and Armand, M. (2001). Issues and challenges facing rechargeable lithium batteries. *Nature, 414*(6861): 359-67.

210. Tian, X., Cheng, C., Yuan, H., Du, J., Xiao, D., Xie, S., et al. (2012). Simultaneous determination of l-ascorbic acid, dopamine and uric acid with gold nanoparticles–β-cyclodextrin–graphene-modified electrode by square wave voltammetry. *Talanta, 93*(5): 79-85.

211. Van Tam, T., Trung, N. B., Kim, H. R., Chung, J. S., and Choi, W. M. (2014). One-pot synthesis of N-doped graphene quantum dots as a fluorescent sensing platform for Fe3+ ions detection. *Sensors and Actuators B: Chemical, 202*(10): 568-573.

212. Venugopal, G., Krishnamoorthy, K., Mohan, R., and Kim, S.-J. (2012). An investigation of the electrical transport properties of graphene-oxide thin films. *Materials Chemistry and Physics, 132*(1): 29-33.

213. Vyskočil, V., Navrátil, T., Daňhel, A., Dědík, J., Krejčová, Z., Škvorová, L., et al. (2011). Voltammetric determination of selected nitro compounds at a polished silver solid amalgam composite electrode. *Electroanalysis, 23*(1): 129-139.

214. Wang, C., Wu, G., and Li, W. (1998). Lithium insertion in ball-milled graphite. *Journal of Power Sources, 76*(1): 1-10.

215. Wang, D., Li, F., Ping, G., Chen, D., Fan, M., Qin, L., et al. (2013). Preparation and Enhanced Electrochemical Anode Performance of Si/Graphene Nanocomposites. *Int. J. Electrochem. Sci, 8*(7): 9618-9628.

216. Wang, F., Gu, Z., Lei, W., Wang, W., Xia, X., and Hao, Q. (2014). Graphene quantum dots as a fluorescent sensing platform for highly efficient detection of copper (II) ions. *Sensors and Actuators B: Chemical, 190*(1): 516-522.

217. Wang, H., Yang, Y., Liang, Y., Robinson, J. T., Li, Y., Jackson, A., et al. (2011). Graphene-wrapped sulfur particles as a rechargeable lithium–sulfur battery cathode material with high capacity and cycling stability. *Nano letters, 11*(7): 2644-2647.

218. Wang, J. (1994). Analytical Electrochemistry, VCH, Publishers. *New York*.

219. Wang, T., Chen, S., Pang, H., Xue, H., and Yu, Y. (2017). MoS_2-based nanocomposites for electrochemical energy storage. *Advanced Science, 4*(2): 1600289.

220. Wang, T., Du, K., Liu, W., Zhang, J., and Li, M. (2015). Electrochemical sensors based on molybdenum disulfide nanomaterials. *Electroanalysis, 27*(9): 2091-2097.

221. Wang, T., Zhu, H., Zhuo, J., Zhu, Z., Papakonstantinou, P., Lubarsky, G., et al. (2013). Biosensor based on ultrasmall MoS_2 nanoparticles for electrochemical detection of H_2O_2 released by cells at the nanomolar level. *Analytical chemistry, 85*(21): 10289-10295.

222. Wang, X.-G., and Fan, Y.-J. (2009). A novel electrochemical method for the determination of trinitrophenol. *Russian Journal of Electrochemistry, 45*(10): 1188-1192.

223. Wang, X.-L., and Han, W.-Q. (2010). Graphene enhances Li storage capacity of porous single-crystalline silicon nanowires. *ACS applied materials and interfaces, 2*(12): 3709-3713.

224. Wang, X., and Zhang, X. (2013). Electrochemical co-reduction synthesis of graphene/nano-gold composites and its application to electrochemical glucose biosensor. *Electrochimica Acta, 112*(12): 774-782.

225. Wang, Y., Cao, W., Wang, L., Zhuang, Q., and Ni, Y. (2018). Electrochemical determination of 2, 4, 6-trinitrophenol using a hybrid film composed of a copper-based metal organic framework and electroreduced graphene oxide. *Microchimica Acta, 185*(6): 315.

226. Wang, Y., Li, Y., Tang, L., Lu, J., and Li, J. (2009). Application of graphene-modified electrode for selective detection of dopamine. *Electrochemistry Communications, 11*(4): 889-892.

227. Wang, Z., Yu, J., Zhang, X., Li, N., Liu, B., Li, Y., et al. (2016). Large-scale and controllable synthesis of graphene quantum dots from rice husk biomass: a comprehensive utilization strategy. *ACS applied materials and interfaces, 8*(2): 1434-1439.

228. Wei, Y., Gao, C., Meng, F.-L., Li, H.-H., Wang, L., Liu, J.-H., et al. (2011). SnO_2/reduced graphene oxide nanocomposite for the simultaneous electrochemical detection of cadmium (II), lead (II), copper (II), and mercury (II): an interesting favorable mutual interference. *The Journal of Physical Chemistry C, 116*(1): 1034-1041.

229. Welch, C. M., and Compton, R. G. (2006). The use of nanoparticles in electroanalysis: a review. *Analytical and bioanalytical chemistry, 384*(3): 601-619.

230. Welham, N., Berbenni, V., and Chapman, P. (2003). Effect of extended ball milling on graphite. *Journal of Alloys and Compounds, 349*(1-2): 255-263.

231. Wen, S., Zeng, T., Liu, L., Zhao, K., Zhao, Y., Liu, X., et al. (2011). Highly sensitive and selective DNA-based detection of mercury (II) with α-hemolysin nanopore. *Journal of the American Chemical Society, 133*(45): 18312-18317.

232. Wen, Z., Lu, D., Lei, J., Fu, Y., Wang, L., and Sun, J. (2011). The performance enhancement of silicon anode by carbon nanoballs from arc discharge. *Journal of The Electrochemical Society, 158*(7): A809-A813.

233. Wightman, R. M., May, L. J., and Michael, A. C. (1988). Detection of dopamine dynamics in the brain. *Analytical chemistry, 60*(13): 769A-793A.

234. Wu, D., Zhang, Q., Chu, X., Wang, H., Shen, G., and Yu, R. (2010). Ultrasensitive electrochemical sensor for mercury (II) based on target-induced structure-switching DNA. *Biosensors and Bioelectronics, 25*(5): 1025-1031.

235. Wu, H., Chan, G., Choi, J. W., Ryu, I., Yao, Y., McDowell, M. T., et al. (2012). Stable cycling of double-walled silicon nanotube battery anodes through solid–electrolyte interphase control. *Nature nanotechnology, 7*(5): 310 -315.

236. Wu, L., Feng, L., Ren, J., and Qu, X. (2012). Electrochemical detection of dopamine using porphyrin-functionalized graphene. *Biosensors and Bioelectronics, 34*(1): 57-62.

237. Wu, S., He, Q., Tan, C., Wang, Y., and Zhang, H. (2013). Graphene-based electrochemical sensors. *Small, 9*(8): 1160-1172.

238. Wu, S., Zeng, Z., He, Q., Wang, Z., Wang, S. J., Du, Y., et al. (2012). Electrochemically reduced single-layer MoS_2 nanosheets: Characterization, properties, and sensing applications. *Small, 8*(14): 2264-2270.

239. Wu, Z.-S., Ren, W., Wen, L., Gao, L., Zhao, J., Chen, Z., et al. (2010). Graphene anchored with Co_3O_4 nanoparticles as anode of lithium ion batteries with enhanced reversible capacity and cyclic performance. *ACS nano, 4*(6): 3187-3194.

240. Xia, X., Zheng, Z., Zhang, Y., Zhao, X., and Wang, C. (2014). Synthesis of Ag-MoS2/chitosan nanocomposite and its application for catalytic oxidation of tryptophan. *Sensors and Actuators B: Chemical, 192*(3): 42-50.

241. Xiang, C., Xie, Q., and Yao, S. (2003). Electrochemical quartz crystal impedance study of glucose oxidation on a nickel hydroxide modified Au electrode in alkaline solution. *Electroanalysis: An International Journal Devoted to Fundamental and Practical Aspects of Electroanalysis, 15*(11): 987-990.

242. Xu, C., Wang, X., and Zhu, J. (2008). Graphene- metal particle nanocomposites. *The Journal of Physical Chemistry C, 112*(50): 19841-19845.

243. Yang, A., Xue, Y., Zhang, Y., Zhang, X., Zhao, H., Li, X., et al. (2013). A simple one-pot synthesis of graphene nanosheet/SnO_2 nanoparticle hybrid nanocomposites and their application for selective and sensitive electrochemical detection of dopamine. *Journal of Materials Chemistry B, 1*(13): 1804-1811.

244. Yang, L., Liu, D., Huang, J., and You, T. (2014). Simultaneous determination of dopamine, ascorbic acid and uric acid at electrochemically reduced graphene oxide modified electrode. *Sensors and Actuators B: Chemical, 193*(3): 166-172.

245. Yang, T., Chen, M., Kong, Q., Luo, X., and Jiao, K. (2017). Toward DNA electrochemical sensing by free-standing ZnO nanosheets grown on 2D thin-layered MoS_2. *Biosensors and Bioelectronics, 89*(3): 538-544.

246. Yang, T., Yu, R., Chen, H., Yang, R., Wang, S., Luo, X., et al. (2016). Electrochemical preparation of thin-layered molybdenum disulfide-poly (m-aminobenzenesulfonic acid) nanocomposite for TNT detection. *Journal of Electroanalytical Chemistry, 781*(11): 70-75.

247. Yi, H. (2003). Anodic stripping voltammetric determination of mercury using multi-walled carbon nanotubes film coated glassy carbon electrode. *Analytical and bioanalytical chemistry, 377*(4): 770-774.

248. Yi, R., Zai, J., Dai, F., Gordin, M. L., and Wang, D. (2014). Dual conductive network-enabled graphene/Si–C composite anode with high areal capacity for lithium-ion batteries. *Nano energy, 6*(5): 211-218.

249. Yin, W., Yan, L., Yu, J., Tian, G., Zhou, L., Zheng, X., et al. (2014). High-throughput synthesis of single-layer MoS_2 nanosheets as a near-infrared photothermal-triggered drug delivery for effective cancer therapy. *ACS nano, 8*(7): 6922-6933.

250. Yin, W., Yu, J., Lv, F., Yan, L., Zheng, L. R., Gu, Z., et al. (2016). Functionalized nano-MoS_2 with peroxidase catalytic and near-infrared photothermal activities for safe and synergetic wound antibacterial applications. *ACS nano, 10*(12): 11000-11011.

251. Yuan, H., Cheng, G., You, L., Li, H., Zhu, H., Li, W., et al. (2015). Influence of metal–MoS_2 interface on MoS_2 transistor performance: Comparison of Ag and Ti contacts. *ACS applied materials and interfaces, 7*(2): 1180-1187.

252. Zhang, D., Jiang, C., and Sun, Y. e. (2017). Room-temperature high-performance ammonia gas sensor based on layer-by-layer self-assembled molybdenum disulfide/zinc oxide nanocomposite film. *Journal of Alloys and Compounds, 698*(3): 476-483.

253. Zhang, D., Jiang, C., and Zhang, Y. (2017). Room temperature hydrogen gas sensor based on palladium decorated tin oxide/molybdenum disulfide ternary hybrid via hydrothermal route. *Sensors and Actuators B: Chemical, 242*(4): 15-24.

254. Zhang, F., Li, Y., Gu, Y.-e., Wang, Z., and Wang, C. (2011). One-pot solvothermal synthesis of a Cu_2O/graphene nanocomposite and its application in an electrochemical sensor for dopamine. *Microchimica Acta, 173*(1-2): 103-109.

255. Zhang, H., Yu, X., and Braun, P. V. (2011). Three-dimensional bicontinuous ultrafast-charge and-discharge bulk battery electrodes. *Nature nanotechnology, 6*(5): 277-281.

256. Zhang, J., Zhao, C., Liu, N., Zhang, H., Liu, J., Fu, Y. Q., et al. (2016). Tunable electronic properties of graphene through controlling bonding configurations of doped nitrogen atoms. *Scientific reports, 6*(28330): 1-10.

257. Zhang, L., Shi, H. W., Wang, C., and Zhang, K. Y. (2011). Preparation of a nanocomposite film from poly (diallydimethyl ammonium chloride) and gold nanoparticles by in-situ electrochemical reduction, and its application to SERS spectroscopy and sensing of ascorbic acid. *Microchimica Acta, 173*(3-4): 401-406.

258. Zhang, M., Bai, L., Shang, W., Xie, W., Ma, H., Fu, Y., et al. (2012). Facile synthesis of water-soluble, highly fluorescent graphene quantum dots as a robust biological label for stem cells. *Journal of Materials Chemistry, 22*(15): 7461-7467.

259. Zhang, Q.-X., Peng, D., and Huang, X.-J. (2013). Effect of morphology of α-MnO_2 nanocrystals on electrochemical detection of toxic metal ions. *Electrochemistry Communications, 34*(9): 270-273.

260. Zhang, Y., Wen, F., Tan, J., Jiang, C., Zhu, M., Chen, Y., et al. (2017). Highly efficient electrocatalytic oxidation of nitrite by electrodeposition of Au nanoparticles on molybdenum sulfide and multi-walled carbon nanotubes. *Journal of Electroanalytical Chemistry, 786*(2): 43-49.

261. Zhang, Y., Zhao, H., Wu, Z., Xue, Y., Zhang, X., He, Y., et al. (2013). A novel graphene-DNA biosensor for selective detection of mercury ions. *Biosensors and Bioelectronics, 48*(10): 180-187.

262. Zhang, Z., Tang, A., Liao, S., Chen, P., Wu, Z., Shen, G., et al. (2011). Oligonucleotide probes applied for sensitive enzyme-amplified electrochemical assay of mercury (II) ions. *Biosensors and Bioelectronics, 26*(7): 3320-3324.

263. Zhao, J., Chen, G., Zhu, L., and Li, G. (2011). Graphene quantum dots-based platform for the fabrication of electrochemical biosensors. *Electrochemistry Communications, 13*(1): 31-33.

264. Zhao, X., Hayner, C. M., Kung, M. C., and Kung, H. H. (2011). In-plane vacancy-enabled high-power Si–graphene composite electrode for lithium-ion batteries. *Advanced Energy Materials, 1*(6): 1079-1084.

265. Zhi, L., Zuo, W., Chen, F., and Wang, B. (2016). 3D MoS_2 composition aerogels as chemosensors and adsorbents for colorimetric detection and high-capacity adsorption of Hg^{2+}. *ACS Sustainable Chemistry and Engineering, 4*(6): 3398-3408.

266. Zhou, M., Zhai, Y., and Dong, S. (2009). Electrochemical sensing and biosensing platform based on chemically reduced graphene oxide. *Analytical chemistry, 81*(14): 5603-5613.

267. Zhou, W., Upreti, S., and Whittingham, M. S. (2011). Electrochemical performance of Al–Si–graphite composite as anode for lithium–ion batteries. *Electrochemistry Communications, 13*(2): 158-161.

268. Zhou, X., Cao, A.-M., Wan, L.-J., and Guo, Y.-G. (2012). Spin-coated silicon nanoparticle/graphene electrode as a binder-free anode for high-performance lithium-ion batteries. *Nano Research, 5*(12): 845-853.

269. Zhou, X., Huang, X., Qi, X., Wu, S., Xue, C., Boey, F. Y., et al. (2009). In situ synthesis of metal nanoparticles on single-layer graphene oxide and reduced graphene oxide surfaces. *The Journal of Physical Chemistry C, 113*(25): 10842-10846.

270. Zhou, X., Yin, Y.-X., Cao, A.-M., Wan, L.-J., and Guo, Y.-G. (2012). Efficient 3D conducting networks built by graphene sheets and carbon nanoparticles for high-performance silicon anode. *ACS applied materials and interfaces, 4*(5): 2824-2828.

271. Zhou, X., Yin, Y. X., Wan, L. J., and Guo, Y. G. (2012). Self-assembled nanocomposite of silicon nanoparticles encapsulated in graphene through electrostatic attraction for lithium-ion batteries. *Advanced Energy Materials, 2*(9): 1086-1090.

272. Zhou, Z., Bouwman, W., Schut, H., and Pappas, C. (2014). Interpretation of X-ray diffraction patterns of (nuclear) graphite. *Carbon, 69*(4): 17-24.

273. Zhu, C., Yang, G., Li, H., Du, D., and Lin, Y. (2014). Electrochemical sensors and biosensors based on nanomaterials and nanostructures. *Analytical chemistry, 87*(1): 230-249.

274. Zhu, S., Zhang, J., Qiao, C., Tang, S., Li, Y., Yuan, W., et al. (2011). Strongly green-photoluminescent graphene quantum dots for bioimaging applications. *Chemical Communications, 47*(24): 6858-6860.

275. Zhu, Z., Qu, L., Guo, Y., Zeng, Y., Sun, W., and Huang, X. (2010). Electrochemical detection of dopamine on a Ni/Al layered double hydroxide modified carbon ionic liquid electrode. *Sensors and Actuators B: Chemical, 151*(1): 146-152.

276. Zhuang, J., Fu, L., Tang, D., Xu, M., Chen, G., and Yang, H. (2013). Target-induced structure-switching DNA hairpins for sensitive electrochemical monitoring of mercury (II). *Biosensors and Bioelectronics, 39*(1): 315-319.

277. Zhuo, S., Shao, M., and Lee, S.-T. (2012). Upconversion and downconversion fluorescent graphene quantum dots: ultrasonic preparation and photocatalysis. *ACS nano, 6*(2): 1059-1064.

278. Zou, Y., and Wang, Y. (2011). NiO nanosheets grown on graphene nanosheets as superior anode materials for Li-ion batteries. *Nanoscale, 3*(6): 2615-2620.